transactions of the ASME

Published Quarterly by
The American Society of
Mechanical Engineers
Volume 96 • Series C • Number 1
FEBRUARY 1974

journal of heat transfer

EDITED and PUBLISHED quarterly at the offices of The American Society of Mechanical Engineers, United Engineering Center, 345 E. 47th St., New York, N.Y. 10017. Cable address, "Mechaneer," New York. Second-class postage paid at New York, N. Y., and at additional mailing offices.

CHANGES OF ADDRESS must be received at Society headquarters seven weeks before they are to be effective. Please send old label and new address.

PRICES: To members, $15.00, annually; to nonmembers, $30.00. Single copies, $10.00 each. Add $1.50 for postage to countries outside the United States and Canada.

STATEMENT from By-Laws. The Society shall not be responsible for statements or opinions advanced in papers or . . . printed in its publications (B13, Par. 4).

INDEXED by the Engineering Index, Inc.

Technical Briefs

(Contents continued on page 64)

CONTENTS
(CONTINUED)

Discussion

Errata

C. C. GENTRY
Mechanical Engineer,
U. S. Army Materiel Command,
Air Mobility R&D Laboratory,
Fort Eustis, Va.
Assoc. Mem. ASME

D. E. WOLLERSHEIM
Associate Professor,
Department of Mechanical
and Aerospace Engineering,
University of Missouri-Columbia,
Columbia, Mo.

Local Free Convection to Non-Newtonian Fluids From a Horizontal, Isothermal Cylinder

An experimental investigation of local free convection heat transfer rates from a horizontal, isothermal cylinder to non-Newtonian, power-law fluids has been conducted. Experimental data were obtained employing a cylindrical test section 2.304 in. dia and 8.018 in. long, constructed of twenty aluminum segments each independently, electrically heated. Non-Newtonian fluids utilized included four aqueous, carboxypolymethylene solutions. Both local and average Nusselt number results were compared with theoretical and empirical models.

Introduction

THE PRIMARY OBJECTIVE of this investigation was to experimentally determine local free convection heat transfer rates from a horizontal, isothermal cylinder to non-Newtonian, power-law fluids. These experimental data were then compared with the approximate integral solution form developed during this study as well as with similar solution results appearing in the literature.

Previous investigations involving local free convection from horizontal cylinders have dealt principally with Newtonian fluids. Theoretical studies included the analysis by Hermann [1][1] and the integral solution results of both Merk and Prins [2] and Levy [3]. Experimental investigations included the interferometric studies by both Eckert and Soehngen [4] and Jones and Masson [5], as well as the effort by Fand [6]. All the experimental studies employed air as the fluid medium.

Acrivos [7] stimulated interest in free convection to non-Newtonian fluids with his analytical treatment of local heat transfer from two-dimensional, isothermal surfaces to constant property, power-law fluids. The boundary layer equations, utilizing the power-law shear stress relationship, were reduced to dimensionless form employing generalized Grashof and Prandtl number groups, which reduce to conventional Newtonian fluid form at $n = 1$. Imposing the restriction that the value of the generalized Prandtl number form approaches infinity, Acrivos was able to obtain similar solution results in terms of the local Nusselt number as follows:

$$N_{\mathrm{Nu}_x} = \left[-\theta_a'(0) \left(\frac{2n+1}{3n+1}\right)^{\frac{n}{3n+1}} (N_{\mathrm{Gr}_{ar}})^{\frac{1}{2(n+1)}} \times (N_{\mathrm{Pr}_{ar}})^{\frac{n}{3n+1}} \frac{(\sin\phi)^{\frac{1}{2n+1}}}{\left\{\int_{\phi=0}^{\phi} (\sin\phi)^{\frac{1}{2n+1}}\, d\phi\right\}^{\frac{n}{3n+1}}} \right] \quad (1)$$

The term $\theta_a'(0)$ represents the flow behavior index dependent temperature gradient at the cylinder surface.

Several recent investigations have considered free convection from vertical flat plates to power-law fluids. Reilly, Tien, and Adelman [8] and Sharma and Adelman [9] have obtained average free convection data using various Carbopol solutions. Tien [10] has proposed an approximate integral solution assuming that Prandtl number group values are infinite. Dale [11] has conducted an extensive experimental investigation for the constant heat flux condition, which agrees with the similar solution results by Chen [12].

Analysis

Details of an approximate integral analysis, developed during the course of this investigation, are presented in reference [17] for steady, two-dimensional, laminar flow under the condition that $N_{\mathrm{Pr}_{ar}} \to \infty$. In this analysis, which is a logical extension of Tien's [10] effort for an isothermal, vertical flat plate, physical properties were assumed constant except for the density difference term. As has been the case in previous approximate integral studies [3, 10, 13, 14], no distinction was made between the hydrodynamic and thermal boundary layer thicknesses. Frictional dissipation and circumferential conduction were both neglected in the energy equation. A physical representation of the free convection boundary layer is illustrated in Fig. 1.

Integration of Acrivos' [7] simplified boundary layer equations, utilizing the velocity and temperature profile forms of Tien [10],

[1] Numbers in brackets designate References at end of paper.

Contributed by the Heat Transfer Division and presented at the Winter Annual Meeting, Detroit, Mich., November 11–15, 1973, of THE AMERICAN SOCIETY OF MECHANICAL ENGINEERS. Manuscript received by the Heat Transfer Division, January 30, 1973. Paper No. 73-WA/HT-32.

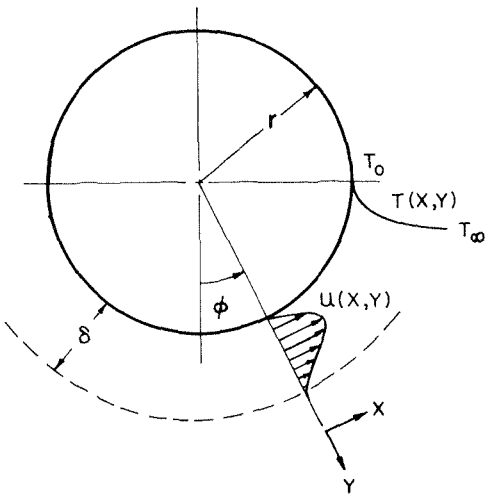

Fig. 1 Free convection boundary layer

results in the following momentum and energy integral expressions:

$$Bg\beta(T_0 - T_\infty)\delta \sin\phi - C\frac{K}{\rho}\left(\frac{u_x}{\delta}\right)^n = 0 \tag{2}$$

$$D\frac{d}{dx}(u_x\delta) = E\frac{\alpha}{\delta} \tag{3}$$

Unlike Tien's momentum integral expression, equation (2) contains a sine term which represents buoyancy force variation with circumferential position. Combining equations (2) and (3) and differentiating the resulting combined expression produces a linear, first order differential equation having the following product solution form for δ in terms of Tien's constants B, C, D, and E:

$$\delta = \left[(r)^{\frac{n}{3n+1}}\left(\frac{3n+1}{2n+1}\right)^{\frac{n}{3n+1}}\left(\frac{C}{B}\right)^{\frac{1}{3n+1}}\left(\frac{E}{D}\right)^{\frac{n}{3n+1}} \times \frac{\left(\frac{K\alpha^n}{\rho g\beta(T_0 - T_\infty)}\right)^{\frac{1}{3n+1}}\left\{\int_{\phi=0}^{\phi}(\sin\phi)^{\frac{1}{2n+1}}\,d\phi\right\}^{\frac{1}{3n+1}}}{(\sin\phi)^{1/2n+1}}\right] \tag{4}$$

The local Nusselt number is expressed in terms of Tien's dimensionless temperature gradient $\theta'(0)$ and the boundary layer thickness δ

$$N_{\mathrm{Nu}_x} = \frac{h_x r}{k} = \frac{-r\theta'(0)}{\delta} = \frac{rE}{\delta} \tag{5}$$

Recognizing that Acrivos' dimensionless groups appear as

$$N_{\mathrm{Gr}_{ar}}^{\frac{1}{2(n+1)}}\,N_{\mathrm{Pr}_{ar}}^{\frac{n}{3n+1}} = \left[\frac{\rho g\beta(T_0 - T_\infty)r^{2n+1}}{K\alpha^n}\right]^{\frac{1}{3n+1}} \tag{6}$$

permits expression of the local Nusselt number in the following form:

$$N_{\mathrm{Nu}_x} = \left[G(n)\left(\frac{2n+1}{3n+1}\right)^{\frac{n}{3n+1}}(N_{\mathrm{Gr}_{ar}})^{\frac{1}{2(n+1)}}(N_{\mathrm{Pr}_{ar}})^{\frac{n}{3n+1}} \times \frac{(\sin\phi)^{\frac{1}{2n+1}}}{\left\{\int_{\phi=0}^{\phi}(\sin\phi)^{\frac{1}{2n+1}}\,d\phi\right\}^{\frac{n}{3n+1}}}\right] \tag{7}$$

The term $G(n)$, comprised of Tien's constants

$$G(n) = E\left(\frac{B}{C}\right)^{\frac{n}{3n+1}}\left(\frac{D}{E}\right)^{\frac{1}{3n+1}} \tag{8}$$

is comparable to Acrivos' term $\theta_a'(0)$. As is evident in Fig. 2, both terms are moderately dependent on flow behavior index values.

Nomenclature

A_{seg} = segment area, ft²
B, C, D, E = Tien's integral solution constants
C_p = specific heat, Btu/lb$_m$-deg F
d = diameter, ft
$F''(0)$ = derivative of similarity function, $d^2F/d\eta^2$ at $\eta = 0$
g = gravitational acceleration, ft/sec²
g_c = gravitational constant, 32.2 lb$_m$-ft/lb$_f$-sec²
$G(n)$ = integral solution function
h = free convection coefficient, Btu/hr-ft²-deg F
i = current, amperes
k = thermal conductivity, Btu/hr-ft-deg F
K = consistency index, lb$_m$/ft-(sec)$^{2-n}$
n = flow behavior index, dimensionless
$N_{\mathrm{Gr}_{ad}}$ = Acrivos' Grashof number form, $\left(\frac{\rho}{K}\right)^2(d)^{n+2}[g\beta(T_0 - T_\infty)]^{2-n}$
$N_{\mathrm{Gr}_{ar}}$ = Acrivos' Grashof number, $\left(\frac{\rho}{K}\right)^2(r)^{n+2}[g\beta(T_0 - T_\infty)]^{2-n}$
$N_{\mathrm{Nu}_{avg}}$ = average Nusselt number, $h_{avg}d/k$
N_{Nu_x} = local Nusselt number, $h_x r/k$
$N_{\mathrm{Pr}_{ad}}$ = Acrivos' Prandtl number form, $\left[\left(\frac{\rho C_p}{k}\right)\left(\frac{K}{\rho}\right)^{\frac{2}{n+1}} \times (d)^{\frac{1-n}{1+n}}\{g\beta d(T_0 - T_\infty)\}^{\frac{3(n-1)}{2(n+1)}}\right]$
$N_{\mathrm{Pr}_{ar}}$ = Acrivos' Prandtl number, $\left[\left(\frac{\rho C_p}{k}\right)\left(\frac{K}{\rho}\right)^{\frac{2}{n+1}} \times (r)^{\frac{1-n}{1+n}}\{g\beta r(T_0 - T_\infty)\}^{\frac{3(n-1)}{2(n+1)}}\right]$
q_0 = surface heat flux, Btu/hr-ft²
R_s = strip resistance, ohms
r = radius, ft
T = temperature, deg F
u = velocity component in x direction, ft/sec
u_x = arbitrary velocity varying with x coordinate, ft/sec
x = coordinate parallel to the surface
y = coordinate normal to the surface
α = thermal diffusivity, ft²/hr
β = coefficient of thermal expansion, 1/deg F
δ = boundary layer thickness, ft
ΔT = surface-to-bulk fluid temperature difference $T_0 - T_\infty$, deg F
θ = dimensionless temperature, $(T - T_\infty)/(T_0 - T_\infty)$
$\theta_a'(0)$ = Acrivos' dimensionless surface temperature gradient
ρ = density, lb$_m$/ft³
τ = shear stress, lb$_f$/ft²
ϕ = circumferential angle

Subscripts

avg = average
f = film
o = surface
s = strip
x = local
∞ = bulk fluid

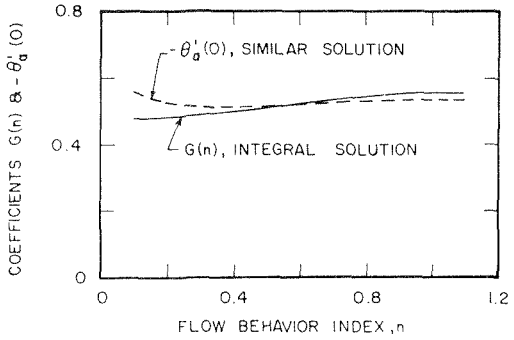

Fig. 2 Similar and integral solution coefficients

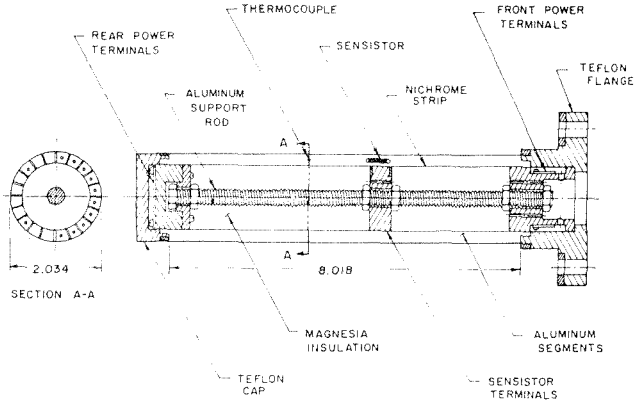

Fig. 3 Cylindrical test section assembly

Experimental Apparatus

Test Fluids. Test fluids utilized during the heat transfer phase of this investigation were water and four dilute, aqueous Carbopol 940 solutions,[2] having mass concentrations of 0.053 percent, 0.055 percent, 0.056 percent, and 0.058 percent. Over the shear rate range encountered, the four Carbopol solutions exhibited power-law fluid characteristics, expresed as

$$\tau = \frac{K}{g_c}\left(\frac{du}{dy}\right)^n \tag{9}$$

Based on the findings of Reilly [8] and Dale [11], all nonrheological properties for the Carbopol solutions were considered to be the same as for water. Rheological properties, summarized in Table 1, were determined using a Brookfield Synchro-Lectric Viscometer, Model LVT, in conjunction with a UL Adapter and with a specially constructed concentric cylinder arrangement. Shear rates produced in these viscometric tests ranged from 0.076 to 7.305 1/sec, which were representative of values encountered at the test section surface. The more dilute Carbopol concentrations were produced by adding additional distilled water to the initial 0.058 percent solution. All solutions were neutralized to a pH $\approx$ 7 using an aqueous, 10 percent by mass sodium hydroxide solution, producing transparent heat transfer fluids. All heat transfer fluids were contained in a 125 gal, rectangular, stainless steel tank. Bulk fluid temperatures were measured using two 30 gal copper-constantan thermocouples and two 30 deg F to 100 deg F precision thermometers, located at the test section horizontal center line, $6^1/_2$ in. on either side of the vertical center line. In addition to the heat transfer fluids, a smaller quantity of 0.058 percent Carbopol 940, having slightly different rheological properties than the 0.058 percent heat transfer solution, was separately prepared for use in estimating shear rates at the test section surface.

Cylindrical Test Section. In order to achieve the desired isothermal surface conditions, the cylindrical test section, depicted in Fig. 3, was constructed of twenty independently heated segments. The twenty segments were produced by longitudinally slotting a previously machined 6061-T6 aluminum tube, 2.000 in. OD and 1.525 in. ID. Each segment was electrically heated using 0.002 in. thick, 0.168 in. wide Tophet C nichrome resistance strips bonded to the segment interior surface utilizing a thin, 0.005 in. thickness of RTV silicone adhesive. Prior to bonding, each segment was coated with a 0.005 in. thickness of Eccocoat 672 on all but the fluid exposed surface to provide electrical insulation. Since symmetry existed about the test section vertical center line, only ten individual heating and temperature measurement circuits were required, corresponding to angular positions of 9 deg, 27 deg, 45 deg, 63 deg, 81 deg, 99 deg, 117 deg, 135 deg, 153 deg, and 171 deg, measured from the lower stagnation point.

Temperature measurements were made using 30 gal, Teflon insulated, copper-constantan thermocouples installed within the aluminum segment at a diameter of 1.806 in. Surface temperatures were then determined from these measured values using Fourier's conduction equation. Within the same segments, Texas Instrument No. TI-TG-1/8, 120 ohm sensitors, 0.105 in. dia and 0.300 in. long, were installed as temperature detectors for the power supply and controller unit.

The interior of the reassembled test section, having a mean outer diameter of 2.034 in. and a heated length of 8.018 in., was filled with loose fitting, magnesia insulation. Thermal insulation between adjoining aluminum segments was provided by sealing the 0.031 in. wide slots with silicone adhesive. The support flange was constructed of Teflon (TFE) to minimize longitudinal conduction losses to the support structure.

Power Supply and Controller. The ten channel power supply and controller unit consisted of a triac trigger circuit, sensistor bridge circuit, and voltage measurement circuit, as shown in Fig. 4. The triac trigger circuit served as the output voltage control device, utilizing a bi-directional silicon triac. Control was acccomplished by imposing an excitation voltage on the triac, resulting in the triac being in a conducting state over some time period less than half the 60 Hz input voltage period. The net effect of this action was that only a portion of the input sine wave voltage was utilized, providing precise heater control.

The sensistor bridge circuit provided the activation voltage necessary for the triac circuit. This activation voltage resulted from an imbalance between the Spectrol Precision Ten Turn Potentiometers No. 570-246 and temperature sensitive Texas Instrument Sensistors No. TI-TG-1/8.

Measurement of the true rms voltage for the triac modified output was accomplished by the voltage measurement circuit, consisting of five scale resistors, a limiting amplifier, and an incan-

[2] Carboxypolymethylene type 940, B. F. Goodrich Chemical Co.

Table 1 Rheological properties for Carbopol 940 solutions

Temperature deg F	0.053 percent solution		0.055 percent solution		0.056 percent solution		0.058 percent solution	
	n	K	n	K	n	K	n	K
70	0.856	0.0157	0.794	0.0303	0.747	0.0499	0.642	0.101
80	0.909	0.0121	0.819	0.0245	0.763	0.0411	0.660	0.0852
90	0.926	0.0101	0.842	0.0202	0.774	0.0336	0.675	0.0715
100	0.932	0.00868	0.857	0.0166	0.773	0.0284	0.689	0.0611

descent lamp. The 6 v, type 47 incandescent lamp was enclosed in a light free container along with a type 868, vacuum phototube. Light from the lamp produced a small change in the phototube anode current. This change in anode current, which was dependent only on the heater circuit voltage drop, was detectable in the form of a voltage drop across a large coupling resistor, producing a three digit output display on the Weston meter. All five range scales of the voltage measurement circuit were calibrated using a true rms voltmeter.

Local heat transfer coefficients for each of the ten angular positions were obtained from voltmeter circuit and temperature difference measurements, in accordance with

$$h_x = \frac{(q_0)_x}{(T_0 - T_\infty)} = \frac{3.413(i^2)(R_s)}{A_{\text{seg}}(T_0 - T_\infty)} \tag{10}$$

Current i for each segment was determined from total rms voltage drop measurements and total circuit resistance values. Special tests were conducted to assure resistance uniformity, 0.131 ohm/in. ± 1.64 percent, of the nichrome heater strip material. Strip resistance change with temperature was determined to be approximately 0.7 percent and was therefore neglected.

Shear Rate Apparatus. The technique employed for estimating shear rates at the test section surface is similar to the dye injection schemes utilized by Eichhorn [15] and Dale [11]. Surface shear rates were determined from velocity profile slopes which were obtained from motion picture photographs of dye streak lines. The heated test section was installed in a plexiglass tank, which was equipped with a syringe holder-ramp assembly. The syringe holder-ramp assembly permitted radial movement of the injection needles at angles of 0 deg, 27 deg, 45 deg, 63 deg, and 90 deg, although measurements were made only at 45 deg and 63 deg. Dye used was neutral density blue food coloring, composed of a 1.5 percent propylene glycol-water solution. A precision digital timer provided the time base and known needle tip dimensions provided the displacement scale. Bulk fluid temperatures were determined using two precision thermometers. Filming was accomplished using a Bolex 155, 8 mm movie camera with Kodachrome II, Type A film.

Experimental Results

Surface Shear Rates. Shear rates at the test section surface influence heat transfer results to the extent that flow behavior index and consistency index values are moderately shear rate dependent. As is evident in rheological curves appearing in [11, 17], significant changes in n and K values occur only with relatively large changes in shear rate. The objective of this simple experiment was to establish the approximate location on the rheological curve at which the test section was operating, in a representative Carbopol 940 solution, for viscometric purposes. In addition, these data would serve to provide some degree of experimental verification for the shear rate expression arising from Acrivos' [7] work.

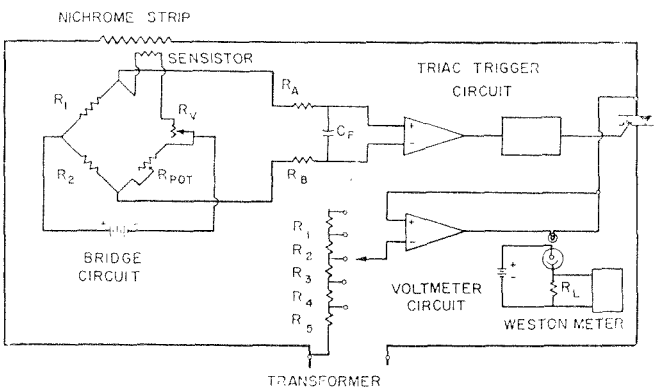

Fig. 4 Power supply and controller unit schematic

Table 2 Experimental and theoretical surface shear rates

Angle ϕ	Temperature difference	Experimental shear rates 1/sec	Acrivos' theoretical shear rates 1/sec 0.056 percent	Acrivos' theoretical shear rates 1/sec 0.058 percent
45 deg	20 deg F	0.46	0.55	0.33
45 deg	40 deg F	1.33	1.72	0.83
63 deg	39 deg F	1.88	2.36	1.17

$$\left(\frac{\partial u}{\partial y}\right)_0 = \left[\left(\frac{3n+1}{2n+1}\right)^{\frac{1}{3n+1}} \frac{\{g\beta r(T_0 - T_\infty)\}^{1/2}}{r} \frac{(N_{\text{Gr}_{ar}})^{\frac{1}{2(n+1)}}}{(N_{\text{Pr}_{ar}})^{\frac{1}{3n+1}}} \times (\sin\phi)^{\frac{2}{2n+1}} \left\{\int_{\phi=0}^{\phi} (\sin\phi)^{\frac{1}{2n+1}} d\phi\right\}^{\frac{1}{3n+1}} F''(0)\right] \tag{11}$$

In the present experiment, shear rate data were obtained at angles of 45 deg for ΔT values of 20 deg F and 40 deg F, and 63 deg for a ΔT value of 39 deg F, utilizing a test solution having rheological properties comparable to the 0.056 percent and 0.058 percent heat transfer solutions. No direct comparison between experimental and predicted shear rates for the shear rate test fluid is provided. The reason is that rheological degradation was detected in the shear rate test fluid during the three week time lapse between completion of the dye injection phase and attempts to obtain viscometric data at temperatures other than 70 deg F. However, a comparison is provided in Table 2 between experimental shear rates and predicted values from equation (11) for the 0.056 percent and 0.058 percent heat transfer fluids at comparable angles and temperature difference values. Based on the results appearing in Table 2, it was concluded that reasonable confidence could be placed in predicted shear rate values from equation (11), which ranged from 0.024 to 8.048 1/sec for all heat transfer test solutions. Viscometric data were obtained over the shear rate range from 0.076 to 7.305 1/sec.

Local Free Convection. Experimental free convection data were obtained for the five test fluids at surface-to-bulk fluid temperature difference of from 14 deg F to 49 deg F. Heat transfer rates ranged from 14.3 Btu/hr-ft²-deg F for the 0.058 percent solution at ϕ = 171 deg to 114.2 Btu/hr-ft²-deg F for water at ϕ = 9 deg. Flow behavior index values for the Carbopol 940 solutions varied from 0.655 to 0.933. All local free convection data were expressed in terms of Acrivos' [7] dimensionless groups. Effects of variable fluid properties were accounted for by evaluating physical properties at the film temperature, which is defined as the mean of the surface and bulk fluid temperatures. Comparisons are made between experimental data and theoretical similar and integral solution results. Over the range of n values encountered, similar and integral solution forms, equations (1) and (7), are very nearly equal and are represented by a single curve.

Local free convection data for water, obtained at ΔT values from 20 deg F to 36 deg F, are presented in Fig. 5. As is evident in this comparative plot, the water data are represented rather well by the theoretical curve, although the data are approximately 10 percent below predicted values for ϕ = 0 deg to 120 deg. Similar plots are provided for the 0.053 percent, 0.055 percent, and 0.056 percent Carbopol 940 solutions in Figs. 6, 7, and 8. Experimental data for these solutions are also in general agreement with the theoretical curves, although at angular values greater than 150 deg, the data appear above the predicted curve. It is suggested that this phenomena evident in the upper stagnation region results from boundary layer interaction not accounted for in the theoretical treatment. Local free convection results for the 0.058 percent solution, representing ten test cases having ΔT values from 14 deg F to 45 deg F, appear in Fig. 9. It is for this solution, exhibiting the greatest degree of non-Newtonian

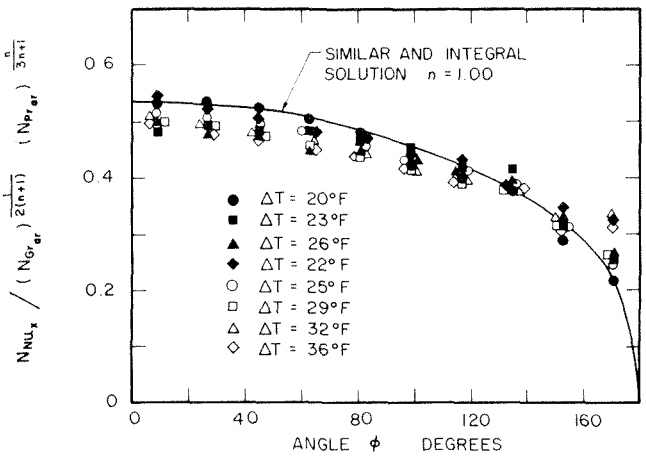

Fig. 5 Local free convection results for water

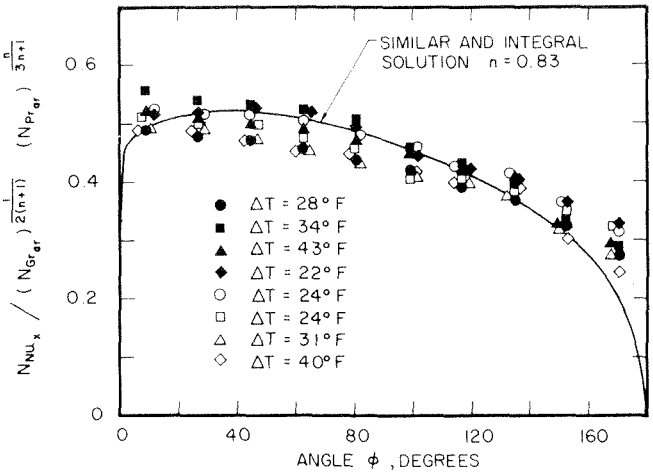

Fig. 7 Local free convection results for 0.055 percent Carbopol 940

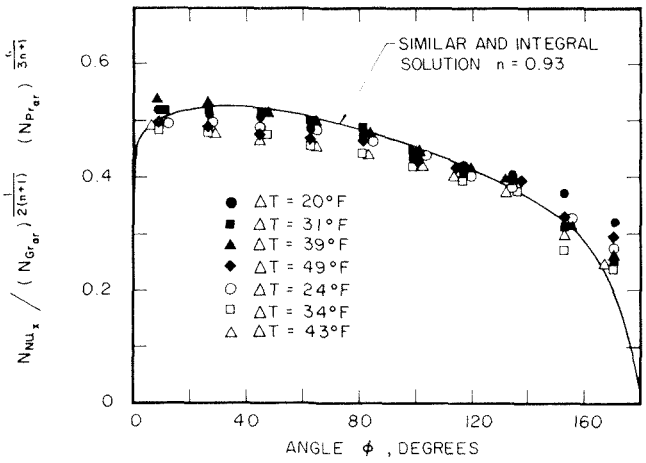

Fig. 6 Local free convection results for 0.053 percent Carbopol 940

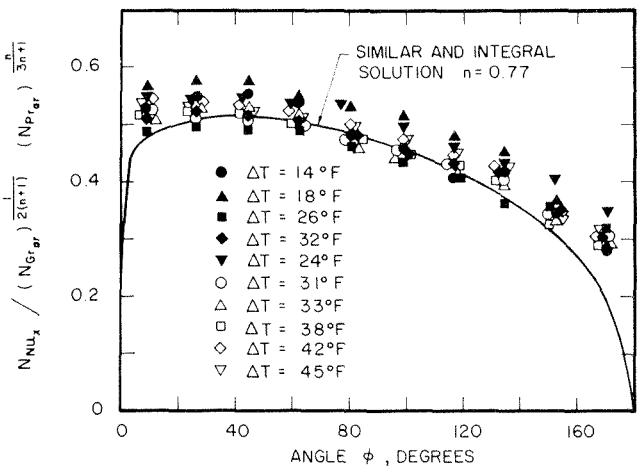

Fig. 8 Local free convection results for 0.056 percent Carbopol 940

behavior, that the most pronounced difference between theory and experiment exists. A comparison of experimental data for the more concentrated solutions reveals a gradual increase in results with increasing fluid concentration. This behavior may indicate that Acrivos' generalized dimensionless groups are not as sensitive to rheological property change as conventional, Newtonian fluid groups are to absolute viscosity change. However, previous results [4, 5, 6] involving local free convection from horizontal cylinders to a well defined Newtonian fluid such as air exhibit data variation comparable to that of the present 0.058 percent solution.

Average Free Convection. Average free convection results were obtained by integrating local Nusselt, Prandtl, and Grashof numbers over the test section surface area. Since average results for Newtonian fluids usually appear with diameter as the characteristic dimension, the same procedure was followed in this analysis involving non-Newtonian fluids. Grashof and Prandtl numbers are the same as proposed by Acrivos, except that the diameter was used as the characteristic length.

Results for water and for the four Carbopol solutions, extending over the Grashof-Prandtl product range from 7.79×10^4 to 7.42×10^7, are compared in Fig. 10 with the McAdams [16] correlation. As is evident in this plot, the maximum difference between the experimental data and McAdams' curve is approximately 20 percent. A least square curve fit of all experimental data revealed a slope of 0.20 and an intercept of 1.19, compared to the McAdams values of 0.25 and 0.53.

Conclusions

The following conclusions may be drawn from this investigation:

1 An approximate integral solution was developed which agreed well with the more rigorous similar solution formulated by Acrivos [7].

2 Local free convection data obtained from a horizontal, isothermal cylinder immersed in water and in four Carbopol 940 solutions were in general agreement with the similar and integral solution results.

3 Average free convection data for all test fluids, expressed in terms of Acrivos' dimensionless groups with diameter as the characteristic length, were satisfactorily represented by the McAdams' [16] correlation.

4 Limited experimental surface shear rate data increase confidence in the theoretical expression based on Acrivos' similar solution results.

Acknowledgments

This investigation was conducted under the sponsorship of the National Science Foundation through Grant GK-5454 and the University of Missouri-Columbia. Appreciation is expressed to Dr. James E. Rathke, Department of Electrical Engineering, for his efforts in designing the power supply and controller unit used in this investigation.

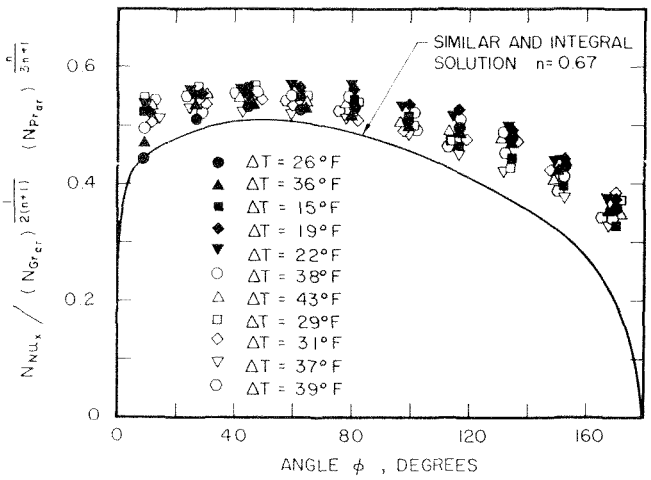

Fig. 9 Local free convection results for 0.058 percent Carbopol 940

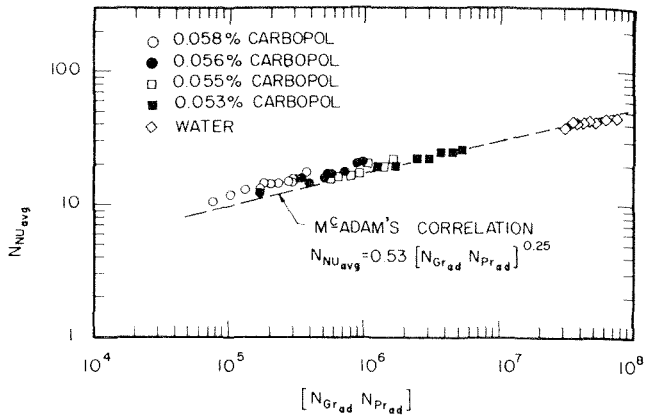

Fig. 10 Average free convection results

References

1 Hermann, R., "Heat Transfer by Free Convection From Horizontal Cylinders in Diatomic Gases," NACA Technical Memorandum 1366, (translation), 1954.

2 Merk, H. J., and Prins, J. A., "Thermal Convection in Laminar Boundary Layers," *Appl. Sci. Res.*, Section A, Vol. 4, 1954, pp. 195–221.

3 Levy, S., "Integral Methods in Natural Convection Flow," *Journal of Applied Mechanics, Trans. ASME*, 1955, pp. 515–522.

4 Eckert, E. R. G. and Soehngen, E. E., "Studies on Heat Transfer in Laminar Free Convection With the Zehnder-Mach Interferometer," USAF Air Materiel Command, Technical Report No. 5747, Dayton, Ohio, 1948.

5 Jones, C. D., and Masson, D. J., "An Interferometric Study of Free Convection Heat Transfer From Enclosed Isothermal Surfaces," TRANS. ASME, 1955, pp. 1275–1281.

6 Fand, R. M., et al., "The Local Heat Transfer Coefficient Around a Heated Horizontal Cylinder in an Intense Sound Field," JOURNAL OF HEAT TRANSFER, TRANS. ASME, 1962, pp. 245–250.

7 Acrivos, A., "A Theoretical Analysis of Laminar Natural Convection Heat Transfer to Non-Newtonian Fluids," *A.I.Ch.E. Journal*, Vol. 6, No. 4, 1960, pp. 584–590.

8 Reilly, I. G., Tien, C., and Adelman, M., "Experimental Study of Natural Convection Heat Transfer From a Vertical Plate in a Non-Newtonian Fluid," *Can. J. Chem. Eng.*, Vol. 43, 1965, pp. 157–160.

9 Sharma, K. K., and Adelman, M., "Experimental Study of Natural Convection Heat Transfer From a Vertical Plate in a Non-Newtonian Fluid," *Can. J. Chem. Eng.*, Vol. 47, 1969, pp. 553–555.

10 Tien, C., "Laminar Natural Convection Heat Transfer From Vertical Plate to Power-Law Fluid," *Appl. Sci. Res.*, Vol. 17, 1967, pp. 233–248.

11 Dale, J. D., "Laminar Free Convection of Non-Newtonian Fluids From a Vertical Flat Plate With Uniform Surface Heat Flux," PhD thesis, University of Washington, Seattle, Wash., 1969.

12 Chen, T. Y., "On the Solution of External Laminar Free Convection to Power Law Fluids," PhD thesis, University of Missouri-Columbia, Columbia, Mo., 1971.

13 Fujii, T., "Mathematical Analysis of Heat-Transfer From a Vertical Flat Surface by Laminar Free Convection," *Bulletin of JSME*, Vol. 2, No. 7, 1959, pp. 365–369.

14 Eckert, E. R. G., and Drake, R. M., *Heat and Mass Transfer*, Second ed., McGraw-Hill, New York, 1959, pp. 312–315.

15 Eichhorn, R., "Flow Visualization and Velocity Measurement in Natural Convection With the Tellurium Dye Method," JOURNAL OF HEAT TRANSFER, TRANS. ASME, 1961, pp. 379–381.

16 McAdams, W. H., *Heat Transmission*, third ed., McGraw-Hill, New York, 1954, pp. 175–177.

17 Gentry, C. C., "Local Free Convection to Non-Newtonian Fluids From a Horizontal, Isothermal Cylinder," PhD thesis, University of Missouri-Columbia, Columbia, Mo., 1972.

ERRATA

An errata on V. K. Dhir and J. H. Lienhard, "Similar Solutions for Film Condensation With Variable Gravity or Body Shape," published in the November, 1973, issue of the Journal of Heat Transfer, pp. 483–486.

Equation (10) should be $\theta'' + AF\theta' = 0$ instead of $\theta'' + AF\theta'' = 0$.
0.1 on the ordinate in Fig. 3 should be 0 (zero).
The words "since inertia contributions are minimal" should be deleted from the last paragraph of the "Conclusions" section.
In reference [3] the words *Journal of Heat Transfer* should be deleted and Vol. 87, 1965, should be Vol. 78, 1956.

J. W. YANG
Associate Professor,
Department of Mechanical Engineering,
State University of New York at Buffalo
Buffalo, N. Y. Mem. ASME

C. SCACCIA
Assistant Staff Engineer,
Union Carbide Corp., Linde Division,
Tonawanda, N. Y.

J. GOODMAN
Lecturer,
Faculty of Mechanical Engineering,
Technion—Israel Institute of Technology,
Technion, Israel

Laminar Natural Convection About Vertical Plates With Oscillatory Surface Temperature

The characteristics of laminar natural convection about a vertical plate with periodically changing surface temperature have been studied by the finite-difference method. The effects of the amplitude and period of the surface temperature oscillation on the instantaneous and time-average Nusselt numbers, temperature and velocity profiles are demonstrated by several examples. High amplitude and a large range of frequency of the oscillation were considered in these examples. The time-wise variation of the fluid temperature in the inner region adjacent to the surface produces back heat flow at high amplitude, high frequency, and at high local Grashof number.

Introduction

Natural convection with a periodically changing surface temperature is important in many engineering applications. For example, in automatic control systems, electrical and electronic components are frequently subjected to periodic heating and are cooled by the natural convection mechanism. It appears that this type of convection process has not yet been studied in detail. Several authors have performed analysis for the general unsteady problem with the arbitrarily time-dependent surface temperature. Sparrow and Gregg [1][1] studied the case in which the surface temperature varies slightly about a mean level which is higher than the ambient temperature. After the usual similarity analysis, they carried out a perturbation analysis in terms of the amplitude of the surface temperature variation. Their results are restricted to small amplitude and are valid if the high order derivatives of the surface temperature with respect to time decrease rapidly. Chung and Anderson [2] considered the same problem and used a slightly different perturbation expansion to solve it. Their results are still subjected to restrictions in amplitude. The effect of sinusoidal variation in the surface temperature was studied by Nanda and Sharma [4, 5]. By writing the temperature and the velocity as sums of steady and oscillatory components, they obtained solutions for large and for small values of frequency. Their work has been extended by Kelleher and Yang [5] to include the nonuniform surface temperature variation. Solutions were again obtained in the low and high-frequency regions by means of formal asymptotic expansions. Their results are valid for small amplitude of the surface temperature variation. The case of sinusoidal variation of surface temperature was also included in the asymptotic solutions of unsteady natural convection obtained by Schetz and Eichhorn [6], and Monold and Yang [7]. These solutions were developed for the parallel-flow regime which represents the short period after the transient has been started and in which heat is transferred by conduction only.

In view of the foregoing references, it is seen that the natural convection oscillatory flow with high amplitude and in the intermediate-frequency region has not been treated yet and cannot be treated by the general perturbation and asymptotic expansions. The application of finite-difference method on such a problem is presented in this paper. It will be shown that the finite-difference method has no restriction on the amplitude and frequency of the surface temperature variation. Solutions can be obtained for both short and long period time after the transient has been started. The effects of surface temperature oscillation on the heat transfer rate, and temperature and velocity profiles are demonstrated through numerical examples.

Analysis

A schematic diagram of the physical model and coordinate system is shown in Fig. 1. A vertical flat plate is maintained at spatially uniform temperature $T_w(t)$. The time-dependent surface temperature oscillates around a mean temperature T_m, which is higher than the ambient temperature T_∞. The timewise variation of the surface temperature is described by the following equation:

[1] Numbers in brackets designate References at end of paper.

Contributed by the Heat Transfer Division for publication (without presentation) in The Journal of Heat Transfer. Manuscript received by the Heat Transfer Division February 16, 1973. Paper No. 74-HT-B.

$$T_w - T_m = (T_m - T_\infty)A \sin \omega t \tag{1}$$

where A is the dimensionless amplitude parameter and $\omega/2\pi$ is the frequency of the oscillation. In practice, A is a positive number less than unity. Due to the difference between the surface and the ambient temperatures, a thermal boundary layer flow is induced by the buoyancy effect. The equations expressing conservation of mass, momentum, and energy for unsteady laminar flow in dimensionaless form are as follows:

$$\frac{\partial U}{\partial X} + \frac{\partial V}{\partial Y} = 0 \tag{2}$$

$$\frac{\partial U}{\partial \tau} + U\frac{\partial U}{\partial X} + V\frac{\partial U}{\partial Y} = 2\varphi + \frac{\partial^2 U}{\partial Y^2} \tag{3}$$

$$\frac{\partial \varphi}{\partial \tau} + U\frac{\partial \varphi}{\partial X} + V\frac{\partial \varphi}{\partial Y} = \frac{1}{\mathrm{Pr}}\frac{\partial^2 \varphi}{\partial Y^2} \tag{4}$$

where the dimensionless variables are:

$$U = \frac{ux}{\nu}\mathrm{Gr}_m^{-1/3}, \qquad V = \frac{vx}{\nu}\mathrm{Gr}_m^{-1/3}, \qquad \varphi = \frac{T - T_\infty}{2(T_m - T_\infty)},$$

$$X = \mathrm{Gr}_m^{1/3}, \qquad Y = \frac{y}{x}\mathrm{Gr}_m^{1/3}, \qquad \tau = \frac{t\nu}{x^2}\mathrm{Gr}_m^{2/3} \tag{5}$$

and

$$\mathrm{Gr}_m = g\beta(T_m - T_\infty)x^3/\nu^2.$$

It should be pointed out that an arbitrary constant "2" was added to the denominator of the definition of the dimensionless temperature φ, equation (5). This is due to the fact that the stability requirement does not permit the surface temperature to oscillate around unity. The corresponding initial and boundary conditions are

$$U = 0, \qquad V = 0, \qquad \varphi = 0 \quad \text{at} \quad \tau = 0 \tag{6}$$

$$U = 0, \qquad V = 0, \qquad \varphi = {}^1/_2(1 + A \sin(2\pi\tau/P)) \quad \text{at} \quad Y = 0, \qquad \tau > 0 \tag{7}$$

$$U = 0, \qquad \varphi = 0 \quad \text{at} \quad Y \to \infty \quad \text{and} \quad X = 0, \qquad \tau > 0 \tag{8}$$

It is seen that the foregoing system is governed by three parameters: the Prandtl number of the fluid, the amplitude parameter A, and the dimensionless period P defined as

$$P = \frac{2\pi\nu}{\omega}[g\beta(T_m - T_\infty)/\nu^2]^{2/3} \tag{9}$$

Since the solutions are not similar for the present case of oscillatory natural convection, equations (2)–(8) are solved by the finite-difference method. The time-dependent finite-difference method is an extension of the method developed by Hellums and Churchill [8, 9] for step change surface temperature. The stability and convergence requirements were discussed in detail in [8]. The resulting explicit difference equations are indicated in the following:

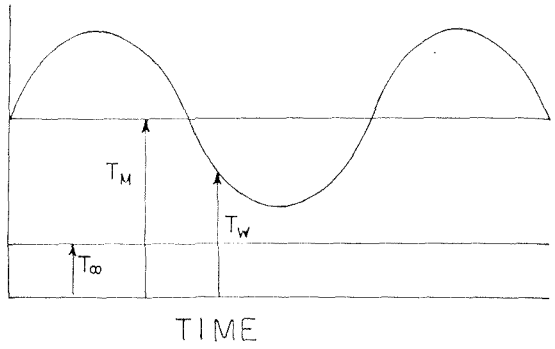

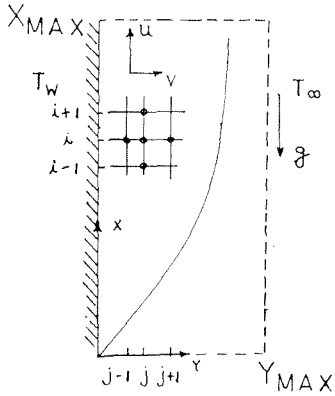

Fig. 1 Physical model and coordinates

$$\varphi_{i,j}' = \varphi_{i,j}(1 - A_1 + A_2 - 2A_3) + \varphi_{i-1,j}A_1 + \varphi_{i,j-1}A_3 + \varphi_{i,j+1}(A_3 - A_2) \tag{10}$$

$$U_{i,j}' = U_{i,j} + \Delta\tau[-U_{i,j}(U_{i,j} - U_{i-1,j})/\Delta X - V_{i,j}(U_{i,j+1} - U_{i,j})/\Delta Y + 2\varphi_{i,j}' + (U_{i,j+1} - 2U_{i,j} + U_{i,j-1})/(\Delta Y)^2] \tag{11}$$

$$V_{i,j}' = V_{i,j-1}' - \Delta Y[(U_{i,j}' - U_{i-1,j}')/\Delta X] \tag{12}$$

where

Nomenclature

A = dimensionless amplitude parameter, equation (1)
g = acceleration due to gravity
Gr = Grashof number
h = heat-transfer coefficient
k = thermal conductivity of fluid
Nu = Nusselt number
P = dimensionless period parameter, equation (15)
Pr = Prandtl number
q = heat flux
t = time
T = temperature
u = component of velocity in vertical direction
U = dimensionless velocity, equation (8)
v = component of velocity in horizontal direction
V = dimensionless velocity, equation (8)
x = vertical distance
X = dimensionless distance, equation (8)
y = horizontal distance from plate
Y = dimensionless distance, equation (8)
α = thermal diffusivity of fluid
β = thermal expansion coefficient
ν = kinematic viscosity
ϕ = dimensionless temperature, equation (8)
τ = dimensionless time, equation (8)
ω = frequency

Subscripts

m = mean value
w = value at wall ($y = 0$)
x = local value of x
∞ = value at infinity

$$A_1 = U_{i,j}\Delta\tau/\Delta X$$
$$A_2 = V_{i,j}\Delta\tau/\Delta Y \quad (13)$$
$$A_3 = \Delta\tau/[(\Delta Y)^2 \,\mathrm{Pr}]$$

The primed quantities in equations (10)–(12) indicate the value of the variables at the new time interval. The set of explicit difference equations are first order accurate in time and in the convective terms. Forsythe [10] and Richtmyer [11] have shown that the "up-wind" finite differences are necessary to ensure convergence and stability in the nonlinear, first order convective terms. The diffusion terms are expressed as central differences with second order accuracy. In the computational procedure φ' is first calculated at each grid point, in terms of the variables of the previous time step, from equation (10). Subsequently U' is calculated at each mesh point from equation (11), using the values of φ' already known. Finally the variable V' is determined by using the values of U' and by scanning the flow field row by row, from left to right, so that the V' calculated at the left of the point of interest is immediately used in equation (12). Several time steps $\Delta\tau$ of decreasing magnitude were considered for each case analyzed. The relative error in the solution at specific real times, τ, was compared, using successive selections of $\Delta\tau$. The final time step $\Delta\tau$ selected was the one corresponding to a relative error less than 10^{-2}.

With oscillating boundary conditions, it is known that at high frequencies, the boundary layer response is confined in a thin region adjacent to the surface. The thickness of this region is proportional to $(\nu/\omega)^{1/2}$. Thus in choosing the mesh size, both stability [8] and oscillating layer thickness have to be considered. The additional criterion for the present case is

$$\nabla y < (\nu/\omega)^{1/2} \quad (14)$$

or, in dimensionless form

$$\nabla Y < (P/2\pi)^{1/2} \quad (15)$$

A 60 × 60 mesh with variable grid spacing in the Y-direction was employed in the numerical calculations. The variable mesh size near the wall, with uniform increasing grid spacing in the Y-direction, was selected to satisfy the criterion of equation (15). Several numerical calculations were performed for Pr = 0.7 at A = 0.2, 0.4, 0.5 and P = 3.2, 6.4, and 32. The amplitudes are considerably higher than that permitted by the perturbation method [3–5]. Kelleher and Yang [5] have expressed the frequency by a dimensionless parameter Z and performed their calculations for $0.1 < Z < 1$ in the low frequency region and $10 < Z < 100$ in the high-frequency region. The parameter Z is related to the present parameter P by the following equation:

$$Z = 4\pi \,\mathrm{Gr}_m^{1/6}/P \quad (16)$$

For Gr_m in the range 10^6 to 10^9 and P between 3.2 to 32, the parameter Z is then in the range 4 to 120. This covers the entire high-frequency region Kelleher and Yang have investigated [5].

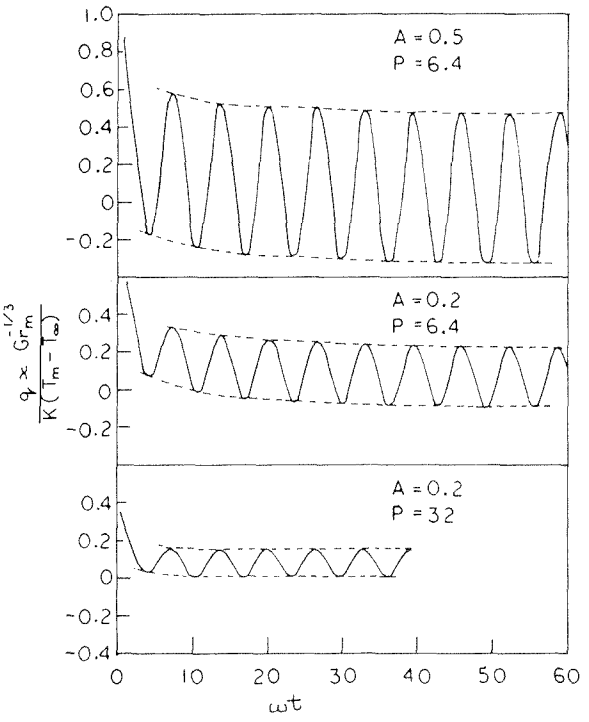

Fig. 2 Representative curves of transient heat flux at X = 487.2

Discussion of Results. Numerical solutions can be obtained by the finite-difference method for both short and long period time after the transient has been started. It is known for the case of step change in surface temperature that the fully developed convective flow is established after a short period of conduction and transition stage [12, 13]. The situation is about the same for the present case of oscillatory surface temperature. A quasi-steady state is reached within a few cycles after the oscillatory surface temperature has been imposed. The quasi-steady state is defined as the state at which the wall heat flux and fluid temperature profiles follow a defined periodic variation of time. Detailed numerical calculation indicates that the number of cycles within which the quasi-steady period is approached depends on the period P but is indifferent to the amplitude parameter A. Some representative curves of the transient heat flux are shown in Fig. 2. It is seen that nine cycles are required to approach the quasi-steady period at P = 6.4 for both A = 0.2 and 0.5. The number of cycles is reduced to three as P increases to 32. Practically, the real time of the transient period is very short for most of the engineering applications. Hence, only the results obtained for the steady-state period will be discussed hereafter.

Hellums and Churchill [8] have shown that, for the case of step change surface temperature, the three independent variables (X, Y, τ) can be reduced so that $U/X^{1/4}$, $VX^{1/4}$, and φ depend only on $Y/X^{1/4}$ and $\tau/X^{1/2}$. The spatial variable $Y/X^{1/4}$ assumes the standard form of the similarity variable for the case of steady state surface temperature, $y\,\mathrm{Gr}_m^{1/4}/x$; the time variable $\tau/X^{1/2}$ is explicitly dependent on the Grashof number based on the mean surface temperature, $(t\nu/x^2)\mathrm{Gr}_m^{1/4}$. As the surface temperature undergoes a periodic variation, numerical calculations show that the foregoing two independent variables cannot specify the convective process. In addition to the timewise variation, the velocity and temperature profiles also depend on the amplitude and period of the oscillation and on the dimensionless distance X (or the local mean Grashof number Gr_m). Representative velocity profiles are shown in Fig. 3, which indicates a slight dependence on the period parameter P and a relatively stronger dependence on length X. Fig. 3 also reveals that the velocity distribution approaches the steady-state case [14] for large X. Due to the propagation of the oscillation in the velocity field, the leading edge effect is probably more important in the oscillatory natural convection. Numerical calculations show that a timewise oscillation of the velocity distribution occurs in a thin region between the wall surface and the point at which the maximum velocity exists. For P = 3.2 to 32 and A = 0.2 to 0.5, the oscillation of the fluid velocity in this region is less than 2 percent during a complete cycle and is not shown in graphs. No dependence on the amplitude parameter A was obtained from numerical calculations.

The variations of temperature profiles with these parameters are much stronger as illustrated in Figs. 4–6. The timewise variation and the dependence on X are shown in Fig. 4 for high amplitude (A = 0.5), and in Fig. 5 for lower amplitude (A = 0.2) and P = 6.4. In both cases, the oscillation of fluid temperature

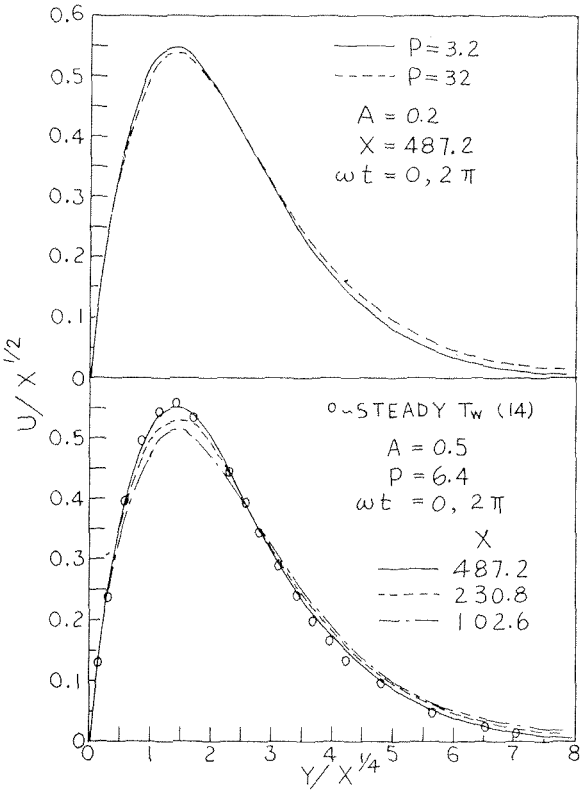

Fig. 3 Representative velocity profiles

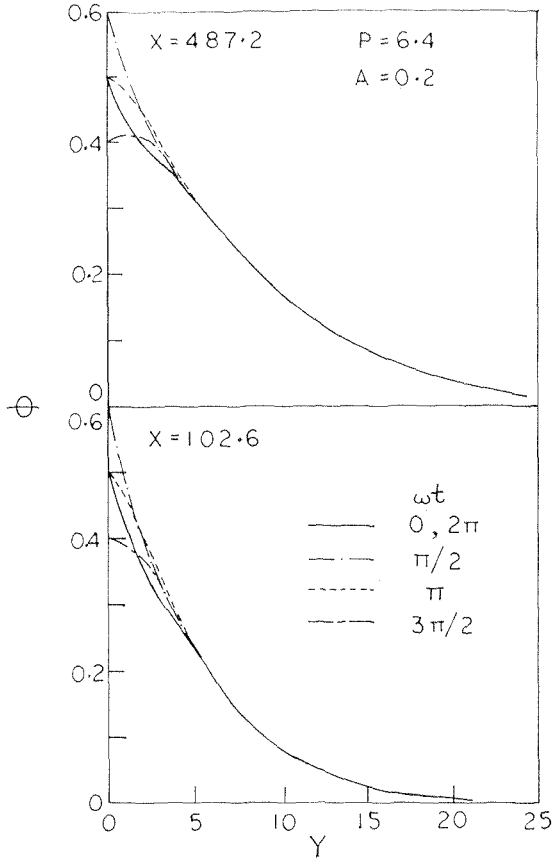

Fig. 5 Representative temperature profiles at low amplitude

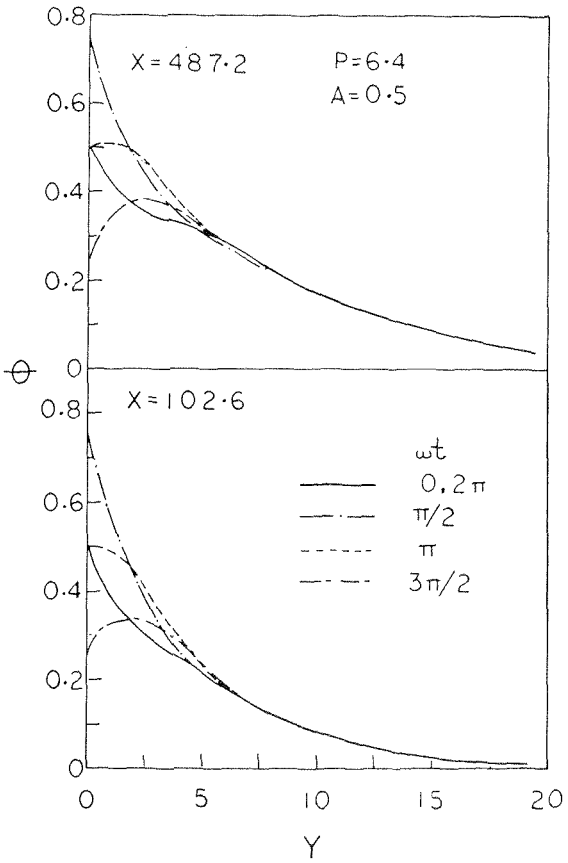

Fig. 4 Representative temperature profiles at high amplitude

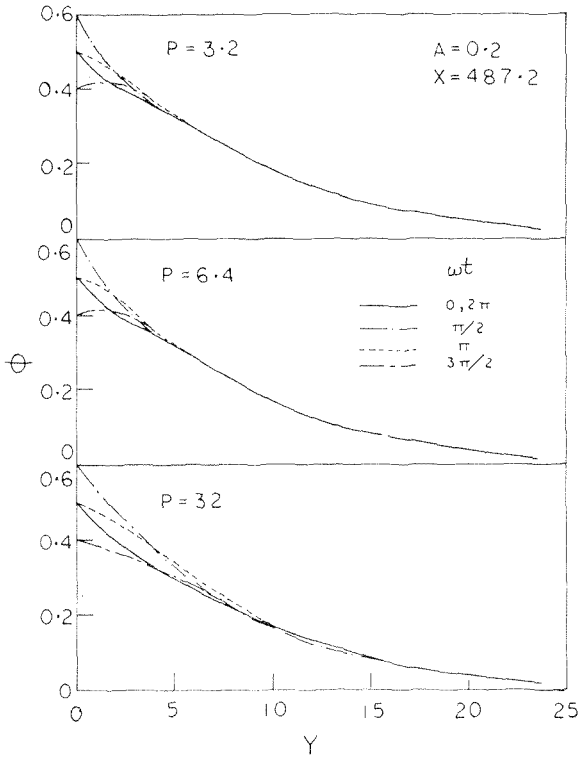

Fig. 6 Effect of period on temperature profiles

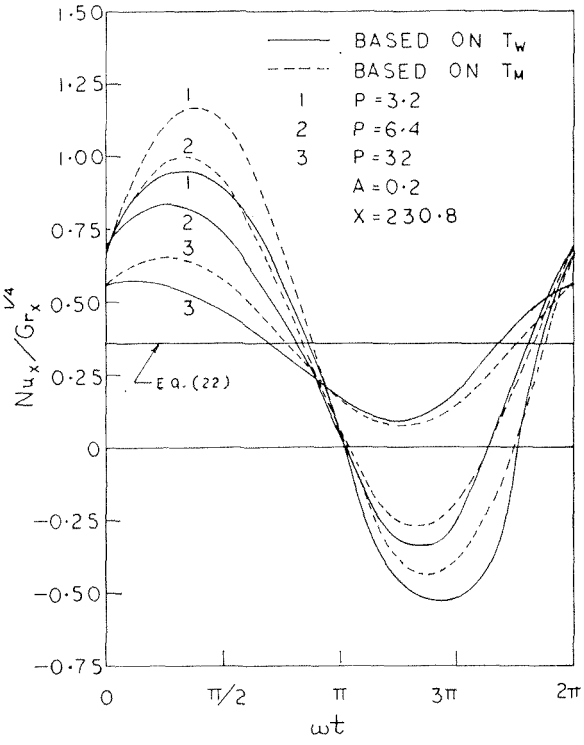

Fig. 7 Effect of amplitude on instantaneous heat transfer

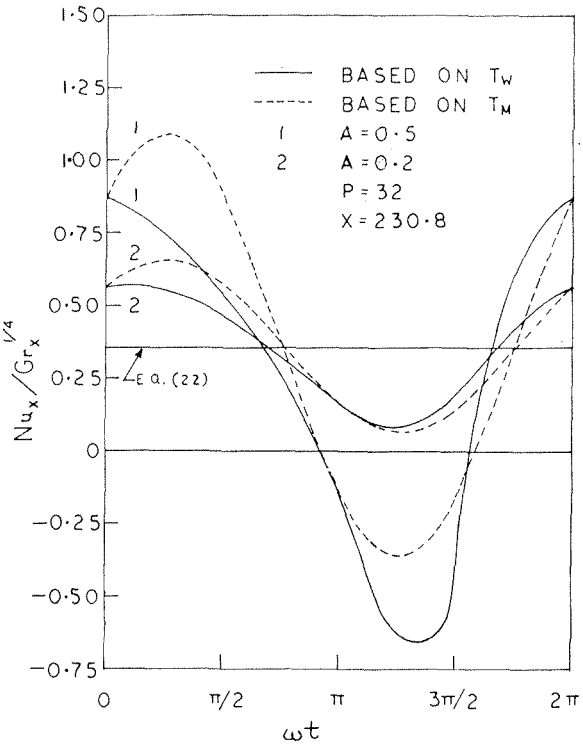

Fig. 8 Effect of period on instantaneous heat transfer

is confined in the region near the surface due to the thermal inertia of the fluid. The oscillation penetrates deeper in the boundary layer at higher amplitude as one expects. It is interesting to note that back heat flow (i.e., positive temperature gradient at the wall) occurs during the second half of the cycle ($\omega t = \pi \sim 2\pi$) at high amplitude for both larger and small values of X, Fig. 4. This back heat flow does not occur at small X ($X = 102.6$) when the amplitude parameter is small ($A = 0.2$), as seen in Fig. 5. The fact that the phase angle with respect to the imposed surface-temperature oscillation depends on X is probably due to the upward propagation of the oscillation in the velocity field. The effect of period on temperature distribution is given in Fig. 6. The region through which the oscillation penetrates increases with period (or, with the decrease of frequency). At $P = 32$, large portion of the flow field is influenced by the imposed periodic variation of surface temperature, but the shift of phase angle is small and no back flow occurs at this period. Comparison of Figs. 4 and 6 concludes that back heat flow occurs at high amplitude, low period, and larger X (or high Grashof number).

The instantaneous heat transfer rate may be evaluated in terms of the surface temperature gradient

$$q = -k\left(\frac{\partial T}{\partial y}\right)_0 = -2k(T_m - T_\infty)[g\beta(T_m - T_\infty)/\nu^2]^{1/3}\left(\frac{\partial \varphi}{\partial Y}\right)_0 \tag{17}$$

There are two reference temperatures from which the Nusselt number and the Grashof number can be constructed. Based on the mean surface temperature T_m, one has

$$\mathrm{Nu}_x = \frac{qx}{(T_m - T_\infty)k} = 2X\left(-\frac{\partial \varphi}{\partial Y}\right)_0 \tag{18}$$

$$\mathrm{Gr}_x = X^3 \tag{19}$$

Based on instantaneous surface temperature T_w, it gives

$$\mathrm{Nu}_x = \frac{qx}{(T_w - T_\infty)k} = \frac{X}{\varphi_w}\left(-\frac{\partial \varphi}{\partial Y}\right)_0 \tag{20}$$

$$\mathrm{Gr}_x = 2\varphi_w X^3 \tag{21}$$

Numerical calculations show that the heat flow rate, expressed by $\mathrm{Nu}_x/\mathrm{Gr}_x^{1/4}$, is strongly dependent on time but slightly affected by the longitudinal distance X, or Gr_m. The effects of amplitude and period on the timewise variations of the instantaneous heat transfer rates are shown in Figs. 7 and 8, respectively. It is revealed from these two figures that at a given longitudinal distance, the ratio $\mathrm{Nu}_x/\mathrm{Gr}_x^{1/4}$ (based on both T_w and T_m) follows a periodic variation with the same period as that of the surface temperature but with different amplitude and phase angle. The amplitude of heat flux increases with the increase of the amplitude and frequency of the imposed surface temperature oscillation. The back heat flow occurring during the second half of the cycle at high amplitude and short period is clearly indicated in Figs. 7 and 8. For the case of steady surface temperature, Ostrach gives [14]:

$$\mathrm{Nu}_x/\mathrm{Gr}_x^{1/4} = 0.354 \quad \text{for} \quad \mathrm{Pr} = 0.7 \tag{22}$$

Equation (22) is plotted in Figs. 7 and 8 for comparison. The ratio $\mathrm{Nu}_x/\mathrm{Gr}_x^{1/4}$ based on T_w, which is the actual driving force for the instantaneous heat flux, has a smaller timewise variation.

In the design of heat transfer devices, it is more convenient to have the average heat transfer coefficient over a complete cycle. The average heat transfer coefficient based on the mean surface temperature is

$$\bar{h} = \frac{\omega}{2\pi}\int_0^{\frac{2\pi}{\omega}} \frac{q}{(T_m - T_\infty)}\,dt \tag{23}$$

and

$$\frac{\overline{\mathrm{Nu}}_x}{\overline{\mathrm{Gr}}^{1/4}} = \frac{\omega X^{1/4}}{\pi}\int_0^{\frac{2\pi}{\omega}} \left(-\frac{\partial \varphi}{\partial Y}\right)_0 dt \tag{24}$$

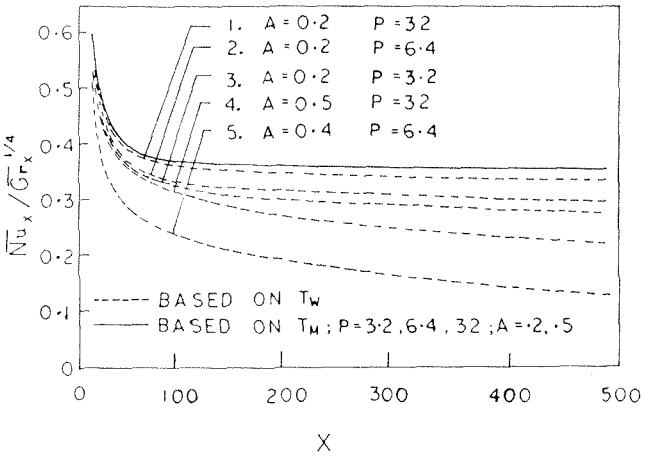

Fig. 9 Average heat transfer over a complete cycle

Based on the instantaneous surface temperature, one has

$$\bar{h} = \frac{\omega}{2\pi}\int_0^{\frac{2\pi}{\omega}} \frac{q}{(T_w - T_\infty)}\, dt \tag{25}$$

and

$$\frac{\overline{Nu}_x}{\overline{Gr}_x^{1/4}} = \frac{\omega}{2\pi} X^{1/4} \int_0^{\frac{2\pi}{\omega}} \frac{1}{\varphi_w}\left(-\frac{\partial \varphi}{\partial Y}\right)_0 dt \tag{26}$$

Equations (24) and (26) are illustrated in Fig. 9. The ratio $\overline{Nu}_x/\overline{Gr}_x^{1/4}$ based on average heat flux and $(T_m - T_\infty)$, i.e., equation (24), yields a single curve for all the values of amplitude A and period P. The curve approaches a constant value (0.354) which is the value for the steady natural convection process, equation (22). This is caused by the symmetry of the curves with respect to the constant value 0.354 in Figs. 7 and 8. The ratio $\overline{Nu}_x/\overline{Gr}_x^{1/4}$ from equation (26) is lower than that of the steady case and also shows the dependence on the amplitude and period of the imposed surface temperature. Since this ratio is based on $(T_w - T_\infty)$, equation (25), (the actual driving force), it reveals the actual process of an oscillatory natural convection.

References

1 Sparrow, E. M., and Gregg, J. L., "Nearly Quasi-Steady Free Convection Heat Transfer in Gases," JOURNAL OF HEAT TRANSFER, TRANS. ASME, Series C, Vol. 82, 1960, pp. 258–260.

2 Chung, P. M., and Anderson, A. D., "Unsteady Laminar Free Convection," JOURNAL OF HEAT TRANSFER, TRANS. ASME, Series C, Vol. 83, 1961, pp. 473–478.

3 Nanda, R. J., and Sharma, V. P., "Free Convection Laminar Boundary Layers in Oscillatory Flow," *Journal of Fluid Mechanics*, Vol. 15, 1963, pp. 419–428.

4 Nanda, R. J., and Sharma, V. P., "Free Convection Laminar Boundary Layers in Oscillatory Flow," *AIAA Journal*, Vol. 1, 1963, pp. 937–938.

5 Kelleher, M. D., and Yang, K. T., "Heat Transfer Response of Laminar Free-Convection Boundary Layers Along a Vertical Heated Plate to Surface-Temperature Oscillations," *ZAMP*, Vol. 19, 1968, pp. 31–44.

6 Schetz, J. A., and Eichhorn, R., "Unsteady Natural Convection in the Vicinity of a Double Infinite Vertical Plate," JOURNAL OF HEAT TRANSFER, TRANS. ASME, Series C, Vol. 84, 1962, pp. 334–338.

7 Monold, E. R., and Yang, K. T., "Asymptotic Solutions for Unsteady Laminar Free Convection on a Vertical Plate," *Journal of Applied Mechanics*, Vol. 29, 1962, pp. 124–126.

8 Hellums, J. D., and Churchill, S. W., "Computation of Natural Convection by Finite Difference Methods," *Proceedings of the International Heat Transfer Conference*, Part V, 1961, pp. 985–994.

9 Hellums, J. D., and Churchill, S. W., "Transient and Steady State, Free and Natural Convection, Numerical Solutions: Part 1. The Isothermal, Vertical Plate," *AIChE Journal*, Vol. 8, 1962, pp. 690–692.

10 Forsythe, G. E., and Wasow, W. R., *Finite Difference Method for Partial Difference Equations*, Wiley, New York, 1960.

11 Richtmyer, R. C., *Difference Methods for Initial Value Problems*, *Interscience*, 1957.

12 Siegel, R., "Transient Free Convection From a Vertical Flat Plate," TRANS. ASME, Vol. 80, 1958, pp. 347–359.

13 Goldstein, R. J., and Briggs, D. G., "Transient Free Convection About Vertical Plates and Circular Cylinders," JOURNAL OF HEAT TRANSFER, TRANS. ASME, Series C, Vol. 86, 1964, pp. 490–500.

14 Ostrach, S., "An Analysis of Laminar Free-Convection Flow and Heat Transfer About a Flat Plate Parallel to the Direction of the Generating Force," NACA TN 2635, 1952.

E. M. SPARROW
Heat Transfer Laboratory,
University of Minnesota,
Minneapolis, Minn. Mem. ASME

P. D. KRUGER

R. P. HEINISCH
Honeywell, Inc.,
Aerospace and Defense Group,
Minneapolis, Minn.

Radiation From Cavities With Nonisothermal Heat Conducting Walls

The radiant efflux from a cylindrical cavity having nonisothermal bounding surfaces is determined by solving a problem of combined radiation and conduction. The cavity may be visualized as a circular hole machined into the exposed face of a solid, with the solid being heated uniformly from behind. A two-dimensional temperature distribution is set up in the solid owing to radiative heat losses from the cavity and from the exposed face of the solid. A solution method is employed whereby the radiation and conduction problems are dealt with successively. Results are obtained for parametric values of the cavity emittance and depth-radius ratio and of a group which fixes the axial temperature variation. The results indicate that the radiant efflux from the cavity increases with increasing values of the aforementioned parameters. The effect of the presence of the cavity is confined to a region of the solid whose depth and radius are, respectively, twice and four times the depth and radius of the cavity.

Introduction

THE RADIANT INTERCHANGE and emission characteristics of heated cavities have been studied extensively during the past decade and a half, and a substantial literature has been built up. Representative publications are cited in textbooks and survey articles, for example [1, 2, 3].[1] In the main, the published analyses have dealt with the case in which the thermal conditions at the bounding surfaces of the cavity are prescribed. A consequence of this type of formulation is that the radiative exchange within the cavity can be solved without any consideration of the heat conduction processes in the walls of the cavity.

There are practical situations where the thermal boundary conditions on the cavity walls are carefully controlled, for instance, in black body cavities. On the other hand, it may often be true that the thermal conditions on the cavity walls find their own level and distribution as a result of the coupling between heat conduction in the walls and radiative transport in the cavity. Since in these cases the thermal conditions on the walls are not known in advance, the large body of information that is available for cavities with specified surface conditions cannot be directly applied. Furthermore, as will be documented shortly, there is only a sparse literature dealing with radiating cavities having conduction coupling.

In the present paper, such a problem of coupled cavity radiation and wall conduction is investigated. Consideration is given to a circular cylindrical cavity of finite length situated in a heat conducting solid. The physical situation may be visualized as a circular hole drilled, or otherwise machined, into the exposed face of a solid, with the solid being uniformly heated from behind. Radiative heat losses to the environment from the cavity opening and from the exposed face of the solid give rise to temperature variations in the solid and, in particular, to a temperature gradient along the bounding surfaces of the cavity.

The just-described, coupled radiative-conductive heat transfer problem can be advantageously analyzed in two steps. First, a partial solution of the radiative transfer problem for the cavity was carried out which yielded a relation between the local heat flux on the cavity wall and the cavity surface temperature distribution. This relation then served as the boundary condition for the heat conduction problem for the solid. The numerical results were obtained by finite difference techniques.

For the solutions, parametric values were assigned to the surface emittance, to the cavity depth-radius ratio, and to a dimensionless group which sets the steepness of the temperature variation in the direction of the cavity axis. Results are presented for the radiant energy efflux characteristics of the cavity and for the temperature distribution along the bounding surfaces.

A search of the literature did not uncover any prior publications dealing with coupled radiative transfer in nonblack cavities and two-dimensional conduction in the surrounding medium. Winter [4] analyzed the radiative transfer in infinitely deep black-walled grooves cut into a heat conducting semi-infinite solid. The radiation characteristics of a thin-walled cylindrical cavity were studied in [5] under the assumption that the conduction in the wall was one-dimensional.

[1] Numbers in brackets designate References at end of paper.

Contributed by the Heat Transfer Division for publication (without presentation) in THE JOURNAL OF HEAT TRANSFER. Manuscript received by the Heat Transfer Division April 9, 1973. Paper No. 74-HT-F.

Analysis

Although both the distributions of temperature and of heat flux along the bounding surfaces of the cavity are not known in advance, it is possible to develop a relationship between them. This relationship can be determined by solving the equations of radiant interchange for the cavity and, once obtained, serves as a thermal boundary condition for the heat conduction problem in the solid. It is, therefore, appropriate to subdivide the analysis into two discrete steps, with the radiation and conduction problems being treated successively. Whereas the radiation problem is linear in the fourth power of the temperature, the conduction problem is nonlinear owing to the radiation boundary conditions.

In the analysis, it will be assumed that the temperature field is axisymmetric with respect to the axis of the cavity.

Radiative Interchange in the Cavity. The formulation of the radiant interchange problem is facilitated by reference to Fig. 1, which pictures a cylindrical cavity of depth L and radius r_0. For the analysis, the bounding surfaces of the cavity are envisioned as being subdivided into axisymmetric area elements $i = 1, 2, 3, \ldots, N$. Each element is assumed to have a uniform temperature T_i. The disposition of the area elements was chosen with the *forthcoming heat conduction problem in mind*. In particular, elements 1 and m_s represent elements whose areas are half of that of the other elements on the side wall of the cavity. Furthermore, the corner element m consists of two subelements m_s and m_b, respectively situated on the side wall and on the cavity base. Although these subelements share a common temperature T_m, they have different normals and must be separately taken into account in the radiation analysis.

If it is assumed that the cavity walls are gray, diffuse emitters and reflectors of radiant energy (graybody emittance ϵ), a radiosity equation can be written at each element as follows [2]

$$B_i = \epsilon\sigma T_i^4 + (1 - \epsilon)\sum_{j=1}^{N} F_{ij}B_j, \qquad 1 \le i \le N \tag{1}$$

The radiosity B represents the radiant energy leaving a surface location per unit time and unit area, and the F_{ij} are angle factors. In writing equation (1), it was assumed that any external radiation that enters the cavity through its opening is negligible.

In the present problem, the F_{ij} correspond to interchange between pairs of ring elements on the side walls and to interchange between a ring element on the side wall and an annulus or a disk on the base. The numerical values of these angle factors have been calculated without approximation by employing angle factor algebra in conjunction with the well-established expression for the angle factor for two parallel disks. The determination of the required angle factors is detailed in the Appendix of [6].

The rate of heat loss by radiation at any element can be expressed as [2]

$$\frac{Q_i}{A_i} = \frac{\epsilon}{1 - \epsilon}(\sigma T_i^4 - B_i), \qquad 1 \le i \le N \tag{2}$$

By elimination of σT_i^4 between equations (1) and (2), it is seen that the heat loss at any element is equal to a weighted summation of the radiosities at all the elements. Unfortunately, such a relationship between the local heat loss and the radiosities is not very useful as input to the conduction problem, where the dependent variable is the temperature, not the radiosity. It would be much more advantageous to eliminate the radiosity between equations (1) and (2) in order to obtain a relation between heat transfer and temperature, but this cannot be done with these equations as they now stand.

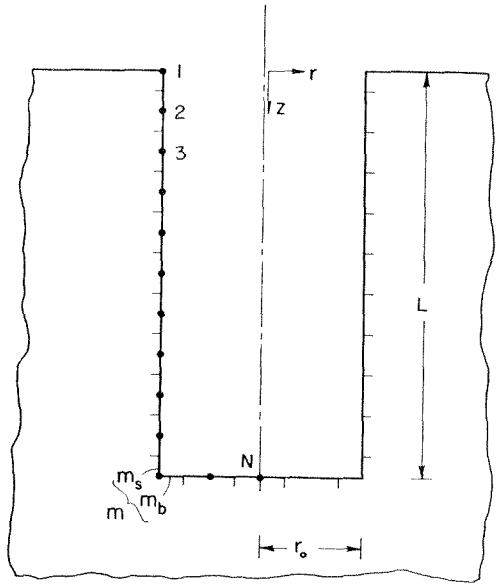

Fig. 1 Schematic of cavity and surrounding solid

To proceed toward a heat transfer—temperature relation, it is useful first to rewrite equation (1) in the form

$$\sum_{j=1}^{N} \chi_{ij}B_j = \sigma T_i^4, \qquad 1 \le i \le N \tag{3}$$

where

$$\chi_{ij} = [\delta_{ij} - (1 - \epsilon)F_{ij}]/\epsilon \tag{4}$$

and δ_{ij} is the Kronecker delta. The numerical values of the x_{ij} are readily calculable once the disposition of the elements has been made (thereby fixing the F_{ij}) and ϵ has been chosen.

The χ_{ij} can be arranged into an N by N matrix which can be inverted to give a new matrix whose elements are ψ_{ij}. The inversion of the matrix also inverts equation (3), so that

$$B_i = \sum_{j=1}^{N} \psi_{ij}\sigma T_j^4, \qquad 1 \le i \le N \tag{5}$$

Then, substitution of (5) into (2) yields

$$Q_i/A_i = \sum_{j=1}^{N} \Lambda_{ij}\sigma T_j^4, \qquad 1 \le i \le N \tag{6}$$

where the Λ_{ij} are known constants given by

$$\Lambda_{ij} = \epsilon(\delta_{ij} - \psi_{ij})/(1 - \epsilon) \tag{7}$$

Equation (6) indicates that the rate of heat loss by radiation at

Nomenclature

A = surface area
B = radiosity
F_{ij} = angle factor
k = thermal conductivity of solid
L = depth of cavity
Q = rate of radiant efflux from cavity
Q_i = local rate of heat transfer
R = dimensionless coordinate, r/r_0
r = radial coordinate
r_0 = radius of cavity
T = temperature
T_b = temperature at center of base
T_e = effective temperature of cavity
T_s = surface temperature of solid in absence of cavity
Z = dimensionless coordinate, z/L
z = axial coordinate
ϵ = emittance
θ = dimensionless temperature, T/T_s
σ = Stefan-Boltzmann constant

any surface element is equal to a weighted sum of the T^4 values at all the elements.

Once the numerical values of the A_{ij} are available, equation (6) represents a highly convenient form of input from the radiation problem to the conduction problem. It will serve as the thermal boundary condition for that portion of the solid which bounds the cavity. A particular advantage of equation (6) is that it represents a set of algebraic equations whose numerical coefficients remain fixed even if an iterative-type solution of the conduction problem is employed.

Heat Conduction in the Surrounding Solid. The temperature distribution in the solid is governed by the two-dimensional Laplace equation in r,z cylindrical coordinates. The complete specification of the problem requires a statement of the boundary conditions. For the surfaces of the solid which bound the cavity, the heat transfer—temperature relation of equation (6) serves as the boundary condition. Since a finite-difference type of solution is to be used, the heat transfer rate Q_i referred to a finite area A_i is directly applicable. The temperatures T_j are associated with nodal points as indicated by the blackened dots in Fig. 1.

At the surface of the solid that is exposed to the external surroundings, there is a local radiative heat loss per unit time and unit area given by $\epsilon\sigma T^4$ or, for a finite size surface element with area A_i,

$$Q_i = \epsilon\sigma T_i^4 A_i \tag{8}$$

The radiant energy from the surroundings that is absorbed by the exposed surface is assumed to be negligible.

Other boundary conditions can be deduced by noting that the presence of the cavity will effect the temperature field in only a finite portion of the solid. Let $r = r_\infty$ denote the greatest radial penetration of the presence of the cavity effect and $z = z_\infty$ the greatest axial penetration. For $r \geq r_\infty$ and any z, and for $z \geq z_\infty$ and any r, the temperature field in the solid coincides with that which would exist if the cavity were not present. If the solid is uniformly heated from behind (i.e., along a surface z = constant) and edge effects are negligible, then the temperature field in the solid is governed by $\partial^2 T/\partial z^2 = 0$ when there is no cavity. Furthermore, if T_s denotes the temperature of the exposed surface of the solid in the absence of the cavity, with corresponding radiative heat loss $\epsilon\sigma T_s^4 = (k\partial T/\partial z)_{z=0}$, the temperature distribution in the solid is given by $T(z) = T_s + \epsilon\sigma T_s^4 z/k$. Therefore, with the cavity present, the boundary conditions along $r = r_\infty$ and $z = z_\infty$ are

$$T = T_s + \epsilon\sigma T_s^4 z/k, \qquad r = r_\infty \tag{9a}$$

$$T = T_s + \epsilon\sigma T_s^4 z_\infty/k, \qquad z = z_\infty \tag{9b}$$

In order to minimize the number of parameters that have to be specified in the subsequent numerical computations, it is useful to introduce dimensionless parameters as follows

$$R = r/r_0, \qquad Z = z/r_0, \qquad \theta = T/T_s \tag{10}$$

An examination of the dimensionless forms of the energy equation and boundary conditions indicates three independent parameters

$$\epsilon, \qquad L/r_0, \qquad \sigma T_s^3 r_0/k \tag{11}$$

The surface emittance ϵ and the depth-radius ratio L/r_0 have clear physical meanings. The significance of the quantity $\sigma T_s^3 r_0/k$ can be identified by noting that the dimensionless temperature distribution in the solid when there is no cavity (or for $r \geq r_\infty$ when there is a cavity) is

$$\theta = 1 + \epsilon(\sigma T_s^3 r_0/k)Z \tag{12}$$

Therefore, for a given ϵ, the slope of the temperature distribution in the axial direction is fixed by the magnitude of $\sigma T_s^3 r_0/k$.

Owing to the nonelementary shape of the solid, a numerical solution is appropriate. In approaching a finite-difference formulation, one may deduce difference equations either from Laplace's equation or from a direct energy balance on the volume elements of the finite-difference network. There is some uncertainty in using Laplace's equation as a starting point, as witnessed by the fact that the quantities

$$\frac{\partial}{\partial r}\left(r\frac{\partial T}{\partial r}\right), \qquad r\frac{\partial^2 T}{\partial r^2} + \frac{\partial T}{\partial r} \tag{13}$$

do not yield the same finite-difference terms, even though they are analytically identical. This uncertainty arises because the area for conduction in the radial direction varies with the radius, this variation is represented to different degrees of approximation by the finite-difference forms of the first and second members of equation (13). On the other hand, by deriving the difference equations from an energy balance on the finite-difference volume elements themselves, an exact representation of the heat transfer areas can be obtained. This is the approach that was used here.

The grid structure at a typical interior node is shown at the left of Fig. 2. The shaded element, which appears as a rectangle in the sketch, actually represents an axisymmetric annular disk. To enable the use of a more dense concentration of nodal points in regions of more rapid temperature change, the difference equations were written with variable step sizes in both r and z. The grid was laid out so that the faces of the elements are situated midway between the adjacent nodes; therefore, cd lies midway between * and 1, ad lies midway between * and 4, etc. If the coordinates of node * are r^* and z^*, the areas of the faces ab, bc, ... can be expressed as

$$A_{ab} = \pi(r^* - {}^1/_2\Delta r')(\Delta z' + \Delta z'') \tag{14a}$$

$$A_{bc} = A_{ad} = \pi[r^*(\Delta r' + \Delta r'') + (\Delta r''^2 - \Delta r'^2)/4] \tag{14b}$$

$$A_{cd} = \pi(r^* + {}^1/_2\Delta r'')(\Delta z' + \Delta z'') \tag{14c}$$

The temperature gradients needed for expressing the heat fluxes at the faces of the volume element were evaluated via central differences, for example, $(\partial T/\partial r)_{ab} \cong (T^* - T_3)/\Delta r'$. With these, the finite-difference form of the energy equation at node * can be written as

$$T^* = \frac{T_1\left(\frac{A_{cd}}{\Delta r''}\right) + T_2\left(\frac{A_{bc}}{\Delta z'}\right) + T_3\left(\frac{A_{ab}}{\Delta r'}\right) + T_4\left(\frac{A_{ad}}{\Delta z''}\right)}{\left(\frac{A_{cd}}{\Delta r''}\right) + \left(\frac{A_{bc}}{\Delta z'}\right) + \left(\frac{A_{ab}}{\Delta r'}\right) + \left(\frac{A_{ad}}{\Delta z''}\right)} \tag{15}$$

A typical node for an element situated adjacent to the cavity surface is pictured at the right of Fig. 2. As before, the faces of the element bisect the distances between the nodes (e.g., cd is situated midway between * and 1). The face ab of the element lies on the cavity wall. In terms of the face areas A_{ab}, A_{bc}, A_{cd}, A_{ad} and using central differences for the derivatives $(\partial T/\partial r)_{cd}$, $(\partial T/\partial z)_{ad}$, and $(\partial T/\partial z)_{bc}$, the difference equation for node * is

$$T^* = \frac{T_1\left(\frac{A_{cd}}{\Delta r}\right) + T_2\left(\frac{A_{bc}}{\Delta z'}\right) + T_4\left(\frac{A_{ad}}{\Delta z''}\right) - [rhs(6)]\left(\frac{A_{ab}}{k}\right)}{\left(\frac{A_{cd}}{\Delta r}\right) + \left(\frac{A_{bc}}{\Delta z'}\right) + \left(\frac{A_{ad}}{\Delta z''}\right)} \tag{16}$$

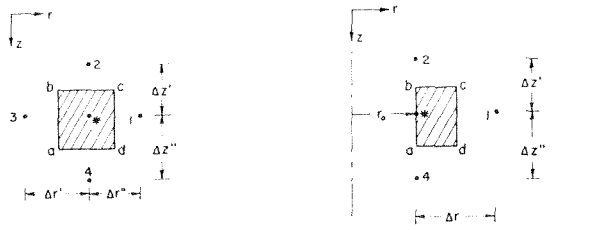

Fig. 2 Typical interior node (left diagram) and typical node adjacent to cavity surface (right diagram)

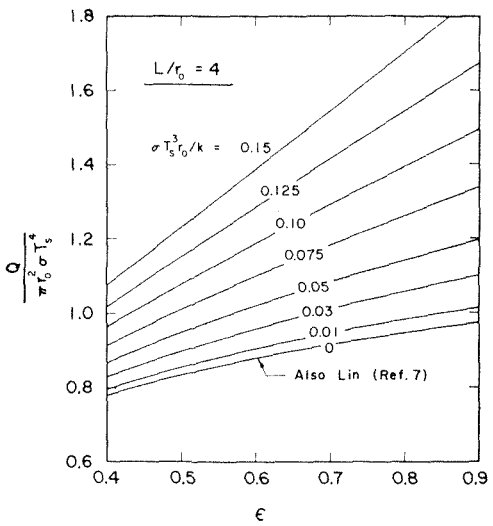

Fig. 3 Radiant energy efflux from cavity opening, $L/r_0 = 4$

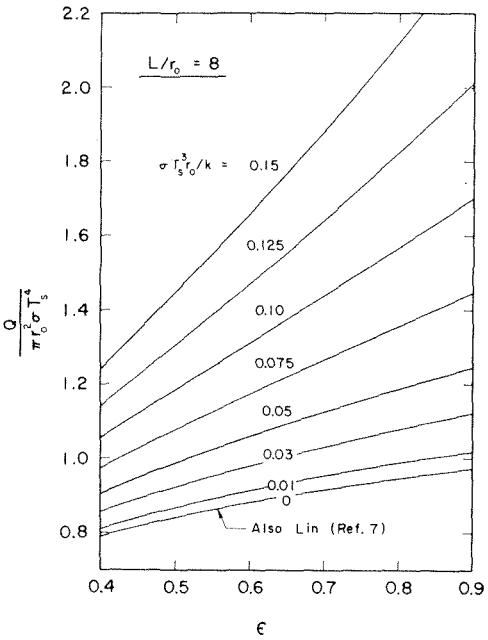

Fig. 4 Radiant energy efflux from cavity opening, $L/r_0 = 8$

where *rhs* (6) denotes the right-hand side of equation (6).

Difference equations expressing energy conservation were derived in a similar manner for the other boundary nodes and for special nodes such as that at the intersection of the cavity side wall and the base, those on the symmetry line, etc. These difference equations are given in [6].

Inasmuch as the boundary conditions on the exposed surface of the solid and on the bounding surfaces of the cavity contain T^4, the set of difference equations is nonlinear. To enable the use of the powerful solution methods associated with linear equations, it is advantageous to linearize the system for interim calculations. The final results will satisfy the full nonlinear system.

To motivate the form of the linearization, suppose that $\hat{T}_i$ is a temperature that is slightly different from T_i. Then, by the binomial expansion

$$T_i^4 = [\hat{T}_i + (T_i - \hat{T}_i)]^4 \cong \hat{T}_i^4 + 4\hat{T}_i^3(T_i - \hat{T}_i) \quad (17a)$$

or

$$T_i^4 = 4\hat{T}_i^3 T_i - 3\hat{T}_i^4 \quad (17b)$$

Clearly, when $\hat{T}_i = T_i$, equation (17*b*) reduces to an identity.

In each of the nonlinear difference equations, T^4 was replaced by the right-hand side of equation (17*b*). Numerical values of the quantities $\hat{T}_i$ at the various nodes i were supplied as input information as described in the following. In this way, the difference equations were made linear in the unknown temperature distribution $T(r, z)$.

The linearized difference equations for all the nodes can be written in matrix form as

$$[S][T] = [C] \quad (18)$$

where $[S]$ is a square matrix, and $[T]$ and $[C]$ are vectors. Since S and C contain the unknown values $\hat{T}$, an iterative solution procedure was employed. The first step in the iteration method was to input numerical values of $\hat{T}$ so that S and C could be evaluated. Then, the matrix S was inverted and the temperature distribution obtained. For the next cycle of the iteration, the values of $\hat{T}$ were set equal to the just-calculated values of T. With these, the matrix equation was solved once again, yielding a new distribution for T. Again, the $\hat{T}$ were set equal to the new values of T, and the process repeated until the values of T and $\hat{T}$ at mesh point converged. The convergence criterion was that T and $\hat{T}$ should differ by less than 0.0001 (note that T is on the order of unity). After experience was developed with respect to the selection of the initial inputs for $\hat{T}$, only a few iterations were required for convergence.

A finite-difference grid containing 189 mesh points was used for the calculations. The layout of the grid is illustrated in Figs. 1 and 2 of [6]. The solutions were carried out on a CDC 6600 computer.

Results and Discussion

The solutions and results depend on three independent parameters: the emittance ϵ, the temperature gradient parameter $\sigma T_s^3 r_0/k$, and the depth-radius ratio L/r_0. Values of 0.4, 0.55, 0.7, and 0.9 were assigned to ϵ, while $\sigma T_s^3 r_0/k$ was varied from 0 (isothermal cavity) to 0.15. For each of these cases, solutions were obtained for $L/r_0 = 4$ and 8.

The quantity that is of primary interest in connection with the radiation characteristics of heated cavities is the rate Q at which radiant energy streams out of the cavity opening. For isothermal cavities, it is customary to present the results for Q in terms of the apparent emittance ϵ_a. This is a dimensionless quantity which is the ratio of Q to the radiant energy emitted by a black surface whose area is equal to that of the cavity opening and whose temperature is the same as that of the isothermal cavity. In the present situation, the physical significance of the apparent emittance is lost because the cavity walls are not isothermal. It is, nevertheless, convenient to employ a dimensionless presentation whose form is similar to that of the apparent emittance, that is, $Q/\pi r_0^2 \sigma T_s^4$. The use of T_s in this dimensionless grouping is motivated by the likelihood that its value would be known in any application of the results.

The results for the energy efflux are presented in Figs. 3 and 4, respectively, for depth-radius ratios L/r_0 of 4 and 8. In each figure, $Q/\pi r_0^2 \sigma T_s^4$ is plotted as a function of ϵ for parametric values of $\sigma T_s^3 r_0/k$. The lowermost curve in each figure corresponds to the isothermal cavity. Inspection of the figures indicates that the curves lie successively higher as $\sigma T_s^3 r_0/k$ increases. Also, along each curve, $Q/\pi r_0^2 \sigma T_s^4$ increases with ϵ. Furthermore, $Q/\pi r_0^2 \sigma T_s^4 > 1$ over much of the investigated range of parameters. It will now be demonstrated that these trends are physically reasonable.

The effect of the parameter $\sigma T_s^3 r_0/k$ may be explained by noting, with the aid of equation (12), that the temperature of the solid increases more rapidly with depth as this parameter becomes larger. Consequently, relative to a fixed value of T_s, the temperature at any location on the cavity wall is higher at larger

values of $\sigma T_s^3 r_0/k$ and, correspondingly, more radiant energy is emitted. Therefore, the increase of $Q/\pi r_0^2 \sigma T_s^4$ with $\sigma T_s^3 r_0/k$ as shown in Figs. 3 and 4 is reasonable.

The trend of the results with ϵ is a consequence of two factors. First, the emissive power increases with increasing ϵ, thereby causing Q to increase. Second, as indicated by equation (12), larger ϵ gives rise to larger temperature gradients and higher temperatures, which further tends to increase the emitted radiation. This second factor is more important at larger values of $\sigma T_s^3 r_0/k$ and causes the curves to straighten out rather than bend over as they do at small values of $\sigma T_s^3 r_0/k$.

From a comparison of Figs. 3 and 4, it is seen that similar trends prevail in both figures. The values of $Q/\pi r_0^2 \sigma T_s^4$ of Fig. 4 are generally higher than those of Fig. 3. This is because, for fixed values of ϵ and of $\sigma T_s^3 r_0/k$, substantially higher temperatures are attained in the cavities of Fig. 4 ($L/r_0 = 8$) than in the cavities of Fig. 3 ($L/r_0 = 4$).

The reason that $Q/\pi r_0^2 \sigma T_s^4$ exceeds unity for certain ranges of the parameters is that temperatures on the cavity walls may be much greater than T_s.

An indication of the accuracy of the present results may be obtained from the isothermal cavity curves of Figs. 3 and 4. Within the scale of the figures, the present results are indistinguishable from those of Lin [7], who employed an integral equation formulation, the solutions to which involved integration over 100 points distributed along the walls of the cavity. This excellent level of agreement lends support to the present formulation and solution method.

Although Figs. 3 and 4 contain an easily applicable presentation of the results, other presentations may be made which highlight other features of the results. For instance, one may seek effective temperatures T_e to characterize the nonisothermal cavities so that $Q/\pi r_0^2 \sigma T_e^4$ can be plotted against ϵ as a single curve for each L/r_0. In other words, by a proper choice of T_e all the curves of Fig. 3 can be collapsed onto that for the isothermal cavity ($\sigma T_s^3 r_0/k = 0$), and similarly in Fig. 4.

The T_e values which give rise to such universal curves are shown in Fig. 5. The left-hand part of the figure is for $L/r_0 = 4$, and the right-hand part is for $L/r_0 = 8$. Both parts of the figure have the same ordinate scale, but the left-hand part is referred to the upper abscissa. The abscissa variable is the ratio $(T_b/T_s)^4$, where T_b is the temperature at the center of the cavity base.

The main message of the figure can be obtained by noting that along any curve, $(T_e/T_s)^4$ is substantially less than $(T_b/T_s)^4$. In other words, the effective temperature of the cavity is much closer to the surface temperature T_s than to the base temperature T_b. This finding indicates that of the radiant energy which streams out of the cavity, the majority is emitted from the lower temperature portion that is situated near the cavity opening. Radiation emitted in portions of the cavity more remote from the opening is absorbed to a considerable degree before it reaches the plane of the opening. At a given value of T_b/T_s, smaller values of T_e/T_s are encountered as ϵ increases, indicating that a larger fraction of the outstreaming radiation originates from surface locations near the opening.

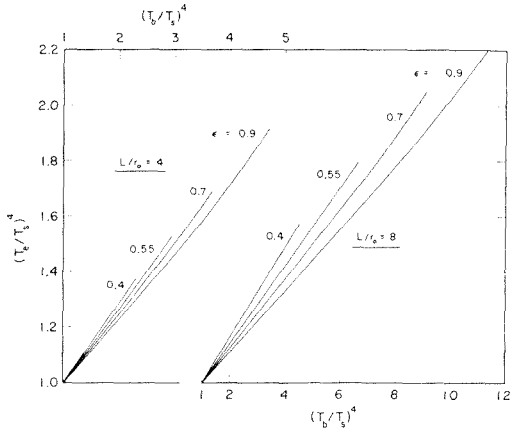

Fig. 5 Effective temperature of nonisothermal cavities

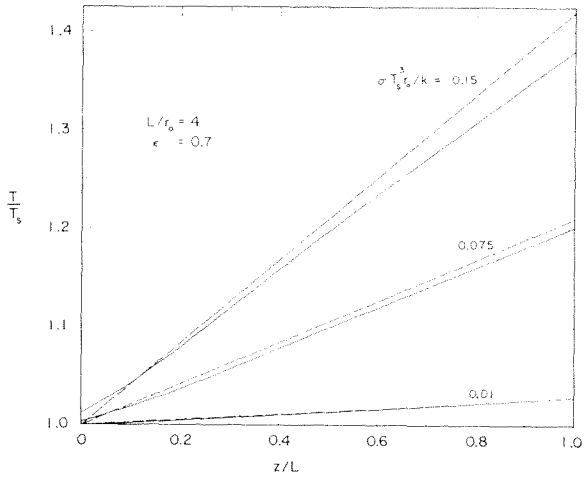

Fig. 6 Representative temperature distributions along cavity side wall, $L/r_0 = 4$

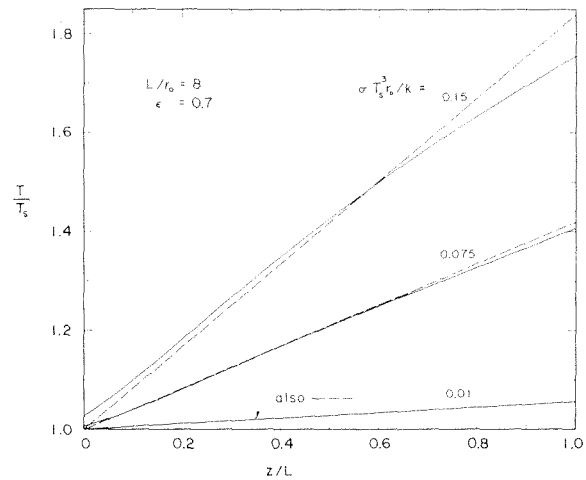

Fig. 7 Representative temperature distributions along cavity side wall, $L/r_0 = 8$

Another quantity of interest furnished by the solutions is the temperature distribution along the bounding surfaces of the cavity. Representative results are shown in Figs. 6 and 7, where the temperature along the cavity side wall is plotted against the dimensionless axial coordinate z/L. These figures correspond respectively to cavity depth-radius ratios of 4 and 8, and to an intermediate emittance value of 0.7. It should also be noted that the ordinate of Fig. 7 covers a substantially larger range than does Fig. 6, and its scale is correspondingly compressed. The solid lines in these figures represent the results for the coupled radiation-conduction problem, whereas the dashed straight lines represent the temperature field in the absence of the cavity, equation (12).

Inspection of the figures indicates that for small temperature gradients, the temperature distribution along the cavity wall is nearly coincident with the straight line distribution that prevails in the solid when the cavity is absent. For larger gradients, the deviations increase.

When derivations do occur, the temperatures in the deeper parts of the cavity lie below those of the dashed lines. On the other hand, near the cavity opening, the cavity wall temperatures

may exceed those of the dashed lines. This effect is accentuated in cavities where higher values of T/T_s are attained and also at larger values of ϵ. The reason for the just-cited increase in the cavity wall temperature adjacent to the opening is that these portions of the wall intercept and absorb substantial amounts of high temperature radiation that originates in the deeper portions of the cavity.

Turning next to the solid, it is of interest to inquire how much of the solid is effected by the presence of the cavity. This information is relevant, for instance, to the placement of instrumentation on the surface and to the thickness that is required for the simulation of a semi-infinite solid. From the solutions of the conduction problem, a number of temperature distributions were plotted in [6]. An examination of these graphs indicated that for all the cases investigated, the effects of the cavity were confined to the region $r/r_0 < 4$ and $z/L < 2$. For many cases, the region of influence of the cavity was substantially smaller.

References

1 Hottel, H. C., and Sarofim, A. F., *Radiative Transfer*, McGraw-Hill, New York, 1967.

2 Sparrow, E. M., and Cess, R. D., *Radiation Heat Transfer*, Brooks/Cole, Belmont, Cal., 1966.

3 Williams, C. S., "Specularly vs Diffusely Reflecting Walls for Cavity-Type Sources of Radiant Energy," *Journal of the Optical Society of America*, Vol. 59, 1969, pp. 249–252.

4 Winter, D. F., "Transient Radiative Cooling of a Semi-Infinite Solid With Parallel-Walled Cavities," *International Journal of Heat and Mass Transfer*, Vol. 9, 1966, pp. 527–532.

5 Sparrow, E. M., Bifano, W. J., and Healy, J. A., "Efficiencies of Honeycomb Absorbers of Solar Radiation," NASA TN D-6337, 1971.

6 Kruger, P. D., "Radiative Transfer in Cavities With Nonisothermal Walls," MS thesis, Department of Mechanical Engineering, University of Minnesota, 1973.

7 Lin, S. H., "Radiant Interchange in Cavities and Passages With Specularly and Diffusely Reflecting Surfaces," PhD thesis, Department of Mechanical Engineering, University of Minnesota, 1964.

A. T. Wassel

D. K. Edwards
Professor.

School of Engineering and Applied Science,
University of California,
Los Angeles, Calif.

Molecular Gas Band Radiation in Cylinders

The radiative heat flux in a molecular gas within a cylinder is formulated in terms of an axial band absorptance. The axial band absorptance function is used to reduce the two angular, one spatial, and one spectral integrals encountered to one angular and one spatial integral such as is encountered in radiative transfer problems with spherical symmetry. A closed form is obtained for the axial band absorptance for the exponential-winged band model. Illustrative results are presented for a cylindrical gas volume with trapezoidal, parabolic, or Gaussian temperature profile. Mean beam length, absorptivity, and emissivity of a cylinder of gas are obtained as a function of the optical depth at the band head.

Introduction

Radiative transfer in a cylindrical gas volume occurs, for example, in the plume from a fire, chimney stack, cooling tower, or rocket engine. Radiation from hot gases in cylindrical configurations also occurs in gas turbine combustors, furnaces, and boilers. In addition to contributing to the major heat transfer to the walls of such chambers, the radiation significantly affects flame temperatures and, hence, nitric oxide emission levels.

Usiskin and Sparrow [1][1] studied thermal radiation between parallel plates separated by an absorbing-emitting, nonisothermal, gray gas. Sparrow, Usiskin, and Hubbard [2] investigated radiative transfer in a nonisothermal gray spherical medium. Viskanta [3] studied the interaction of conduction, laminar convection, and radiation in a plane layer of a radiating fluid. A good review for the case of pure conduction (or laminar Couette flow) and gray radiation can be found in [4 and 5].

Einstein [6] considered radiant heat transfer in an absorbing-emitting gray gas flowing within a black-walled cylindrical pipe. Nichols [7] studied the influence of the absorption of radiation on the temperature profile and heat transfer to an absorbing medium flowing turbulently in an annulus. DeSoto and Edwards [8] predicted the radiative interchange between a black tube and a nonisothermal nongray gas within the tube. DeSoto [9] investigated the coupling of radiation with conduction and convection in a nonisothermal, nongray gas flowing in the entrance region of a black-walled tube. Kesten [10] presented the equations for the spectral radiant heat flux distribution in an absorbing-emitting gas contained in a long cylinder whose internal surface is black. Viskanta and Merriam [11] investigated combined conduction and radiation between concentric spheres. Lamdram, Greif, and Habib [12] studied heat transfer in turbulent pipe flow with optically thin radiation. Habib and Greif [13] investigated nongray radiative transport in a cylindrical medium. Tiwari and Cess [14] studied heat transfer to laminar flow of nongray gases through a circular tube. The analyses of both [13 and 14] are based upon an approximation suitable only for the optically thick limit [15, 16] and are thus of questionable validity for a molecular gas having radiation transfer occurring in optically thin band wings.

It is the object of this paper to transform the problem of determining the local radiative flux in a cylinder to one very similar to finding the flux in a sphere, the latter problem being much simpler, because integrations are required over only one angular coordinate and the radial coordinate. It will be shown that the quadruple integrals encountered in cylindrical gas radiation problems may be reduced to double integrals which involve a quantity defined as the axial band absorptance, which depends upon gas properties fixed by laboratory measurements of line-of-sight band absorptance. Closed-form expressions for this latter quantity will be obtained for cases when gas properties can be represented by the exponential-winged band model.

Formulation of Radiative Flux

The spectral radiative flux in the radial direction can be written in the following form [10, 13, 17]

$$q_\nu(r) = 4\int_{\gamma=0}^{\pi/2}\cos\gamma\Big\{I_\nu(R)\Big[D_3\Big(\int_{r\sin\gamma}^{R}\frac{\rho k_\nu dr'}{\cos\gamma'} + \int_{r\sin\gamma}^{r}\frac{\rho k_\nu dr'}{\cos\gamma'}\Big) - D_3\Big(\int_{r}^{R}\frac{\rho k_\nu dr'}{\cos\gamma'}\Big)\Big] + \int_{r\sin\gamma}^{R}\frac{\rho k_\nu B_\nu}{\cos\gamma'}D_2\Big(\int_{r\sin\gamma}^{r'}\frac{\rho k_\nu dr''}{\cos\gamma''} + \int_{r\sin\gamma}^{r}\frac{\rho k_\nu dr'}{\cos\gamma'}\Big)dr' + \int_{r\sin\gamma}^{r}\frac{\rho k_\nu B_\nu}{\cos\gamma'}D_2\Big(\int_{r'}^{r}\frac{\rho k_\nu dr''}{\cos\gamma''}\Big)dr' - \int_{r}^{R}\frac{\rho k_\nu B_\nu}{\cos\gamma'}D_2\Big(\int_{r}^{r'}\frac{\rho k_\nu dr''}{\cos\gamma''}\Big)dr'\Big\}d\gamma, \quad (1)$$

[1] Numbers in brackets designate References at end of paper.

Contributed by the Heat Transfer Division for publication in the JOURNAL OF HEAT TRANSFER. Manuscript received by the Heat Transfer Division July 20, 1973. Paper No. 74-HT-N.

where

$$B_\nu(r') = \frac{2hc^2\nu^3}{e^{hc\nu/kT(r')} - 1} \tag{2}$$

$$\cos\gamma' = [1 - (r/r')^2 \sin^2\gamma]^{1/2} \tag{3a}$$

$$\cos\gamma'' = [1 - (r/r'')^2 \sin^2\gamma]^{1/2} \tag{3b}$$

and

$$D_n(x) = \int_0^{\pi/2} \cos^{n-1}\alpha \exp(-x/\cos\alpha)d\alpha = \int_0^1 \frac{\mu^{n-1}}{(1-\mu^2)^{1/2}} \exp(-x/\mu)d\mu. \tag{4}$$

The first term inside the curly brackets gives the wall radiation transmitted through the core and out through the r-surface less that transmitted through the outer shell into the r-surface. The second and third terms give the radiation emitted in the gas and passing through the core *out* of the r-surface while the last term is that emitted by the gas in the outer shell and passing inward through the r-surface (Fig. 1).

Equation (1) is valid for an absorbing, emitting, nonscattering medium in local thermodynamic equilibrium bounded by a diffuse wall. If equations (3*a*) and (3*b*) are introduced into equation (1) and the volumetric absorption coefficient, ρk_ν, is assumed to be a weak function of temperature and position, the resulting expression is (again see Fig. 1)

$$q_\nu(r) = 4\int_{\gamma=0}^{\pi/2} \cos\gamma \{I_\nu(R)[D_3(\rho k_\nu r\cos\gamma + \rho k_\nu R[1-(r/R)^2\sin^2\gamma]^{1/2}) - D_3(\rho k_\nu R[1-(r/R)^2\sin^2\gamma]^{1/2} - \rho k_\nu r\cos\gamma)] + \int_{r\sin\gamma}^{R} \frac{\rho k_\nu B_\nu}{[1-(r/r')^2\sin^2\gamma]^{1/2}} D_2(\rho k_\nu r'[1-(r/r')^2\sin^2\gamma]^{1/2} + \rho k_\nu r\cos\gamma)dr' + \int_{r\sin\gamma}^{r} \frac{\rho k_\nu B_\nu}{[1-(r/r')^2\sin^2\gamma]^{1/2}} D_2(\rho k_\nu r\cos\gamma - \rho k_\nu r'[1-(r/r')^2\sin^2\gamma]^{1/2})dr' - \int_r^R \frac{\rho k_\nu B_\nu}{[1-(r/r')^2\sin^2\gamma]^{1/2}} D_2(\rho k_\nu r'[1-(r/r')^2\sin^2\gamma]^{1/2} - \rho k_\nu r\cos\gamma)dr'\} d\gamma. \tag{5}$$

Real gases radiate in discrete wave-number bands with essentially transparent windows separating the bands. Under the band assumption, the total radiative flux can be written as

$$q(r) = \sum_{i=1}^{N} q_i(r) = \sum_{i=1}^{N} \int_{\Delta\nu_i} q_{\nu_i}(r)d\nu, \tag{6}$$

where N is the number of bands of a given gas, and $\Delta\nu_i$ is the band width. Under the assumption that the bands are narrow (that is, that the band-wing spectral decay width ω_i is small compared to the spectral separation between bands $|\nu_i - \nu_{i\pm1}|$ and that the radiant intensity $I_\nu(R)$ and the Planck black body intensity $B_\nu(r')$ do not vary greatly with ν within a few ω_i of ν_i), the total flux of the ith band is given by

$$q_i(r) = 4\int_{\gamma=0}^{\pi/2} \cos\gamma \{I_{\nu_i}(R)[\int_{\Delta\nu_i} D_3(\rho k_\nu r\cos\gamma + \rho k_\nu R[1-(r/R)^2\sin^2\gamma]^{1/2})d\nu - \int_{\Delta\nu_i} D_3(\rho k_\nu R[1-(r/R)^2\sin^2\gamma]^{1/2} - \rho k_\nu r\cos\gamma)d\nu] + \int_{r\sin\gamma}^{R} \frac{B_{\nu i}}{[1-(r/r')^2\sin^2\gamma]^{1/2}} \int_{\Delta\nu_i} \rho k_\nu D_2(\rho k_\nu r'[1-(r/r')^2\sin^2\gamma]^{1/2} + \rho k_\nu r\cos\gamma)d\nu dr' + \int_{r\sin\gamma}^{r} \frac{B_{\nu i}}{[1-(r/r')^2\sin^2\gamma]^{1/2}} \int_{\Delta\nu_i} \rho k_\nu D_2(\rho k_\nu r\cos\gamma - \rho k_\nu r'[1-(r/r')^2\sin^2\gamma]^{1/2})d\nu dr' - \int_r^R \frac{B_{\nu i}}{[1-(r/r')^2\sin^2\gamma]^{1/2}} \int_{\Delta\nu_i} \rho k_\nu D_2(\rho k_\nu r'[1-(r/r')^2\sin^2\gamma]^{1/2} - \rho k_\nu r\cos\gamma)d\nu dr'\} d\gamma. \tag{7}$$

To make this difficult and lengthy expression more convenient for use in engineering analysis, it is desirable to obtain closed-form representations for the terms integrated with respect to ν.

Nomenclature

A = band absorptance
A_a^* = axial band absorptance
B = Planck black body spectral intensity
B_ν' = first derivative of B with respect to $r^{*\prime}$
c = speed of light
D_n = cylindrical exponential integral function of order n
E_1 = exponential integral function of order 1
h = Planck's constant
I_ν = spectral intensity of radiation
j = integer = ±1
k = Boltzmann constant
k_ν = spectral absorption coefficient
L = mean beam length
N = number of bands
q = radiative flux
r, r', r'' = local radius
$r^*, r^{*\prime}$ = dimensionless radius
R = cylinder radius
T = absolute temperature
u = ratio of mean beam length to cylinder radius
α = angle between a line of sight and a plane perpendicular to the axis of the cylinder measured in a plane parallel to the cylinder axis; also absorptivity
α_i = band integrated intensity
$\gamma, \gamma', \gamma''$ = angle in the cross-sectional plane from the radial direction to the projected line of sight
γ_e = 0.5772156...
$\Delta\nu$ = band width
ϵ = emissivity
η = integer = ±1
λ = constant parameter
μ = dummy variable of integration
ν = wave number
ν_i = band head for the ith band
ξ = integer = ±1
π = 3.1415927
ρ = gas density
σ = Stefan-Boltzmann constant
τ = optical depth at band head
ω = bandwidth parameter

Subscripts

c = center line
i = ith band
n = order of cylindrical exponential integral function
w = wall
ν = spectral

Development of the Axial Band Absorptance

The spectral absorption coefficient of many molecular gases can be represented, for heat transfer purposes, by the exponential-winged band model [18, 19, 20, 21, 22]. For just-overlapped lines k_ν can be written as follows

$$k_\nu = \sum_{i=1}^{N} k_{\nu_i} \tag{8}$$

$$k_{\nu_i} = \frac{\alpha_i}{\omega_i} \exp[-(\nu_i - \nu)/\omega_i], \quad \nu < \nu_i, \tag{9}$$

where α_i is the integrated intensity of the ith band, ω_i is the band wing decay width and ν_i is the band head. Let there be defined here

$$A^*_{a,i}(x_i) = \frac{1}{\omega_i} \int_{\Delta\nu_i} \{1 - \frac{4}{\pi} D_3(x_i \exp[-(\nu_i - \nu)/\omega_i])\}\, d\nu, \tag{10}$$

where

$$x_i = \tau_{R,i}\, \bar{r}^*, \quad \tau_{R,i} = \frac{\alpha_i}{\omega_i} \rho R \text{ and } \bar{r}^* = \bar{r}/R. \tag{11}$$

The general form of $\bar{r}$ is

$$\bar{r} = \eta r \cos\gamma + \xi r_1 [1 - (r/r_1)^2 \sin^2\gamma]^{1/2},$$

where the parameters η and ξ take the values ± 1, and r_1 is equal to either R or r' of equation (7). To simplify notation we define

$$x'_{i,j} = \tau_{R_i} [(r^{*\prime 2} - r^{*2} \sin^2\gamma)^{1/2} - j r^* \cos\gamma]; \quad r^* = r/R \tag{12}$$

and we let the unprimed symbol $x_{i,j}$ denote the primed quantity with $r^{*\prime} = 1$. Due to the complex cylindrical geometry the axial band absorptance retains one angular dependency, unlike the slab band absorptance [21].

With these simplifications both in concept (the introduction of $A^*_{a,i}$) and in notation (the introduction of the $x'_{i,\pm 1}$ convention), equation (7) becomes

$$\begin{aligned} q_i(r^*) = \pi\omega_i \int_{\gamma=0}^{\pi/2} \cos\gamma \{ & I_{\nu_i}(R)[A^*_{a,i}(x_{i,+1}) - A^*_{a,i}(x_{i,-1})] \\ & + \int_{r^* \sin\gamma}^{1} B_{\nu_i} \frac{d}{dr^{*\prime}} [A^*_{a,i}(x'_{i,-1})] dr^{*\prime} \\ & - \int_{r^* \sin\gamma}^{r^*} B_{\nu_i} \frac{d}{dr^{*\prime}} [A^*_{a,i}(-x'_{i+1})] dr^{*\prime} \\ & - \int_{r^*}^{1} B_{\nu_i} \frac{d}{dr^{*\prime}} [A^*_{a,i}(x'_{i,+1})] dr^{*\prime} \} \, d\gamma \end{aligned} \tag{13}$$

It is often preferable to write the radiative flux in terms of $A^*_{a,i}$ rather than its derivative. Such a form can be achieved by integrating equation (13) by parts and manipulating it to yield the following:

$$\begin{aligned} q_i(r^*)/\omega_i = \pi \int_{\gamma=0}^{\pi/2} \cos\gamma \{ & [I_{\nu_i}(R) - B_{\nu_i}(R)][A^*_{a,i}(x_{i,+1}) \\ & - A^*_{a,i}(x_{i,-1})] - \int_{r^* \sin\gamma}^{1} B'_{\nu_i}(r^{*\prime}) A^*_{a,i}(x'_{i,-1}) dr^{*\prime} \\ & + \int_{r^* \sin\gamma}^{r^*} B'_{\nu_i}(r^{*\prime}) A^*_{a,i}(-x'_{i,+1}) dr^{*\prime} \\ & + \int_{r^*}^{1} B'_{\nu_i}(r^{*\prime}) A^*_{a,i}(x'_{i,+1}) dr^{*\prime} \} d\gamma. \end{aligned} \tag{14}$$

where

$$B'_{\nu_i}(r^{*\prime}) = \frac{d}{dr^{*\prime}} [B_{\nu_i}(r^{*\prime})]$$

For black walls with no temperature jump (radiation slip), equation (14) reduces to

$$\begin{aligned} q_i(r^*)/\omega_i = \pi \int_{\gamma=0}^{\pi/2} \cos\gamma \{ & \int_{r^*}^{1} B'_{\nu_i}(r^{*\prime}) A^*_{a,i}(x'_{i,+1}) dr^{*\prime} \\ & - \int_{r^* \sin\gamma}^{1} B'_{\nu_i}(r^{*\prime}) A^*_{a,i}(x'_{i,-1}) dr^{*\prime} \\ & + \int_{r^* \sin\gamma}^{r^*} B'_{\nu_i}(r^{*\prime}) A^*_{a,i}(-x'_{i,+1}) dr^{*\prime} \} d\gamma. \end{aligned} \tag{15}$$

The foregoing relations show that introducing the axial band ab-

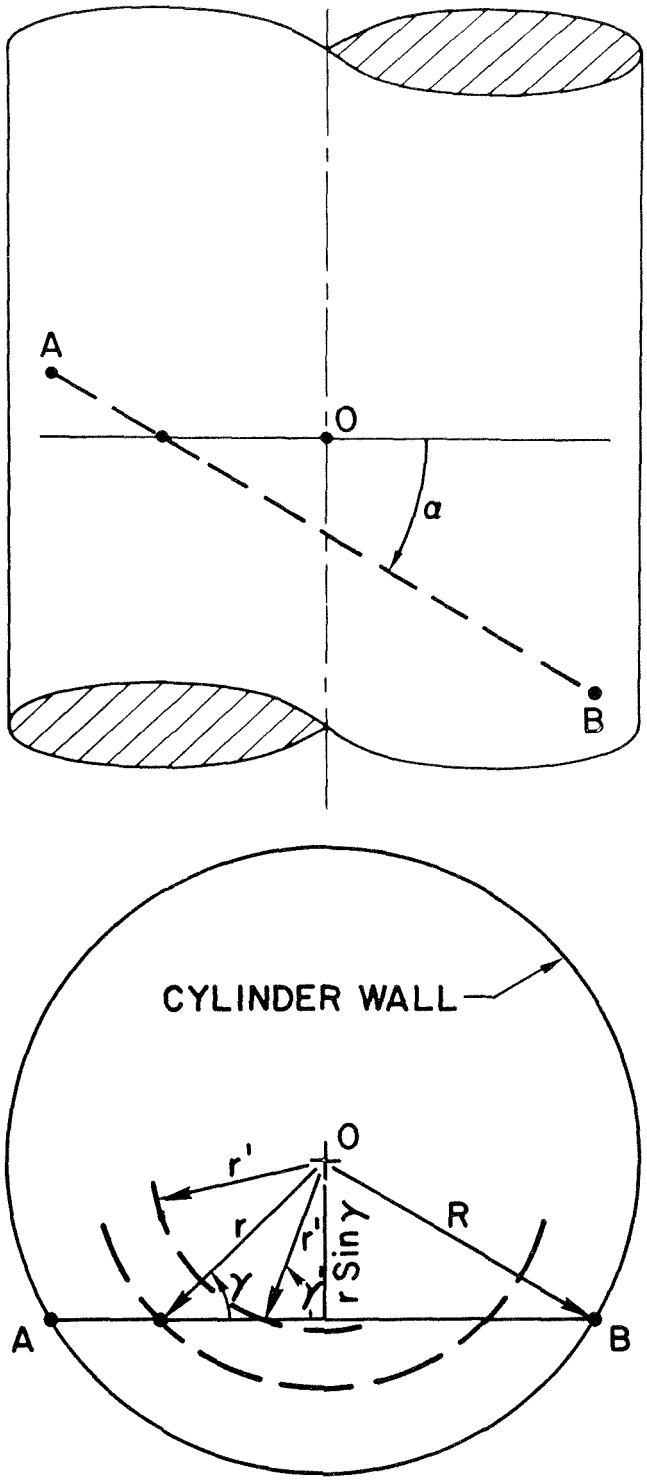

Fig. 1 The cylindrical geometry showing the complementary axial angle α and radial angle γ

sorptance leads to a considerable simplification compared to equation (5) or (7) provided a closed-form expression for $A^*_{a,i}$ is found. The problem of evaluating the radiative flux is reduced to evaluating the double integrals of equation (15) instead of the quadruple integrals inherent in equation (1), which requires integration over ν, or in equation (7), which contains triple integrals. The problem is thus made similar to that of finding the radiant flux in a sphere, but the axial band absorptance replaces the ordinary line-of-sight band absorptance.

Axial Band Absorptance in Closed Form

From the definition of the optical depth at the band head, $\tau_{R,i}$, and the further definition of τ_i^* as

$$\tau_i^* = \exp\left[-(\nu_i - \nu)/\omega_i\right] , \tag{16}$$

one can write equation (10) as follows:

$$A^*_{a,i}(x_i) = \int_0^1 \left\{1 - \frac{4}{\pi} D_3(x_i \tau_i^*)\right\} \frac{d\tau_i^*}{\tau_i^*} . \tag{17}$$

Introducing the first approximation into the analysis by affecting the following kernel approximation of the form suggested by Habib and Greif [13],

$$D_3(x) \doteq \frac{\pi}{4} e^{-bx} ,$$

in equation (17) allows one to write the following:

$$A^*_{a,i}(x_i) = \ln(bx_i) + E_1(bx_i) + \gamma_e \tag{18}$$

where γ_e is the Euler-Mascheroni constant [23],

$$\gamma_e = \int_0^1 (1 - e^{-t}) \frac{dt}{t} - \int_1^\infty e^{-t} \frac{dt}{t} = 0.5772156\ldots, \tag{19}$$

and $E_1(x)$ is the exponential integral function

$$E_1(x) = \int_0^1 e^{-x/t} \frac{dt}{t} = \int_1^\infty e^{-xt} \frac{dt}{t} . \tag{20}$$

The quantity b used by Habib and Greif [13] was 5/4. Somewhat better accuracy is obtainable by using two values of b, as shown in the Appendix, one for small x_i and the other for larger x_i. In this way two relations were found for $A^*_{a,i}$ and patched together at $x_i = 0.38$:

$$A^*_{a,i} = \ln(4x_i/\pi) + E_1(4x_i/\pi) + \gamma_e, \quad x_i \le 0.38 \tag{21a}$$

$$A^*_{a,i} = \ln x_i + E_1(3\pi x_i/8) + \gamma_e + \ln 2 - 1/2 , \quad x_i > 0.38 \tag{21b}$$

Table 1 Comparison between exact numerical and approximate values of the axial band absorptance

x_i	Exact value	Approximate value
0.01	0.012683	0.012692
0.02	0.025268	0.025304
0.03	0.037758	0.037836
0.04	0.05015	0.05029
0.05	0.06246	0.06266
0.06	0.07467	0.07496
0.08	0.09883	0.09932
0.1	0.12265	0.12338
0.2	0.23685	0.23931
0.3	0.3436	0.3484
0.4	0.4438	0.4503
0.5	0.5380	0.5418
0.6	0.6268	0.6285
0.8	0.7902	0.7890
1.0	0.9370	0.9344
2.0	1.4965	1.4937
3.0	1.8770	1.8757
4.0	2.1588	2.1583
5.0	2.3804	2.3802
6.0	2.5623	2.5622
8.0	2.8498	2.8498
10.0	3.0729	3.0729

Table 1 shows that agreement between values calculated numerically and the approximate closed-form expressions in the foregoing is excellent.

Two applications of the axial band absorptance follow.

Wall Radiative Flux

Consider a hot gas enclosed by a black-walled pipe. The radiative flux at the wall is given by equation (15) with $r^* = 1$,

$$q_i(r^* = 1) = \pi\omega_i \frac{dB_{\nu_i}}{dT} \int_{\gamma=0}^{\pi/2} \cos\gamma \int_{\sin\gamma}^1 \frac{d}{dr^{*\prime}} T(r^{*\prime}) \left\{A^*_{a,i}(-x'_{i,+1}) - A^*_{a,i}(x'_{i,-1})\right\} dr^{*\prime} d\gamma . \tag{22}$$

The temperature profile within the pipe can be written generally

$$T - T_o = [T_c - T_o] f(r^{*\prime}) \tag{23}$$

Consider the following specific profiles:

(a) Trapezoidal profile, $T_0 = T_w$

$$f(r^{*\prime}) = 1, \; f'(r^{*\prime}) = 0 \qquad 0 \le r^{*\prime} \le \delta^*$$
$$f(r^{*\prime}) = \frac{1 - r^{*\prime}}{1 - \delta^*} , \; f'(r^{*\prime}) = \frac{-1}{1 - \delta^*} \quad \delta^* < r^{*\prime} \le 1 \tag{24}$$

(b) Parabolic profile, $T_0 = T_w$

$$f(r^{*\prime}) = 1 - r^{*\prime 2}, \; f'(r^{*\prime}) = -2r^{*\prime} \tag{25}$$

(c) Gaussian profile, $T_0 = (T_w e^{1/\lambda^2} - T_c)/(e^{1/\lambda^2} - 1)$

$$f(r^{*\prime}) = e^{-(r^{*\prime}/\lambda)^2}, \; f'(r^{*\prime}) = -\frac{2r^{*\prime}}{\lambda^2} e^{-(r^{*\prime}/\lambda)^2} . \tag{26}$$

If the profiles (24), (25), or (26) are substituted into equation (22), there results

$$q_i(\tau_{R,i})/(\pi\omega_i \frac{dB_{\nu_i}}{dT}(T_c - T_w)) = \int_{\gamma=0}^{\pi/2} \cos\gamma \int_{\sin\gamma}^1 \left\{A^*_{a,i}(-x'_{i,+1}) - A^*_{a,i}(x'_{i,-1})\right\} f'(r^{*\prime}) dr^{*\prime} d\gamma \tag{27}$$

where $f'(r^*)$ takes the forms shown for the different profiles.

Tables 2(*a*) and 2(*b*) show computed fluxes at $r^* = 1$ as a function $\tau_{R,i}$. They are useful, for example, in evaluating how much wall radiation is affected by departures from isothermal conditions within cylinders.

Mean Beam Length, Emissivity, and Absorptivity

Of use in analysis of radiant transfer from isothermal gas volumes, the mean band absorptance $\bar{A}_i$ for a gas volume completely enclosed by a black wall is simply

$$\bar{A}_i = q_{i,w}/[\pi B_{\nu_i}(T_c) - \pi B_{\nu_i}(T_w)] \tag{28}$$

This quantity may be used to calculate total emissivity or absorptivity by writing

$$\epsilon\sigma T_c^4 = \sum_{i=1}^N \bar{A}_i \pi B_{\nu_i}(T_c) \tag{29}$$

$$\alpha\sigma T_w^4 = \sum_{i=1}^N \bar{A}_i \pi B_{\nu_i}(T_w) \tag{30}$$

It is common practice in engineering, e.g., [24], to estimate A_i or ϵ (or α) using the line-of-sight relation for the band absorption or the emissivity (or absorptivity),

$$\bar{A}_i \doteq A_i(\bar{L})$$

and a single value of path length, called the mean beam length $\bar{L}$. In actuality, in the cylinder, radiation on the wall is received from beams having path lengths ranging from zero to infinity.

Equation (14) permits us to find an exact value of $\bar{A}_i$ and hence $\bar{L}$ without difficulty. For the isothermal case $B'_{\nu(i)} = 0$, and

$$\bar{A}_i = \omega_i \int_0^{\pi/2} A^*_{a,i}(\tau_{R,i} \cos\gamma) \cos\gamma d\gamma \tag{31}$$

This expression with equation (21) substituted, was integrated

Table 2(*a*) Wall radiative flux, trapezoidal temperature profile

τ_R	δ^*	Wall flux	τ_R	δ^*	Wall flux
0.01	0.3	0.0092126	2.0	0.3	0.76844
	0.6	0.012992		0.6	1.10880
	0.9	0.017967		0.9	1.63194
0.02	0.3	0.018319	3.0	0.3	0.88060
	0.6	0.025836		0.6	1.28264
	0.9	0.035738		0.9	1.93709
0.03	0.3	0.027320	4.0	0.3	0.94549
	0.6	0.038535		0.6	1.38728
	0.9	0.053316		0.9	2.14255
0.04	0.3	0.036219	5.0	0.3	0.98706
	0.6	0.051090		0.6	1.45628
	0.9	0.070702		0.9	2.29266
0.05	0.3	0.045015	10.0	0.3	1.07505
	0.6	0.063504		0.6	1.60725
	0.9	0.087901		0.9	2.68991
0.1	0.3	0.087515	20.0	0.3	1.12093
	0.6	0.12352		0.6	1.68745
	0.9	0.17117		0.9	2.96334
0.2	0.3	0.16563	30.0	0.3	1.13645
	0.6	0.23399		0.6	1.71461
	0.9	0.32503		0.9	3.06783
0.3	0.3	0.23313	40.0	0.3	1.14425
	0.6	0.32940		0.6	1.72827
	0.9	0.45851		0.9	3.12187
0.4	0.3	0.29165	50.0	0.3	1.14894
	0.6	0.41335		0.6	1.73649
	0.9	0.57819		0.9	3.15462
0.5	0.3	0.34425	100.0	0.3	1.15837
	0.6	0.48914		0.6	1.75294
	0.9	0.68723		0.9	3.22049
1.0	0.3	0.54581			
	0.6	0.77962			
	0.9	1.11501			

Table 2(*b*) Wall radiative flux, parabolic and Gaussian profiles

τ_R	Parabolic profile	Gaussian profile, $\lambda = 1$
0.01	0.0099422	0.0083115
0.02	0.019771	0.016527
0.03	0.029487	0.024648
0.04	0.039093	0.032675
0.05	0.048590	0.040611
0.1	0.094492	0.078950
0.2	0.17894	0.14941
0.3	0.25193	0.21030
0.4	0.31565	0.26300
0.5	0.37307	0.31037
1.0	0.59367	0.49184
2.0	0.84115	0.69173
3.0	0.96975	0.79193
4.0	1.04642	0.84956
5.0	1.09681	0.88626
10.0	1.20795	0.96295
20.0	1.26883	1.00200
30.0	1.28992	1.01500
40.0	1.30060	1.02148
50.0	1.30706	1.02536
100.0	1.32015	1.03313

numerically and the parameter

$$u = \bar{L}/R \tag{32}$$

was found from equating the result with

$$A_i(u\tau_{R,i}) = \omega_i \left[\ln (u\tau_{R,i}) + E_1 (u\tau_{R,i}) + \gamma_c \right] \tag{33}$$

Table 3 shows the results for u. When $\tau_{R,i}$ goes to zero, u goes to the known result $u = 2$ [25], and when $\tau_R \to \infty$, u goes the other limit $8e^{-3/2} = 1.785$ found by Tien and Wang [26].

Table 3 Ratio of mean beam length to cylinder radius for the exponential-winged band model with overlapped lines

τ_R	u	Band absorptance $A_i(L)/\omega_i$
0.0	2.0	0.0
0.01	1.9992	0.01989
0.02	1.9984	0.03957
0.03	1.9976	0.05904
0.04	1.9968	0.07830
0.05	1.9960	0.09736
0.1	1.992	0.1897
0.2	1.984	0.3606
0.3	1.950	0.5095
0.4	1.925	0.6439
0.5	1.907	0.7670
1.0	1.858	1.2564
2.0	1.818	1.8742
3.0	1.802	2.2656
4.0	1.795	2.5487
5.0	1.792	2.7697
10.0	1.787	3.4601
20.0	1.785	4.1526
30.0	1.785	4.5580
40.0	1.785	4.8456
50.0	1.785	5.0687
100.0	1.785	5.7618

Summary and Conclusions

The axial band absorptance for a molecular gas having vibration-rotation spectra according to the exponential-winged band model has been developed. Approximate closed forms have been derived and shown to compare well with exact values. With the axial band absorptance, the problem of evaluating radiative heat flux in a cylinder is formulated as for the sphere, but the axial band absorptance replaces the ordinary line-of-sight band absorptance measured in the laboratory.

The axial band absorptance was used to derive the radiative flux at the wall of a cylinder containing a gas with trapezoidal, parabolic, or Gaussian temperature profiles. Mean beam length, absorptivity, and emissivity were shown to be easily found as a function of the optical depths at the band heads based on the cylinder radius, $\tau_{R,i}$, for exponential-winged bands with overlapped lines.

References

1 Usiskin, C., and Sparrow, E. M., "Thermal Radiation Between Parallel Plates Separated by an Absorbing-Emitting Non-Isothermal Gas," *International Journal of Heat and Mass Transfer*, Vol. 1, 1960, pp. 28–36.

2 Sparrow, E. M., Usiskin, C. M., and Hubbard, H. A., "Radiation Heat Transfer in a Spherical Enclosure Containing a Participating, Heat-Generating Gas," JOURNAL OF HEAT TRANSFER, TRANS. ASME, Series C, Vol. 82, 1961, pp. 197–206.

3 Viskanta, R., "Interaction of Heat Transfer by Conduction, Convection, and Radiation in Radiating Fluids," JOURNAL OF HEAT TRANSFER, TRANS. ASME, Series C, Vol. 85, 1963, pp. 318–328.

4 Cess, R. D., "The Interaction of Thermal Radiation With Conduction and Convection Heat Transfer," *Advances in Heat Transfer* (T. F. Irvine, Jr., and J. P. Hartnett, eds.), Academic Press, New York, Vol I, 1964, pp. 1–49.

5 Viskanta, R., "Radiation Transfer and Interaction of Convection With Radiation Heat Transfer," *Advances in Heat Transfer*, Academic Press, New York, Vol. III, 1966, pp. 176–248.

6 Einstein, T. H., "Radiant Heat Transfer in Absorbing Gases Enclosed in a Circular Pipe With Conduction, Gas Flow and Internal Heat Generation," NASA TR R-156, 1963.

7 Nichols, L. D., "Temperature Profile in the Entrance Region of an Annular Passage Considering the Effects of Turbulent Convection and Radiation," *International Journal of Heat and Mass Transfer*, Vol. 8, 1965, pp. 589–607.

8 deSoto, S., and Edwards, D. K., "Radiative Emission and Absorption in Nonisothermal Nongray Gases in Tubes," *Proceedings 1965 Heat Transfer and Fluid Mechanics Institute*, Stanford University Press, Stanford, Calif., 1965, pp. 358–372.

9 deSoto, S., "Coupled Radiation, Conduction and Convection in Entrance Region Flow," *International Journal of Heat and Mass Transfer*, Vol. 11, 1968, pp. 39–53.

10 Kesten, A. S., "Radiant Heat Flux Distribution in a Cylindrically Symmetric Nonisothermal Gas With Temperature Development Absorption Coefficient," *J. Quant. Spectrosc. Radiat. Transfer*, Vol. 8, 1968, pp. 419–434.

11 Viskanta, R., and Merriam, R. L., "Heat Transfer by Combined Conduction and Radiation Between Concentric Spheres Separated by Radiating Medium," JOURNAL OF HEAT TRANSFER, TRANS. ASME, Series C, Vol. 90, 1968, pp. 248–256.

12 Landram, C. S., Greif, R., and Habib, I. S., "Heat Transfer in Turbulent Pipe Flow With Optically Thin Radiation," JOURNAL OF HEAT TRANSFER, TRANS.ASME, Series C, Vol. 91, 1969, pp. 330–336.

Table 4 Comparison of exact and approximate values of $D_3(x)$

x	$D_3(x)$	$\pi/4 \exp(-3\pi x/8)$	$\pi/4 \exp(-4x/\pi)$
0.0	0.78540	0.78540	0.78540
0.01	0.77458	0.77620	0.77546
0.02	0.76570	0.76711	0.76565
0.03	0.75608	0.75812	0.75596
0.04	0.74660	0.74925	0.74640
0.05	0.73726	0.74047	0.73696
0.06	0.72805	0.73180	0.72763
0.08	0.71004	0.71476	0.70934
0.1	0.69254	0.69811	0.69150
0.2	0.61206	0.62053	0.60883
0.3	0.54186	0.55157	0.53605
0.4	0.48038	0.49027	0.47196
0.5	0.42636	0.43578	0.41554
0.6	0.37879	0.38735	0.36586
0.8	0.29974	0.30604	0.28361
1.0	0.23785	0.24180	0.21985
2.0	0.076964	0.074440	0.061542
3.0	0.025647	0.022917	0.017227
4.0	0.0086988	0.0070555	0.0048222
5.0	0.0029863	0.0021721	0.0013499
6.0	0.0010342	0.00066872	0.00037786
8.0	0.00012642	0.000063381	0.000029608
10.0	0.000015728	0.0000060073	0.0000023200

13 Habib, I. S., and Greif, R., "Nongray Radiative Transport in a Cylindrical Medium," JOURNAL OF HEAT TRANSFER, TRANS. ASME, Series C, Vol. 92, 1970, pp. 28-32.

14 Tiwari, S. N., and Cess, R. D., "Heat Transfer to Laminar Flow of Nongray Gases Through a Circular Tube," *Applied Scientific Research*, Vol. 25, 1971, pp. 155-169.

15 Chiba, Z., and Greif, R., Discussion of "Nongray Radiative Transport in a Cylindrical Medium," JOURNAL OF HEAT TRANSFER TRANS. ASME, Series C, Vol. 95, 1973, p. 142.

16 Edwards, D. K., and Wassel, A. T., "The Radial Radiative Heat Flux in a Cylinder," JOURNAL OF HEAT TRANSFER, TRANS. ASME, Series C, Vol. 95, 1973, pp. 276-277.

17 Kuznetsov, Y. S., "Temperature Distribution in an Infinite Cylinder and in a Sphere in a State of Non-Monochromatic Radiation Equilibrium," English translation in USSR *Computational Mathematics and Mathematical Physics*, Vol. 2, 1963, pp. 230-254.

18 Edwards, D. K., and Balakrishnan, A., "Thermal Radiation by Combustion Gases," *International Journal of Heat and Mass Transfer*, Vol. 16, 1973, pp. 25-40.

19 Tien, C. L., "Thermal Radiation Properties of Gases," *Advances in Heat Transfer*, Academic Press, New York, Vol. V, 1968, pp. 253-324.

20 Cess, R. D., and Tiwari, S. N., "Infrared Radiative Energy Transfer in Gases," *Advances in Heat Transfer*, Academic Press, New York, Vol. VIII, 1962, pp. 229-283.

21 Edwards, D. K., and Balakrishnan, A., "Slab Band Absorptance for Molecular Gas Radiation," *J. Quant. Spectrosc. Radiat. Transfer*, Vol. 12, 1972, pp. 1379-1387.

22 Bratis, J. C., and Novotny, J. L., "Radiation-Convection Interaction in the Boundary-layer Regime of an Enclosure," Department of Aerospace and Mechanical Engineering, University of Notre Dame, Technical Report No. 72-30, submitted for publication to the *Int. J. Heat Mass Transfer*.

23 Chandrasekhar, S., *Radiative Transfer*, Dover Publications, New York, Appendix I, 1960, p. 373.

24 Dunkle, R. V., "Geometric Mean Beam Lengths for Radiant Heat-Transfer Calculations," JOURNAL OF HEAT TRANSFER, TRANS. ASME, Series C, Vol. 84, 1964, pp. 75-80.

25 Hottel, H. C., "Radiant Heat Transmission," Chapter 4 of W. H. McAdams, *Heat Transmission*, McGraw-Hill, New York, 1964.

26 Tien, C. L., and Wang, L. S., "On the Calculation of Mean Beam Length for a Radiating Gas," *J. Quant. Spectrosc. Radiat. Transfer*, Vol. 5, 1965, pp. 453-456.

APPENDIX

Exponential Kernel Approximations for $D_n(x)$

Members of the set of functions

$$D_n(x) \equiv \int_0^1 \frac{\mu^{n-1}}{(1-\mu^2)^{1/2}} e^{-(x/\mu)}\, d\mu\ ,\quad n = 1, 2, \ldots \tag{34}$$

have the following properties:

$$\frac{d}{dx} D_n(x) = -D_{n-1}(x) \qquad n > 1 \tag{35}$$

$$D_{n+1}(x) = \int_x^\infty D_n(x)dx \tag{36}$$

$$D_1(0) = \pi/2\ ,\ D_2(0) = 1,\ D_3(0) = \pi/4,\ D_4(0) = 2/3 \tag{37}$$

Let $D_n(x)$ be approximated by

$$D_n(x) \doteq ae^{-bx} \tag{38}$$

Taking the zeroth moment of both sides gives

$$\int_0^\infty D_n(x)dx \doteq \int_0^\infty ae^{-bx}dx$$

$$D_{n+1}(0) \doteq a/b \tag{39}$$

Taking the first moment similarly gives

$$\int_0^\infty xD_n(x)dx \doteq \int_0^\infty xae^{-bx}dx$$

$$D_{n+2}(0) \doteq a/b^2 \tag{40}$$

The exact values of $D_n(0)$, equation (37), and the two relations, equations (39) and (40), serve to fix values of a and b, if one chooses a value of n.

Choosing $n = 1$ yields $a = 4/\pi$ and $b = 4/\pi$. Equation (36) applied two successive times yields

$$D_3(x) \doteq (\pi/4)e^{-(4/\pi)x} \tag{41}$$

Comparison of $D_3(x)$ with values obtained from numerical integration of equation (34), tabulated in Table 4, shows good agreement at low x, but they differ somewhat at higher values of x.

Choosing $n = 2$ yields $a = 3\pi^2/32$ and $b = 3\pi/8$. Equation (36) then gives

$$D_3(x) \doteq \frac{\pi}{4} e^{-(3\pi/8)x} \tag{42}$$

At larger values of x this relation agrees better with exact values than does equation (41), but equation (41) is superior at low values of x.

J. L. NOVOTNY
Professor.
D. E. NEGRELLI
Research Assistant.
Department of Aerospace and Mechanical Engineering, University of Notre Dame, Notre Dame, Ind.
T. Van den DRIESSCHE
Student,
Purdue University,
Fort Wayne, Ind.

Total Band Absorption Models for Absorbing-Emitting Liquids: CCl_4[1]

Predictions of the total band absorption are useful for describing the absorption process in calculations dealing with radiation interaction in absorbing-emitting liquids. Two two-parameter models, similar to the Elsasser and the statistical narrow band models used in gas radiation work, are developed for predicting the total band absorption in regions of the liquid CCl_4 spectrum. The parameters, which are considered to be adjustable, can be determined from experimental total band absorption data or, if available, basic spectroscopic information. Results from the models are compared to experimental total band absorption measurements for CCl_4 as well as a prediction based on spectral integration.

Introduction

It has been pointed out in recent investigations [1–5][2] that radiative transfer can have a significant effect on heat transfer in weakly absorbing liquids. This effect is important not only in normal heat transfer situations but is especially important in the experimental determination of the thermal conductivity of an absorbing liquid. The majority of the prior studies [1–4] have been slanted toward the latter objective which is the determination of an effective conductivity. Schödel and Grigull [1] studied the interaction of radiation with conduction in a horizontal liquid layer heated from above. Data obtained with a Mach-Zehnder interferometer and a calorimetric method were compared to an approximate analysis due to Poltz [2] based on an effective absorption coefficient reduced from transmission data. Agreement between experiment and theory was fair. Poltz [3] and Poltz and Jugel [4] experimentally examined the same problem obtaining an effective conductivity for a number of liquids. Novotny and Bratis [5] investigated the use of basic spectroscopic information, such as band intensities, band widths and band shapes, to theoretically predict the interaction of radiation with conduction in a liquid CCl_4 layer. Results were obtained for the experimental conditions reported in references [1, 3]. It was found that the effect of radiation could be satisfactorily predicted if certain band shapes were used in the analysis [5].

Examination of the literature reveals that very little basic spectroscopic information exists for absorbing liquids. This is clearly brought out when one examines the case of CCl_4. Although the absorption spectrum of CCl_4 is probably better known than the spectrum of any other liquid, it is still necessary to estimate a large number of the spectroscopic parameters from meager information [5]. This does not even account for the fact that the true shape of the absorption bands is unknown. Since information such as band intensities, band widths, and band profiles is very difficult to obtain in the laboratory, it was decided to try to develop an analytical approach based on rather simple laboratory measurements.

The radiation term in the governing energy equation for heat transfer processes can be formulated in terms of the total band absorption [5, 6, 7]. The approach used in Novotny and Bratis [5] was to determine the total band absorption as a function of distance in selected regions of the spectrum from band intensities, widths and profiles. Here, two two-parameter band models are developed for the total band absorption; experimental total band absorption data then provide the means for determining the two adjustable parameters in the models. This approach requires very little expertise in spectroscopy; experimental total band absorption data are rather easy to obtain in the laboratory, at least to the degree of accuracy needed for heat transfer calculations.

The band models are an Elsasser-type (regular) model and a statistical-type (random) model both based on an exponential profile; these models have been extensively used in gas radiation work [8].[3] Comparisons between the results of [5] and the approximate models are presented for the total band absorption

[1] Sponsored by the National Science Foundation under Grant GK 20382. The third author also received summer support under Grant GY9898.

[2] Numbers in brackets designate References at end of paper.

Contributed by the Heat Transfer Division of The American Society of Mechanical Engineers and presented at the ASME-AIChE Heat Transfer Conference, Atlanta, Ga., August 5–8, 1973. Manuscript received by the Heat Transfer Division April 23, 1973; revised manuscript received May 31, 1973. Paper No. 73-HT-7.

[3] For gas radiation predictions, these models are based on the Lorentz profile.

Table 1 Band Data CCl_4 (293K)

Region (cm^{-1})	ω_j Center (cm^{-1})	S_j Intensity (cm^{-2})	α_j Half-Width (cm^{-1})
285–400	320	60.[a]	11.0[a]
	493	54.4	11.0[a]
400–690	533	21.2	12.5[a]
	569	12.8	12.5[a]
	628	84.2	8.0[a]
690–900	762	377,600	9.2
	784	496,000	11.0
	979	770	12.0
	1004	880	13.0
900–1350	1067	340	12.5
	1108	140	12.5
	1214	760	16.5
	1247	860	13.0
1350–1700	1536	5640	33.5
	1850	60.4	30.0[a]
1700–3300	2015	46.2	18.0[a]
	2340	188	40.0[a]

[a]Estimated value.

and the first derivative of the band absorption with respect to path length. To help substantiate the use of the exponential profile, total band absorption data for CCl_4 are also compared to the analytical results.

Analysis

The total band absorption is given by

$$A_i(L) = \int_{\Delta\omega_i} [1\text{-}\exp(-\kappa_\omega L)]d\omega \tag{1}$$

where $\Delta\omega_i$ refers to ith portion of the spectrum and κ_ω takes into account the contribution in the ith region of all bands in the spectrum. For discussion purposes, the pertinent band data for CCl_4 used in [5] are given in Table 1. From these data, it is obvious that one can not separate the spectrum into sections treating each band individually with no overlap. Thus an analytical model must not only take into account the proper wing behavior [5] but also the overlap between bands. To accomplish this without specifying the basic properties for each individual band, models similar to the Elsasser (regular) model and the statistical (random) model are used. The use of a model represented by a set of lines (bands in this case) of equal intensity and half-width does not represent the exact details of the absorption process but should give the characteristic behavior of the total band absorption.

The basic Elsasser model [8] originally developed for spectral lines uses the Lorentz distribution. In [5], it was found that the 12.8 μm doublet could not be represented by the Lorentz profile; the wings of a Lorentz representation incorrectly overwhelms the rest of the absorption spectrum. Although it has been suggested (see reference [5]) that the shape of the 12.8 μm doublet is Gaussian, good agreement between analytical results and existing heat transfer data was obtained using an exponential distribution for each band in the spectrum [5]. The agreement between experiment and analysis for the exponential profile was better than the case of using the Gaussian profile for the 12.8 μm region and a Lorentz profile for the remaining bands.

The basic exponential profile is given by

$$\kappa_\omega = \frac{S}{2\alpha}\exp\left[-\frac{|\omega-\omega_0|}{\alpha}\right] \tag{2}$$

where S is the line (band) intensity, α the line (band) half-width, and ω_0 the location of the center of the profile. Incorporating this into an Elsasser-type band model one obtains

$$\kappa_\omega = \sum_{-\infty}^{\infty}\frac{S}{2\alpha}\exp\left[-\frac{|\omega-nd|}{\alpha}\right] \tag{3}$$

where $n = 0, \pm1, \pm2$,----. The average absorption of this band model is then evaluated by integrating equation (1) with respect to ω from $-\frac{1}{2}d$ to $\frac{1}{2}d$

$$\bar{A} = 1 - \int_0^1 \exp[-f(\eta)]d\eta \tag{4}$$

where $\beta = \dfrac{2\alpha}{d}$, $\eta = \dfrac{2\omega}{d}$ and

$$f(\eta) = \frac{SL}{d\beta}\frac{e^{-\eta/\beta} + e^{(\eta-2)/\beta}}{1 - e^{-2/\beta}} \tag{5}$$

The total band absorption in a given region $\Delta\omega_i$ of the spectrum is given by $A_i = \bar{A}\Delta\omega_i$.

Equation (5) for the average absorption is a function of two parameters S/d and β. These parameters are considered to be adjustable and to be determined in selected regions of the absorption spectrum from experimental data. In the small path-length limit, equation (4) reduces to the linear limit

$$\bar{A} = \frac{SL}{d} = \frac{S_T L}{\Delta\omega} \tag{6}$$

This limit allows the determination of $\dfrac{S}{d}$ (or S_T) from experimental data in a given region $\Delta\omega_i$ of the absorption spectrum. The remaining parameter β can be determined by matching equation (5) to experimental data at a path length beyond those for which equation (6) is valid; a best value of β can be found by systematically matching the data to equation (5).

The alternate band model is the random or statistical model [9]. This model here is constructed from a set of equally intense lines (bands in this case) randomly distributed. The average absorption for such a set of lines (bands) is given by [9]

$$\bar{A} = 1 - \exp\left[-\left(\frac{A_L}{d}\right)\right] \tag{7}$$

where d is the average line (band) spacing and A_L is the absorption for a single line (band). Equation (7) with the definition of A_L applies to lines (bands) of any shape as long as they are of equal intensity and the number of lines (bands) approaches infinity along with the frequency interval. The absorption for a single exponential line (band) is given by equations (1) and (2) where the interval $\Delta\omega$ is allowed to approach infinity. The

Nomenclature

A_i = total band absorption, ith region
$\bar{A}$ = dimensionless total band absorption, $A_i/\Delta\omega_i$
A_L = absorption for a single band
d = band spacing
f = function defined by equation (5)
L = path length
n = summation index
S = band intensity
S_T = total band intensity in region $\Delta\omega_i$
α = band half-width
β = line width to spacing parameter, $2\alpha/d$
γ = Euler's constant, 0.5777----
η = wave number parameter, $2\omega/d$
κ_ω = absorption coefficient
ω = wave number

Subscripts

i = ith region of spectrum
j = jth band

resulting expression for A_L is the same expression used by Edwards and Menard [10] for the total band absorption in completely pressure-broadened gases.[4] There exists a number of closed-form expressions that could be used for A_L; for example, one could use the formulations given in [11, 12, 13] for gases in the pressure-broadened limit.

The expression given in [11], which also results from the integration of equation (1) for an exponential line (band) over an infinite frequency interval, is chosen for this work

$$A_L = 2\alpha \left\{ E_1\left(\frac{SL}{2\alpha}\right) + \ln\left(\frac{SL}{2\alpha}\right) + \gamma \right\} \tag{8}$$

where γ is Euler's constant (0.577---) and E_1 is the exponential integral. The total band absorption averaged over the region $\Delta\omega$ of the spectrum is then given by

$$\bar{A} = 1 - \exp\left\{ -\beta\left[E_1\left(\frac{SL}{2\alpha}\right) + \ln\left(\frac{SL}{2\alpha}\right) + \gamma \right]\right\} \tag{9}$$

As before, this model has two adjustable parameters $\frac{S}{d}$ and β. The $\frac{S}{d}$ is obtained as in the Elsasser-type model from the linear absorption region whereas β is determined in the absorption region beyond the linear region. It should be mentioned that equations (4) and (9) reduce to the correct limits for limiting values of β and SL/d.

These models have a definite advantage over the top hat or box model (constant κ_ω in a given region) in that the box model does not allow for overlap and, therefore, overestimates the absorption at intermediate optical depths. It should be noted that the box model has only one adjustable parameter $\frac{S}{d}$ which should be obtained from the linear absorption region.

Experiment

Although the analysis presented here could be compared to the total band absorption obtained analytically in reference [5] instead of experimental data, it is still necessary to verify the correctness of not only the approximate models but also the exponential profile. The only prior indication of the exponential profile satisfactorily representing the band absorption in liquids is a comparison with experimental heat transfer data [5]; this is not a very sensitive test of the correctness of the profile.

To this end, the total band absorption of CCl_4 was measured; results in the wave number range 900–3300 cm^{-1} are presented here. The data were obtained with a Model 21 Perkin-Elmer spectrophotometer with a NaCl prism.[5] A sealed-demountable type cell was used for path lengths of 17 to 158 μm, whereas a variable spacing cell was used for path lengths in the range of 0.2 to 6 mm. The demountable cell was calibrated according to the method of Smith and Miller [14]; cell depth readings were taken directly from the micrometer head on the variable cell. A slit program recommended by the manufacturer for resolution work was used in obtaining the data; the automatic slit program gives approximately constant resolution. It should be noted that the integrated band absorption given by equation (1) is quite insensitive to slit width [15]; the instrument slit widths used here are thought to be in a range such that slit corrections are unnecessary. The carbon tetrachloride was a spectrophotometric grade manufactured by J. B. Baker Co.

Once the absorption spectrum was obtained, the area under the absorption curve was measured with a planimeter.[6] The spectrum was broken up into the regions indicated in Table 1. This division is somewhat arbitrary; however, it does correspond to the calculations carried out in reference [5]. The base line and scale was determined from the 100 percent to 0 percent transmission lines, respectively. Except for a few isolated points, the data show a maximum scatter of about ±10 percent; this was determined by completely repeating a run.

Results and Discussion

Since experimental data were not obtained for all spectral regions, it was decided to also determine the adjustable parameters S/d and $2\alpha/d$ from the spectral integration results of [5]. The limited experimental results then serve as a check on the validity of the exponential profile. Discussing the spectral ingegration matching first, the values of S/d were obtained from the linear absorption region. Both the regular and random models reduce to $\bar{A} = (S/d)L$ in the linear limit; thus the values of S/d are the same for both models. Table 2 presents the best values of S/d for the six regions of the spectrum used in [5]. It should be noted that these are slightly different from the values of $S_T/\Delta\omega$ given in Table 1; the difference is due to overlap between regions.

The best line width to spacing ratio for each region is determined by systematically matching the all exponential profile results of [5] at numerous values of L. It is felt that a great deal of accuracy in the choice of β is not needed for purposes of heat transfer calculations. The values of β for both the random and regular models are also given in Table 2. As expected from the behavior of models [9], the values of β for the random model are larger than those for the regular model in the equivalent region.

Figs. 1–3 present comparison between the spectral integration

Table 2 Band Parameters CCl_4 (~300K); Determined from spectral integration results [5]

Region (cm^{-1})	(S/d), cm^{-1}		$(2\alpha/d)$	
	Regular	Random	Regular	Random
285–400	0.51	0.51	0.17	0.30
400–690	1.02	1.02	0.20	0.40
690–900	4166	4166	0.13	0.21
900–1350	8.40	8.40	0.19	0.47
1350–1700	16.0	16.0	0.18	0.41
1700–3300	0.196	0.196	0.11	0.15

[4] The parameters A_0 and C_0^2 in [10] are replaced by α and $\frac{S}{2\alpha}$, respectively.

[5] With some difficulty, the spectral region could have been extended to lower wave numbers with prism interchanges. Although some data were obtained down to about 650 cm^{-1}, it was felt that the spectral regions above 900 cm^{-1} were sufficient for the purposes of this manuscript. All results were obtained for $T \approx 300$K; a temperature dependency study is beyond the scope of this manuscript.

[6] Since the output of the Model 21 used here is linear in wavelength, the absorption curves had to be transferred to a linear wave number scale.

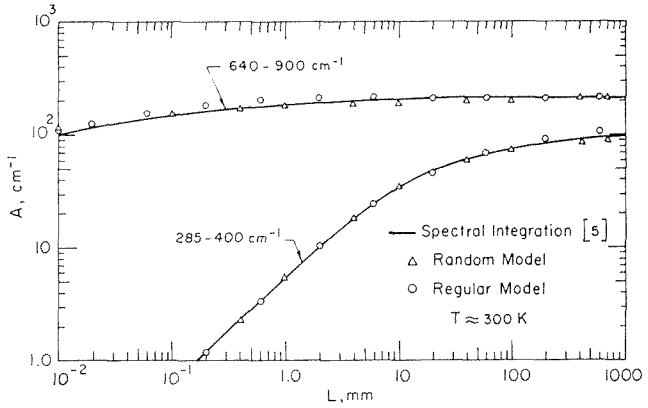

Fig. 1 Total band absorption versus path length; spectral regions 285–400 and 690–900 cm^{-1}

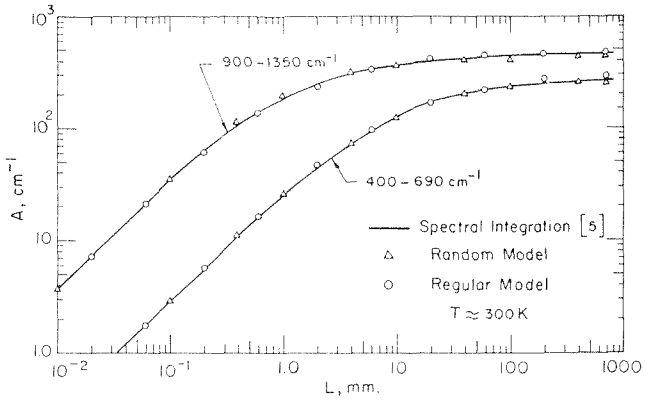

Fig. 2 Total band absorption versus path length; spectral regions 400–690 and 900–1350 cm^{-1}

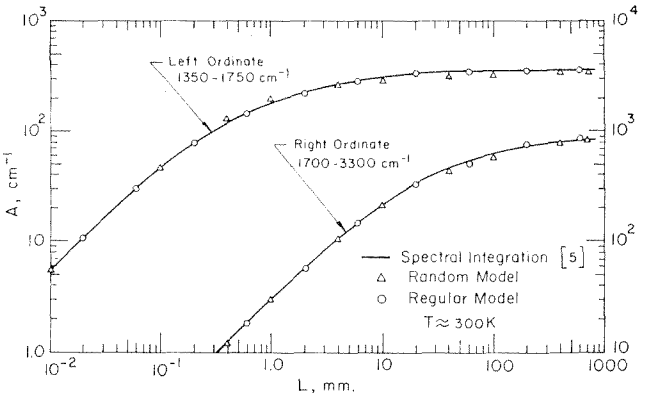

Fig. 3 Total band absorption versus path length; spectral regions 1350–1700 and 1700–3300 cm^{-1}

results of [5] using all exponential profiles and the approximate models. To clearly show the small differences between the analyses, it was necessary to violate the usual practice of presenting an analysis by a line and data by points. The regular and random model results are presented in the figures as open points. The agreement between the analyses is excellent. The random model has a slight tendency to overestimate the spectral integration results at intermediate optical depths and to underestimate the absorption at large optical depths. This, of course, is somewhat due to the manner in which β was determined. The regular model tends to saturate at smaller optical depths than the spectral integration or random model results. The differences between the analyses are slight.

Since the differences between the analyses are slight, the data will only be matched to the random model. The values of S/d and β are determined from the data in the same manner as described in the previous paragraphs; Table 3 presents the best values of S/d and β. Although there is a lack of data for $L >$ 6mm in the 1700–3300 cm^{-1} region, the path lengths are sufficiently large enough for the absorption to be sensitive to the choice of β. The random model as well as the spectral integration results of [5] are compared to the data in Fig. 4. The data are correlated very well by the adjustable band model. Considering the approximate methods used in determining the band information given in Table 1, the agreement between the spectral integration results of [5] and the experimental data is excellent. A slight change in band intensities and band widths used in the spectral calculations accounts for the majority of the differences shown in the figures. If the Lorentz profile were used in the calculations (12.8 μm band Gaussian) rather than the exponential shape, the dimensionless band absorption $A_i/\Delta\omega_i$ would approach one at a smaller value of L than the exponential profile results. This

Table 3 Band Parameters CCl_4 (~300K) Determined from experimental data

Region cm^{-1}	Random S/d, cm^{-1}	$2\alpha/d$
900–1350	8.34	0.38
1350–1700	11.4	0.19
1700–3300	0.225	0.23

behavior is not exhibited by the experimental results thus lending support to the conclusion drawn in [5] that the exponential profile is more representative of the actual absorption process.

A quantity which is often used in heat transfer calculations is the derivative dA/dL [5, 6, 7]. To properly predict temperature profiles in a radiation interaction problem, a realistic representation of dA/dL is required. Figs. 5 and 6 present the derivative of the total band absorption with respect to path length for the absorption results shown in Figs. 1 to 3. Considering the sensitivity of the comparisons, the agreement is excellent. The regular model, because of its tendency to saturate at a smaller L, overestimates the derivative at the larger optical depths shown in the figures; the random model is a better representation of the spectral integration results.[7]

As in the case of gas radiation, it is extremely useful to have correlations for the total band absorption for input to heat transfer calculations. Reference [7] has shown that it is absolutely

[7] The derivative for the regular model in the 690–900 cm^{-1} region approaches zero at a much faster rate than the other results; this behavior would also be evident for the other regions at values of L greater than those shown in the figures.

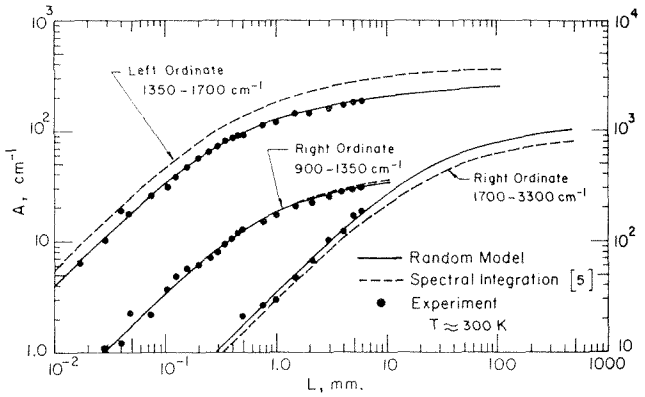

Fig. 4 Comparison of experimental data to the random model and the spectral integration results of [5]

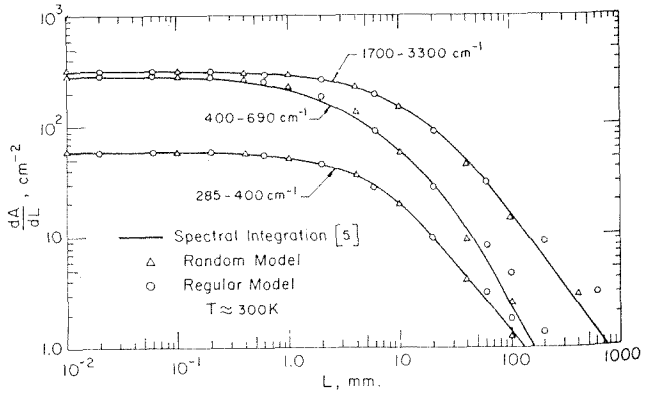

Fig. 5 Derivative of band absorption with respect to path length; spectral regions 285–400, 400–690, and 1700–3300 cm^{-1}

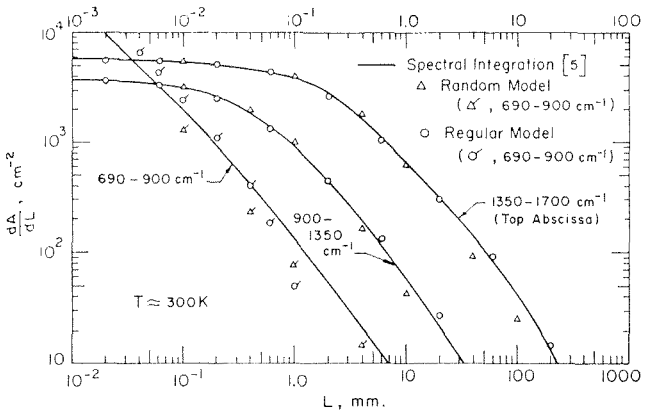

Fig. 6 Derivative of band absorption with respect to path length; spectral regions 690–900, 900–1350, and 1350–1700 cm $^{-1}$

necessary to properly represent the wing behavior of the absorption bands in these calculations; for example, the top hat and gray models do not even properly represent trends in gas work. In liquids and gases, these correlations can be built from basic spectroscopic information on the behavior of κ_ω; however, this information is not generally available and very difficult to obtain in the laboratory. To this end, useful correlations have been developed based on total band absorption data which are much easier to obtain in the laboratory than κ_ω information. Here, two models for the total band absorption in liquids have been suggested. Using liquid CCl_4 as an example, the results indicate that both models should be of sufficient accuracy for heat transfer calculations [5]; the random model better represents the spectral results and because of its closed form it might be simplier to use in some situations.

Acknowledgments

The authors gratefully acknowledge the assistance of D. Bankston for a portion of the computer programming.

References

1 Schödel, G., and Grigull, U., "Kombinierte Wärmeleitung and Wärmestrahlung in Flüssigkeiten," *Journal Heat Transfer 1970*, Vol. 3, Article R.2.2. Elsevier, Amsterdam, 1970.

2 Poltz, H., "Die Wärmeleitfahigkeit von Flüssigkeiten II. Der Strahlungsanteil der Effektiven Wärmeleitfähigkeit," *International Journal of Heat Mass Transfer*, Vol. 8, No. 4, Apr. 1965, pp. 515–527.

3 Poltz, H., "Die Wärmeleitfähigkeit von Flüssigkeiten III. Abhängigkeit der Wärmeleitfahigkeit von der Schichtdicke bei rganischen Flüssigkeiten," *International Journal of Heat Mass Transfer*, Vol. 8, No. 4, Apr. 1965, pp. 609–620.

4 Poltz, H., and Jugel, R., "The Thermal Conductivity of Liquids-IV. Temperature Dependence of Thermal Conductivity," *International Journal of Heat Mass Transfer*, Vol. 10, No. 8, Aug. 1967, pp. 1075–1088.

5 Novotny, J. L., and Bratis, J. C., "Radiative Transfer in Liquid CCl_4," *Journal of Quantitative Spectroscopy and Radiative Transfer*, Vol. 12, No. 5, May 1972, pp. 901–911.

6 Schimmel, W. P., Novotny, J. L., and Kast, S., "Effect of Surface Emittance and Approximate Kernels in Radiation-Conduction Interaction," *Wärme-und Stoffübertragung*, Vol. 3, 1973, pp. 1–6.

7 Schimmel, W. P., Novotny, J. L., and Olsofka, F. A., "Interferometric Study of Radiation-Conduction Interaction," *Heat Transfer 1970*, Vol. 3, Article R. 2. 1. Elsevier, Amsterdam, 1970.

8 Goody, R. M., *Atmospheric Radiation*, First ed., Oxford, London, 1964, pp. 122–167.

9 Plass, G. N., "Models for Spectral Band Absorption," *Journal Optical Society of America*, Vol. 48, No. 10, Oct. 1958, pp. 690–703.

10 Edwards, D. K., and Menard, W. A., "Comparison of Models for Correlation of Total Band Absorption," *Applied Optics*, Vol. 3, No. 5, May 1964, pp. 621–625.

11 Hsieh, T. C., and Greif, R., "Theoretical Determination of the Absorption Coefficient and the Total Band Absorptance Including a Specific Application to Carbon Monoxide," *International Journal of Heat Mass Transfer*, Vol. 15, No. 8, Aug. 1972, pp. 1477–1488.

12 Tien, C. L., and Lowder, J. E., "A Correlation of Total Band Absorptance of Radiating Gases," *International Journal of Heat Mass Transfer*, Vol. 9, No. 7, July 1966, pp. 698–701.

13 Cess, R. D., and Tiwari, S. N., "Infrared Radiative Energy Transfer in Gases," Report No. 205, College of Engineering, State University of New York at Stony Brook, New York, May 1971.

14 Smith, D. C., and Miller, E. C., *Journal Optical Society of America*, Vol. 34, 1944, p. 130.

15 Brügel, W., *An Introduction to Infrared Spectroscopy*, Wiley, New York, 1962.

C. A. RHODES
Associate Professor. Mem. ASME
C. C. CHEN[1]
Graduate Student.
University of South Carolina, Columbia, S. C.

Thermal Radiation in Laminar Boundary Layers on Continuous Moving Surfaces

Thermal radiation heat transfer is studied in boundary layers on continuous moving surfaces. An analytical study is performed for two-dimensional laminar flow of an absorbing and emitting fluid. Solutions were obtained for limiting conditions of optically thin and thick boundary layers. Comparisons indicate that the radiation flux in these boundary layers is less than that for flow over semi-infinite flat plates for optically thin flows. The radiation contribution becomes more nearly equal as optical thickness increases. The normal velocity induced in the free stream by the wall motion significantly affects the radiation heat transfer.

Introduction

When a metal sheet is extruded continuously from a die or rolling mill into a fluid, the flow situation in the surrounding fluid is referred to as a boundary layer on a continuous moving surface. This flow situation is shown in Fig. 1. A similar flow condition can be shown to occur on the wall of a shock tube behind the shock wave. In Fig. 1 the vertical wall would coincide with the shock wave and the continuous moving surface with the shock wall.

Mirels [1][2] first considered the flow and convective heat transfer on the wall behind a shock wave and Sakiadis [2, 3, 4] considered the flow on flat plates and cylindrical filaments during extrusion. Erickson, Fan, and Cha [5] and Tsou, Sparrow, and Goldstein [6] studied the heat transfer characteristics of the continuous moving flat plate.

For laminar two-dimensional steady flow on a continuous moving surface, the boundary layer flow equations reduce to the Blasius equation which was derived for the semi-infinite flat plate. The boundary conditions for the continuous moving surface are a uniform velocity U at the surface; and in the present study, the free-stream horizontal velocity component is assumed zero. The assumption of zero free-stream horizontal velocity is certainly valid for extrusion problems; however, in shock tubes the assumption is only valid for strong waves. Convective heat transfer results for laminar flow on continuous moving surfaces were obtained by Tsou, Sparrow, and Goldstein [6] and Rhodes and Kaminer [7].

The present study considers the effect of thermal radiation heat transfer on a continuous moving surface in an emitting and absorbing media. Thermal radiation can be important since, in many applications, the fluid and/or surface is at high temperature. The effect of thermal radiation on the temperature distribution and heat transfer is determined for an optically gray, nonscattering fluid near thermodynamic equilibrium. Steady laminar flow is studied and solutions are obtained for the limiting conditions of optically thin and thick boundary layers. Radiant heat transfer characteristics of flow over semi-infinite flat plates with optically thin and thick boundary layer are compared with these results. The limiting conditions of optically thin and optically thick boundary layers are studied in order to obtain results which can easily be compared with results presently available for the semi-infinite flat plate. Although computer techniques are available to obtain solutions for general optical thicknesses, the purpose of this paper is to apply the limiting techniques developed for the semi-infinite flat plate to the continuous moving surface. This allows a reasonably accurate solution in a somewhat simplified form and also we can compare the characteristics of the continuous moving surface with those of the semi-infinite flat plate. We will first present the optically thin analysis and results followed by a similar presentation of the optically thick case.

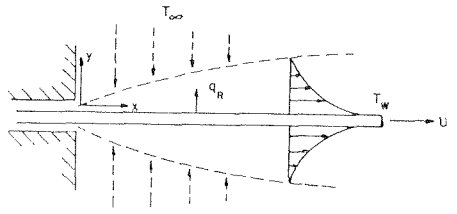

Fig. 1 Boundary layer on a continuous moving surface

[1] Presently Graduate Student at University of Kentucky.
[2] Numbers in brackets designate References at end of paper.
Contributed by the Heat Transfer Division for publication (without presentation) in the Journal of Heat Transfer. Manuscript received by the Heat Transfer Division September 7, 1972. Paper No. 73-HT-X.

Optically Thin Boundary Layer Analysis

The optically thin approximation has been applied to boundary layer heat transfer on semi-infinite flat plate by several authors; for example, Howe [8], Koh and De Silva [9], and Cess [10]. The first two papers assumed that the boundary layer emits but does not absorb thermal radiation. The latter paper, however, included first-order interaction effects between convection and radiation with emission and absorption in the boundary layer.

The analytical technique used in the present analysis assumes that the radiation interaction within the boundary layer can be neglected. Radiation passes through the boundary layer unaffected by the fluid present. Adjacent to the boundary layer is a radiation layer whose thickness is large compared to the boundary layer. In the radiation layer thermal conduction is neglected but convection which is induced by the boundary layer flow is included.

A nonconducting fluid is assumed having a velocity equal to that at the outer edge of the boundary layer. Since the horizontal velocity component is zero, the normal velocity component induced by the moving plate cannot be neglected as in the case of flow over a semi-infinite flat plate. The normal velocity relation was determined by Sakiadis [3] and is given by

$$v_\infty = -0.808(U\nu/x)^{1/2} \tag{1}$$

The velocity is seen to be negative and decreases with distance from the origin. In this analysis we assume constant properties; however, the results are equally applicable to an ideal gas where $\rho\mu$, ρk, and κ/ρ are constants.

The free-stream temperature is equal to T_∞ outside the radiation layer and the wall temperature is equal to T_w. Longitudinal radiation and viscous dissipation are neglected in the energy equation. The applicable form of the energy equation becomes

$$\rho c_p v_\infty \frac{\partial T}{\partial y} = -\frac{\partial q_R}{\partial y} \tag{2}$$

Although equation (2) only contains partial derivatives with respect to y, T is a function of x also since by equation (1), v_∞ is a function of x. The thickness of the velocity boundary layer is small compared to the radiation layer and thus can be neglected.

Although the optical thickness of the boundary layer is assumed small, the optical thickness of the radiation layer is assumed optically thick. This analysis applies to a shock tube only when the optical thickness across the tube diameter is large. The method applied is similar to that employed by Sparrow and Cess [11] to determine radiant heat transfer from a semi-infinite plate in an ideal fluid. A gray, nonscattering fluid and an optically black wall are assumed and T^4 is linearized by expanding in a Taylor series about T_∞ and retaining only first-order terms. $E(t)$ kernels are approximated by exponentials (i.e., $E_1(t) \approx 2e^{-2t}$). With these approximations, the energy equation reduces to the third-order partial differential equation given by,

$$\frac{\partial^3\theta}{\partial\tau^3} - 2Z\frac{\partial^2\theta}{\partial\tau^2} - 4\frac{\partial\theta}{\partial\tau} = 0 \tag{3}$$

where θ is the dimensionless temperature

$$\theta(x, y) = (T(x, y) - T_w)/(T_\infty - T_w) \tag{4}$$

In addition, τ is the optical thickness, and Z is a combination of Boltzman and Reynolds numbers given by

$$Z = 9.90\mathrm{Bo}^{-1}\mathrm{Re}^{1/2} \tag{5}$$

The independent variables in equation (3) are the dimensionless variables Re and τ, which are functions of x and y, respectively; therefore, its solution gives $\theta(\mathrm{Re}, \tau)$. Since the coefficients of equation (3) are only functions of Z, it can be easily integrated, which yields the following general solution:

$$\theta = f_1(\mathrm{Re}) + e^{Z\tau}[f_2(\mathrm{Re})\exp(\tau\sqrt{Z^2+4}) + f_3(\mathrm{Re})\exp(-\tau\sqrt{Z^2+4})] \tag{6}$$

The functions $f_1(\mathrm{Re})$, $f_2(\mathrm{Re})$, and $f_3(\mathrm{Re})$ must be determined so that the solution satisfies the boundary conditions and the original integrodifferential equation used to derive equation (3). Substituting these conditions we obtain,

$$\theta = 1 - \tfrac{1}{2}\{(Z + 2 - \sqrt{Z^2+4})\exp[\tau(Z - \sqrt{Z^2+4})]\} \tag{7}$$

Equation (7) is the temperature distribution within the radiation layer. Setting $\tau = 0$ in equation (7) we obtain the temperature jump at the wall. Thus

$$\theta(\mathrm{Re}, 0) = (\sqrt{Z^2+4} - Z)/2 \tag{8}$$

Using equation (7) the wall heat flux within the boundary layer can be determined. Sparrow and Cess [11] show that

$$\frac{q_{Rw}}{\sigma(T_w - T_\infty^4)} = 2\int_0^\infty \theta(\mathrm{Re}, t)E_2(t)dt \tag{9}$$

Substituting the exponential approximation $E_2(t) \simeq e^{-2t}$ and equation (7) into equation (9) and integrating gives,

$$\frac{q_{Rw}}{\sigma(T_w^4 - T_\infty^4)} = 2(Z - \sqrt{Z^2+4})/(Z - 2 - \sqrt{Z^2+4}) \tag{10}$$

The relative importance of radiation to the convection heat transfer can be determined by combining the radiation heat transfer result with the convective. The total heat transfer can be approximated by the sum of the convective and radiative transfer

Nomenclature

Bo = Boltzmann number, $\rho_\infty c_p U/\sigma T_\infty^3$
c_p = specific heat at constant pressure
$E(t)$ = exponential integral
f = dimensionless Blasius stream function
k = thermal conductivity
N = dimensionless parameter, $\kappa k/4\sigma T^3$
Nu = Nusselt number, $q_w x/k(T_w - T_\infty)$
Pr = Prandtl number, $c_p\mu/k$
q = heat flux
Re = Reynolds number, Ux/ν
t = dummy variable of integration
T = absolute temperature
u = velocity component in x-direction
U = velocity of surface
v = velocity component in y-direction
x = coordinate along plate surface
y = coordinate normal to plate surface
Z = function defined by $9.90\ \mathrm{Bo}^{-1}\ \mathrm{Re}^{1/2}$
η = similarity variable, $y\sqrt{U/\nu x}$
θ = dimensionless temperature $(T - T_w)/(T_\infty - T_w)$
κ = absorption coefficient
μ = dynamic viscosity
ν = kinematic viscosity
ξ = dimensionless parameter, $2\sigma\kappa T_\infty^3 x/\rho c_p U$
ρ = density
σ = Stefan-Boltzmann constant
τ = optical thickness
ϕ = dimensionless temperature, T/T^*

Subscripts

c = convection
R = radiation
w = wall
∞ = free stream

Superscripts

$*$ = reference temperature
$'$ = differentiation with respect to η

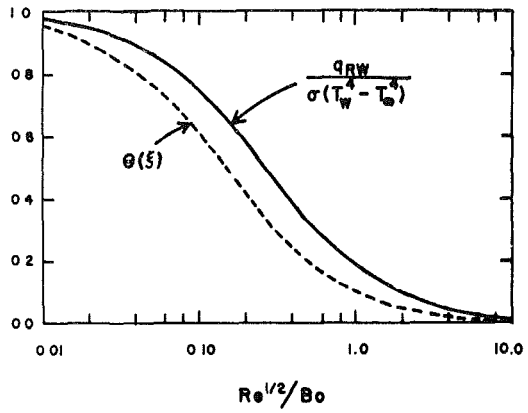

Fig. 2 Thermal radiation heat flux and temperature jump for optically thin boundary layers

$$q_w = q_{cw} + q_{Rw}$$

where q_{cw} is the convective heat transfer. From reference [6] we find that for Pr equal to unity and convection alone, $Nu/\sqrt{Re} = 0.444$. Combining convection and radiation heat transfer yields,

$$\frac{Nu}{\sqrt{Re}} = 0.444 + 4\left(\frac{q_{Rw}}{T_w^4 - T_\infty^4}\right)(\sigma Bo)^{-1}Re^{1/2} \qquad (11)$$

By substituting equation (10) in the second term on the right of equation (11) and letting Pr = 1.0, the combined $Nu/\sqrt{Re}$ can be determined.

Optically Thin Boundary Layer Results

The dimensionless wall heat flux and temperature are plotted in Fig. 2 as a function of $Re^{1/2}/Bo$. Near the origin where $Re \to 0$, black-body radiation

$$q_{Rw} = \sigma(T_w^4 - T_\infty^4)$$

is obtained but radiation exchange between fluid and surface decrease with distance from the origin. This characteristic can be explained physically by noting in equation (1) that the magnitude of the normal velocity also decreases with the distance from the origin since $v_\infty \sim x^{-1/2}$. Since the velocity component is negative, the free stream fluid is brought near the surface where radiation exchange is occurring. The magnitude of the velocity is higher near the origin; consequently, the fluid temperature is maintained more nearly equal to that of free stream.

The combined wall convection and radiation heat transfer is given by equation (11) and is shown in Fig. 3. Although the $Nu/\sqrt{Re}$ is constant for convective heat transfer, it is seen that the radiation may cause this parameter to change significantly. When $Re^{1/2}/Bo$ is greater than approximately 5.0, $Nu/\sqrt{Re}$ remains constant at approximately 1.25.

The radiation heat transfer characteristics of the continuous moving surface cannot be compared directly with those of the semi-infinite flat plate because the important parameters are different. Rather than the independent variable $Re^{1/2}/Bo$, the dimensionless parameter ξ was obtained for a semi-infinite flat plate. These parameters can be related by introducing, for instance, the two additional parameters N and Pr. One can show

$$Re^{1/2}/Bo = (\xi/8N\Pr)^{1/2}$$

We now have a relation between the parameters $Re^{1/2}/Bo$ and ξ but have introduced the product of N and Pr. Fig. 4 shows the dimensionless heat flux now plotted as a function of ξ with constant values of the product NPr. The dashed curve was determined by Sparrow and Cess [11] for the semi-infinite flat plate and is applicable for all NPr. Since N must be small for optically thin boundary layers [11], radiation heat transfer will generally be lower for a continuous moving surface than for a semi-infinite flat plate. A physical explanation for the difference is that the free stream flow on the semi-infinite flat plate is much larger and consequently, the fluid temperature remains near that of free stream. As N increases the optical thickness of the boundary layer also increases and the radiation heat flux for the continuous surface and semi-infinite flat plate become more nearly equal as seen in Fig. 4. This characteristic is demonstrated further in the results for optically thick boundary layers, as will be seen later.

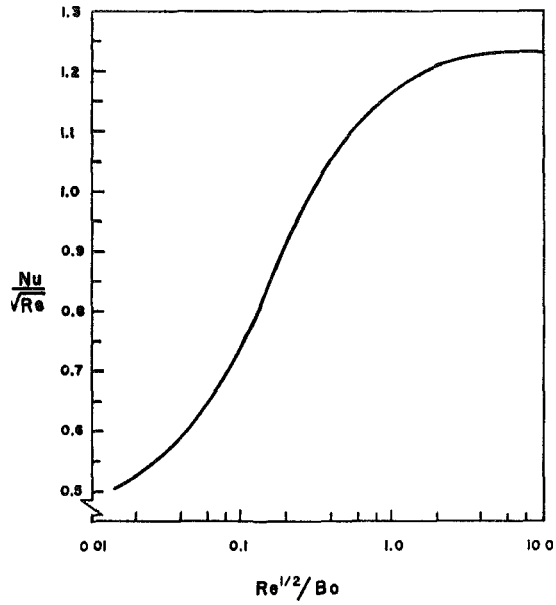

Fig. 3 Heat transfer coefficient including radiation for optically thin boundary layers, Pr = 1.0

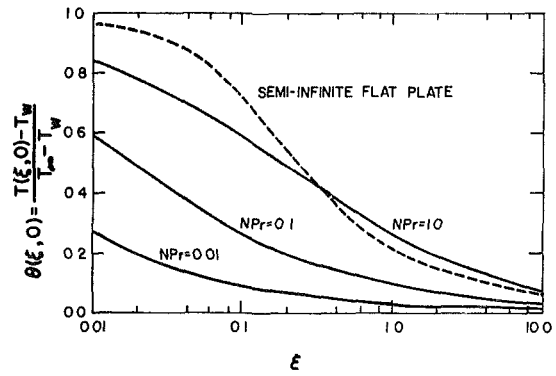

Fig. 4 Comparison of temperature jump at surface of continuous moving surface with semi-infinite flat plate. Semi-infinite flat plate data is the dashed line and was given by Sparrow and Cess [11].

Optically Thick Boundary Layer Analysis

The opposite extreme to the weak interaction of radiation is that of fluids with intense absorption where the Rosseland formulation [13] is used to determine the radiant energy flux for this condition. Viskanta and Grosh [14] used this technique to study the temperature distribution and heat transfer during flow of an absorbing medium along a wedge. Their analysis included the zero wedge angle case, and these results will be compared with the continuous moving surface in the present study.

If radiation transfer in the x-direction is neglected, then the radiant transfer by the Rosseland formulation is,

$$q_R = -\frac{16\sigma T^3}{3\kappa}\frac{\partial T}{\partial y} \tag{12}$$

Following the analysis of Viskanta and Grosh [14], the total heat flux can be expressed by an effective conductivity including conduction and radiation. Thus

$$k_{\text{eff}} = k + k_R = k + \frac{16\sigma T^3}{3\kappa} \tag{13}$$

Substitution into the energy equation and simplifying one obtains,

$$[(k_{\text{eff}}/k)\phi']' + {}^1/_2 \text{Pr} f\phi' = 0 \tag{14}$$

where the prime denotes differentiation with respect to η and ϕ is a dimensionless temperature given by $\phi = T/T^*$. The asterisk denotes a reference temperature; for example, the wall temperature T_w or free stream temperature T_∞. Properties are again assumed constant but results are applicable to ideal fluids where $\rho\mu$, ρk, and κ/ρ are constants.

The dimensionless stream function f has already been determined for the continuous moving surface by Sakiadis [3]. Due to the large difference in the shape of this curve from that of the semi-infinite plate used by Viskanta and Grosh [14], it was anticipated that the radiant heat transfer results for the continuous moving surface would differ considerably from those of the semi-infinite flat plage.

The radiative transfer term in equation (13) can be expressed in the dimensionless parameter N by

$$k_{\text{eff}}/k = 1 + 4\phi^3/3N \tag{15}$$

The boundary conditions for equation (14) are

$$T = T_w \text{ at } \eta = 0$$
$$T = T_\infty \text{ at } \eta \to \infty$$

Optically Thick Boundary Layer Results

Numerical integrations of equation (14) using the digital computer were performed to find temperature distributions and heat transfer rates as a function of the parameter N. Prandtl number is assumed equal to one in all cases presented. Since the energy equation is nonlinear and no suitable dimensionless temperature was found that would have eliminated the specification of the particular values of ϕ_w and ϕ_∞ in the boundary conditions, solutions have been obtained for several values. Linearization can be performed by the method used in the optically thin boundary layer in the foregoing; however, the solution would suffer a loss of generality.

Figs. 5 and 6 show the temperature distributions in the boundary layers for values of N equal 0.1, 1.0, and 10. In Fig. 5 the values of ϕ_w and ϕ_∞ are 0.1 and 1.0, respectively; and consequently, the wall is cold compared to the surrounding fluid and T_∞ is the reference temperature T^*. The values of ϕ_w and ϕ_∞ are 1.0 and 0.1, respectively, in Fig. 6; and therefore, the wall temperature is higher than that of the fluid and now $T^* = T_w$. Prandtl number is set equal to unity in all cases. The curves for $N = 10$ are approximately equal to those for infinite values of N. Radiation heat transfer decreases to zero as $N \to \infty$ since the fluid becomes opaque at large N.

The temperatures in Fig. 5 are very little different from those obtained by Viskanta and Grosh [14] for flow over a semi-infinite plate with the same condition present. However, the results obtained by Viskanta and Grosh for the conditions in Fig. 6 are the dashed lines and significant differences are seen between the semi-infinite flat plate and continuous moving surface.

Since Prandtl number is equal to unity and the fluid becomes opaque at large values of N, the thermal boundary layer thickness is approximately equal to that of the velocity boundary layer at $N = 10$. As N decreases, the radiation contribution becomes greater. Radiation heat transfer thus increases the thermal boundary layer thickness which is the same effect as a decrease in Prandtl number.

The heat flux at the wall is the sum of conductive and radiative heat flux. For strongly absorbing medium the heat flux can be expressed as

$$q_w = -k\left.\frac{\partial T}{\partial y}\right|_w - \left.\frac{16\sigma T^3}{3\kappa}\frac{\partial T}{\partial y}\right|_w \tag{16}$$

Substituting equation (15) and ϕ we obtain after rearranging,

$$\frac{q_w x}{kT^*\sqrt{\text{Re}}} = -\left(1 + {}^4/_3\frac{\phi_w^3}{N}\right)\left.\frac{\partial\phi}{\partial\eta}\right|_w \tag{17}$$

We can further show,

$$\frac{\text{Nu}}{\sqrt{\text{Re}}} = \left(\frac{1}{\phi_\infty - \phi_w}\right)\left(1 + {}^4/_3\frac{\phi_w^3}{N}\right)\left.\frac{\partial\phi}{\partial\eta}\right|_w \tag{18}$$

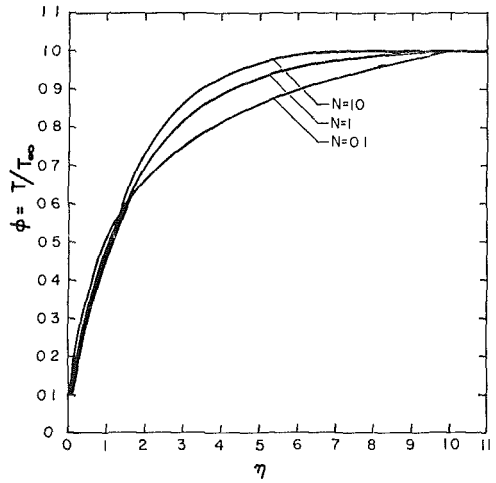

Fig. 5 Temperature as a function of η for Pr = 1.0, ϕ_W = 0.1, and ϕ_∞ = 0.1

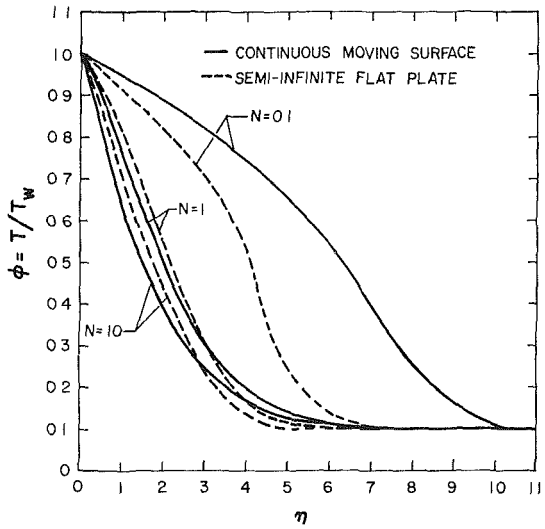

Fig. 6 Temperature as a function of η for Pr = 1.0, ϕ_W = 1.0 and ϕ_∞ = 0.1 on a continuous moving surface and semi-infinite flat plate. *Semi-infinite flat plate data is the dashed line and was given by Viskanta and Grosh [14].*

Table 1 Heat transfer results for optically thick boundary layer on continuous moving surfaces

(a) Cool wall ($\phi_\infty = 1.0$, $\phi_W = T_W/T_\infty$)

	$\phi_W = 0.1$		$\phi_W = 0.5$	
N	$\frac{qx}{kT_\infty\sqrt{\mathrm{Re}}}$	$\mathrm{Nu}/\sqrt{\mathrm{Re}}$	$\frac{qx}{kT_\infty\sqrt{\mathrm{Re}}}$	$\mathrm{Nu}/\sqrt{\mathrm{Re}}$
10.	−0.402	0.446	−0.225	0.450
1.0	−0.420	0.466	−0.250	0.500
0.1	−0.677	0.752	−0.525	1.05

(b) Hot Wall ($\phi_w = 1.0$, $\phi_\infty = T_\infty/T_w$)

	$\phi_\infty = 0.1$		$\phi_\infty = 0.5$	
N	$\frac{qx}{kT_W\sqrt{\mathrm{Re}}}$	$\mathrm{Nu}/\sqrt{\mathrm{Re}}$	$\frac{qx}{kT_W\sqrt{\mathrm{Re}}}$	$\mathrm{Nu}/\sqrt{\mathrm{Re}}$
10.	0.409	0.455	0.228	0.456
1.0	0.473	0.526	0.273	0.546
0.1	0.693	0.770	0.507	1.01

Table 1 lists the heat flux results given by equations (17) and (18) for cool and hot wall conditions. It is seen that for $N = 10$, the radiation transfer is small but as N decreases the radiation becomes more important. This effect is illustrated in Fig. 7 where $\mathrm{Nu}/\sqrt{\mathrm{Re}}$ is plotted as a function of N for the cool wall conditions.

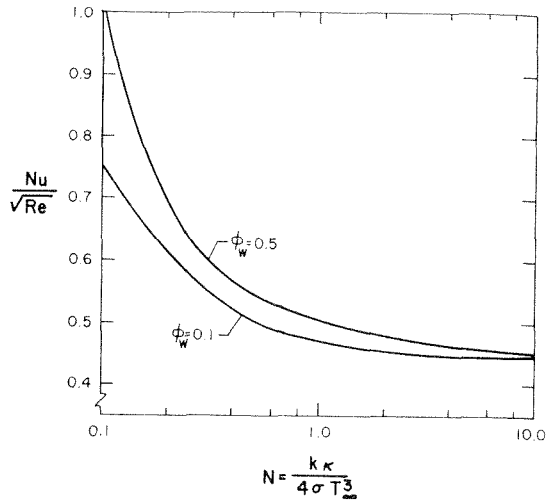

Fig. 7 Heat transfer coefficient including radiation for optically thick boundary layers. Pr = 1.0 and $\phi_\infty = 1.0$.

Discussion

The normal velocity component induced in the surrounding fluid by the surface motion contributes appreciably to the radiation heat transport. Since the velocity component normal to the surface is toward the plate, the free stream fluid flows toward the surface where radiative is more important. The radiation heat flux at the wall of a semi-infinite flat plate also decreases with distance from the origin but the reduction results from a continual heat exchange between the fluid and wall as the fluid flows horizontally over the plate.

An error analysis has not been performed but it is expected that the results are of the same accuracy as those obtained for the semi-infinite flat plate using the same techniques. Viskanta [16] compared the optically thin and optically thick analysis of the semi-infinite flat plate with the exact results obtained by Zamuraev [17]. It was concluded that the thin gas analysis is valid only for $\xi < 0.1$ and the total heat flux values predicted by the thick gas analysis is within 10 percent of the results of Zamuraev for all conditions compared. Similar comparisons would be expected for the results presented here for the continuous moving surface.

We have assumed a uniform free-stream temperature and a negligible radiation parallel to the surface. In shock tube flows it may be necessary to include these effects which necessitate the simultaneous solution of the energy equation in the free stream. Chien and Compton [15] obtained solutions to the energy equation in the free stream but neglected boundary layer flow effects. Although their comparisons with test data obtained by Borucki, et al. [18] are favorable, some improvement might be obtained by including induced flow considered in the present study.

References

1 Mirels, H., "Laminar Boundary Layer Behind a Strong Shock Moving Into Air," NACA TM 3712, 1956.

2 Sakiadis, B. C., "Boundary-Layer Behavior on Continuous Solid Surfaces; I. Boundary-Layer Equations for Two Dimensional and Axisymmetric Flow," *AIChE Journal*, Vol. 7, No. 2, 1961, pp. 26–28.

3 Sakiadis, B. C., "Boundary-Layer Behavior on Continuous Solid Surfaces; II. The Boundary-Layer on a Continuous Flat Surface," *AIChE Journal*, Vol. 7, No. 3, 1961, pp. 221–225.

4 Sakiadis, B. C., "Boundary-Layer Behavior on Continuous Solid Surface; The Boundary-Layer on a Continuous Cylindrical Surface," *AIChE Journal*, Vol. 7, No. 3, 1961, pp. 467–472.

5 Erickson, L. E., Fan, L. G., and Cha, L. C., "The Cooling of a Continuous Flat Sheet," AIChE Preprint No. 29, presented at the *Eighth National Heat Transfer Conference*, Los Angeles, Calif., 1965.

6 Tsou, F. K., Sparrow, E. M., and Goldstein, R. J., "Flow and Heat Transfer in the Boundary Layer on a Continuous Moving Surface," *International Journal of Heat and Mass Transfer*, Vol. 10, 1967, pp. 219–235.

7 Rhodes, C. A., and Kaminer, H., Jr., "Laminar Boundary Layers on Continuous Surfaces," *AIAA Journal*, Technical Note, Vol. 10, No. 3, 1972, pp. 331–333.

8 Howe, J. F., "Radiation Emission Effects of the Equilibrium Boundary Layer in the Stagnation Region," NASA TN D-1031, 1961.

9 Koh, J. C. Y., and De Silva, C. N., "Interaction Between Radiation and Convection in the Hypersonic Boundary Layer on a Flat Plate," *ARS Journal*, Vol. 30, 1962, pp. 739–743.

10 Cess, R. D., "Radiation Effects Upon Boundary-Layer Flow of an Absorbing Gas," JOURNAL OF HEAT TRANSFER, TRANS. ASME, Series C, Vol. 86, 1964, pp. 469–475.

11 Sparrow, E. M. and R. D. Cess, *Radiation Heat Transfer*, Brooks-Cole, Belmont, Calif., Ch. 10, 1966.

12 Lick, W., "Transient Energy Transfer by Conduction and Radiation," *International Journal of Heat and Mass Transfer*, Vol. 8, 1965, pp. 119–128.

13 Rosseland, S., *Astrophysik, Auf Atom-Theoretischer Grundlage*, Springer, Berlin, 1931.

14 Viskanta, R., and Grosh, R. J., "Boundary Layer in Thermal Radiation Absorbing and Emitting Media," *International Journal of Heat and Mass Transfer*, Vol. 5, 1962, pp. 795–806.

15 Chien, K. Y., and Compton, D. L., "Flow in a Cylindrical Shock Tube With Radiative Loss," *Proceedings of the 1970 Heat Transfer and Fluid Mechanics Institute*, Monterey, Calif., 1970.

16 Viskanta, R., "Radiation Transfer and Interaction of Convection With Radiation Heat Transfer," *Advances in Heat Transfer*, Vol. 3, 1966, pp. 175–251.

17 Zamuraev, V. P., "Laminar Boundary Layer in a Radiation Absorbing Gas Near a Flat Plate," *Zh. Prikl. Mekhani. Tekhni. Fiz.*, No. 3, 1964, pp. 73–80.

18 Borucki, W. J., Cooper, D. M., and Page, W. A., "Instrumentation for Measuring Flow Properties in an Explosively Driven Shock Tube," paper presented at the *Seventh Shock Tube Symposium*, Toronto, Canada, June 23–25, 1969.

A. Balakrishnan

D. K. Edwards

University of California, Los Angeles, Calif.

Radiative Flame Cooling for Reduction of Nitric Oxide Emissions

The effect of soot upon heat transfer in combusting gases is investigated. The medium considered is a turbulent gas-soot mixture contained in a plane parallel enclosure. The nongray radiative nature of the soot and the effects of the geometrical configuration are taken into account using an "internal" or "modified" slab emissivity especially developed for the purpose. The simultaneous turbulent transport and radiation are treated with full nonlinearity. It is shown that small amounts of soot greatly aid the radiative cooling of combustion gases, which undergo microrecirculation by turbulent mixing. Larger amounts of soot increase combustion temperature and hence unwanted nitric oxide emissions.

Introduction

It is well known that large stationary fossil fuel combustion units produce more than proportionately larger amounts of nitric oxide. For example, a single 300,000-kw unit produces approximately $3^{0.18} = 1.22$ times more NO than three 100,000-kw units [1].[1] Reasons for this greater production may be a longer residence time in the high temperature zone and a smaller area of water wall per unit of fired heat release in the larger unit. But in addition to these factors, and very likely of much more effect, is the reduction of radiative cooling per unit volume of combustion gas brought about by the increased optical depth of soot in the larger unit. Even a small increase in flame temperature can cause a significant increase in NO emissions [2].

Nitric oxide, which participates in photochemical reactions in the atmosphere, is a serious atmospheric pollutant in some urban areas. Breen, et al. [2] describe some successful quick-fixes to reduce NO emissions from existing units. In mixing-controlled combustion or two-stage combustion, radiative cooling of the combustion gases, which are subsequently entrained into the air and fuel, occurs. In an atomized-oil or powdered-coal-fired unit, the bulk of the combustion chamber then exhibits no recognizable burner plumes but appears to be filled with a ball of fire. Large amounts of soot are formed and consumed.

There has been undertaken at UCLA a systematic study of radiative transfer accompanied by simultaneous turbulent convection. This study has been pursued, because it is the belief of the authors that radiation heat transfer in utility boilers and furnaces can be significantly improved and that, at the same time, lower combustion temperatures in such units can be achieved with consequently less production of nitric oxide.

This paper is the first work of the present authors to consider the influence of soot upon the radiative process, previous work having been concerned with the action of molecular gases. It will be shown that the radiator soot, when present in a *small* amount, is highly beneficial because it promotes high radiative cooling of the combustion and hence greatly reduces the rate of formation of NO. But, in sharp contrast to the behavior shown by molecular gases, more than a small amount of soot is highly deleterious to the radiative transfer process.

Analysis

Simultaneous Radiation and Turbulent Transport. The model used previously in examining the effects of molecular gas radiation is retained [3, 4]. Two plane, parallel, black, isothermal cooled walls contain a turbulent gas as shown in Fig. 1. In this case the gas contains soot, which absorbs and radiates heat. Turbulence in the gas is manifested through an eddy diffusivity specified by the Van Driest law of the wall [5] modified by a channel factor [6]. Both molecular and turbulent Prandtl numbers are taken to be approximately 0.7 with the result that the eddy diffusivity for heat is

$$\epsilon_H = \frac{k_m/\rho c_p}{1 + \beta y^*} (\epsilon_H^+ - 1), \quad \epsilon_H^+ = \frac{1}{2} + \frac{1}{2}\left[1 + 4K^2 y^{+2}(1 - \exp(-y^+/A^+))^2\right]^{1/2} \tag{1}$$

where the von Karman constant K is 0.4, A^+ is 26, and $\beta = 3.4$. The quantity y^* is the distance from the wall normalized by the channel half width δ, and

$$y^+ = (\rho_l \mu_c/\rho_c \mu)\mathrm{R}_t y^* \tag{2}$$

$$\mathrm{R}_t = \frac{1}{4}\sqrt{\frac{f}{8}}\,\mathrm{Re}_{D_h,\,c} \tag{3}$$

In heterogeneous combustion, volatiles may burn in a thin reaction zone between fuel-rich gases and oxygen-bearing gases, while fuel particles or eddies of air burn throughout the combustion chamber volume. The thin reaction zone is modeled here as a

[1] Numbers in brackets designate References at end of paper.

Contributed by the Heat Transfer Division of THE AMERICAN SOCIETY OF MECHANICAL ENGINEERS and presented at the ASME-AIChE Heat Transfer Conference, Atlanta, Ga., August 5–8, 1973. Manuscript received at ASME Headquarters April 23, 1973; revised manuscript received September 14, 1973. Paper No. 73-HT-32.

plane heat source of negligible thickness at which a heat flux q_{ff} Btu/hr ft^2 is released. The combustion taking place around the droplets or particles distributed throughout the volume is modeled by a volume heat release $\dot{Q}_V$ Btu/hr ft^3. But in addition to this volume combustion, often written $\Sigma_i \dot{r}_i \hat{h}_i^0$, where $\dot{r}_i$ is the rate of formation of species i per unit volume and $\hat{h}_i^0$ is the specific enthalpy of formation of species i, there is a volume cooling effect due to convection, usually written $\rho c_p v \cdot \nabla T$. The quantity $\dot{Q}_V$ is used here to represent difference $\Sigma_i \dot{r}_i \hat{h}_i^0 - \rho c_p v \cdot \nabla T$. It thus models both the volume combustion heat release and the convective sweeping of the combustion gases through the chamber.

With this model the energy equation takes the form

$$0 = \frac{d}{dy}\left[k_m \epsilon_H^+ \frac{dT}{dy}\right] + \frac{d}{dy}\left[-q_R\right] + \dot{Q}_V \tag{4}$$

Symmetry exists within the channel; consequently the boundary conditions are

$$y = 0: \quad T = T_w \tag{5}$$

$$y = \delta: \quad \frac{dT}{dy} = 0 \tag{6}$$

$$y = \delta_{ff}: \quad q_{ff} = k_m \epsilon_H^+ \frac{dT}{dy}\bigg|_{\delta_{ff}^-} - k_m \epsilon_H^+ \frac{dT}{dy}\bigg|_{\delta_{ff}^+} \tag{7}$$

Because of the symmetry in the temperature profile, the radiant flux q_R is zero at the center of the channel.

Integration of equation (4) with respect to y and imposition of boundary conditions (6) and (7) yields two energy equations

$$0 \le y < \delta_{ff}: \quad \dot{Q}_V(\delta - y) + q_{ff} = k_m \epsilon_H^+ \frac{dT}{dy} - q_R \tag{8a}$$

$$\delta_{ff} < y \le \delta: \quad \dot{Q}_V(\delta - y) = k_m \epsilon_H^+ \frac{dT}{dy} - q_R \tag{8b}$$

These relations must be solved subject to equation (5) and continuity in temperature at the flame front.

The Radiant Flux in a Sooty Gas. Unlike molecular gases, soot radiates as a continuum over a broad portion of the spectrum. Soot is formed by the condensation and agglomeration of carbon with some hydrogen from cracked hydrocarbon molecules [7, 8]. The properties depend somewhat on the size and composition of the particles.

There is general agreement that the isothermal spectral emissivity of small soot particles is given approximately by

$$\epsilon_\lambda = 1 - e^{-k_\lambda cL} \tag{9}$$

$$k_\lambda = K_0 \lambda^{-n} \tag{10}$$

and n is close to unity. Howarth, Foster, and Thring [9] report that K_0 is insensitive to temperature. Kuniotmo and Sato [10] surveyed the literature and collected optical constants for insertion into the Mie equations and made measurements of particle size distributions. Their infrared calculations agree with equation (10) with n near unity, but their experimental measurements indicated a value of n of approximately 0.70. Beer and Siddall [8] recommend 1.086, and Hottel recommends $n = 1.39$ in the visible and 0.95 in the infrared.

There is also general agreement that scattering by soot is negligible, e.g. [8, 9]. The sizes and optical properties of the particles give an albedo for a single scattering of less than 0.01 at a photon wavelength of 1 micron and considerably smaller values at longer wavelengths. (See Fig. 12 of reference [10].)

In order to use a convenient formulation of the radiant flux q_R, as shown by Wang [11], it is necessary to have an expression for the modified or "internal" total emissivity. The internal total emissivity is given by [12]

$$\epsilon_i(T, cL) = \int_0^1 \left[1 - e^{-k_\lambda cL}\right] df_i(\lambda T) \tag{11}$$

Using a standard three-point Gaussian quadrature, e.g. [13], one obtains

$$\epsilon_i(T, cL) = \sum_{k=1}^{3} g_k \left[1 - e^{-K_0 cL (T/a_k)^n}\right] \tag{12}$$

where a_1, a_2, a_3 are given by [12, 13]

$$f_i(a_1) = 0.11270 \quad a_1 = 1882\ \mu \text{ deg K} \quad g_1 = 5/18$$
$$f_i(a_2) = 0.5000 \quad a_2 = 3218\ \mu \text{ deg K} \quad g_2 = 4/9$$
$$f_i(a_3) = 0.88729 \quad a_3 = 6445\ \mu \text{ deg K} \quad g_3 = 5/18$$

Equation (12) is quite similar to the three-gray-band approximation procedure recommended by Hottel [7]. The fact that Hottel found three bands to be sufficient for many technical calculations suggested to the authors that three-point Gaussian quadrature should be adequate here. In contrast to the older procedure, which requires laborious and arbitrary curve fitting, equation (12) is logical and unambiguous. For $K_0 cL = 0.01$ to 100 and $T = 2300$ to 3500 deg F, equation (12) agrees with exact equation (11) within 3.1 percent.

The internal total emissivity for the slab geometry then is

$$\epsilon_{s,i}(T, y^*) = \int_0^1 \epsilon_i(T, cy^*/\mu)\, 2\mu d\mu = \sum_{k=1}^{3} g_k \left[1 - 2E_3(\tau_0 y^* (T/a_k)^n)\right] \tag{13}$$

where

$$\tau_0 = K_0 c\delta \tag{14}$$

$$E_n(x) = \int_0^1 e^{-x/\mu} \mu^{n-2} d\mu \tag{15}$$

In the same way that equations (8), (18), and (19) of reference [3] were derived for molecular gas radiation, expressions for soot

Nomenclature

a_i = Gaussian quadrature abscissa
A = surface area
A_{i-j} = matrix element, equation (23)
c = soot concentration
c_p = specific heat
D_h = hydraulic diameter, 4δ
e = extent of incompleteness
E_n = exponential integral, order n
f = friction factor
f_i = internal Planckian fraction
F_{i-j} = radiant flux element
g_i = Gaussian coefficient
k_m = molecular conductivity
k = absorption coefficient
K_T = radiant flux kernel, equation (17)
l = node number at flame front
L = mean beam length
m = number of subdivisions
$\dot{m}$ = mass flow rate
n = soot absorption exponent
P = temperature gradient
q = heat flux
$\dot{Q}_V$ = volume heat release
$\dot{Q}$ = combustion heat release
R_{dm} = radiation-conduction ratio
R_t = turbulent Reynolds number
Re = Reynolds number
T = temperature
x = mole fraction
y = distance from wall
δ = half thickness of channel
ϵ_H = eddy diffusivity of heat
ϵ = emissivity
μ = viscosity
ν = wave number
ρ = density of mixture
σ = Stefan-Boltzmann constant
τ_0 = optical depth at $\nu = 10^4$ cm^{-1}

Subscripts

c = center line
ff = flame front
i = ith location, also internal total radiative property
j = jth location
R = radiation
s = slab
T = total
v = volume
w = wall
λ = spectral

Superscripts

$*$ = dimensionless quantity
$+$ = turbulent quantity

radiation may be found. When account is taken of the symmetry in temperature about the center of the channel there results

$$q_R = -\int_0^{\delta} K_T(y^*, y'^*) 4\sigma T^3 \frac{dT}{dy'}\, dy' \tag{16}$$

where the symmetric kernel is

$$K_T(y^*, y'^*) = \epsilon_{s,i}(T, 2-y^*-y'^*) - \epsilon_{s,i}(T, |y^*-y'^*|) \tag{17}$$

Equations (16) and (17) take into account the nongray radiative behavior of soot described in the foregoing and the spatial variation of temperature. In this analysis it is assumed, for simplicity, that the soot concentration is uniform throughout the channel width, even though in actual situations it is position dependent.

Solution of the Energy Equation. Let any of m discrete values of the y coordinate be singled out with subscript i. The wall is located at $y_{i=1} = 0$ and the center of the channel at $y_{i=m} = \delta$. Then equation (16) can be approximated with a numerical quadrature. A simple scheme is

$$-q_R(y_i) = \sum_{j=2}^{m} \left[\int_{y_{j-1}}^{y_j} K_{T_j}(y_i^*, y'^*)\, dy'\right] \frac{1}{2}\left[B_{j-1}' P_{j-1} + B_j' P_j\right]$$

where

$$\overline{T}_j = \frac{1}{2}(T_j + T_{j-1}) \tag{18}$$

$$T_j = T_{j-1} + \frac{1}{2}(P_j + P_{j-1}),\ (y_j - y_{j-1}) T_1 = T_w \tag{19}$$

$$B_j' = 4\sigma T_j^3 \tag{20}$$

$$P_j = \left.\frac{dT}{dy}\right|_{y=y_j} \tag{21}$$

The numerical quadrature may be recast into the form

$$-q_R(y_i) = \sum_{j=1}^{m} A_{i,j} B_j' P_j \tag{22}$$

where

$$A_{i,j} = \frac{1}{2}\left[F_{i,j} + F_{i,j+1}\right],\ A_{i,1} = \frac{1}{2} F_{i,2},\ A_{i,m} = \frac{1}{2} F_{i,m} \tag{23}$$

$$F_{i,j} = \int_{y_{j-1}}^{y_j} K_{\overline{T}(j)}(y_i^*, y'^*)\, dy' \tag{24}$$

When a flame front exists at location y_l, two values of dT/dy exist, one at δ_{ff}^- and the other at δ_{ff}^+. Hence the y_i scale and the $F_{i,j}$ values are renumbered with

$$y_i = y_{i,\text{old}},\quad i = 1, l \qquad y_i = y_{i-1,\text{old}},\quad i = l+1,\ m+1$$

The $F_{i,j}$ matrix is expanded by inserting a column of zeros to form a new $l+1$ column, and a row of values equal to those at row l are inserted to form a new $l+1$ row. Equation (23) is used to generate the new $A_{i,j}$ matrix.

For numerical solution by iteration, the energy equation (8 *ab*) is written

$$i = 1,\quad l: \dot{Q}_V(\delta - y_i) + q_{ff} = k_m \epsilon_{H,i}{}^* P_i + \sum_{j=1}^{m+1} A_{i,j} B_j' P_j \tag{25a}$$

$$i = l+1, m+1: \quad \dot{Q}_V(\delta - y_i) = k_m \epsilon_{H,i}{}^* P_i + \sum_{j=1}^{m+1} A_{i,j} B_j' P_j \tag{25b}$$

With a starting set of T_i, the property and $\epsilon_{H,i}{}^*$ vectors and $F_{i,j}$ and $A_{i,j}$ matrices are generated, and equations (25*ab*) solved for P_i. With the new set of P_i, equations (18) and (19) are used to generate a temperature vector T_i, and the procedure is repeated until convergence is obtained.

The Total Heat Balance. In order to assess the extent to which blockage of radiation heat transfer by soot might increase nitric oxide emissions, it is necessary to make comparisons for equal rates of firing. Account is taken of incompleteness of combustion by the following procedure:

1 Except for the fraction of NO, which is reaction-rate controlled, the composition of the combustion products is assumed to that corresponding to equilibrium at the volume average temperature. This composition is fixed by an incompleteness of combustion parameter e.

2 The combustion heat release per unit area is taken to be $(\dot{m}c_p/2A)T_{\max}(e)$ where $T_{\max}(e)$ is the theoretical flame temperature.

3 The combustion heat release equals the radiant and convective heat transfer to the water wall plus the heat flow to the convective section, taken to be $(\dot{m}c_p/2A)T_v$. The total heat balance is thus written

$$q_{ff} + \dot{Q}_V \delta = (\dot{m}c_p/2A)\left[T_{\max}(e) - T_v\right] \tag{26}$$

Under this assumption, when there is no radiative cooling, T_v rises to $T_{\max}(e)$, which is then the theoretical adiabatic flame temperature.

For utmost simplicity a combustion reaction with a single incompleteness parameter was taken.

$$C + O_2 + 3.76\ N_2 \rightarrow (1-e)CO_2 + eCO + \frac{e}{2} O_2 + 3.76\ N_2$$

The soot is assumed to be formed by a portion of the C fuel, continuously supplied as in "mixing controlled combustion" [2]. Equilibria data from reference [14] then lead to a curve of e versus T_v shown in Fig. 2. Theoretical flame temperature versus e is also found [15] as shown in Fig. 2. If relative values of q_{ff} and $\dot{Q}_V\delta$ are fixed, the analysis of simultaneous radiation and turbulent trans-

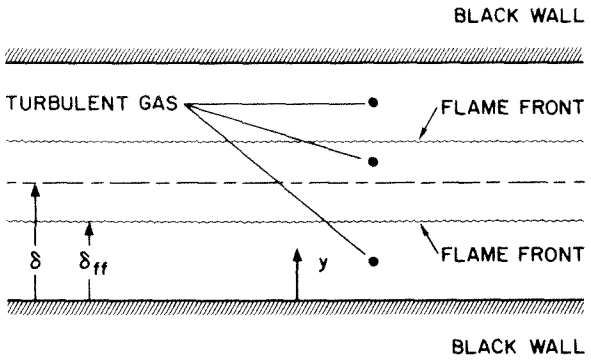

Fig. 1 Flame front model geometry

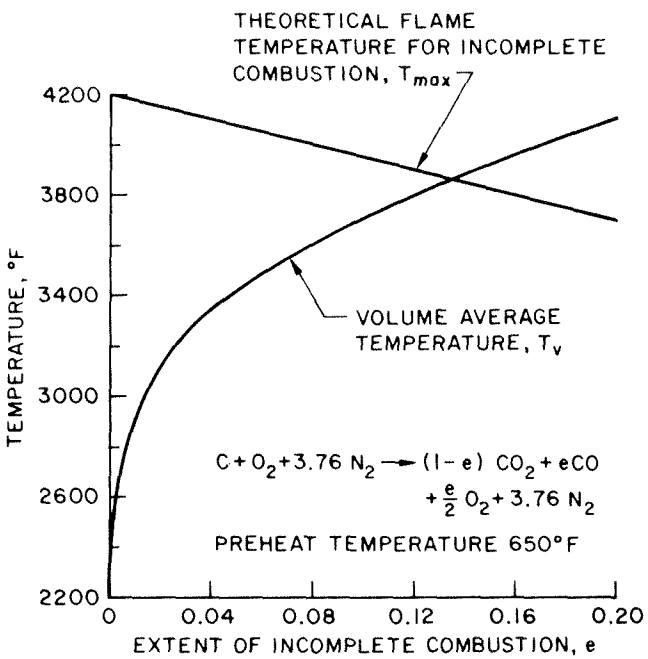

Fig. 2 Extent of incomplete combustion at equilibrium and theoretical flame temperature

port and a chosen value of center line or flame front temperature fixes both $q_{ff} + \dot{Q}_V\delta$ and T_c. The value of T_c fixes an equilibrium value of e from Fig. 2, and this value in turn fixes $T_{\max}$ in the figure. With these values, the value of $\dot{m}c_p/2A$ in equation (26) is fixed for a value of T_c or T_{ff}. A nominal value of $\dot{m}c_p/A$ then shows how T_c or T_{ff} and T_ι varies with τ_0.

Nitric Oxide Emissions. In order to evaluate how an increase in flame temperature affects nitric oxide emission levels, the authors have made use of the Zeldovich-based reaction kinetics of reference [2]. It was assumed that the NO concentration actually achieved was brought about in two steps. The frozen concentration that would result from a time of 0.05 sec at the flame front or center-line temperature was found, as was the concentration that would be caused by a time of 1 sec at the volume average temperature. An upper limit to the NO emission concentration was found by adding the two values.

Results

Radiation calculations were made for two relative values of q_{ff} and $\dot{Q}_V\delta$. In one case q_{ff} was taken to be zero, and all the heating from combustion and cooling (in effect) from convective sweeping was assumed to manifest itself in a net positive volume heating. In the other case $\dot{Q}_V$ was taken to be zero, and all of the heat *delivered to the cold wall* was assumed to be produced at the flame front. This latter case was not the upper limit of complete flame front heat release, for only a fraction of the total combustion heat release is absorbed by the wall, and the remainder is swept away to the convective section of the boiler or furnace. The turbulence level was considered fixed by $R_t = 1000$. The flame front case calculations show that, in order to maintain low flame front temperature, only relatively low firing rates can be used so that the fraction of heat transferred to the wall by radiation and turbulent diffusion is as high as one-third. Therefore, the case of flame front heat release investigated may be viewed on an overall basis as approximately ⅓ heat release at the flame front and ⅔ distributed over the volume counterbalanced by that ⅔ being swept away by convection.

Table 1 Simultaneous Radiation and Turbulent Diffusion

$R_t = 1000$, $\delta = 1$ ft, $T_w = 980$ deg F

Case	τ_0	T_c deg F	T_ι deg F	q_R Btu/hr ft²	q_T Btu/hr ft²
Volume heating	10	3500	3203	131,300	147,500
	5	2960	2774	118,800	129,800
		3140	2940	142,400	145,000
		3320	3105	169,000	184,200
		3500	3273	198,400	215,800
	2	2960	2839	145,500	157,700
		3140	3010	178,100	190,900
		3320	3180	215,400	230,200
		3500	3351	257,600	274,700
	1	2960	2871	133,300	143,200
		3140	3040	165,900	177,800
		3320	3219	203,800	217,700
		3500	3396	247,400	263,200
	0.5	2960	2881	101,100	110,500
		3140	3060	127,800	138,700
		3320	3236	159,200	171,800
		3500	3414	195,900	210,500
Flame front heating	10	3500	2968	65,500	74,600
	5	2960	2449	55,600	61,700
		3140	2600	65,400	72,300
		3320	2754	76,000	84,000
		3500	2910	87,600	96,700
	2	2960	2358	60,400	65,800
		3140	2496	71,700	78,000
		3320	2637	84,500	91,600
		3500	2784	98,500	106,600
	1	2960	2307	54,000	58,900
		3140	2434	64,700	70,132
		3320	2564	76,600	83,100
		3500	2694	90,100	97,200
	0.5	2960	2289	42,900	47,253
		3140	2408	51,900	56,800
		3320	2529	62,000	67,600
		3500	2651	73,400	79,700

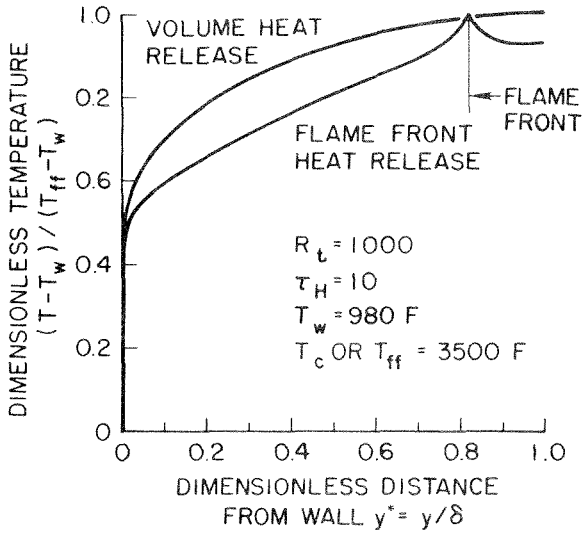

Fig. 3 Temperature profile for an optical depth of 10

Table 1 shows the radiation-turbulent-diffusion results. The only two parameters varied parametrically were optical depth τ_0 and center temperature T_c. In all cases wall temperature was fixed at 980 deg F, R_t at 1000, and channel width 2δ at 2 ft. A value of $n = 1$ was used for the soot absorption coefficient exponent. While the calculations were all made in dimensionless form, parameterized by τ_0, R_t, $R_{dm} = 4\sigma T^3\epsilon_{H,t}\delta/k_c$, $u = hcv_0/kT_c$, $r = T_w/T_c$, and assumed property variations, $(\rho/\mu) = (\rho_0/\mu_0)\ (T/T_0)^{1.7}$, and $k_m = k_0(T/T_0)^{0.7}$, the results are presented in dimensional form.

The table shows that at equal peak temperature much more heat transfer can be obtained in the volume heating case than in the flame front case, but, for both, the highest rates occur at an optimum optical depth of soot in the neighborhood of 2. Peak temperatures tend to be considerably above volume average temperatures for the flame front case and less so for the volume heat release case. Fig. 3 shows a temperature profile.

Table 2 shows the nitric oxide emissions which result from a volume heat release rate of firing equal to 1.13 million Btu/hr per sq ft of one channel wall. An optical depth of 10 gives rise to 440 ppm of NO, while the optimum value of 2 results in a value of only 24 ppm, some 18 times smaller. For the flame front heat release case the rate of firing is some two and one-half times smaller. The quantity $\dot{Q}/A$ is obtained from $\dot{m}c_p/2A$ from equation (26) using nominal values of 14,093 Btu per lb of fuel, 12.53 lb of combustion products per lb of fuel, and $c_p = 0.31$ Btu/lb deg F for the combustion products.

Fig. 4 compares the two results. The flame front heat release has a minimum ppm of NO almost twice as high as the volume heat release case even though the total heat release rate per unit area of one wall is 2.5 times smaller, because flame front heat re-

Table 2 Effect of Soot on Nitric Oxide Emissions

Case	τ_0	T_c deg F	T_ι deg F	q_T Btu/hr ft²	x_{NO} ppm
Volume heating	10	3500	3200	147,500	440
	5	3270	3060	167,500	76
$\dot{Q}/A =$	2	3100	2975	183,000	24
1.13×10^6	1	3140	3040	177,800	66
Btu/hr ft²	0.5	3230	3150	154,000	172
Flame front heating	10	3500	2968	74,600	210
	5	3360	2788	86,900	47
	2	3355	2665	92,100	46
$\dot{Q}/A =$	1	3465	2667	94,500	120
0.446×10^6	0.5	3600	2720	87,000	420
Btu/hr ft²					

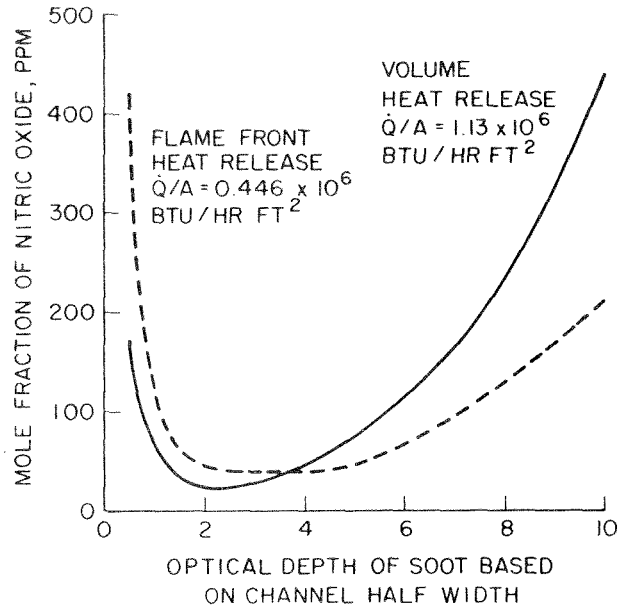

Fig. 4 Comparison of nitric oxide emissions for flame front and volume heat release versus optical depth of soot

Table 3 Effect of Spectral Variation Exponent n Upon Volume Average Temperature and Wall Heat Flux

$R_f = 1000$, $\delta = 1$ ft, $T_c = 3500$ deg F, $T_w = 980$ deg F, $\epsilon(T_c, c\delta) = 0.64$

n	τ_0 (at 1 μ)	T_v deg F	q_R Btu/hr ft^2	q_T Btu/hr ft^2
0.7	1.65	3355	266,160	283,225
0.95	1.96	3351	258,897	276,000
1.00	2.00	3351	257,600	274,700
1.086	2.14	3349	254,493	271,604
1.39	2.64	3343	243,230	260,344

lease results in a peak temperature considerably greater than the volume average temperature. The sharp minimum in the case of volume heat release occurs near $\tau_0 = 2$, while the flame front case is less sensitive and can tolerate a somewhat larger amount of soot. Both curves climb steeply as the soot optical depth drops below a value of unity. A moderate amount of soot is seen to be highly beneficial in promoting high heat transfer rates in the radiant section and in suppressing the formation of NO in the combustion zone.

Discussion

While eddies of flame have been thought to be too small and to exist for too short a time for radiation to play a role in controlling nitric oxide production in utility boilers, the present authors find a large effect. The reason is not hard to discern. It is well known that recirculating exhaust products (which have been cooled below adiabatic flame temperature) will reduce the combustion temperature of a flame. In a turbulent gas there is a *microrecirculation* brought about by turbulent eddies of exhaust products mixing with combustion air. On a statistical basis some of these eddies will contain gases which have cooled off by the strong radiative cooling mechanism which operates, unless the visibility of the cold wall is masked by too much soot.

The results obtained here corroborate a number of empirical findings. For example, it is known that mixing-controlled or two-stage combustion, either of which tends away from flame front heat release toward volume heating, reduces nitric oxide emissions. It is also known that a natural gas burner adjusted to produce little soot and tending toward flame front heat release can produce large amounts of NO. Overly sooty fuels produce more

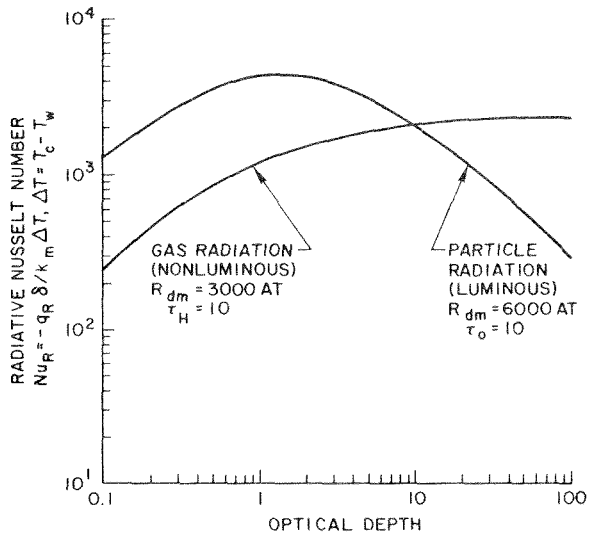

Fig. 5 Comparison of gas and soot radiative cooling versus optical depth. Turbulence Reynolds number $R_f = 1000$

NO than does natural gas during controlled combustion, and larger units produce more than proportionately larger amounts of NO. The reason for the latter appears to be twofold, larger units having too great an optical depth of soot as well as too little radiant wall area. There is also the possibility that soot-producing fuels tend to contain more nitrogen impurities which may add to the formation of NO.

Existing units could benefit from control of soot formation during mixing-controlled or two-stage combustion. As shown in Fig. 4, an optical depth based on channel half width should be approximately 2; then the value based upon geometric mean beam length is 8. Exhaust gas recirculation or steam injection can be used to control soot formation.

New units would benefit from partitioning the combustion volume such that the half channel optical depth would be approximately 2. With clever design, the larger amount of radiant wall surface introduced could be put to good use, since the radiant heat fluxes are high. The wall heating rate calculated here for a 980 deg F wall and $\tau_0 = 2$ (see Table 2) is 183,000 Btu/hr ft^2. This value is in good agreement with empirical observation of fluxes of 175,000 Btu/hr ft^2 on clean water wall [16].

It is perhaps interesting to note that Viskanta [17] showed that radiant transfer to the wall from a gray gas flowing laminarly in a parallel plate channel becomes maximum at an optical depth of 2, based upon the total channel spacing 2δ. Here we have found that minimum nitric oxide production at a flame front within a nongray, turbulent sooty gas occurs for an optical depth of 4 based upon total channel width 2δ, a photon wavelength of 1.0 μ, and a gas temperature on the order of 3000 deg F.

Since larger-sized particles of soot have lower values of spectral exponent n in equation (10), the sensitivity of the temperature profiles and heat fluxes obtained here to variations in n was investigated. Values of n equal to 0.7 [10], 0.95 [7], 1.0, 1.086 [8], and 1.39 [7] were used. Turbulence parameter R_f, thickness δ, center temperature T_c, wall temperature T_w, and external total emissivity $\epsilon(T_c, c\delta)$ were held constant. Results are shown in Table 3. The magnitudes of the variations in volume average temperature T_v and heat fluxes q_R and q_T are thought to be sufficiently small in view of the broad optimum shown in Fig. 4 that departures of k_λ from equation (10) with $n = 1$ due to differences in particle size or composition [10] do not affect the validity of the conclusions reached here regarding an optimum optical depth of soot for combustion chambers.

The behavior of soot in rendering the radiant wall invisible to the flame, when the amounts of soot are too large, is in marked contrast to the behavior of the CO_2 and H_2O molecular gas combustion products found previously [3, 4]. Fig. 5 shows this differ-

ence. As optical depth is increased, the gas band radiation merely shifts in the wings of the bands so that a plateau in radiative cooling is reached. But in the case of soot, the added optical depth masks the high temperature regions from being able to radiate to cold wall, and at higher values of optical depth the transfer at the wall itself is reduced as the boundary layer becomes more absorbing. While the present analysis considered soot radiation only, it appears that in the case of combined soot and gas radiation too much soot will block the gas radiation as well. The problem of combined soot and gas radiation is a nontrivial extension of the present work, and the authors will attempt to treat the problem in the future.

Acknowledgment

Computations were carried out at the UCLA Campus Computing Network. A. Balakrishnan gratefully acknowledges support received from State of California, School of Engineering, Air Pollution Grant No. 4-402474.

References

1 Woolrich, P. F., "Methods of Estimating Oxides of Nitrogen Emissions From Combustion Processes," *Industrial Hygiene Journal*, Vol. 22, 1961, pp. 481–484.

2 Breen, B. P., Bell, A. W., Bayard deVolo, N., Bagwell, F. A., and Rosenthal, K., "Combustion Control for Elimination of Nitric Oxide Emissions From Fossil-Fuel Power Plants," *Thirteenth Symposium (International) on Combustion*, The Combustion Institute, 1971, pp. 391–401.

3 Edwards, D. K., and Balakrishnan, A., "Self-Absorption of Radiation in Turbulent Molecular Gases," *Combustion and Flame*, Vol. 20, 1973, pp. 401–417.

4 Edwards, D. K., and Balakrishnan, A., "Radiative Cooling of a Turbulent Flame Front," to be published, JOURNAL OF HEAT TRANSFER.

5 Van Driest, E. R., "On Turbulent Flow Near a Wall," *J. Aero. Sci.*, Vol. 23, 1956, pp. 1007–1011.

6 Mei, J., and Squire, M., "A Simple Eddy Viscosity Model for Turbulent Pipe and Channel Flow," *AIAA Journal*, Vol. 10, 1972, pp. 350–352.

7 Hottel, H. C., "Radiant Heat Transmission," *Heat Transmission*, Ch. 4, by McAdams, W. H., McGraw-Hill, N. Y., 1954.

8 Beer, J. M., and Siddall, R. G., "Radiative Heat Transfer in Furnaces and Combustors," ASME Paper No. 72-WA/HT-29.

9 Howarth, C. R., Foster, P. J., and Thring, M. W., "The Effect of Temperature on the Extinction of Radiation by Soot Particles," *Proc. Third International Heat Transfer Conference*, 1966, pp. 122–128.

10 Kunitomo, T., and Sato, T., "Experimental and Theoretical Study on the Infrared Emission of Soot Particles in Luminous Flame," *Heat Transfer 1970*, Vol. III, Elsevier Publishing Co., Amsterdam, paper R1.6, 1970.

11 Wang, L. S., "The Role of Emissivities in Radiative Transport Calculations," *J. Quant. Spectrosc. Radia. Transfer*, Vol. 8, 1968, pp. 1233–1240.

12 Edwards, D. K., "Radiative Transfer Characteristics of Materials," JOURNAL OF HEAT TRANSFER, TRANS. ASME, Series C, Vol. 91, 1969, pp. 1–15.

13 Love, T. J., *Radiative Heat Transfer*, Merrill Publishing Co., Columbus, Ohio, 1968, p. 262.

14 Lewis, B., and Von Elbe, G., "Heat Capacities and Dissociation Equilibria of Gases," *J. Am. Chem. Soc.*, Vol. 57, 1935, p. 612.

15 Lee, J. F., and Sears, F. W., *Thermodynamics*, Addison-Wesley, Cambridge, Mass., 1955, pp. 462–463.

16 *Steam*, Babcock and Wilcox, New York, 37th ed., Ch. 7, 1963.

17 Viskanta, R., "Interaction of Heat Transfer by Conduction, Convection, and Radiation in a Radiating Fluid," JOURNAL OF HEAT TRANSFER, TRANS. ASME, Series C, Vol. 85, 1963, pp. 318–328.

K. R. CHUN
Member Senior Technical Staff,
Northrop Research and Technology Center,
Hawthorne, Calif. Mem. ASME

Surface Heating of Metallic Mirrors in High Power Laser Cavities

The effect of the absorptance increase with the rising mirror surface temperature on the final surface temperature is examined. For noble metals such as silver, copper, and gold, the Drude theory predicts an approximately linear dependence of the normal spectral absorptivity on the temperature in an absolute scale for the wavelengths 1 $\mu \sim 15$ μ and the temperatures 100 deg K $\sim$ 1200 deg K approximately. For such a regime, it is shown that gross underestimates of the final surface temperature rise result from the assumption of the constant absorptivity at the initial temperature when the estimated value becomes comparable to the initial temperature in an absolute scale.

Introduction

THE FIELD of laser interaction with materials has been an area of extensive investigations in recent years as can be evidenced in the literature [1, 2].[1] With the escalating power levels of CO_2 and CO lasers in pulsed or continuous wave mode, the problem of distortion and melting of optical mirrors in the laser system can become the limiting factor on the permissible level of output power.

The problem of transient heating of a semi-infinite medium without phase change has been considered for the time-varying beam intensities and the gaussian beam distributions [1, 3]. However, the dependence of the surface absorptance on the surface temperature has not been taken into consideration so far.

For typical mirror materials such as silver, copper, and gold, the normal spectral absorptivity increases with temperature even though it is typically only a few percent at room temperature. Thus for a constant beam intensity the absorbed power increases with the surface temperature rise and the increased absorption rate further raises the surface temperature establishing a positive feed-back loop. The main thrust of this paper is to estimate the effect of the surface absorptivity increase with the temperature on the heating of mirror surfaces in high power laser systems. In pursuit of this objective, some important simplifications had to be made as described in the following.

1 No phase change occurs on the mirror surface. Thus the analysis presented here cannot be applied beyond the melting point.

2 Cooling from the irradiated side by convection and radiation to the surroundings is negligible compared with the absorbed power. At 1200 deg K surface temperature and 300 deg K ambient temperature, for example, the heat loss by front face cooling amounts to a few tens of w/cm^2 and can be neglected when the instantaneous absorbed power is in the order of kw/cm^2.

3 Laterial conduction parallel to the surface is negligible compared with that normal to it, i.e., one-dimensional. This can lead to a serious error when the thermal penetration depth $\sqrt{\kappa t}$ becomes comparable to the beam size.

4 The beam intensity is constant in time. This is again a doubtful assumption for beams such as Q-switched lasers.

5 Heat is absorbed at the surface and the beam penetration depth is infinitesimal.

6 The normal spectral absorptivity varies as the Drude theory predicts.

For noble metals, the classical theory by Drude based on the free electron model is believed to predict satisfactorily the normal spectral reflectivity above moderately low temperatures ($>$ 100 deg K) and at long wavelengths ($>1\mu$) [4, 5]. At wavelengths shorter than 1μ, and at very low temperatures, the quantum mechanical effects and the anomalous skin effect come into play and extensive discussions of such effects are given in the literature [6–8].

Drude Theory for Optical Constants of Metals

On the basis of electromagnetic theory, the spectral normal reflectivity is given by

$$\rho_{n,\lambda}(\lambda, T) = \left|\frac{(\bar{N} - 1)}{(\bar{N} + 1)}\right|^2 = \frac{(n - 1)^2 + k^2}{(n + 1)^2 + k^2} \tag{1}$$

or

$$\alpha_{n,\lambda} = 1 - \rho_{n,\lambda} = \frac{4n}{(n + 1)^2 + k^2} \tag{2}$$

[1] Numbers in brackets designate References at end of paper.

Contributed by the Heat Transfer Division for publication (without presentation) in THE JOURNAL OF HEAT TRANSFER. Manuscript received by the Heat Transfer Division June 14, 1973. Paper No. 74-HT-A.

where $\bar{N} = (n - ik)$ is the complex refractive index. For non-absorbing (ideal dielectric) media, $k = 0$. Drude's theory for optical constants of metals result in the expressions [4],

$$n^2 - k^2 = 1 - \left(\frac{\lambda}{\lambda_1}\right)^2 \frac{1}{1 + \left(\frac{\lambda}{\lambda_2}\right)^2} = a \tag{3}$$

$$2nk = \left(\frac{\lambda}{\lambda_2}\right)\left(\frac{\lambda}{\lambda_1}\right)^2 \frac{1}{1 + \left(\frac{\lambda}{\lambda_2}\right)^2} = b \tag{4}$$

where

$\lambda_1 = \dfrac{c^2\pi m}{Ne^2}$

$\lambda_2 = 2\pi c\tau$

m = electronic mass

N = number density of free electrons, assumed to be one

c = speed of light

$\tau = \dfrac{m\sigma_0}{Ne^2}$, relaxation time of the free electrons

σ_0 = direct current electrical conductivity

Solving for n and k from equations (3) and (4), and substituting these into equation (2), the normal spectral absorptivity of a metal can be expressed as

$$\alpha_{n,\lambda} = \frac{[8(a + \sqrt{a^2 + b^2})]^{1/2}}{\sqrt{a^2 + b^2} + [2(a + \sqrt{a^2 + b^2})]^{1/2} + 1} \tag{5}$$

where the constants a and b are as defined in equations (3) and (4). Thus the normal spectral absorptivity is dependent on σ_0 in addition to the incident beam wavelength, λ.

In the limit $(\lambda/\lambda_2) \gg 1$, namely at long wavelength and short relaxation time (or low d-c conductivity), equation (5) reduces to the well-known Hagen-Rubens relation

$$\alpha_{n,\lambda} \cong 0.365\sqrt{\frac{r}{\lambda}} \tag{6}$$

where r is in ohm-cm and λ is in cm.

The dependence of the resistivity of a metal on temperature may be expressed by the Bloch-Grüneisen relation

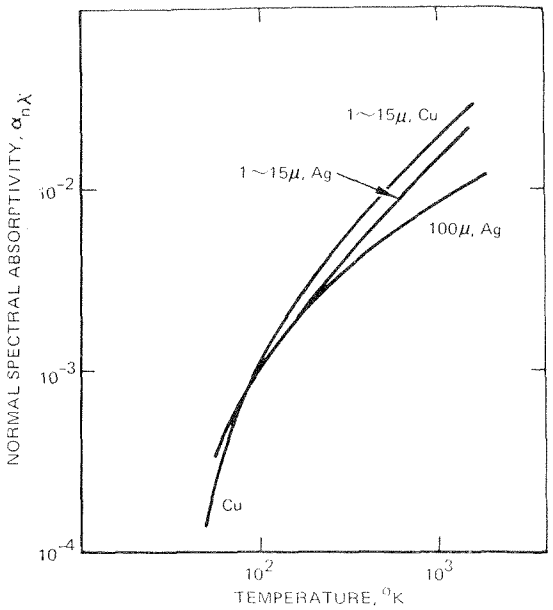

Fig. 1 Temperature dependence of normal spectral absorptivity of silver and copper based on Drude theory

$$r = \frac{1}{\sigma_0} = \frac{KT^5}{M\theta^6}\int_0^{\theta/T} \frac{Z^5 dZ}{(e^Z - 1)(1 - e^{-Z})} \tag{7}$$

where

K = a material constant

M = atomic weight

θ = Debye characteristic temperature of the material

(For silver, $\theta \cong 223$ deg K and copper, $\theta \cong 333$ deg K.)

Using the conductivity values of equation (7) in equation (5), values for the normal spectral absorptivity of silver versus temperature and wavelength were calculated and are plotted in Figs. 1 and 2, respectively. In the range of temperatures of interest, 100 deg K ~ 1200 deg K (melting point of silver), and wavelength, range of $1\mu \sim 15\mu$, a good linear approximation can be made as

Nomenclature

c = speed of light (cm/sec) or specific heat of mirror substrate $\left(\dfrac{\text{joule}}{\text{gr deg C}}\right)$

$E = \dfrac{I_0\alpha_i}{T_i\sqrt{k\rho c}}$ (sec$^{-1/2}$)

e = electronic charge (coulomb)

h = heat transfer coefficient between the mirror back face and the coolant fluid (w/cm^2 deg C)

I_0 = incident beam intensity (w/cm^2)

J = energy absorbed by the surface in time t (joule)

k = thermal conductivity of mirror substrate $\left(\dfrac{\text{w}}{\text{cm deg C}}\right)$ or extinction coefficient

m = electronic mass (gr)

N, n = integer or refractive index

q = heat flux per unit area (w/cm^2)

R = overall thermal resistance $\left(\dfrac{\text{cm}^2\text{ deg C}}{\text{w}}\right)$

r = d-c resistivity (ohms)

T = absolute temperature (deg K)

t = time (sec)

V_c = surface temperature rise based on the constant absorptivity α_i (deg K)

v = $T - T_i$ (deg K)

x = coordinate normal to mirror surface (cm)

$Y = Et^{1/2} = \dfrac{\sqrt{\pi}}{2}\dfrac{V_c}{T_i}$

α = absorptivity

δ = mirror thickness (cm)

κ = thermal diffusivity $\left(\dfrac{\text{cm}^2}{\text{sec}}\right)$

ρ = density of mirror substrate (gr/cm^3) or reflectivity

σ_0 = d-c conductivity (mho)

λ = wavelength (cm), or a constant in equation (17)

$\lambda_1 = \dfrac{c^2\pi m}{Ne^2}$ (cm)

$\lambda_2 = 2\pi c\tau$ (cm)

τ = relaxation time of electron (sec) or time variable in equation (11)

ν = frequency (sec^{-1})

$\omega = 2\pi\nu$ (sec^{-1})

Subscripts

c = based on a constant α

i = at time $t = 0$

f = value at the coolant fluid temperature

0 = condition at the surface, $x = 0$

r = at reference state, 300 deg K

n = normal to the surface

λ = at wavelength λ

$$\alpha_{n,\lambda} = (\text{constant})T \tag{8}$$

or

$$\frac{\alpha_{n,\lambda} \text{ at } T}{\alpha_{n,\lambda} \text{ at } T_r} = \frac{T}{T_r} \tag{9}$$

where T_r is the reference temperature in deg K at which resistivity is measured, say 300 deg K.

In case of silver, Hagen-Rubens relation is seen to be valid only at very long wavelengths and high temperatures. For example, at 1200 deg K, it is valid at $\lambda > 20\ \mu$ and at 300 deg K, $\lambda > 100\mu$. In these extremes,

$$\frac{\alpha_{n,\lambda} \text{ at } T}{\alpha_{n,\lambda} \text{ at } T_r} = \sqrt{\frac{T}{T_r}} \tag{10}$$

Single Pulse Into a Semi-Infinite Solid

The temperature distribution of a semi-infinite solid, initially at a uniform temperature T_i and with a time dependent heat flux $f(t)$ at its surface $x = 0$, can be written as [9]

$$v(x, t) = T(x, t) - T_i = \frac{1}{\sqrt{k\rho c}\sqrt{\pi}} \int_0^t f(t - \tau) e^{-\frac{x^2}{4\pi\tau}} \frac{d\tau}{\tau^{1/2}} \tag{11}$$

The surface temperature at $x = 0$ can be written as

$$v_0(t) = \frac{1}{\sqrt{k\rho c}\sqrt{\pi}} \int_0^t f(t - \tau) \frac{d\tau}{\tau^{1/2}} \tag{12}$$

If a beam of constant intensity I_0 and a constant absorptivity of α_i evaluated at T_i, are assumed, namely,

$$f(t) = I_0\alpha_i = \text{constant},$$

then (12) gives the well-known result

$$\frac{V_e}{T_i} = \frac{I_0\alpha_i}{T_i\sqrt{k\rho c}} \frac{2}{\sqrt{\pi}} t^{1/2} = \frac{2}{\sqrt{\pi}} Et^{1/2} \tag{13}$$

where

$$E \equiv \frac{I_0\alpha_i}{T_i\sqrt{k\rho c}}$$

Let us consider the case of absorptivity varying linearly with temperature as in (9)

$$\alpha = \alpha_i \frac{T}{T_i} \tag{14}$$

The flux absorbed by the surface becomes

$$f(t) = I_0\alpha = I_0\alpha_i \left[1 + \frac{v_0(t)}{T_i}\right] \tag{15}$$

Substituting (15) into (12)

$$v_0(t) = \frac{I_0\alpha_i}{\sqrt{k\rho c}\sqrt{\pi}} \int_0^t \left[1 + \frac{v_0(t - \tau)}{T_i}\right] \frac{d\tau}{\tau^{1/2}}$$

Changing the variable τ to $(t - \zeta)$ and then setting $\zeta = \tau$

$$v_0(t) = E \frac{2T_i}{\sqrt{\pi}} t^{1/2} + \frac{E}{\sqrt{\pi}} \int_0^t \frac{v_0(\tau)}{(t - \tau)^{1/2}} d\tau \tag{16}$$

This is a linear integral equation of the Volterra type,

$$v_0(t) = g(t) + \lambda \int_0^t K(t, \tau) v_0(\tau) d\tau \tag{17}$$

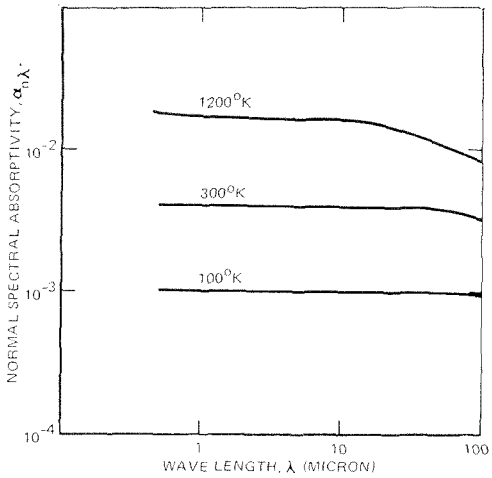

Fig. 2 Wavelength dependence of normal spectral absorptivity of silver based on Drude theory

and the solution by successive substitution can be shown as an infinite series [10]

$$v_0(t) = g(t) + \lambda \int_0^t K(t, \tau) g(\tau) d\tau + \lambda^2 \int_0^t K(t, \tau) \int_0^\tau K(\tau, \tau_1) g(\tau_1) d\tau_1 + \ldots + \lambda^n \int_0^t K(t, \tau) \int_0^\tau K(\tau, \tau_1) \ldots \int_0^{\tau_{n-2}} K(\tau_{n-2}, \tau_{n-1}) g(\tau_{n-1}) \times d\tau_{n-1} \ldots d\tau_1 dt + \ldots \tag{18}$$

Solving (16) in the manner of (18) one obtains

$$\frac{v_0(t)}{T_i} = \frac{1}{\Gamma(1 + 1/2)} Y + \frac{1}{\Gamma(2)} Y^2 + \frac{1}{\Gamma(2 + 1/2)} Y^3 + \frac{1}{\Gamma(3)} Y^4 + \ldots \frac{1}{\Gamma(1 + n/2)} Y^n + \ldots$$

$$= \sum_{n=1}^{\infty} \frac{1}{\Gamma(1 + n/2)} Y^n \tag{19}$$

where

$$Y \equiv Et^{1/2} = \frac{I_0\alpha_i}{T_i\sqrt{k\rho c}} t^{1/2} = \frac{\sqrt{\pi}}{2} \frac{V_e}{T_i}$$

$$\Gamma(n) = (n - 1)!$$

$$\Gamma(n + 1/2) = (n - 0.5) \ldots . (2.5)(1.5)(0.5)\sqrt{\pi}$$

The first term on the right side of the first equality of (19) is nothing but the constant absorptivity solution (13). It becomes obvious that as Y gets larger, the magnitude of additional terms can dominate the first. The proof of convergence and the estimate of truncation error are given in the Appendix.

Numerical values of (19) for $n = 10$ are plotted in Fig. 3. For $Y = 1$ and 1.3, the truncation errors are 0.6 percent and 13.5 percent, respectively. The same figure also shows the ratio v_0/V_e, namely the ratio of actual surface temperature to the "constant absorptivity" solution (13). For example, for $Y = 1$, $v_0 \cong 3.5\ V_e$.

By knowing v_0/T_i, one can find the temperature distribution within the solid via (15) and (11).

$$f(t) = I_0\alpha_i\left[1 + \sum_{n=1}^{\infty}\frac{1}{\Gamma\left(1+\frac{n}{2}\right)}Y^n\right]$$

$$= \sum_{n=0}^{\infty}\left[\frac{I_0\alpha_i E^n}{\Gamma\left(1+\frac{n}{2}\right)}t^{\frac{n}{2}}\right] \tag{20}$$

Substituting (20) into (11), and utilizing the equation (16), [p. 77, reference 9],

$$v(x,t) = \sum_{n=0}^{\infty}\left[E^{n+1}(4t)^{\frac{(n+1)}{2}}i^{n+1}erfc\,\frac{x}{2\sqrt{\kappa t}}\right] \tag{21}$$

Equation (21) can be shown to reduce to (19) for $x = 0$. Energy absorbed J during a pulse duration of t is

$$J = \int_0^t f(t)dt = \int_0^t \sum_{n=0}^{\infty}\frac{I_0\alpha_i E^n}{\Gamma\left(1+\frac{n}{2}\right)}t^{\frac{n}{2}}\,dt$$

$$= \sum_{n=0}^{\infty}\frac{I_0\alpha_i E^n}{\Gamma\left(1+\frac{n}{2}\right)}\frac{1}{\left(1+\frac{n}{2}\right)}t^{\frac{n}{2}+1}$$

$$= I_0\alpha_i t + I_0\alpha_i\sum_{n=1}^{\infty}\frac{E^n}{\Gamma\left(2+\frac{n}{2}\right)}t^{\frac{n}{2}+1} \tag{22}$$

Defining $J_c \equiv I_0\alpha_i t$, i.e., the energy absorbed if constant absorptivity is assumed,

$$\frac{J}{J_c} = 1 + \sum_{n=1}^{\infty}\frac{Y^n}{\Gamma\left(2+\frac{n}{2}\right)} \tag{23}$$

as plotted in Fig. 3.

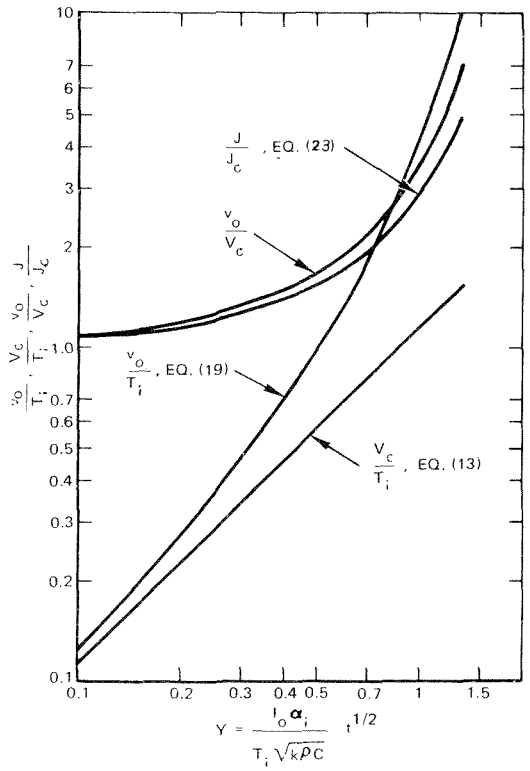

Fig. 3 Theoretical surface temperature for the cases of constant absorptivity and absorptivity varying linearly with absolute temperature

This concludes the solution for a semi-infinite medium with an absorptivity varying linearly with the absolute temperature of its surface for an incident beam of constant intensity; the temperature distribution by (21), the surface temperature by (19), and the total energy absorbed by (22).

Steady Heating of a Finite Thickness Mirror by CW Beam

For a steady uniform beam of intensity I_0 incident on a solid at $x = 0$ whose back face at $x = \delta$ is cooled by fluid at T_f, the steady heat flux is

$$q = \frac{1}{\left(\frac{\delta}{k}+\frac{1}{h}\right)}(T_0 - T_f) = \frac{1}{R}(T_0 - T_f) \tag{24}$$

where h is the heat transfer coefficient between the back face and the coolant.

Again assuming the loss from the front face to be negligible and $\alpha = \alpha_f$ = constant,

$$T_0 - T_f = I_0\alpha_f R.$$

If $\dfrac{\alpha}{\alpha_f} = \dfrac{T_0}{T_f}$

$$q = I_0\alpha = I_0\alpha_f\frac{T_0}{T_f} \tag{25}$$

By equating (24) with (25)

$$\frac{T_0}{T_f} = \frac{1}{1 - \left(\frac{I_0\alpha_f R}{T_f}\right)} \tag{26}$$

Since α cannot exceed one, equation (26) is valid only when

$$\frac{T_0}{T_f} \leq \frac{1}{\alpha_f} \text{ or } \frac{I_0\alpha_f R}{T_f} \leq 1 - \alpha_f$$

If $\dfrac{I_0\alpha_f R}{T_f} > 1 - \alpha_f$, α is already unity and $T_0 = T_f + I_0 R$, unless the other limiting assumptions already invalidate equation (26).

Conclusions

For noble metal reflectors, in the wavelength regions $1 \sim 15\mu$ and temperatures $100 \sim 1200$ deg K, the normal spectral absorptivity is approximately proportional to the absolute temperature. For such a regime, an analytical solution is obtained for semi-infinite mirror temperature distribution and energy absorbed. For high intensity pulsed beams, if $\dfrac{I_0\alpha_i}{\sqrt{k\rho c}}t^{1/2}$ reaches an order of the initial temperature, T_i, the actual surface temperature rise can be at least three times that based on constant absorptivity at T_i.

Acknowledgments

This work was supported by the Northrop Research and Technology Center, Northrop Corp.

References

1 Ready, J. F., *Effects of High-Power Laser Radiation*, Academic Press, New York, 1971.

2 *Applied Optics*, Vol. 12, No. 4, Apr., 1973, pp. 637–709.

3 Paek, U. C., and Kestenbaum, A., "Thermal Analysis of Thin-Film Micro-Machining With Lasers," *Journal of Applied Physics*, Vol. 44, No. 5, May, 1973, p. 2260.

4 Mott, N. F., and Jones, H., "The Theory of the Properties of Metals and Alloys," Dover Publications, Inc., New York, 1958.

5 Born, M., and Wolf, E., *Principles of Optics*, Macmillan, Second ed., New York, 1964.
6 Bennett, H. E., Bennett, J. M., Ashley, E. J., and Motyka, R. J., "Verification of the Anomalous-Skin-Effect Theory for Silver in Infrared," *Physical Review*, Vol. 165, Jan. 15, 1968, p. 755.
7 Tien, C. L., and Caravalho, E. G., "Thermal Radiation of Solids at Cryogenic Temperatures," *Advances in Cryogenic Heat Transfer*, Chemical Engineering Progress Symposium Series, Vol. 64, No. 87, 1968, p. 56.
8 Domoto, G. A., Boehm, R. F., and Tien, C. L., "Predictions of the Total Emissivity of Metals at Cryogenic Temperatures," *Advances in Cryogenic Engineering*, Vol. 14, 1969, p. 230.
9 Carslaw, H. S., and Jaeger, J. C., *Conduction of Heat in Solids*, Oxford University Press, Second ed., 1959, p. 76.
10 Lovitt, W. V., "Linear Integral Equations," Dover Publications, First ed., New York, 1950.
11 Thomas, G. B., Jr., "Calculus and Analytic Geometry," Addison-Wesley, Second ed., 1958, p. 600.

APPENDIX

Proof of Convergence

The infinite series of (19) can be written as the sum of two power series;

$$\frac{v_0(t)}{T_i} = \sum_{n=1}^{\infty} \frac{1}{\Gamma\left(1+\frac{n}{2}\right)} Y^n = \sum_{N=1}^{\infty} \left[\frac{1}{\Gamma\left(N+\frac{1}{2}\right)} Y^{2N-1} + \frac{1}{\Gamma(N+1)} Y^{2N} \right] \quad \text{(A1)}$$

The ratio r_{odd} of the odd powered series is

$$r_{odd} = \frac{\Gamma(N+1/2)}{\Gamma(N+1+1/2)} \frac{Y^{2(N+1)-1}}{Y^{2N-1}} = \frac{Y^2}{N+0.5} \quad \text{(A2)}$$

The ratio r_{even} of the even powered series is

$$r_{even} = \frac{\Gamma(N+1)}{\Gamma(N+2)} \frac{Y^{2(N+1)}}{Y^{2N}} = \frac{Y^2}{N+1} \quad \text{(A3)}$$

Since both ratios approach zero as $N \to \infty$, the series is shown to converge for a finite Y. The truncation error ϵ for taking only N terms in (A1) [11] is

$$0 \leq \epsilon \leq \left(\frac{r_{odd}}{1-r_{odd}}\right) \frac{Y^{2N-1}}{\Gamma(N+1/2)} + \left(\frac{r_{even}}{1-r_{even}}\right) \frac{Y^{2N}}{\Gamma(N+1)} \quad \text{(A4)}$$

where

$$\epsilon \equiv \sum_{N=1}^{\infty} \left(\frac{v_0}{T_i}\right) - \sum_{N=1}^{N} \left(\frac{v_0}{T_i}\right) \quad \text{(A5)}$$

For a specified ϵ, more terms (N) are required as Y grows. For a valid use of (A4), it is necessary to take enough terms so that

$$N > Y^2 - 1/2$$

M. Necati Özişik

Department of Mechanical and Aerospace Engineering, North Carolina State University, Raleigh, N. C.

R. L. Murray

Department of Nuclear Engineering, North Carolina State University, Raleigh, N. C.

On the Solution of Linear Diffusion Problems With Variable Boundary Condition Parameters

A method of solution is presented for the treatment of a class of boundary value problems of linear diffusion theory for finite homogeneous media which have applications in transient heat conduction (or mass diffusion) in a finite medium subjected to convective type boundary condition with time and space dependent coefficient, in the processes of neutron slowing in a finite medium with absorbing boundaries that exhibit energy-dependent cross sections, and in many related areas.

Introduction

A large class of boundary value problems of neutron slowing down, transient and steady heat conduction or mass diffusion can be solved by the application of the classical methods of solution described in various references such as Morse and Feshbach [1],[1] Carslaw and Jaeger [2], Davison [3], and Weinberg and Wigner [4], or they can be solved more systematically by the application of integral transform technique described by Sneddon [5], Tranter [6], Ölcer [7], and Özisik [8]. However, a gap remains in the literature on the solution of a class of boundary value problems involving boundary condition parameters that vary with time (or equivalent variables in analogous problem). Examples of these more general problems appear in several partical physical situations: *(a)* transient heat conduction in finite homogeneous media subjected to convective type boundary condition with time- and space-dependent heat transfer coefficient, *(b)* neutron slowing and thermalization in finite media with an energy-dependent boundary condition associated with typical neutron absorbers.

Standard analytical approaches as cited in the foregoing references cannot be applied to the solution of such problems because the eigenfunctions and eigenvalues of the appropriate eigenvalue problem depend on time (or corresponding independent variable). In an attempt to circumvent this difficulty, Thompson and Holy [9] and Holy [10] separated the heat transfer coefficient into a constant and time dependent part, and used the method of eigenfunction expansion to transform the problem to the Volterra-type integral equation for the boundary surface temperature; but the solution of the resulting integral equation was extremely difficult. Another approach tried by Ivanov and Salomatov [11] involved a change of the dependent variable which simplified the boundary condition but introduced a nonlinear term into the differential equation.

Therefore, it appears that there is still no satisfactory analytical method of solution of the problem of transient heat conduction subject to convective type of boundary condition with time and space dependent heat transfer coefficient, or neutron diffusion problems in a finite medium with energy dependent boundary conditions.

Analysis

Consider the following boundary value problem in a homogeneous, finite region R

$$\nabla\cdot[k(\underline{r})\nabla u(\underline{r},t)] + c(\underline{r})u(\underline{r},t) + g(\underline{r},t) = w(\underline{r})\frac{\partial u(\underline{r},t)}{\partial t},$$

$$\text{in region R, for } t > 0 \qquad (1a)$$

subject to the boundary conditions

$$k(\underline{r}_s)\frac{\partial u(\underline{r}_s,t)}{\partial n} + h(\underline{r}_s,t)u(\underline{r}_s,t) =$$

$$f(\underline{r}_s,t) \text{ on boundary } s, \text{ for } t > 0 \qquad (1b)$$

and the initial condition

$$u(\underline{r},t) = F(\underline{r}) \text{ in region } R, \text{ for } t = 0. \qquad (1c)$$

The analytical solution of this boundary value problem with the straightforward application of the standard mathematical technique will pose a difficulty because the coefficient $h(\underline{r}_s,t)$ appearing in the boundary condition depends both on the space variable r and the time variable t. If the finite integral transform technique, for example, is applied to solve this problem, the transformation of the partial differential equation (1*a*) into an ordinary differential equation in the variable t is not readily possible because the integral transform kernel depends on t; hence the right-hand side of equation (1*a*) can not be transformed into a derivative with re-

[1] Numbers in brackets designate References at end of paper.

Contributed by the Heat Transfer Division for publication in the JOURNAL OF HEAT TRANSFER. Manuscript received by the Heat Transfer Division, July 5, 1973. Paper No. 74-HT-I.

spect to t of the integral transform of the function.

To solve the foregoing boundary value problem the appropriate eigenvalue problem is taken as

$$\nabla\cdot[k(\underline{r})\nabla\psi(\underline{r},t)] + c(\underline{r})\psi(\underline{r},t) + \lambda^2(t)w(\underline{r})\psi(\underline{r},t) = 0 \text{ in region } R, \quad (2a)$$

subject to the boundary condition

$$k(\underline{r}_s)\frac{\partial\psi(\underline{r}_s,t)}{\partial n} + h(\underline{r}_s,t)\psi(\underline{r}_s,t) = 0 \text{ on boundary } s. \quad (2b)$$

Here the eigenfunctions and eigenvalues depend on t because $h(\underline{r}_s,t)$ depends on t. It can readily be shown that these eigenfunctions are orthogonal with respect to the weight function $w(\underline{r})$ as

$$\int_R w(\underline{r})\psi_m(\underline{r},t)\psi_n(\underline{r},t)dv = 0 \text{ for } m \neq n \quad (3)$$

where the integration is over the region R.

The function $u(\underline{r}, t)$ can be expanded in terms of the eigenfunction $\psi_m(\underline{r}, t)$ over the region R in the form

$$u(\underline{r},t) = \sum_m a_m(t)\psi_m(\underline{r},t) \quad (4a)$$

and the expansion coefficients $a_m(t)$ are determined by utilizing the foregoing orthogonality conditions as

$$a_m(t) = \frac{1}{N_m(t)}\int_R w(\underline{r})\psi_m(\underline{r},t)u(\underline{r},t)dv \quad (4b)$$

where

$$N_m(t) \equiv \int_R w(\underline{r})\psi_m^2(\underline{r},t)dv \quad (4c)$$

For convenience in the subsequent analysis the expansion given by equations (4) is now rewritten as the finite integral transform and the inversion of the function $u(\underline{r}, t)$ developed in the forms

$$\text{Transform: } \bar{u}_m(t) = \int_R w(\underline{r}')K_m(\underline{r}',t)u(\underline{r}',t)dv' \quad (5a)$$

$$\text{Inversion: } u(\underline{r},t) = \sum_m K_m(\underline{r},t)\bar{u}_m(t) \quad (5b)$$

where the kernel $K_m(\underline{r}, t)$ is the normalized eigenfunction

$$K_m(\underline{r},t) = \frac{\psi_m(\underline{r},t)}{\sqrt{N_m(t)}} \quad (5c)$$

and $N_m(t)$ has been defined previously.

The integral transform and the inversion as defined by equation (5) will now be utilized to solve the boundary value problem given by equation (1). Equation (1a) is multiplied by $K_m(\underline{r}, t)$ and integrated over the region R to yield

$$\int_R K_m(\underline{r},t)\nabla\cdot[k(\underline{r})\nabla u(\underline{r},t)]dv + \int_R c(\underline{r})K_m(\underline{r},t)u(\underline{r},t)dv + \int_R K_m(\underline{r},t)g(\underline{r},t)dv = \int_R w(\underline{r})K_m(\underline{r},t)\frac{\partial u(\underline{r},t)}{\partial t} \quad (6)$$

The first integral on the left-hand side of equation (6) can be written in the alternative form as

$$\int_R K_m(\underline{r},t)\nabla\cdot[k(\underline{r})\nabla u(\underline{r},t)]dv = \int_R u(\underline{r},t)\nabla\cdot[k(\underline{r})\nabla K_m(\underline{r},t)]dv + \int_S k(\underline{r}_s)\left[K_m(\underline{r}_s,t)\frac{\partial u(\underline{r}_s,t)}{\partial n} - u(\underline{r}_s,t)\frac{\partial K_m(\underline{r}_s,t)}{\partial n}\right]ds \quad (7)$$

This result is obtained by integrating the identity $K_m\nabla\cdot(k\nabla u) = u\nabla\cdot(k\nabla K_m) + \nabla\cdot[k(K_m\nabla u - u\nabla K_m)]$ over the region R and by changing the volume integral to a surface integral. By utilizing the eigenvalue problem given by equation (2a), the integrand of the first integral on the right-hand side of equation (7) becomes

$$u(\underline{r},t)\nabla\cdot[k(\underline{r})\nabla\cdot K_m(\underline{r},t)] = -c(\underline{r})K_m(\underline{r},t)u(\underline{r},t) - \lambda_m^2(t)w(\underline{r})K_m(\underline{r},t)u(\underline{r},t) \quad (8)$$

By making use of the boundary conditions equations (1b) and (2b), the integrand of the second integral on the right-hand side of equation (7) can be determined.

$$k(\underline{r}_s)\left[K_m(\underline{r}_s,t)\frac{\partial u(\underline{r}_s,t)}{\partial n} - u(\underline{r}_s,t)\frac{\partial K_m(\underline{r}_s,t)}{\partial n}\right] = K_m(\underline{r}_s,t)f(\underline{r}_s,t) \quad (9)$$

Substitution of equations (8) and (9) on the right-hand side of equation (7) and utilizing the definition of the transform as given by equation (5a) yields

$$\int_R K_m(\underline{r},t)\nabla\cdot[k(\underline{r})\nabla u(\underline{r},t)]dv = -\int_R c(\underline{r})K_m(\underline{r},t)u(\underline{r},t)dv - \lambda_m^2(t)\bar{u}_m(t) + \int_S K_m(\underline{r}_s,t)f(\underline{r}_s,t)ds \quad (10)$$

and the substitution of equation (10) into equation (6) gives

$$Z_m(t) + \lambda_m^2(t)\bar{u}_m(t) = A_m(t) \quad (11a)$$

where we have defined

$$Z_m(t) \equiv \int_R w(\underline{r})K_m(\underline{r},t)\frac{\partial u(\underline{r},t)}{\partial t}dv \quad (11b)$$

$$A_m(t) \equiv \int_S K_m(\underline{r}_s,t)f(\underline{r}_s,t)ds + \int_R K_m(\underline{r},t)g(\underline{r},t)dv \quad (11c)$$

The integral transform of the initial condition equations (1c) becomes

$$\bar{u}_m(t) = \int_R w(\underline{r})K_m(\underline{r},t)F(\underline{r})dv \equiv \bar{F}_m(0) \text{ for } t = 0 \quad (12)$$

If the eigenfunctions and the eigenvalues were independent of time, i.e., $h(\underline{r}, t)$ were independent of time, the equation (11a) would be an ordinary differential equation for $\bar{u}_m(t)$ and could be readily solved with the initial condition equation (12). Knowing $\bar{u}_m(t)$, the function $u(\underline{r}, t)$ could be determined by the inversion formula equation (5b). In the present analysis, however, this is not possible because $Z_m(t)$ given by equation (11b) cannot be written as $d\bar{u}_m(t)/dt$. In order to express $Z_m(t)$ in terms of $\bar{u}_m(t)$, we consider the eventual solution given by the inversion formula as

$$u(\underline{r},t) = \sum_n K_n(\underline{r},t)\bar{u}_n(t) \quad (13)$$

and substitute this relation in equation (11b)

$$Z_m(t) \equiv \int_R w(\underline{r})K_m(\underline{r},t)\frac{\partial}{\partial t}\left[\sum_n K_n(\underline{r},t)\bar{u}_n(t)\right]dv \quad (14a)$$

We perform the differentiation with respect to t on the right-hand side of equation (14) and obtain

$$Z_m(t) \equiv \sum_n \frac{d\bar{u}_n(t)}{dt}\int_R wK_mK_n dv + \sum_n \bar{u}_n(t)\int_R wK_m\frac{\partial K_n}{\partial t}dv \quad (14b)$$

or

$$Z_m(t) = \frac{d\bar{u}_m(t)}{dt} + \sum_n \bar{u}_n(t)\int_R wK_m\frac{\partial K_n}{\partial t}dv \quad (14c)$$

since $\int_v wK_mK_n\,dv = \delta_{mn}$ by equation (3), where δ_{mn} is the kronecker delta. Equation (15b) can be written in the alternative form as

$$Z_m(t) = \frac{d\bar{u}_m(t)}{dt} - \sum_n \bar{u}_n(t)\int_R wK_n\frac{\partial K_m}{\partial t}dv \quad (14d)$$

since it can be shown that

$$\int_R wK_m\frac{\partial K_n}{\partial t}dv = -\int_R wK_n\frac{\partial K_m}{\partial t}dv \quad (15)$$

from the relations

$$\frac{\partial}{\partial t}\left[K_m(\underline{r},t)K_n(\underline{r},t)\right] = K_m(\underline{r},t)\frac{\partial K_n(\underline{r},t)}{\partial t} + K_n(\underline{r},t)\frac{\partial K_m(\underline{r},t)}{\partial t} \tag{16a}$$

and

$$\int_v w K_m K_n dv = \delta_{mn} \tag{16b}$$

When equation (14*d*) is introduced into equation (11*a*), the following set of coupled ordinary differential equations are obtained for the transform $\bar{u}_m(t)$:

$$\frac{d\bar{u}_m(t)}{dt} + \lambda_m^2(t)\bar{u}_m(t) - \sum_{n=1}^{\infty}\bar{u}_n(t)\bar{B}_{nm}(t) = A_m(t) \tag{17a}$$

subject to the conditions

$$\bar{u}_m(t) = \bar{F}_m(0) \text{ for } t = 0, \tag{17b}$$

where $m = 1, 2, 3, \ldots$, and various quantities are defined as

$$A_m(t) \equiv \int_S K_m(\underline{r}_s,t)f(\underline{r}_s,t)ds + \int_R K_m(\underline{r},t)g(\underline{r},t)dv \tag{18a}$$

$$\bar{F}_m(0) \equiv \int_R w(\underline{r})K_m(\underline{r},0)F(\underline{r})dv \tag{18b}$$

$$\bar{B}_{nm}(t) \equiv \int_R w(\underline{r})K_n(\underline{r},t)\frac{\partial K_m(\underline{r},t)}{\partial t}dv \tag{18c}$$

We note the following properties of functions $\bar{B}_{nm}(t)$:

$$\bar{B}_{nm}(t) = -\bar{B}_{mn}(t) \tag{19a}$$

$$\bar{B}_{mm}(t) = 0 \text{ for } n = m. \tag{19b}$$

The formal solution of the problem can now be considered as complete. Once the functions $\bar{u}(t)$ are determined from the solution of simultaneous equations (17), the desired function $u(\underline{r}, t)$ is immediately obtained by the inversion formula, equation (5*a*). However, in practice, it is not possible to solve an infinite number of simultaneous ordinary differential equations; but analytical approximations can be obtained by taking only a finite number of terms in the summation in equation (17). Therefore, an *s-order approximation* is obtained by taking s number of terms in the summation in equation (17); that is

$$\frac{d\bar{u}_m(t)}{dt} + \lambda_m^2(t)\bar{u}_m(t) - \sum_{n=1}^{s}\bar{u}_n(t)\bar{B}_{nm}(t) = A_m(t), \tag{20}$$

$$m = 1,2,3,\ldots,\infty$$

which should be solved subject to the conditions give by equation (17*b*) for $t = 0$.

The *zeroth order* solution is obtainable by neglecting the summation entirely (i.e., $s = 0$) in equation (20), the *first order* solution is obtainable by taking the first term in the series (i.e., $s = 1$), etc. We note that simple analytical solutions are obtainable for $\bar{u}_m$ for the cases $s = 0$ and 1. For values of s larger than one, the first s equations (i.e., $m = 1, 2, \ldots, s$) in equation (20) are coupled and to be solved simultaneously, the remaining equations $m = s + 1, s + 2, \ldots \infty$ are uncoupled. Once these equations are solved and the integral transforms $\bar{u}_m(t)$, $m = 1, 2, \ldots, s, \ldots, \infty$ are determined, the function $u(\underline{r}, t)$ is obtained by the inversion formula given by equation (5*a*).

It is convenient to separate the coupled and uncoupled groups on equation (17) and write them in the matrix form as:

For $m = 1, 2, \ldots, s$

$$\frac{d\bar{\mathbf{u}}(t)}{dt} + \Lambda\bar{\mathbf{u}}(t) = \mathbf{A}(t) \tag{21a}$$

$$\bar{\mathbf{u}}(0) = \bar{\mathbf{F}}(0) \tag{21b}$$

where various matrices and vectors are defined as

$$\Lambda \equiv \begin{bmatrix} \lambda^2 & B_{12} & \ldots\ldots & B_{1s} \\ B_{21} & \lambda_2^2 & \ldots\ldots & B_{2s} \\ \cdot & & & \\ \cdot & & & \\ \cdot & & & \\ B_{s1} & B_{s2} & \ldots\ldots & \lambda_s^2 \end{bmatrix}, \tag{21c}$$

$$\bar{\mathbf{u}}(t) \equiv \begin{bmatrix} \bar{u}_1(t) \\ \bar{u}_2(t) \\ \cdot \\ \cdot \\ \cdot \\ \bar{u}_s(t) \end{bmatrix}, \quad \mathbf{A}(t) \equiv \begin{bmatrix} A_1(t) \\ A_2(t) \\ \cdot \\ \cdot \\ \cdot \\ A_s(t) \end{bmatrix}, \quad \bar{\mathbf{F}}(0) \equiv \begin{bmatrix} \bar{F}_1(0) \\ \bar{F}_2(0) \\ \cdot \\ \cdot \\ \cdot \\ \bar{F}_s(0) \end{bmatrix}, \tag{22}$$

For $m = s + 1, s + 2, \ldots, \infty$:

$$\frac{d\bar{u}_m(t)}{dt} + \lambda_m^2(t)\bar{u}_m(t) = c_m(t) \tag{23a}$$

$$\bar{u}_m(0) = \bar{F}_m(0) \tag{23b}$$

where

$$c_m(t) \equiv A_m(t) + \sum_{n=1}^{s}\bar{u}_n(t)B_{nm}(t) \tag{23c}$$

In the foregoing system of equations, the coupled equations (21) are first solved simultaneously and the transform $\bar{u}_n(t)$, $n = 1, 2, \ldots, s$ is determined. Then the functions $c_m(t)$ on the right-hand side of equations (23) are considered known, and the solution of equations (23) is written as

$$\bar{u}_m(t) = \bar{F}_m(0)e^{-\int_0^t \lambda_m^2(t')dt'} + \int_0^t c_m(t')e^{-\int_{t'}^t \lambda_m^2(t'')dt''}dt'$$

for $m = s + 1, s + 2, \ldots, \infty$: (24)

Knowing the transforms $\bar{u}_m(t)$, $m = 1, 2, \ldots, \infty$, the function $u(r, t)$ is obtained by the inversion formula given by equation (5*b*).

For example, the zeroth order solution $u^{(0)}(r, t)$ is given by

$$u^{(0)}(\underline{r},t) = \sum_{m=1}^{\infty}K_m(\underline{r},t)\left[\bar{F}_m(0)e^{-\int_0^t \lambda_m^2(t')dt'} + \int_0^t A_m(t')e^{-\int_{t'}^t \lambda_m^2(t'')dt''}dt'\right] \tag{25}$$

and the first order solution $u^{(1)}(\underline{r}, t)$ is given by

$$u^{(1)}(\underline{r},t) = u^{(0)}(\underline{r},t) + \sum_{m=2}^{\infty}K_m(\underline{r},t)\int_0^t E(t')B_{1m}(t')e^{-\int_{t'}^t \lambda_m^2(t'')dt''}dt' \tag{26a}$$

where

$$E(t') \equiv \bar{F}_1(0)e^{-\int_0^t \lambda_1^2(t')dt'} + \int_0^t A_1(t')e^{-\int_{t'}^t \lambda_1^2(t'')dt''}dt' \tag{26b}$$

Thus simple analytical results are obtainable for the zeroth and first order solutions, but explicit results cannot be given for the higher order solutions because the equations are coupled.

Acknowledgment

This work was supported in part by the National Science Foundation through grant GK-41605.

References

1 Morse, P. M., and Feshbach, H., *Methods of Theoretical Physics*, McGraw-Hill, New York, 1953.

2 Carslaw, H. S., and Jaeger, J. C., *Conduction of Heat in Solids*, Oxford University Press, London, 1959.

3 Davison, B., *Neutron Transport Theory*, Oxford at the Clarendon Press, London, 1957.

4 Weinberg, A. M., and Wigner, E. P., *The Physical Theory of Neutron Chain Reactors*, The University of Chicago Press, Chicago, 1958.

5 Sneddon, I. N., *Fourier Transforms*, McGraw-Hill, New York, 1951.

6 Tranter, C. J., *Integral Transforms in Mathematical Physics,* Oxford University Press, London, 1958.

7 Ölcer, N. Y., "On the Theory of Conductive Heat Transfer in Finite Regions," *International Journal of Heat and Mass Transfer*, Vol. 7, 1964, p. 304.

8 Özişik, M. N., *Boundary Value Problems of Heat Conduction,* International Textbook Co., Scranton, Pa., 1968.

9 Thompson, J. J., and Holy, Z. J., "Axisymetric Thermal Response Problems for a Spherical Fuel Element With Time Dependent Heat Transfer Coefficient," *Nuclear Engineering and Design,* Vol. 9, 1969, pp. 29–44.

10 Holy, Z. J., "Temperature and Stresses in Reactor Fuel Elements Due to Time- and Space-dependent Heat-transfer Coefficient," *Nuclear Engineering and Design,* Vol. 18, 1972, pp. 145–197.

11 Ivanov, V. V., and Salomatov, V. V., "On the Calculation of the Temperature Fields in Solids With Variable Heat-Transfer Coefficients," *Inzhenerno-Fizicheskii Zhurnal,* Vol. 9, 1965, pp. 83–85

C. K. Chan
Research Assistant.

C. L. Tien
Professor.

Department of Mechanical Engineering,
University of California,
Berkeley, Calif.

Radiative Transfer in Packed Spheres

Radiative transfer through a packed bed of microspheres is analyzed on the basis of a new conceptual model, which combines the continuous and discontinuous models in predicting the scattering and absorption properties of packed microspheres. The basic elements of the formulation consist of the determination of the scattering diagram of a unit cell, the optical properties of a series of thin microsphere layers, and the solution of the two-flux equations. Results show a strong dependence of these radiative properties on the particle diameter and emissivity. Qualitative agreement is shown in the comparison of the predictions with existing experimental data.

Introduction

Radiative transfer through packed spheres has long been a subject of great importance in the performance evaluation of packed-sphere insulation and pigment coatings. Accurate prediction methods are particularly needed in high-performance cryogenic insulations [1, 2].[1] In the new microsphere insulation [2, 3] that consists of packed hollow dielectric microspheres (20 to 200μ in. dia) with a highly reflective metallic coating of about 400 Å thick, the major heat transfer mechanisms are radiative transfer through voids and conduction through the contact spheres. The present paper is concerned with the prediction of the radiation contribution, while an earlier paper [4] analyzes the conduction problem.

General Consideration

The radiant intensity through a slab of packed spheres or powder is attenuated by particle absorption and scattering, and is augmented by particle emission. Two different analytical models have been commonly employed to describe the radiation transport in such a dispersed medium. The medium can be regarded either as continuous, having homogeneous and isotropic properties, or as discontinuous, being composed of a series of discrete layers whose thicknesses are determined by the size of the particles [5].

In the continuum model, three parameters, namely, the scattering and absorption coefficients and the phase function, are required to describe the radiative transfer in an absorbing and anisotropic scattering medium. Attempts have been made to solve the transfer problem by introducing the Mie solution for single particle scattering into the radiative transport equation [6]. However, when the particles are tightly packed, as in the case of microsphere insulation, the transport equation with the Mie solution is no longer valid because of dependent scattering [7].

For a sufficiently thick slab of packed particles, an isotropic distribution of scattered intensity always exists inside the medium [5]. This observation implies that scattering and absorption in radiant transport can be characterized by only two parameters instead of three. Assuming the existence of two discrete fluxes inside the medium (i.e., two-flux model), one forward and the other backward, and after making an energy balance on an infinitesimal layer of thickness dx_3, the fluxes are given by the following pair of equations [8]:

$$\frac{dq^+}{dx_3} = -(K + S)\, q^+ + Sq^- \tag{1}$$

$$-\frac{dq^-}{dx_3} = -(K + S)\, q^- + Sq^+ \tag{2}$$

where x_3 is the coordinate perpendicular to the boundary plane of the slab, q^+ and q^- are the radiant fluxes in the positive and negative x_3 directions and K and S are the apparent absorption and scattering parameters. The parameters K and S are empirical in nature and should not be interpreted in terms of the scattering and absorption coefficients in the transport equation, although a similar form of equations (1) and (2) can be derived from the transport equation by assuming semi-isotropic intensity in the positive and negative directions [9].

As shown by Kubelka [10], the transmittance τ and the reflectance ρ of a slab of packed particles having a finite thickness L can be found by solving the two-flux equations with the boundary conditions:

$$q^+ = q_0^+ \qquad (x_3 = 0) \tag{3}$$

$$q^- = 0 \qquad (x_3 = L) \tag{4}$$

The results are:

[1] Numbers in brackets designate References at end of paper.

Contributed by the Heat Transfer Division for publication in the JOURNAL OF HEAT TRANSFER. Manuscript received by the Heat Transfer Division, May 3, 1973. Paper No. 74-HT-O.

$$\tau = \frac{2\beta_0}{(1 + \beta_0^2)\sin h\sigma_0 L + 2\beta_0 \cos h\sigma_0 L} \quad (5)$$

$$\rho = \frac{(1 - \beta_0^2)\sin h\sigma_0 L}{(1 + \beta_0^2)\sin h\sigma_0 L + 2\beta_0 \cos h\sigma_0 L} \quad (6)$$

where

$$\beta_0 = \left(\frac{K}{K + 2S}\right)^{1/2} \quad (7)$$

$$\sigma_0 = [K(K + 2S)]^{1/2} \quad (8)$$

The parameters K and S of a given sample can be determined by measuring either the transmittances or the reflectances of two different sample thicknesses. But both of these methods encounter certain technical difficulties. For instance, in order to obtain measurable transmission data, a thin-layer sample has to be used in the measurements [11]. If the layer is only a few particles thick, a portion of radiant energy can be transmitted directly without interacting with the particles. This direct radiative transfer would not fulfill the diffuse assumption of the two-flux model. On the other hand, reflectance measurements on finite sample thicknesses do not yield the substantial differences in reflectances which are necessary to determine accurately the parameters [5].

Due to the homogeneity assumption of the continuous model, there is no direct relation between the flux parameters and the properties of the medium such as void fraction, particle size, and surface reflectance of the particles. The relationship, however, can be established by considering the discontinuous model, in which the slab of particles is regarded as a series of plane parallel layers. The thickness of these layers depends on the particle size and their packing arrangement. From thin film optics it is well known that the transmittance and reflectance of a whole series of layers can be expressed in terms of the transmittance and reflectance of the individual layers.

One of the key elements of the present study is the new concept of relating the continuous and discontinuous models so that the bulk properties, such as the apparent absorption and scattering parameters of the medium, can be determined from the physical and optical properties of the constituent particles and other system paramters. In order that a packed medium can be described by both models, two conditions must be fulfilled. First, the particle diameter must be small in comparison to the layer thickness, so that the medium can be considered homogeneous. Second, the particle diameter has to be large compared to the characteristic wavelength of the radiation so that the slab can be divided into optical layers. For opaque microspheres of normal insulation thickness, these two conditions are fulfilled even though the cold boundary temperature is extremely low (say 4 deg K).

In the present analysis the radiative properties are assumed to be gray and temperature independent, and other secondary radiation phenomena, such as polarization and diffraction, are neglected. The fundamental formulations and concepts, however, are not restricted to these conditions.

Analysis

Physical Model. The physical model consists of an infinite slab of identical metal-coated microspheres packed in a simple cubic arrangement. The slab is n-particle thick and is divided into parallel planar layers (Fig. 1). Each layer is defined by the center-to-center distance between two planes of contacting spheres. The slab is bounded by two half layers, one at the top and the other at the bottom. The layers are subdivided into identical unit cells as shown in Fig. 1. The void volume in each cell is enclosed by sections of solid spherical surfaces and of imaginary planar openings. Therefore, for layers within the slab, the void space is bounded by fourteen surfaces and for the half layers it is bounded by ten surfaces.

Scattering and Absorption of a Unit Cell. Under the present consideration, a diffuse radiation flux enters the void of the unit cell through one of the planar openings as shown in Fig. 2. Since inside the enclosure the refractive index of the solid surface differs from that of the void space and the physical dimension of the cell is large in comparison to the incident wavelength, it is possible to distinguish rays striking various parts of the surface. The incident ray is reflected with some of its energy absorbed by the surfaces. For specularly reflecting surfaces, the path of an incident ray within the unit cell can be traced by means of geometrical optics until the ray escapes through one of the openings. An opening can be regarded as a black surface that absorbs all the energy passing through it. By tracing a large number of incident

Nomenclature

a_1, a_2, a_3 = coordinates of the origin of the ray vector
b, b_1, b_2, b_3 = backward component in flux diagrams
d = distance between two points
D = sphere diameter
$\hat{e}_i$ = unit vector in the x_i direction
E_0 = incident flux
$E_1, E_2, E_3, E_4, E_5, E_6$ = orthogonal flux components inside a layer
E_r = energy carried by a ray
f, f_1, f_2, f_3 = forward component in flux diagrams
h_i = mathematical function of surface i
$\hat{i}$ = ray vector
K = apparent absorption parameters
l_1, l_2, l_3 = directional cosines of an incident vector
l_1', l_2', l_3' = directional cosines of a reflected vector
L = insulation thickness
n = number of layers
$\hat{n}$ = unit normal vector
n_i = the component of the normal vector in the x_i direction
N = number of particles per unit volume
q^+, q^- = radiant heat fluxes in the positive and negative x_3 direction, respectively
q^+_0 = q^+ at the boundary $x_3 = 0$
s_1', s_2', s_3' = coordinates of the sphere center
$s, s_1, s_2, s_3, s_{35}, s_{36}$ = sidewise component in flux diagrams
S = apparent scattering parameter
v_s = sphere volume
x_1, x_2, x_3 = Cartesian coordinates
x_1', x_2', x_3' = coordinates of the intersecting point
y = $(1 + \rho^2 - \tau^2)$
α = absorptance
β_0 = $[K/(K + 2S)]^{1/2}$
δ_S = solid fraction
ϵ_p = emissivity of particle surface
θ = polar angle
Π = defined in equation (45)
ρ = reflectance
ρ_p = reflectivity of particle surface
σ_0 = $[K(K + 2S)]^{1/2}$
τ = transmittance
ϕ = azimuthal angle
$\omega_0, \omega_{01}, \omega_{02}, \omega_{03}$ = fraction of the incident energy scattered for different flux diagrams
$\Delta\omega$ = differential solid angle

Subscript

l = layer, $l = 1$ for layer 1, $l = 2$ for layer 2, $l = 12$ for combined layers 1 and 2, etc.

Superscript

= reversed direction

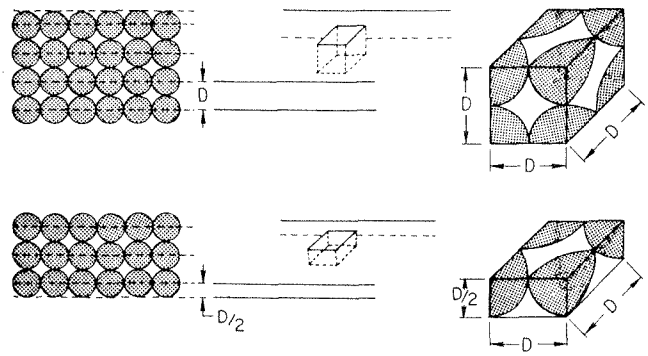

Fig. 1 Analytical model: *(a)* packed spheres, *(b)* regular and half layers, *(c)* unit cell

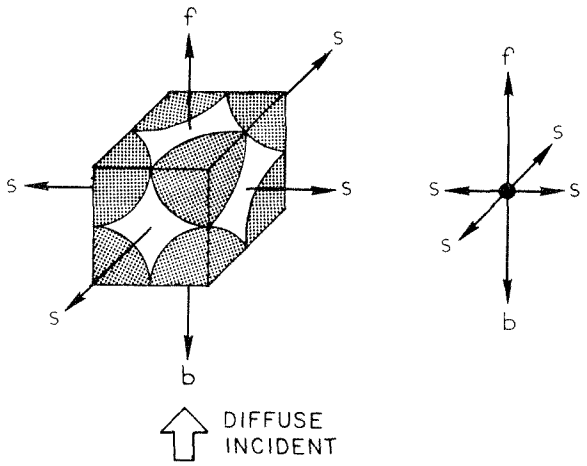

Fig. 2 Flux diagram of a unit cell in a regular layer

rays, the scattering and absorption of the unit cell can be described by the distribution of the incident energy on each of the enclosure surfaces. A convenient representation of the distribution would be a flux diagram with six components (Fig. 2). For layers within the slab this diagram will be the same for energy incident on each of the six openings of the cube. The forward component f, the backward component b, and four equal sidewise components s represent the fractions of the incident energy reaching the planar openings at the top, the bottom, and at the four sides, respectively. If $(1 - \omega_0)$ is the fraction of the incident energy which is absorbed, then from conservation of energy, f, b, s, and ω_0 are related as:

$$f + b + 4s = \omega_0 \tag{9}$$

For the unit cell of the half layer, the energy distribution on the enclosing surfaces depends on the opening through which the incident energy passed. As a result, three flux diagrams, rather than one, are required (see Fig. 3).

The determination of the flux diagrams is a problem of radiant interchange inside an enclosure. Except for certain simple geometries [12], the general problem of the radiant interchange among curved reflecting surfaces in an enclosure is very complicated. Solutions have been obtained by using a probabilistic model of the radiative process and Monte Carlo sampling techniques [13]. The main disadvantage of the Monte Carlo method is the excessive computer time required. Recent approaches include an extension of the image method originally developed for planar specular surfaces to general nonplanar surfaces [14], and an analytical attempt involving the transformation and mapping of the reflecting surface [15]. However, these analytical methods are restricted to a single reflector and receiver system.

In the present study, a deterministic model of the radiative process is developed. A ray can be viewed as a bound vector carrying a certain amount of energy E_r in the three-dimensional space. The vector is specified by an initial point (a_1, a_2, a_3) and the directional cosines (l_1, l_2, l_3) of a line segment. The quantities (l_1, l_2, l_3) are the cosines of the angles between the line segment and the fixed Cartesian axes x_1, x_2, x_3. Each of the enclosure surfaces is analytically represented by a mathematical function:

$$h_i(x_1, x_2, x_3) = 0 \qquad i = 1, 2, \ldots \rho \tag{10}$$

where p is the total number of surfaces inside the enclosure. For a smooth surface, $h_i(x_1, x_2, x_3)$ is a continuous function specified in some closed region. The boundary of the region depends on the intersection of neighboring surfaces. The intersecting point (x_1', x_2', x_3') between the unit ray vector $\hat{i}$ and the surface j can be determined by the following relations:

$$x_1' - a_1 = l_1 d \tag{11}$$

$$x_2' - a_2 = l_2 d \tag{12}$$

$$x_3' - a_3 = l_3 d \tag{13}$$

$$h_j(x_1', x_2', x_3') = 0 \tag{14}$$

where d is the distance between the initial and the intersecting point:

$$d = \left[\sum_{i=1}^{3} (x_i' - a_i)^2 \right]^{1/2} \tag{15}$$

since

$$\sum_{i=1}^{3} l_i^{\,2} = 1 \tag{16}$$

The ray would strike the surface j if there exist a set of real values x_1', x_2', x_3', and d that satisfy equations (11) to (15) and the two additional conditions: *(a)* d be strictly positive and *(b)* the point (x_1', x_2', x_3') lie in the defined region of the surface. However, there may exist more than one set of feasible solutions that satisfy all the requirements for certain rays and certain enclosure geometries. The reason for this nonuniqueness is simply that the ray can mathematically intersect one physical surface at more than one point or it can intersect with more than one surface inside the enclosure. For opaque surface, the set of feasible solutions with the minimum distance d is the physical intersecting point.

Rays incident on a specular surface are reflected according to the following fundamental laws of geometrical optics: *(a)* the angle of reflection is equal to the angle of incidence; and *(b)* the incident ray, the surface normal at the intersecting point, and the reflected ray all lie on the same plane. These two laws are sufficient to determine the directional cosines l_1', l_2', l_3' of the reflected ray, giving

$$l_i' = l_i - 2n_i \sum_{k=1}^{3} n_k l_k \qquad i = 1, 2, 3 \tag{17}$$

where n_i is the component of the unit vector $\hat{n}$ at the point of in-

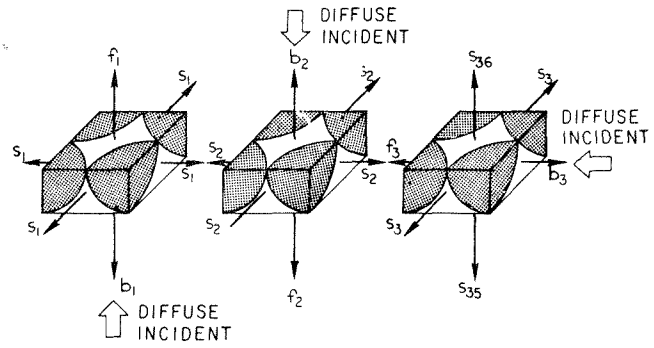

Fig. 3 Flux diagrams of a unit cell in a half layer

tersection and $\hat{n}$ is given by

$$\hat{n} = \frac{\text{grad } h_j(x_1', x_2', x_3')}{|\text{grad } h_j(x_1', x_2', x_3')|} \tag{18}$$

The reflected ray carries $\rho_p E_r$ amount of energy where ρ_p is the reflectivity of the surface. The remaining energy $E_r(1 - \rho_p)$ is absorbed by the surface. The initial point of the reflected vector is (x_1', x_2', x_3'). The process is repeated until either the ray has lost most of its energy by multiple reflections or it hits one of the open surfaces of the unit cell.

Optical Properties of a Single Layer. On passing through a layer of unit cells, the diffuse incident flux will be absorbed and multiply reflected. The optical properties of the layer are the transmittance τ_l, the reflectance ρ_l, and the absorptance α_l. By definition, their sum is equal to unity, i.e.,

$$\tau_l + \rho_l + \alpha_l = 1 \tag{19}$$

Because of the geometrical symmetry, the transmittance and reflectance of a regular layer for both forward and backward directed incident radiation are the same. The layer is thus said to be homogeneous. On the other hand, the optical behavior of the half layer at the boundary of the slab depends on whether forward or backward directed radiation is considered. This layer is thus said to be nonhomogeneous. The reflection and absorption characteristics of such a layer must be defined by two sets of optical properties; one for the forward, and the other for the backward directed incident radiation.

The flux within a layer (regular or half) is represented by six orthogonal components E_1, E_2, E_3, E_4, E_5, and E_6, which are the components opposite and parallel to the fixed Cartesian axes x_1, x_2, and x_3, respectively (Fig. 4). By symmetry, E_1, E_2, E_3, and E_4 are equal to each other and constant throughout the layer. Making an energy balance in the six directions of a unit cell inside the homogeneous layer yields the following equations when only one face of the layer is irradiated:

$$E_6 = E_0 f + (E_1 + E_2 + E_3 + E_4)s \tag{20}$$

$$E_5 = E_0 b + (E_1 + E_2 + E_3 + E_4)s \tag{21}$$

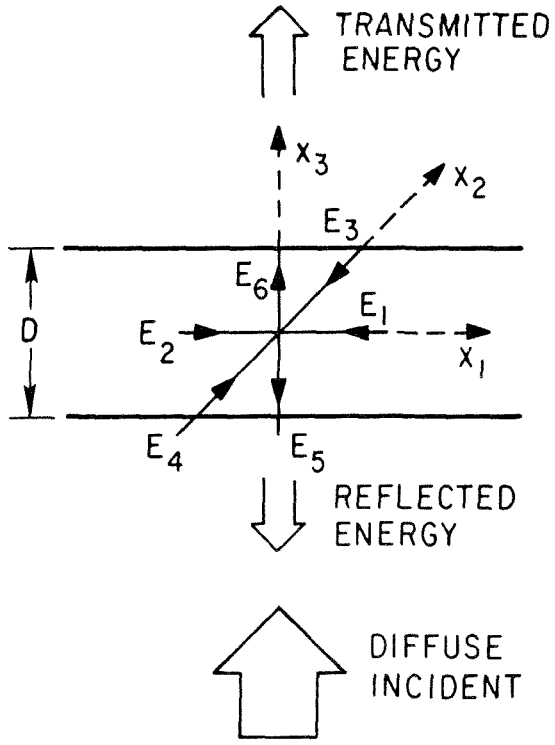

Fig. 4 Six-component representation of radiant flux inside a layer

$$E_1 = E_1 f + E_2 b + E_3 s + E_4 s + E_0 s \tag{22}$$

$$E_2 = E_2 f + E_1 b + E_3 s + E_4 s + E_0 s \tag{23}$$

$$E_3 = E_3 f + E_4 b + E_1 s + E_2 s + E_0 s \tag{24}$$

$$E_4 = E_4 f + E_3 b + E_1 s + E_2 s + E_0 s \tag{25}$$

where E_0 is the incident flux and f, b, and s are the components of the flux diagram (Fig. 2). The solution of equations (20) through (25) can be written as

$$E_1 = E_2 = E_3 = E_4 = \frac{sE_0}{1 - f - b - 2s} \tag{26}$$

$$E_5 = \left(b + \frac{4s^2}{1 - f - b - 2s}\right) E_0 \tag{27}$$

$$E_6 = \left(f + \frac{4s^2}{1 - f - b - 2s}\right) E_0 \tag{28}$$

The transmittance τ_l, reflectance ρ_l, and absorptance α_l of the layer are defined by

$$\tau_l = \frac{E_6}{E_0} = f + \frac{4s^2}{1 - f - b - 2s} \tag{29}$$

$$\rho_l = \frac{E_5}{E_0} = b + \frac{4s^2}{1 - f - b - 2s} \tag{30}$$

$$\alpha_l = \frac{(1 - \omega_0)(E_0 + E_1 + E_2 + E_3 + E_4)}{E_0} = (1 - \omega_0)\left[1 + \frac{4s}{1 - f - b - 2s}\right] \tag{31}$$

Through a similar process, the two sets of optical properties of the half layer can be expressed in terms of the components of the flux diagram shown in Fig. 3. For radiation from the negative x_3 direction, the transmittance and the reflectance of the half layer are at the lower slab boundary

$$\tau_l = f_1 + \frac{4s_1 s_{36}}{1 - f_3 - b_3 - 2s_3} \tag{32}$$

$$\rho_l = b_1 + \frac{4s_1 s_{35}}{1 - f_3 - b_3 - 2s_3} \tag{33}$$

and for radiation from the positive x_3 direction, the transmittance τ_l' and the reflectance ρ_l' are given as:

$$\tau_l' = f_2 + \frac{4s_2 s_{35}}{1 - f_3 - b_3 - 2s_3} \tag{34}$$

$$\rho_l' = b_2 + \frac{4s_2 s_{36}}{1 - f_3 - b_3 - 2s_3} \tag{35}$$

where f_1, b_1, s_1, f_2, b_2, s_2, f_3, b_3, s_3, s_{35}, and s_{36} are the flux components defined in Fig. 3.

Optical Properties of a Slab. The path of the diffuse radiation for a combination of two layers may be represented schematically by Fig. 5. The general case of two nonhomogeneous layers will now be considered. The optical properties for irradiation from the negative x_3 direction are denoted by a superscript prime. The radiant energy incident on surface 1 from below is partially reflected (ρ_1), partially absorbed (α_1), and partially transmitted (τ_1) by the first layer. Of the transmitted fraction (τ_1) falling on layer 2, $\tau_1\rho_2$ is reflected back to layer 1 and $\tau_1\tau_2$ is transmitted through the second layer. When $\tau_1\rho_2$ reaches layer 1, the new fraction $\tau_1\rho_2\tau_1'$ is transmitted and $\tau_1\rho_2\rho_1'$ reflected etc., as indicated in Fig. 6. By summing the transmitted and reflected fractions, the transmittance and reflectance of the combined layer 12 are

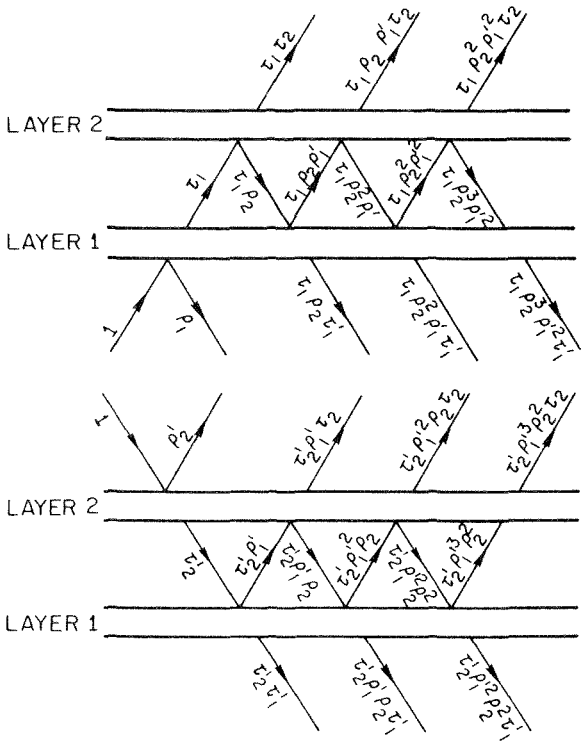

Fig. 5 Reflectance and transmittance of two nonhomogeneous layers *(a)* incident radiation on layer 1, *(b)* incident radiation on layer 2

$$\tau_{12} = \frac{\tau_1 \tau_2}{1 - \rho_2 \rho_1'} \tag{36}$$

$$\rho_{12} = \rho_1 + \frac{\tau_1 \tau_1' \rho_2}{1 - \rho_2 \rho_1'} \tag{37}$$

The corresponding equations for radiation incident on layer 2 from the positive x_3 direction are

$$\tau_{21}' = \frac{\tau_1' \tau_2'}{1 - \rho_2 \rho_1'} \tag{38}$$

$$\rho_{21}' = \rho_2' + \frac{\tau_2 \tau_2' \rho_1'}{1 - \rho_2 \rho_1'} \tag{39}$$

where τ_1, τ_1', ρ_1, ρ_1'; τ_2, τ_2', ρ_2, ρ_2'; τ_{12}, τ_{21}', ρ_{12}, ρ_{21}', the transmittances and the reflectances for layer 1, layer 2, and the combined layer 12.

Equations for three layers can be obtained by considering two adjacent layers as behaving like a single layer with properties as given by equations (36) to (39). This layer is then combined with the third layer. By continuing this process, the transmittance and reflectance of a slab n-particles thick but containing $(n - 1)$ homogeneous layers and two half layers can be determined in terms of the optical properties of the individual layers.

From physical consideration, the transmittance and reflectance of the slab built from the flux diagrams and the properties of a single layer should be the same as those given by the continuous model (e.g., two-flux model). For a slab n-particles thick $(L = nD)$, the parameters K and S can be expressed in terms of the transmittance τ and reflectance ρ by solving equations (5) and (6):

$$K = \frac{1}{nD}\left(\frac{\gamma - 2\rho}{\gamma + 2\rho}\right)^{1/2} \sinh^{-1}\left[\frac{(\gamma^2 - 4\rho^2)^{1/2}}{2\tau}\right] \tag{40}$$

$$S = \frac{1}{2nD}\left[\left(\frac{\gamma + 2\rho}{\gamma - 2\rho}\right)^{1/2} - \left(\frac{\gamma - 2\rho}{\gamma + 2\rho}\right)^{1/2}\right] \sinh^{-1}\left[\frac{(\gamma^2 - 4\rho^2)^{1/2}}{2\tau}\right] \tag{41}$$

where

$$\gamma = 1 + \rho^2 - \tau^2 \tag{42}$$

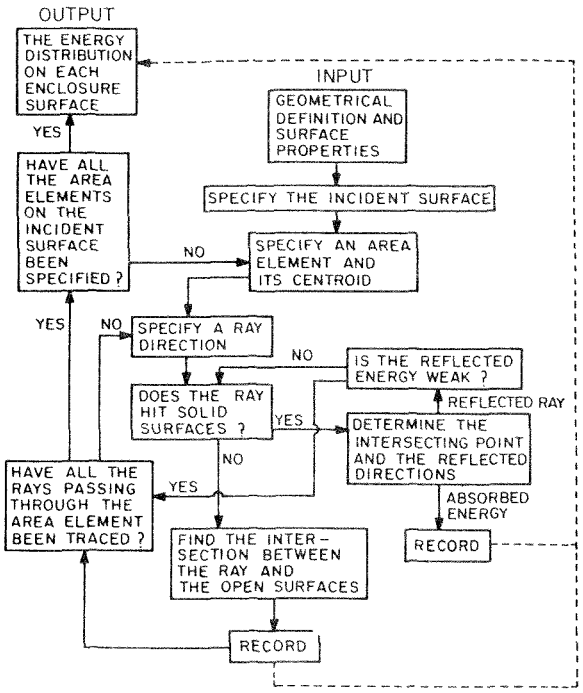

Fig. 6 Flow chart, the ray tracing program

Results and Discussions

The flux components of the unit cell for various particle emissivities ($0 \leq \epsilon_p \leq 1$) were obtained by the method described previously. In order to compare with the experimental results of Chen and Churchill [11], computations were carried out for emissivities of 0.4 and 0.28 which correspond roughly to the steel and the alumina particles used in the experiment.

A simplified flow chart for the ray tracing computation is shown in Fig. 6. For the unit cell of the regular layer, the enclosure consists of eight sections of spherical surfaces and six seg-

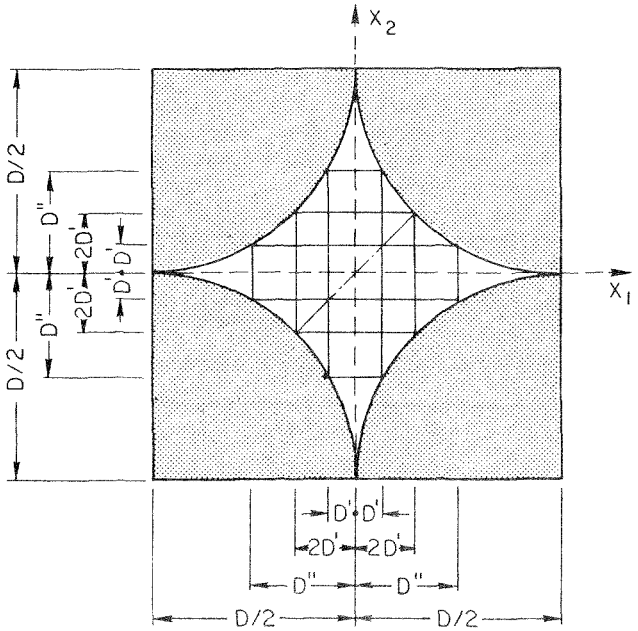

$$D' = \frac{D}{4}\left(1 - \frac{1}{\sqrt{2}}\right)$$

$$D'' = \frac{D}{2} - \sqrt{D'(D - D')}$$

Fig. 7 Area elements of the incident surface

Table 1 The flux components of a unit cell in a regular layer

Particle emissivity	f	b	s	$1 - \omega_0$
1.0	0.059	0.0	0.0378	0.790
0.5	0.114	0.010	0.0701	0.595
0.4	0.131	0.015	0.0809	0.529
0.28	0.158	0.024	0.0976	0.428
0.1	0.213	0.047	0.135	0.201
0.0	0.257	0.071	0.167	0

ments of planar open surfaces of irregular boundaries (Fig. 2). The open surface through which the incident radiation passes is divided into small area elements as shown in Fig. 7. For simplicity, only four divisions for each side are shown. In order to maintain almost the same area for each element, the incident surface is divided up in the following way. Consider the quarter bounded by the positive x_1 and x_2 axes and the circular arc. The quarter is divided into three sections—a square section whose side is $D/2(1 - 1/\sqrt{2})$ and two equal irregular sections. The square section is divided into equal area elements bounded by two orthogonal sets of equally spaced straight lines. These horizontal and vertical lines are extended into the two irregular sections, and their intersections with the circular arc generate the opposite orthogonal set of dividing lines in the irregular sections. For example, if the radius $(D/2)$ is normalized and if $x_1 = z$ is a vertical line in the square section, then from geometrical considerations, $x_2 = 1 - \sqrt{z(2 - z)}$ is the corresponding horizontal line generated in the irregular section. For uniformly diffuse irradiation, the amount of energy received by each element is proportional to its own area ΔA. The hemisphere over the area element in the direction of the incident radiation is divided into small discrete solid angles $\Delta\omega$. According to Lambert's cosine law, the energy contained within the solid angle will be proportional to ΔA, $\Delta\omega$, and $\cos\theta$ where θ is the angle between the surface normal and the solid angle. The amount of energy traveling in a given direction is described in terms of a ray vector whose initial point is the centroid of the area element and whose directions are given by the directional cosines ($\sin\theta\cos\phi$, $\sin\theta\sin\phi$, $\cos\theta$), where ϕ is the azimuthal angle.

In three-dimensional space a sphere is defined by its center (s_1', s_2', s_3') and its diameter D. The mathematical function for a spherical surface is

Table 2 The flux components of a unit cell in a half layer

Particle emissivity	f_1	b_1	s_1	$1 - \omega_{01}$
1.0	0.0916	0	0.04292	0.737
0.5	0.126	0.206	0.0593	0.429
0.4	0.1345	0.2556	0.06303	0.3573
0.28	0.1459	0.3176	0.06823	0.263
0.1	0.1655	0.4243	0.0766	0.1022
0.0	0.1782	0.4913	0.08213	0

f_2	b_2	s_2	$1 - \omega_{02}$	f_3
0.426	0	0.02013	0.493	0.0306
0.584	0	0.02928	0.2986	0.0470
0.6238	0	0.0317	0.25	0.05139
0.6759	0	0.0348	0.1852	0.05741
0.765	0	0.0406	0.0723	0.0681
0.8229	0	0.0443	0	0.0755

b_3	s_3	s_{35}	s_{36}	$1 - \omega_{03}$
0	0.01407	0.412	0.0412	0.488
0.00145	0.0206	0.560	0.0579	0.292
0.001965	0.0222	0.5972	0.06041	0.2431
0.002685	0.0243	0.6435	0.06782	0.1801
0.00412	0.0278	0.7222	0.0778	0.0708
0.00511	0.0306	0.7731	0.0845	0

$$\sum_{i=1}^{3} (x_i - s_i')^2 = (D/2)^2 \tag{43}$$

and the surface normal vector $\hat{n}$ is

$$\hat{n} = \sum_{i=1}^{3} \frac{2(x_i - s_i')}{D} \hat{e}_i \tag{44}$$

where $\hat{e}_i$ is the unit vector in the x_i direction. For a ray whose origin is at (a_1, a_2, a_3) and whose directional cosines are l_1, l_2, l_3, the criterion for the existence of an intersection between it and the sphere is

$$\Pi = \left[\sum_{i=1}^{3} l_i(s_i' - a_i)\right]^2 - \left[\sum_{i=1}^{3} (s_i' - a_i)^2 - \left(\frac{D}{2}\right)^2\right] \geq 0 \tag{45}$$

Except for tangential intersection, there will be two mathematical intersecting points. The physical intersection is the one having the shortest distance and this value is given by

$$d = \left|\sum_{i=1}^{3} l_i(s_i' - a_i)\right| - \Pi^{1/2} \tag{46}$$

In order that the intersection lies within the region of the spherical surface defined by the enclosure, the coordinates x_1', x_2', x_3' have to satisfy the following criteria:

$$x_i' \leq |D/2| \qquad i = 1, 2, 3 \tag{47}$$

where x_1', x_2', x_3' and the directional cosines of the reflected ray are determined by the equations outlined in Section entitled "Scattering and Absorption of a Unit Cell." At each intersection, part of the energy carried by the ray is absorbed by the surface while the remainder is carried away by the reflected ray. This process is repeated for the reflected ray until either the ray has lost most of its energy by multiple reflections or the ray escapes from the unit cell by striking one of the open planar surfaces. These six planar surfaces are defined by the following mathematical function

$$x_j = \pm D/2 \qquad j = 1, 2, 3 \tag{48}$$

By tracing all of the rays which pass through the area elements of the irradiated surface, the distribution of energy leaving the unit cell through each open surface can be determined, and the flux diagram characteristic of the unit cell can be constructed. A computer program was developed to perform the necessary calculations. The effort involved in the computation and the accuracy of the result are a direct function of the number of rays traced. The result becomes exact as this number approaches infinity. However, in order to keep the computer time within a reasonable limit, the number of the rays is chosen in such a way that further increase of this number would not improve the accuracy by more than five percent. The computations have been carried out for eight divisions of the side of the incident surface, sixteen divisions of the angle θ, and thirty-two divisions of the angle ϕ. The results are shown in Tables 1 and 2.

In the evaluation of the radiative properties (i.e., transmittance and reflectance) of a layer, the distribution of energy leaving the unit cell through each open surface has been assumed to be diffuse. To check this assumption, the directions of the rays reaching the open surface were recorded in the ray tracing process. It was found that for particles of emissivity equal to unity, the scattered rays were collimated in certain directions. For other particle emissivities (because of the multiple reflections within the unit cell) the energy was distributed diffusely on each open surface except for the directions near the surface normal of the forward component. In practice the random orientation of the particles would also tend to make the energy scattered in a diffuse manner. Transmittance and reflectance computed from equations (29) to (35) for the regular and the half layers are presented in Table 3. The radiative properties for a series of layers were obtained by the above indicated method for multiple layers.

The numerical techniques for calculating the parameters K and S from equations (40) and (41) involve the computation of the transmittance τ and reflectance ρ for increasing slab thickness

Table 3 Transmittance and reflectance of a regular layer and a half layer

Particle emissivity	Regular layer		Half layer			
	τ_l	ρ_l	τ_l	ρ_l	τ_l'	ρ_l'
1.0	0.0656	0.0066	0.0989	0.0739	0.461	0.00347
0.5	0.141	0.0367	0.141	0.349	0.655	0.00728
0.4	0.1688	0.0528	0.152	0.418	0.705	0.00852
0.28	0.2192	0.0852	0.166	0.510	0.774	0.0103
0.1	0.368	0.202	0.192	0.672	0.869	0.0141
0.0	0.587	0.401	0.210	0.779	0.977	0.0168

until K and S converge to their asymptotic values. Convergence usually requires a slab which is about ten layers thick ($n = 10$).

Equations (40) and (41) indicate that K and S are inversely proportional to the particle diameter D since τ and ρ are not functions of the diameter. This result agrees with the experimental observation [11] and with the rough estimate based on the Mie theory of single scattering. The Mie theory predicts that the scattering cross section of a large sphere is proportional to D^2. Thus the volumetric extinction coefficient should be proportional to ND^2 where N is the number of particles per unit volume. Since N is equal to $\delta_s v_s^{-1}$, where δ_s is the solid fraction and v_s is the volume of the particle, the extinction coefficient is thus proportional to $\delta_s D^{-1}$. While the predicted trend for the dependence of K and S on emissivity appears to agree well with the experimental [11], the discrepancy between the predicted and the measured values, however, is quite large. Generally speaking, the predicted absorption coefficient is much higher while the scattering coefficient is lower than the corresponding experimental values. This large discrepancy can be attributed to the fact that in the experimental system, a thin slab of two or three layers of spheres was involved and there exists a considerable portion of energy passing through the slab without encountering the absorption and scattering process assumed in the analysis. This direct radiation channeling results in smaller values for the absorption coefficient but larger values for the scattering coefficient than the predicted. In actual applications, however, numerous layers of randomly packed spheres are involved and the direct radiation channeling effect is negligible. Therefore, in such cases, a better agreement between the predicted and the measured radiation properties is expected.

References

1 Tien, C. L., and Cunnington, G. R., "Cryogenic Insulation Heat Transfer," in *Advances in Heat Transfer*, Vol. 9, T. F. Irvine and J. P. Hartnett, eds., Academic Press, New York, 1973, pp. 349-417.

2 Tien, C. L., and Cunnington, G. R., "Recent Advances in High-Performance Cryogenic Thermal Insulation," *Cryogenics*, Vol. 12, 1972, pp. 419-421.

3 Cunnington, G. R., and Tien, C. L., "Heat Transfer in Microsphere Cryogenic Insulation," *Advances in Cryogenic Engineering*, Vol. 18, K. D. Timmerhaus, ed., Plenum Press, New York, 1973.

4 Chan, C. K., and Tien, C. L., "Conductance of Packed Spheres in Vacuum," JOURNAL OF HEAT TRANSFER, TRANS. ASME, Series C (in press).

5 Kortum, G., *Reflectance Spectroscopy*, Springer-Verlag, New York, 1969, pp. 104-179.

6 Hottel, H. C., Sarofim, A. F., Evans, L. B., and Vasalos, I. A., "Radiation Transfer in Anisotropically Scattering Media: Allowance for Fresnel Reflection at the Boundaries," JOURNAL OF HEAT TRANSFER, TRANS. ASME, Series C, Vol. 90, 1968, pp. 56-62.

7 Hottel, H. C., Sarofim, A. F., Vasalos, I. A., and Dalzell, W. H., "Multiple Scatter, Comparison of Theory With Experiment," JOURNAL OF HEAT TRANSFER, TRANS. ASME, Series C, Vol. 92, 1970, pp. 285-291.

8 Schuster, A., "Radiation Through a Foggy Atmosphere," *Astrophysical Journal*, Vol. 21, 1905, pp. 1-22.

9 Klier, K., "Absorption and Scattering in Plane Parallel Turbid Media," *J. Opt. Soc. Am.*, Vol. 62, pp. 882-885.

10 Kubelka, P., "New Contributions to the Optics of Intensity Light-Scattering Materials. Part I," *J. Opt. Soc. Am.*, Vol. 38, 1948, pp. 448-457.

11 Chen, J. C., and Churchill, S. W., "Radiant Heat Transfer in Packed Beds," *AIChE Journal*, Vol. 9, 1963, pp. 35-41.

12 Lin, S. H., and Sparrow, E. H., "Radiant Interchange Among Curved Specularly Reflecting Surfaces—Application to Cylindrical and Conical Cavities," JOURNAL OF HEAT TRANSFER, TRANS. ASME, Series C, Vol. 87, 1965, pp. 299-307.

13 Corlett, R. C., "Direct Monte Carlo Calculation of Radiative Heat Transfer in Vacuum," JOURNAL OF HEAT TRANSFER, TRANS. ASME, Series C, Vol. 88, 1966, pp. 376-382.

14 Plamondon, J. A., and Horton, T. E., "On the Determination of the View Function to the Images of a Surface in a Nonplanar Specular Reflector," *International Journal of Heat and Mass Transfer*, Vol. 10, 1967, pp. 665-679.

15 Shealy, D. L., Burkhard, D. G., and Sexl, R. U., "Specular Reflection of Parallel Heat Radiation From an Arbitrary Reflector Surface to an Aribtrary Receiver Surface," *International Journal of Heat and Mass Transfer*, Vol. 16, 1973, pp. 271-280.

J. V. BECK
Professor.

S. AL-ARAJI
Graduate Student.

Department of Mechanical Engineering,
Michigan State University,
East Lansing, Mich.

Investigation of a New Simple Transient Method of Thermal Property Measurement

New transient solutions are derived for the simple calculation of thermal conductivity, specific heat, thermal diffusivity and contact conductance from the results of a single experiment. All the proposed experiments utilize a specimen which has one surface insulated and the opposite one heated by an arbitrary heat flux. The heat flux must have a finite duration and its integrated value must be known. Two types of experiments are discussed and measurements for each type are given. One type uses a flat, thin electric heater and the other uses a material of known specific heat as a calorimeter. Relative advantages are discussed.

1 Introduction

Numerous methods for measuring thermal properties have been proposed over the years. Most of these methods are for measuring a single thermal property at a time, and they usually utilize simple exact solutions for steady state and transient cases. (Many of these are discussed in [1].[1]) A departure from these methods is discussed in papers by Beck [2–4], Pfahl and Mitchel [5, 6] and others in which the digital computer is used in data analysis and a digital data acquisition system is required. These latter methods can be used to estimate several parameters at one time.

The method discussed herein is similar to the classical method in that the working equations for estimating the parameters are relatively simple. This method requires the integration of some signals which can readily be accomplished by using currently available integrated circuits. An advantage of this method is that one surface of the specimen is simply insulated. The opposite surface is heated uniformly over its surface but can be heated arbitrarily in time. The total heat added must be measured, however. After performing the straightforward experiment just described, simple algebraic expressions are used to calculate thermal conductivity, thermal diffusivity, specific heat and contact conductance. All these properties can be determined from a single experiment.

The methods are also important since the experiments are usually of short duration—on the order of seconds or minutes rather than hours. Some simple experiments are described that can be performed in many heat transfer laboratories.

Experiments of short duration provide several unique advantages. One can test materials which might otherwise dry (biological materials, for example) or degrade using conventional slower methods. Also, a rapid method is needed for thermal testing of materials being continuously produced.

2 General Theory

Consider the mathematical problem for the temperature T of the specimen being either a flat plate ($n = 0$), long cylinder ($n = 1$) or sphere ($n = 2$),

$$\frac{1}{r^n}\frac{\partial}{\partial r}\left(kr^n\frac{\partial T}{\partial r}\right) = \rho c_p\frac{\partial T}{\partial t} \tag{1}$$

$$\pm k\frac{\partial T(r_h, t)}{\partial r} = q(t) \tag{2a}$$

where $q(t) \neq 0$ for $0 < t < t_{\max}$

$= 0$ otherwise

$-$ sign for $r_h < r_{\text{in}}$

$+$ sign for $r_h > r_{\text{in}}$

$$\frac{\partial T(r_{\text{in}}, t)}{\partial r} = 0 \tag{2b}$$

$$T(r, 0) = T_{\text{i}} \tag{2c}$$

where r_h is the location of the heated surface, r_{in} is that of the insulated surface and $t_{\max}$ is the maximum duration of the heating (see Fig. 1). The arbitrary heat flux $q(t)$ has a nonzero value only between $t = 0$ and $t_{\max}$ as shown in Fig. 2. The thermal conductivity k and specific heat c_p in (1) can be considered to be functions of temperature. At a certain point below, the assumption is made that k is constant.

[1] Numbers in brackets designate References at end of paper.

Contributed by the Heat Transfer Division for publication (without presentation) in The Journal of Heat Transfer. Manuscript received by the Heat Transfer Division June 21, 1973. Paper No. 74-HT-E.

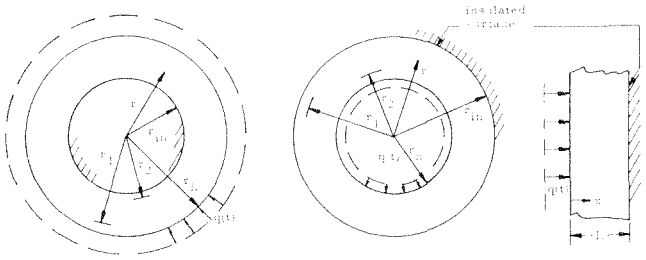

Fig. 1 Various geometries with one surface heated and the other insulated: (a) Hollow sphere on long cylinder heated at outside surface (Fig. 1(a) reduces to aso lid sphere or cylinder if r_{in} goes to zero); (b) Hollow spnere on long cylinder heated at inside surface; (c) Plate geometry

Integrate (1) first over time from $t = 0$ to ∞ and then over r to obtain

$$r^n \int_0^\infty k \frac{\partial T}{\partial r}\, dt = \frac{r^{n+1}}{n+1} \int_{T_i}^{T_f} \rho c_p dT + C_1 \tag{3a}$$

where T_i is the initial temperature and T_f is the final (equilibrium) temperature. Integrate (2a) and (2b) over t from zero to infinity to get

$$\pm \int_0^\infty k \frac{\partial T(r_h, t)}{\partial r}\, dt = \int_0^\infty q(t) dt = Q \tag{3b}$$

$$\frac{d\phi(r_{in})}{dr} = 0 \tag{3c}$$

where $\phi(r)$ is defined by

$$\phi(r) \equiv \int_0^\infty T(r, t) dt. \tag{3d}$$

Evaluate (3a) at r_h and use (3b), then evaluate (3a) at r_{in} and use (3c) to find.

$$r_h{}^n(\pm Q) = \frac{r_h{}^{n+1}}{n+1} \int_{T_i}^{T_f} \rho c_p dT + C_1 \tag{4a}$$

$$0 = \frac{r_{in}{}^{n+1}}{n+1} \int_{T_i}^{T_f} \rho c_p dT + C_1 \tag{4b}$$

which could be considered as two simultaneous equations with the two unknowns being C_1 and the integral. Solving them gives

$$\int_{T_i}^{T_f} \rho c_p dT = \frac{(n+1) r_h{}^n Q}{|r_h{}^{n+1} - r_{in}{}^{n+1}|} \tag{4c}$$

$$C_1 = \frac{r_{in}{}^{n+1} r_h{}^n Q}{|r_h{}^{n+1} - r_{in}{}^{n+1}|}. \tag{4d}$$

Introduce (4c) and (4d) into (3a) to find

$$r^n \int_0^\infty k \frac{\partial T}{\partial r}\, dt = \frac{r_h{}^n Q}{|r_h{}^{n+1} - r_{in}{}^{n+1}|} [r^{n+1} - r_{in}{}^{n+1}]. \tag{5}$$

This result can be further integrated after an assumption is made regarding the temperature dependence of k.

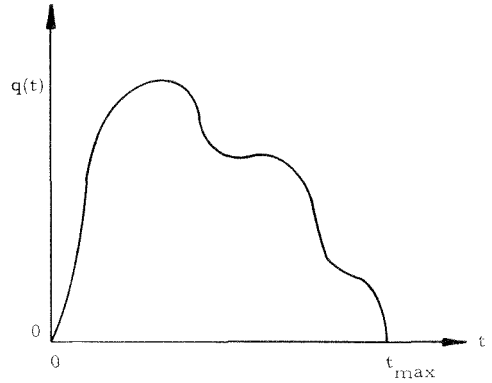

Fig. 2 Arbitrary heat flux $q(t)$ for which t_{max} is finite and $Q = \int_0^{t_{max}} q(t)\, dt$ is known

2.1 Thermal Conductivity. Assume in (5) that the thermal conductivity k is independent of temperature, then divide (5) by r^n, integrate between r_1 and r_2, and solve for k yielding the general result

$$k = \frac{Q r_h{}^n}{|r_h{}^{n+1} - r_{in}{}^{n+1}|} \left[\frac{r_1{}^2 - r_2{}^2}{2} - r_{in}{}^{n+1} \int_{r_2}^{r_1} \frac{dr}{r^n} \right] \Big/ \int_0^\infty [T(r_1, t) - T(r_2, t)] dt \tag{6}$$

which is valid for temperature-independent k in plates ($n = 0$), solid and hollow cylinders ($n = 1$) and solid and hollow spheres ($n = 2$). Note that k is independent of any temperature dependence of c_p.

This analysis can be extended by assuming that k is, for example, a linear function of temperature. For small variations of k in a given experiment one finds that k should be evaluated at the time average of one-half of $T(r_1, t) + T(r_2, t)$, which can be approximated by $(T_i + T_f)/2$.

2.2 Thermal Diffusivity. An expression for thermal diffusivity, defined by $k/\rho c_p$, can be derived using the preceding analysis even if Q is not known. In (4a) and (4b) Q and C_1 are considered to be the unknowns. Assuming that k and ρ are constant, the thermal diffusivity α can be derived:

$$\alpha = \frac{k}{\rho \bar{c}_p} = \frac{\frac{1}{n+1} \left[\frac{r_1{}^2 - r_2{}^2}{2} - r_{in}{}^{n+1} \int_{r_2}^{r_1} \frac{dr}{r^n} \right] (T_f - T_i)}{\int_0^\infty [T(r_1, t) - T(r_2, t)] dt} \tag{7a}$$

where

$$\bar{c}_p = \frac{1}{T_f - T_i} \int_{T_i}^{T_f} c_p dT \tag{7b}$$

which also applies for plates, cylinders, etc. If Q is not known, α can be found but k and c_p cannot be; also, α is unaffected by any errors in Q.

Nomenclature

c_p = specific heat
h = contact conductance
k = thermal conductivity
L = thickness of plate
n = 0 for plate
n = 1 for cylinder
n = 2 for sphere
q = heat flux
Q = integrated heat flux
r = radial coordinate
r_1 = location of thermocouple number 1
r_2 = location of thermocouple number 2
r_h = location of heated surface
r_{in} = location of insulated surface
t = time
T = temperature
T_f = final temperature
T_i = initial temperature
α = thermal diffusivity
ρ = density

2.3 Specific Heat. For the case of constant density but temperature variable c_p, the average specific heat between temperatures T_i and T_f is defined by (7*b*). By using (4*c*) one obtains

$$\bar{c}_p = \frac{(n+1)r_h{}^n Q}{\rho|r_h{}^{n+1} - r_{\text{in}}{}^{n+1}|(T_f - T_i)} \tag{8}$$

which is independent of any temperature dependence of k.

2.4 Calorimeter Method of Measuring Q. There are a number of ways to measure Q. One way is to use electric heating (see Section 5). A simple method, particularly for the flat plate geometry, utilizes as a calorimeter a material with an accurately known density-specific heat product (see Section 6). Its thermal conductivity need not be known but it is most effective to choose a material with a large k. In addition to being simple, this method provides a heat flux which is of reasonable value for all materials (something that is difficult to achieve using electric heaters with high-k specimens) and which approximates the optimum heat flux [3]. The optimum heat flux would cause the specimen's heated surface to take a step rise in temperature; this flux is initially very large and then decays to zero. Unlike the method of electric heating, such a method could be used to either heat or cool the specimen.

The calorimeter is initially at a different uniform temperature than the specimen. It is insulated at all surfaces except the flat surface which is brought into intimate contact with the specimen. The specimen and the calorimeter would be allowed to come to an equilibrium temperature. During this process the heat transferred from the calorimeter would be exactly the same as the amount going *to* the specimen (provided there are no heat losses). Then Q is for the flat plate geometry

$$Q = \rho_c L_c \bar{c}_{p,c}(T_{i,c} - T_f) \tag{9}$$

where the c subscript refers to the calorimeter and $c_{p,c}$ is the specific heat of the calorimeter evaluated at the average temperature $(T_{i,c} + T_f)/2$.

In order to promote intimate and uniform contact between the calorimeter and the specimen some fluid such as water at room temperature or silicone grease at higher temperatures is frequently used.

2.5 Thermal Contact Conductance. With the flat plate geometry of a calorimeter and specimen mentioned in Section 2.4 one might be interested in the measurement of contact conductance of the film between the surfaces or between bare surfaces. If the surfaces are bare (permitting the calculation of the conventional conductance h), several thermocouples should be placed at the mating surfaces to better measure the average interface temperatures.

Suppose that temperatures are measured at the mating surfaces. (It is possible to extend the analysis for other measurement locations using the analysis given in Section 2.1.) A contact conductance, h, is defined by

$$q(t) = h[T_c(0, t) - T(0, t)] \tag{10a}$$

where the surface temperature of the specimen does not have a subscript. Integrating over time gives Q,

$$Q = \int_0^\infty h[T_c(0, t) - T(0, t)]dt \tag{10b}$$

A weighted average contact conductance $\bar{h}$ is now defined by

$$\bar{h} = \frac{\int_0^\infty h[T_c(0, t) - T(0, t)]dt}{\int_0^\infty [T_c(0, t) - T(0, t)]dt} = \frac{Q}{\int_0^\infty [T_c(0, t) - T(0, t)]dt} \tag{11}$$

which could be used for any geometry considered in the preceding involving two materials with imperfect contact. In practice this result would usually be restricted to plates since the uniform interface conditions are more difficult to obtain for other configurations.

3 Applications to Various Geometries

3.1 Flat Plate. The simplest, and usually the preferred, geometry is the flat plate. The analysis of the previous section can be applied by letting $r = x$, $r_1 = x_1$, $r_2 = x_2$, $r_{\text{in}} = L$, $r_h = 0$ and $n = 0$ (see Fig. 1(*c*)). Using these relations (6) yields the thermal conductivity for a plate heated at $x = 0$ and insulated at $x = L$:

$$k = \frac{LQ\left[\left(\frac{x_1}{L} - 1\right)^2 - \left(\frac{x_2}{L} - 1\right)^2\right]}{2\int_0^\infty [T(x_1, t) - T(x_2, t)]dt}. \tag{13}$$

The thermal diffusivity could be found if Q were not known; from (7*a*) it is given by

$$\alpha = \frac{L^2(T_f - T_i)\left[\left(\frac{x_1}{L} - 1\right)^2 - \left(\frac{x_2}{L} - 1\right)^2\right]}{2\int_0^\infty [T(x_1, t) - T(x_2, t)]dt}. \tag{14}$$

The terms in the brackets of the numerator of (14) reduce to the value of unity for $x_1 = 0$ and $x_2 = \text{L}$.

The specific heat is found from (8) to be

$$\bar{c}_p = \frac{Q}{\rho L(T_f - T_i)}. \tag{15}$$

The calorimeter method for finding Q can be implemented by using (9) and the contact conductance is given by (11).

3.2 Solid Cylinder. For a long solid cylinder heated uniformly over the surface at $r = r_h$, the relations $n = 1$ and $r_{\text{in}} = 0$ are used in (6), (7*a*), and (8) to obtain

$$k = \frac{Qr_h\left[\left(\frac{r_1}{r_h}\right)^2 - \left(\frac{r_2}{r_h}\right)^2\right]}{2\int_0^\infty [T(r_1, t) - T(r_2, t)]dt} \tag{16}$$

$$\alpha = \frac{r_h{}^2(T_f - T_i)\left[\left(\frac{r_1}{r_h}\right)^2 - \left(\frac{r_2}{r_h}\right)^2\right]}{4\int_0^\infty [T(r_1, t) - T(r_2, t)]dt} \tag{17}$$

$$\bar{c}_p = \frac{2Q}{\rho r_h(T_f - T_i)}. \tag{18}$$

Provided temperature and position measurements can be made as accurately at $r = 0$ and r_h as elsewhere in the cylinder, the best locations for measurements are $r_1 = r_h$ and $r_2 = 0$. For these locations the bracketed terms in the numerator of (16) and (17) reduce to value of unity.

3.3 Solid Sphere. For the solid sphere, $n = 2$ and $r_{\text{in}} = 0$. Equation (16) applies for this case; the factor 4 in the denominator of (17) becomes 6; and the factor 2 in the numerator of (18) becomes 3. Again the optimum measurement locations are at $r_1 = r_h$, $r_2 = 0$.

3.4 Hollow Cylinder. Some experimentalists prefer to utilize radial heat flow in a long hollow cylinder. Assume that the cylinder is heated at r_h and is insulated at r_{in}. Then use $n = 1$ in (6) to obtain for k

$$k = \frac{Q|r_h - r_{\text{in}}|\Delta_c}{\int_0^\infty (T(r_1, t) - T(r_2, t))dt} \tag{19a}$$

where

$$\Delta_c = \frac{R_1^2 - R_2^2 - 2R^2 \ln \frac{R_1}{R_2}}{2(R-1)(R^2-1)} \tag{19b}$$

$$R = \frac{r_{in}}{r_h}; \quad R_1 = \frac{r_1}{r_h}; \quad R_2 = \frac{r_2}{r_h}. \tag{19c}$$

Note the absolute value sign in (19*a*) which permits the solution to be valid for r_h either greater or less than r_{in} ($0 < R < \infty$). The measurement radii r_1 and r_2 should be between r_{in} and r_h; mathematically for $r_h > r_{in}$ (heated outside)

$$R < R_1 < 1; \quad R < R_2 < 1$$

and for $r_h < r_{in}$ (heated inside)

$$1 < R_1 < R; \quad 1 < R_2 < R.$$

For the special case of $r_1 = r_h$ or $R_1 = 1$ and $r_2 = r_{in}$ or $R_2 = R$ (optimum values of r_1 and r_2) the expression Δ_c in (19*b*) is plotted in Fig. 3. It is equal to 0.5 at $R = 0$ (which corresponds to a solid cylinder) and at $R = 1$ (which corresponds to a flat plate).

The thermal diffusivity from (7*a*) becomes

$$\alpha = \frac{k}{\rho \bar{c}_p} = \frac{(T_f - T_i)(r_h - r_{in})^2}{\int_0^\infty [T(r_1, t) - T(r_2, t)]dt} \left[\frac{(R+1)\Delta_c}{2}\right] \tag{20}$$

and the average specific heat is

$$\bar{c}_p = \frac{2Q}{\rho |r_h - r_{in}| (R+1)(T_f - T_i)}. \tag{21}$$

3.5 Hollow Sphere. For the hollow sphere $n = 2$, k is given by

$$k = \frac{Q|r_h - r_{in}|\Delta_s}{\int_0^\infty (T(r_1, t) - T(r_2, t))dt} \tag{22a}$$

where

$$\Delta_s = \frac{R_1^2 - R_2^2 + 2R^3(R_1^{-1} - R_2^{-1})}{2(1-R)(R^3-1)}. \tag{22b}$$

For the special case of $r_1 = r_h$ and $r_2 = r_{in}$, Δ_s of (22*b*) is plotted in Fig. 3. The maximum Δ_s value occurs at $R = r_{in}/r_h = (\sqrt{3} - 1)/2 = 0.366$. This is the case of a hollow sphere heated at the outside surface.

The thermal diffusivity α is similar to (20) except that bracketed term now becomes

$$\frac{(R^2 + R + 1)\Delta_s}{3}.$$

The average specific heat for a hollow sphere heated either inside or outside is

$$\bar{c}_p = \frac{3Q}{\rho |r_h - r_{in}| (R^2 + R + 1)(T_f - T_i)}. \tag{23}$$

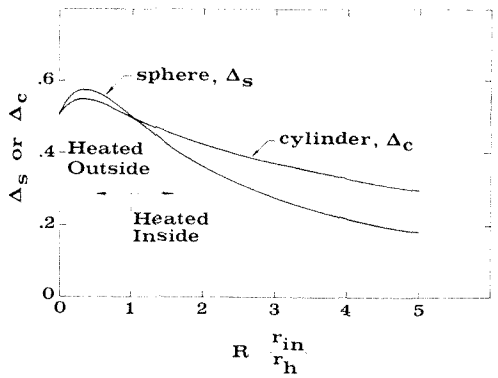

Fig. 3 Δ_c given by equation (19b) and Δ_s by equation (22b) plotted for $R_1 = 1$ and $R_2 = R$

4 Optimum Geometry For Determining k or α

The optimum geometry is a hollow sphere which is heated from the outside; the improvement over the plane geometry is not large, however. The optimum experiment would have thermocouples located only at the heated and insulated surfaces and a heat input which causes the heated surface of the specimen to take a step increase.

5 Electric Heater Device

Several devices based on the preceding theory for the flat plate geometry have been built. Some typical results for measurements of k and c_p for Pyrex glass are given in this section for a device using a thin silicone rubber heater. This device included an electronic integrator to integrate the thermocouple signals. A timer was used to provide a 15 sec duration heating cycle.

The measurements were made using a digital voltmeter (DVM) with a range of ± 1.999 v. The initial and final voltages of a thermocouple were recorded. During the test the voltage difference of the two thermocouples on either side of the specimen was observed (but not recorded). When this voltage difference was almost zero, the integrator was set on "hold" and the value read. A three turn switch was used in order to permit using a single DVM to measure the (1) temperature difference, (2) specimen temperature, and (3) integral of the temperature difference which was on stations No. 1, No. 2, and No. 3 of the switch, respectively.

For the foregoing measurements only two thermocouples were needed. In order to assure more uniform heating and also to avoid affixing thermocouples to the specimen which is 0.4 in. thick and 2 in. in diameter the thermocouples were embedded in two 2 in. dia, $^1/_{16}$ in. thick copper disks. (If the specimens have high values of k, then it is necessary to attach thermocouples directly on the specimen because then the temperature drop in the silicone grease between the specimen and the copper disk would be important.) One disk was attached to one side of the specimen and the other disk to the other side by using silicone grease. Another specimen-disk combination, but without thermocouples, was also made. The heater was placed between the two specimen-disk combinations and again silicone grease was used. Silicone grease will hold the composite together without pressure during the tests if it is squeezed together by hand pressure beforehand. The specimens were placed inside an insulated "can" which was *not* temperature controlled.

About a thousand individual tests have been run. Typical uncorrected results are given in Table 1 which were selected from those run one afternoon over a period of two hr and 17 min or an average of one test every 3.1 min. Each test took about 75 sec.

Because the tests can be run so rapidly, many have been run; however, the tests are by no means optimized experimentally as yet. For this reason, and the fact that no corrections have been applied, the potential accuracy of the method should not be judged on the accuracy of the k and c_p values given in Table 1. (The k values are within a few percent, but c_p becomes quite inaccurate.) Insight into the simplicity, precision and speed of the method can be gained from Table 1, however.

Columns *b–e* give the voltages read before and after the experiment with the switch on No. 3 and No. 2. During the test itself

Table 1 Uncorrected thermal conductivity and specific heat calculations for Pyrex glass

a	*b*	*c*	*d*	*e*	*f*	*g*	*h*	*i*
Test No.	Initial integrator (No. 3)	Start (No. 2)	Finish (No. 2)	Final integrator (No. 3)	d − c ΔV_{sp}	b − e ΔV_I	c_p	k
1	−0.150	−0.182	0.059	−3.52	0.241	3.37	0.316	0.602
2	−0.150	0.048	0.275	−3.51	0.227	3.36	0.336	0.604
3	−0.150	0.255	0.470	−3.49	0.215	3.34	0.355	0.608
4	−0.150	0.444	0.650	−3.53	0.206	3.38	0.370	0.600
15	−0.150	1.845	1.984	−3.47	0.139	3.32	0.549	0.611
30	−0.149	2.61	2.71	−3.40	0.10	3.251	0.763	0.624
42	−0.149	2.74	2.84	−3.42	0.10	3.271	0.763	0.620
43	−0.149	2.75	2.85	−3.41	0.10	3.261	0.763	0.622
44	−0.149	2.77	2.87	−3.40	0.10	3.251	0.763	0.624

Table 2 Summary of thermal properties of Armco iron measured using the calorimeter heating method

	Temperature			
	75 deg F (6 drops of water)	75 deg F (0.015 in. silicone grease)	300 deg F (0.015 in. silicone grease)	400 deg F (0.015 in. silicone grease)
Total No. tests	9	14	3	4
k	42.54	41.56	37.57	34.45
est. std. dev. (k)	0.943	1.110	0.87	0.99
k(TPRC)	41.5	41.5	36.5	34.0
$\bar{c}_p$	0.1089	0.1080	0.1415	0.1325
est. std. dev. (cz)	0.00211	0.00095	0.00012	0.0309
c_p(TPRC)	0.108	0.108	0.120	0.130

the switch is on No. 1 which is for the temperature difference across the specimen; when this difference is sufficiently small the test is terminated, but no readings are recorded for the temperature difference. The equations used for calculating k and c_p are:

$$k = 2.029/\Delta V_I \qquad c_p = 0.076/\Delta V_{sp}$$

which contain certain constants characteristic of the integrator and the energy provided by the heater. ΔV_I and ΔV_{sp} are found by subtracting the voltages indicated in Table 1. In these tests the reference temperature is room temperature so that a voltage of 0 in columns c and d of Table 1 corresponds to 75 deg F; from the calibration curve of iron-constantan thermocouples, 3 v corresponds to about 100 F deg above the ambient temperature.

In terms of precision, the k values appear to be excellent with less than ±1 percent variation at a given temperature level (compare columns c and i). On the other hand c_p is very sensitive to heat losses as the temperature increases, but reproducible values are obtained when the temperature approaches a maximum as for cases 42–44. Over a 100 F deg span, k and c_p should be relatively constant for Pyrex glass. Hence the uncorrected values for k in Table 1 may be accurate, but the c_p values cannot be since there is a factor of over 2 in the values.

Accurate experimental results should incorporate all reasonable corrections. Since heat losses are sufficiently large to cause the specimen to approach an equilibrium temperature, heat losses must be considered. This effect is greatly reduced for the conductivity by zeroing the temperature difference before each run. Also, it can be shown for k that the copper plates on either side of the specimen have no effect except for the temperature drop in the silicone grease layers on either side of the specimen.

The errors in c_p are large in Table 1 due to heat losses. Corrections could be made, but they appear to be too large to permit accurate results. One way to measure c_p more accurately is to reduce the heat losses by maintaining the insulated specimen can near the specimen temperature. This was done for the apparatus described next. For the thermal conductivity the electric heater method described appears to be simple, accurate and rapid even without controlling the can temperature.

6 Calorimeter Method

Tests were run using the calorimeter method of measuring Q which is discussed in Section 2.4. The calorimeter was made of OFHC copper and the specimen was Armco iron; each was 3 in. in diameter while the copper was 0.75 in. thick and the iron was 1.0 in. thick. One thermocouple was attached to the calorimeter. Three thermocouples were embedded in the heated surface of the iron and the signals were averaged. Each thermocouple was attached by placing the thermocouple leads in 0.010 in. × 0.010 in. × 0.375 in. grooves. The grooves were parallel for a given thermocouple and about 0.125 in. apart. The leads were carefully peened tightly into the grooves. It was found that thermocouples attached in this manner can give accurate surface temperatures provided water or silicone grease is carefully applied before the calorimeter and specimen are brought together. At the thermally insulated surface a single thermocouple was used. Because this thermocouple must be electrically insulated from the specimen in order to perform the temperature difference electrically, the leads were welded together and placed in a hole 0.030 in. in diameter and 0.06 in. deep. "Astroceram" cement was used to attach the thermocouple.

A hydraulic system was used to bring the calorimeter and specimen together under pressure. Four different sets of heaters and temperature controllers were used: one set for the specimen, another for the calorimeter, one for the furnace surrounding the sides and bottom of the specimen and the last for a furnace surrounding the calorimeter.

A summary of results of some tests for Armco Magnetic Ingot Iron for DC Applications is given in Table 2. In addition to the average of the measured properties, the estimated standard deviation and the TPRC values [7] are given. The estimated standard deviation for k is given by

$$\hat{\sigma}_k = \left[\sum_{i=1}^{n} (k_i - \bar{k})^2/(n-1) \right]^{1/2}$$

where n is the number of tests and $\bar{k}$ is the average. A similar expression is used for σ_{c_p}.

In the first set of room temperature tests (see the first column of Table 2), six drops of water were placed at the center of the

specimen before bringing the specimen and calorimeter together. In all the other sets of tests a 0.015-in. film of silicone grease was carefully applied using a "comb." There is a 2.4 percent difference between the $\bar{k}$ values measured using water and silicone grease and a 0.8 percent difference in the c_p's. For both $\bar{k}$ and $\bar{c}_p$ at 75 deg F, the silicone grease values are more accurate (if the TPRC values are taken to be the true values). In fact, the values are so close that the differences between the measured values and the TPRC values are less than the accuracy of reading the TPRC graphs. Only the silicone grease can be used at the higher temperatures.

The agreement with the TPRC data for the 300 deg and 400 deg F tests is also good except for the 300 deg F c_p value which is too large. The thermal conductivity like that in the electric heater method is much less sensitive to heat losses than the specific heat.

The experimental procedures given above are not recommended on the basis of accuracy since accuracy depends on the experimenter's skill and the development of the particular method. Rather the methods are recommended for the following reasons. Several properties can be simultaneously found from a single test. The tests are potentially inexpensive to perform because they are transient. Because of the brevity of the tests, biological products can be investigated before significant drying, etc., occurs. A large range of materials can be investigated; the ratio of the thermal diffusivity of Armco iron and Pyrex is nearly 100, but even more diverse materials have been investigated such as potatoes and aluminum.

7 Comparison of the Two Experimental Methods

The electric heater method is much simpler to use and the equipment is less expensive. It is recommended for these reasons. It is, however, limited to heating only and the temperature range is dependent upon the silicone rubber which cannot be heated above 450 deg F. Other materials can be used to extend this range. The calorimeter method can be used to either heat or cool and can be used for a very wide temperature range which is limited by the abilities to measure transient temperatures and to bring a calorimeter into thermal contact (not necessarily physical contact, however) with the specimen.

8 Summary and Conclusions

New transient solutions of the one-dimensional heat conduction equation for plates, cylinders and spheres are given that are particularly convenient for obtaining several thermal properties from a single experiment. All the proposed experiments utilize a specimen with an insulated surface and a heated one which is exposed to an arbitrary heat flux of finite duration but whose integrated value is known.

Two different types of experimental equipment are described and property measurements obtained from each are given. The experimental method using a thin electric heater is particularly attractive due to its simplicity in operation.

Acknowledgment

This research was partially supported by the National Science Foundation under Grant No. GK-16526. The authors appreciate the support and encouragement of Dr. Robert W. Little, Department of Mechanical Engineering and of J. W. Hoffman, Division of Engineering Research, Michigan State University. Mr. David Braisted performed the tests for the electric heater method.

References

1 Tye, R. D., ed., *Thermal Conductivity*, 2 Vol., Academic Press, New York, 1969.

2 Beck, J. V., "Transient Determination of Thermal Properties," *Nuclear Engineering Design*, Vol. 3, 1966, pp. 373–381.

3 Beck, J. V., "Analytical Determination of Optimum Experiments for Measurement of Thermal Properties," *Process Third International Heat Transfer Conf.*, Vol. IV, 1966, pp. 74–80.

4 Beck, J. V., "Determination of Optimum, Transient Experiments for Thermal Contact Conductance," *International Journal of Heat and Mass Transfer*, Vol. 12, 1969, pp. 621–633.

5 Pfahl, R. C., Jr., "Nonlinear Least Squares: A Method for Simultaneous Thermal Property Determination in Ablating Polymeric Materials," *J. Appl. Polymer Sci.*, Vol. 10, 1966, pp. 1111–1116.

6 Pfahl, R. C., Jr., and Mitchel, B. J., "Simultaneous Measurement of Six Thermal Properties of a Charring Plastic," *International Journal of Heat and Mass Transfer*, Vol. 13, 1970, pp. 275–281.

7 Touloukian, Y. S., *Thermophysical Properties of High Temperature Solid Materials*, MacMillan, New York, 1967.

H. G. ELROD
Department of Mechanical Engineering,
Columbia University,
New York, N. Y.

Two Simple Theorems for Establishing Bounds on the Total Heat Flow in Steady-State Heat-Conduction Problems With Convective Boundary Conditions

Introduction

THIS PAPER presents two theorems which can be used to establish limits on the total heat transfer that can take place in certain heat-conduction problems, thereby obviating the need for tedious or complicated calculations. The first of these theorems has often been used intuitively by practitioners of heat transfer engineering; a formal proof is given herein. The second theorem, perhaps more useful than the first, is not generally known.

Theorem I. Consider a solid body composed of material which may be both inhomogeneous and anisotropic, but whose properties are independent of temperature. Let the body be isolated from its surroundings except for exposure through space-variable heat-transfer coefficients to two distinct ambient temperatures. If, within some region of this body, the heat conductivity is increased (decreased), then the total heat flow from one exposed surface to the other will either increase (decrease), or remain the same.

A proof of this quite-obvious principle is given in Appendix A.

Theorem II. The actual heat flow taking place under the circumstances described in Theorem I will be no greater than that calculated when the shapes of the isothermal surfaces within the body are arbitrarily assumed, and no less than that calculated when the adiabatic surfaces within the body are assumed.

A proof of Theorem II is given in Appendix B. In a heuristic manner, however, we can deduce it directly from Theorem I. First note that nearly isothermal surfaces can be created within a conductive medium by locally increasing greatly the conductivity within thin layers. According to Theorem I, such changes can only tend to increase the total heat flow. Yet, if the layer conductivity is increased at a sufficient rate as the layer thicknesses are diminished (so that the layers degenerate to surfaces), the result of the whole process becomes the specification of the shapes of some isothermal surfaces. (It should be observed that the temperatures on these isothermal surfaces are not specified, but must be found from solution of a reduced heat-transfer problem.) Thus the introduction of isotherms into a conductive medium tends only to increase the total heat flow.

An argument similar to that used in the foregoing, but with thin layers of poorly conducting material, establishes that the introduction of adiabats tends only to decrease the total heat flow.

Crudely speaking, arbitrarily-selected isotherms constitute thermal short-circuits which increase heat flow, and arbitrarily-selected adiabats obstruct, and therefore reduce, the total heat flow.

It should be obvious that if the isotherms and adiabats which are assumed for the purposes of using Theorem II happen to be those which would exist anyway in the actual heat-flow problem, an exact result will be obtained. Thus the bounds on accuracy provided by Theorem II can be as close as the intuition and mathematical ability of the investigator permit. Generally, the difficulty of the attendant calculations will increase as the shape specifications are refined. However, a great deal of refinement should seldom be necessary for engineering purposes, and, if it should be, then direct finite-difference or finite-element calculation with an high-speed electronic digital computer should probably be undertaken.

Kirchoff's principle permits the removal of the restriction on temperature dependence for those cases where the surface temperatures are prescribed (tantamount to infinite heat-transfer coefficients), and, no doubt, the theorems are susceptible the generalization in a number of useful ways. In addition, the theorems are applicable in fields where heat-flow analogies are valid (electrostatics, incompressible potential fluid flow, etc.).

The remainder of this paper will be devoted to the presentation of several illustrative examples to show how simply the theorems can be used to obtain meaningful estimates of heat flow. It is hoped that many other applications will occur to the reader as he follows these examples and perceives opportunities to exercise his ingenuity.

Contributed by the Heat Transfer Division for publication (without presentation) in THE JOURNAL OF HEAT TRANSFER. Manuscript received by the Heat Transfer Division November 30, 1973. Paper No. 74-HT-C.

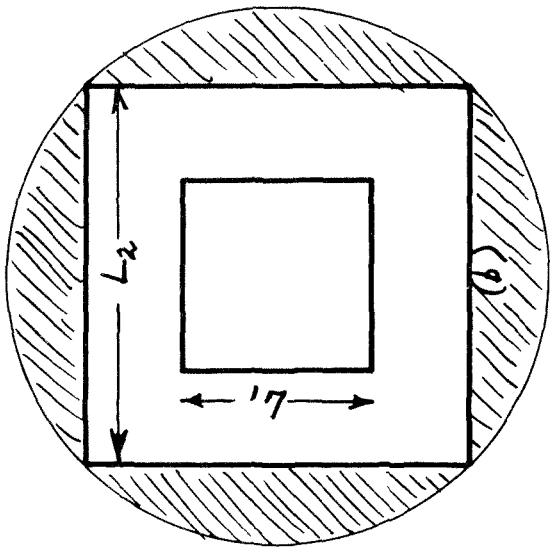

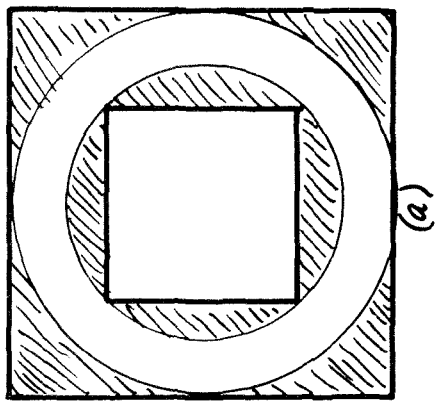

Fig. 1 Use of Theorem I in bounding the heat flow between square ducts

Heat Flow in the Region Bounded by Two Concentric Square Ducts

Fig. 1 depicts the region bounded by two concentric square ducts of sides L_1 and L_2, respectively. The ducts are isothermal at temperatures T_1 and T_2. The intervening medium has the constant conductivity, k. We wish to estimate the total heat flow.

To apply Theorem I to the present problem, we note in Fig. 1(a) that the insertion of extremely large conductivity material in the shaded regions will only increase the heat transfer. It will also turn the problem into one of heat transfer between two concentric circular ducts of radii $L_1\sqrt{2}$ and L_2, therefore

$$Q \leq \frac{2\pi k(T_1 - T_2)}{\ln\left(\frac{L_2}{L_1}\right) - \frac{1}{2}\ln 2} \tag{1}$$

On the other hand, Fig. 1(b) shows that the actual problem can be recovered by short-circuiting in the shaded areas between two circular ducts of radii L_1 and $L_2\sqrt{2}$, therefore

$$Q \geq \frac{2\pi k(T_1 - T_2)}{\ln\left(\frac{L_2}{L_1}\right) + \frac{1}{2}\ln 2} \tag{2}$$

To apply Theorem II, we first assume that the isotherms have the shapes of squares. With reference to Fig. 2, the following inequality is obtained, thus

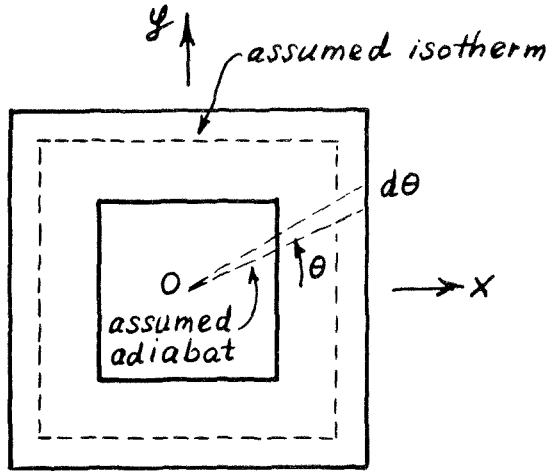

Fig. 2 Use of Theorem II in bounding the heat flow between square ducts

$$Q \leq \frac{(T_1 - T_2)}{\int_1^2 \frac{dl}{kA}} = \frac{k(T_1 - T_2)}{\int_1^2 \frac{dx}{8x}} = \frac{8k(T_1 - T_2)}{\ln\left(\frac{L_2}{L_1}\right)} \tag{3}$$

Next we assume the adiabats consist of radial lines emanating from the duct center. The differential heat flow under such an assumption corresponding to "$d\theta$" would be

$$dQ = \frac{(T_1 - T_2)}{\int_1^2 \frac{dl}{kA}} = \frac{(T_1 - T_2)k}{\int_1^2 \frac{\left(\frac{dx}{\cos\theta}\right)}{\left(\frac{x}{\cos\theta}\right)} d\theta} = \frac{k(T_1 - T_2)d\theta}{\ln\left(\frac{L_2}{L_1}\right)} \tag{4}$$

Then the *actual* total heat flow satisfies the inequality

$$Q \geq \frac{2\pi k(T_1 - T_2)}{\ln\left(\frac{L_2}{L_1}\right)} \tag{5}$$

Examination of the results discloses that equation (5) always yields a higher lower bound than does equation (2), and is therefore to be preferred. On the other hand, equation (3) yields a better (lower) upper bound than equation (1) only for the lower range of L_2/L_1. Interestingly enough, for very large L_2/L_1 we see that the actual heat transfer tends exactly to

$$Q \underset{\left(\frac{L_2}{L_1}\right)}{\longrightarrow} \frac{2\pi k(T_1 - T_2)}{\ln\left(\frac{L_2}{L_1}\right)} \tag{6}$$

Space-Variable Heat-Transfer Coefficients

For a second example, let us analyze a case with space-variable heat-transfer coefficients. Fig. 3 shows the sort of variation that is experienced on circular cylinders in crossflow. The curve for a Reynolds number of 219,000 corresponds to a stainless-steel tube of 1.1 in. OD and 0.05 in. wall thickness located transverse to an airstream moving at 500 ft/sec at a pressure of 1 atm and a temperature of 150 F. To complete the specification of the physical situation, let us assume that internally there is air at 5 atm and 100 F moving at 100 ft/sec.

Theorem II readily provides bounds for the heat flow in this instance. Referring to Fig. 4, we assume that the inner and outer surfaces of the tube are isothermals, and obtain thereby too high an answer, thus

$$Q \leq \frac{2\pi(T_0 - T_1)}{\frac{1}{\bar{h}_1 r_1} + \frac{1}{k_w}\ln\frac{r_2}{r_1} + \frac{1}{\bar{h}_2 r_2}} \tag{7}$$

Here $\bar{h}_1$ and $\bar{h}_2$ are the angular average heat-transfer coefficients. Neglecting the relatively small change of air thermal conductivity, we can rearrange this relation to get

$$Q \leq \frac{\pi k_a(T_0 - T_i)}{\frac{1}{(\overline{\mathrm{Nu}})_1} + \frac{k_a}{2k_s}\ln\frac{r_2}{r_1} + \frac{1}{(\overline{\mathrm{Nu}})_2}} \tag{8}$$

Alternatively, assumption of radial adiabats (which puts the surface resistances locally in series) leads to the following inequality, thus

$$Q \geq k_a(T_0 - T_i)\frac{1}{2}\int_0^{2\pi} \frac{d\theta}{\frac{1}{(\mathrm{Nu})_1} + \frac{k_a}{2k_s}\ln\left(\frac{r_2}{r_1}\right) + \frac{1}{(\mathrm{Nu})_2}} \tag{9}$$

Calculations based on $k_a = 0.017$ and $k_s = 10$ Btu/hr-ft-F and $(\mathrm{Nu})_1 = 320$ yield the inequality

$$191.7 \leq Q \leq 194.8 \text{ Btu/hr-ft}$$

for our example.

Effective Heat Conductivity of a Matrix

Fig. 5 shows a cross-sectional cut through an inhomogeneous solid comprised of a material with conductivity, k_1, into which have been embedded some evenly-spaced square bars with conductivity, k_2. Let us suppose that what we see represents a small segment of a large slab of this composite material, the slab faces being at $y = \pm L$. The dimension "L" is presumed to be much larger than the wavelengths associated with the inhomogeneities, and an effective thermal conductivity is sought for the medium. Since the material is anisotropic, we find the value appropriate to the y-direction.

It is unlikely that the predicted effective thermal conductivity can be sensitive to the thermal boundary conditions imposed on the slab. However, for definiteness let us assume that the two slab surfaces are isotherms. For reasons of symmetry, AD and BC are then recognized to be adiabats, and the temperature difference from AB to DC is independent of "x." It is shown in Appendix C that the heat flow is the same as if both AB and DC

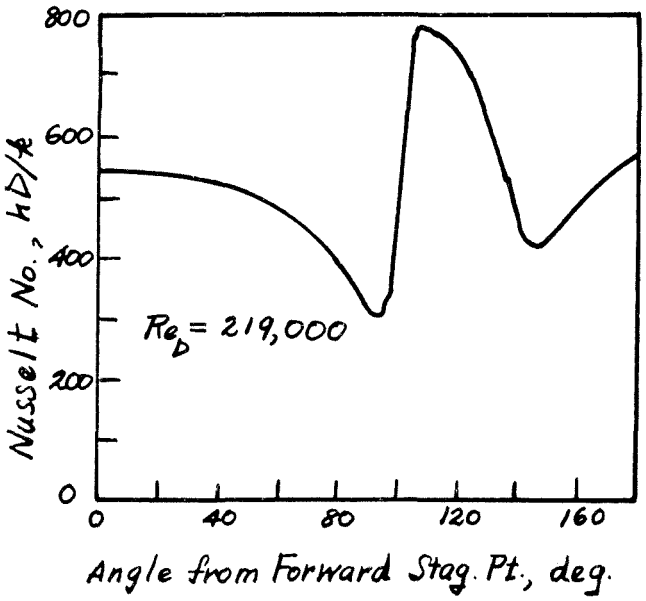

Fig. 3 Local Nusselt numbers for air flowing past circular cylinder (reference [3])

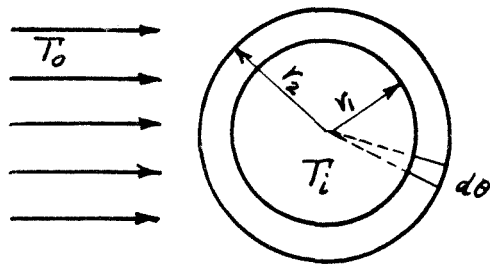

Fig. 4 Schematic diagram of air flowing across cylinder

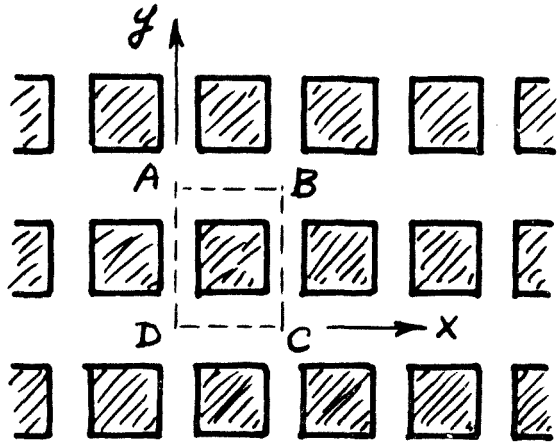

Fig. 5 Cross section of composite material

were isotherms supporting this constant temperature difference, and we shall use this fact for the analysis which follows.

Fig. 6 gives an enlargement of the rectangle ABCD. (Allowance has been made for the insertion of bars with rectangular cross section.) To obtain an upper limit to the heat flow that can take place from AB to CD, assume that lines joining EF and GH are isotherms, thus

$$Q \leq \frac{\Delta T}{\frac{c-b}{k_1 d} + \frac{1}{\left\{k_1\frac{(d-a)}{b} + k_2\frac{a}{b}\right\}}} \tag{9}$$

To obtain a lower limit to the heat flow, assume that the lines joining IL and JK are adiabats, thus

$$Q \geq k_1\frac{(d-a)\Delta T}{c} + \frac{\Delta T}{\frac{(c-b)}{k_1 a} + \frac{b}{k_2 a}} \tag{10}$$

As a definition of effective thermal conductivity, k_e, we take

$$Q \equiv k_e d\Delta T/c \tag{11}$$

It is then readily found that "k_e" satisfies the inequality

$$k_1\left(1 - \frac{a}{d}\right) + \frac{(ca/bd)}{\frac{\left(\frac{c}{b} - 1\right)}{k_1} + \frac{1}{k_2}} \leq k_e \leq \frac{1}{\frac{\left(1 - \frac{b}{c}\right)}{k_1} + \frac{(db/ca)}{k_2 + k_1\left(\frac{d}{a} - 1\right)}} \tag{12}$$

The last expression satisfies all the obvious extreme tests to which it can be subjected; e.g., $a = 0$, $b = 0$, $a = d$, $b = c$, etc. For an interesting specific example, let us take $c = d = 2a = 2b$ and $k_2 = 4k_1$. We immediately find

$$1.30 \leqq k_e/k_1 \leqq 1.43 \tag{13}$$

To "hedge" our bets, we split the difference and write

$$k_e/k_1 = 1.365 \pm 0.065$$

The error cannot exceed 5 percent, and, for engineering purposes, further calculation is unnecessary.

Conclusion

Two simple theorems have been presented which establish bounds on the heat flow which can take place in a wide class of heat-conduction problems with surface convection. Illustrative examples have been given in which the theorems are applied to a rectangular annulus, a cylinder with a widely-variable heat-transfer coefficient, and to a matrix medium composed of materials with distinctly different thermal conductivities.

APPENDIX A

Proof of Theorem I

Fig. 7 illustrates the situation envisioned for the validity of Theorem I. We treat a solid body composed of material which may be both inhomogeneous and anisotropic, but whose properties are temperature-independent. The body is isolated (insulated) except for exposure to temperature, N, as ambient at S_1, and temperature zero as ambient at S_2 (no generality is thereby lost in this linear problem).

To commence the proof, form the quantity

$$I \equiv N \iint_{S_1} q_n dS + \iint_{S_1+S_2} \frac{q_n^2}{h} dS = N \iint_{S_1} q_n dS + \iint_{S_1} (T - N) q_n dS + \iint_{S_2} T q_n dS = \iint_{S_1+S_2} T q_n dS = \iint_{S} T q_n dS \tag{A1}$$

Here we have used the facts that $q_n = h(T - T_a)$ on S_1 and S_2 and $q_n = 0$ on all the insulated surfaces.

Gauss' theorem can be used on the last integral in equation (A1). Rearrangement then gives

$$NQ = \iiint \vec{q} \cdot \nabla T dV - \iint \frac{q_n^2 dS}{h} \tag{A2}$$

Here "Q" denotes the total heat flow from S_1 to ambient, and use has been made of the fact that, for steady-state heat conduction $\mathrm{div}(\vec{q}) = 0$. To prevent violation of the Second Law of Thermodynamics, heat must now flow "uphill," so that $\vec{q} \cdot \nabla T \leq 0$. Then it is seen that Q is necessarily negative, as was to be expected.

Let us now consider the variations in equation (A2) that can be effected by variations internally of the thermal conductivity. First note that on the convective surfaces

$$\delta q_n = \delta\{h(T - T_a)\} = h\delta T \tag{A3}$$

then, from (A2) we get

$$N\delta Q = \iiint (\delta\vec{q} \cdot \nabla T) dV + \iiint (\vec{q} \cdot \nabla \delta T) dV - 2 \iint_{S_1+S_2} \delta T q_n dS \tag{A4}$$

but

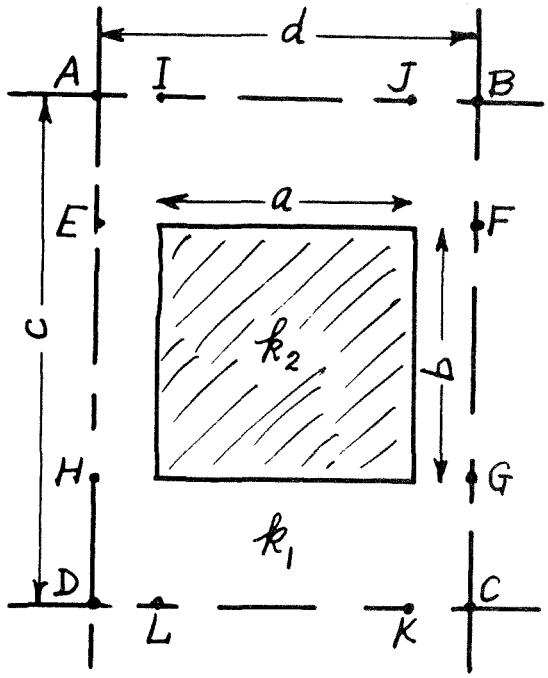

Fig. 6 Detail enlargement from Fig. 5 for effective-conductivity analysis

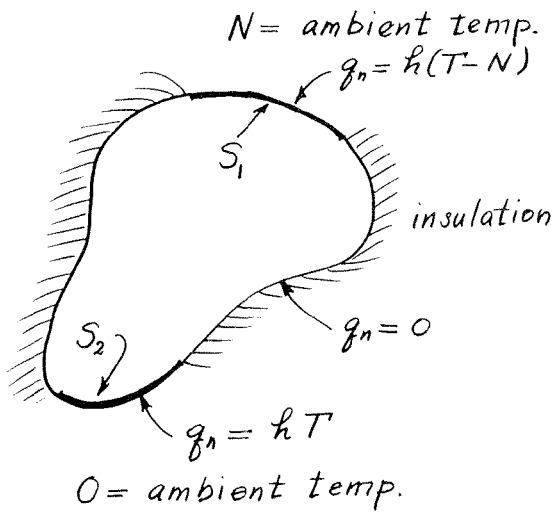

Fig. 7 Configuration assumed for Theorem I

$$\iint_{S_1+S_2} \delta T q_n dS = \iint_{S} \delta T q_n dS$$

therefore

$$N\delta Q = \iiint (\delta\vec{q} \cdot \nabla T - \vec{q} \cdot \nabla \delta T) dV \tag{A5}$$

If the solid material is isotropic, then

$$\vec{q} = -k\nabla T \tag{A6}$$

and

$$\delta\vec{q} \cdot \nabla T - \vec{q} \cdot \nabla \delta T = -\delta k(\Delta T)^2 - k\nabla\delta T \cdot \Delta T + k\nabla T \cdot \nabla \delta T$$

or

$$N\delta Q = -\iiint \delta k (\nabla T)^2 dV \tag{A7}$$

It is therefore seen that Q, which is already negative, will become more negative with any augmentation of the thermal conductivity within the body.

If the material is anisotropic, then

$$q_j = -k_{ij} \frac{\partial T}{\partial x_i} \tag{A8}$$

and

$$\delta\vec{q}\cdot\nabla T - \vec{q}\cdot\nabla\delta T = -\delta k_{ij} \frac{\partial T}{\partial x_i}\frac{\partial T}{\partial x_j} - k_{ij}\frac{\partial}{\partial x_i}\delta T \frac{\partial T}{\partial x_j} + k_{ij}\frac{\partial T}{\partial x_i}\frac{\partial \delta T}{\partial x_j} \tag{A9}$$

As a consequence of Onsager's principle, it is generally considered that the conductivity tensor of an anisotropic medium can be treated as symmetric (2).[1] Then $k_{ij} = k_{ji}$, and equation (A5)

$$N\delta Q = -\iiint \delta k_{ij} \frac{\partial T}{\partial x_i}\frac{\partial T}{\partial x_j} dV \tag{A10}$$

At this point, in the case of an anisotropic medium, it is necessary to be more specific in what is meant by the words "increase the heat conductivity." Since the conductivity tensor is symmetric, there exists at each point within the body a principal axis system with direction unit vectors $\hat{e}_1'$, $\hat{e}_2'$, and $\hat{e}_3'$ such that the tensor referred to this system is diagonalized, with principal values K_1, K_2, and K_3. The heat conductivity is said to be increased if any of these principal conductivities is increased *without* alteration of the principal directions. Transformation of the tensor from the primed to the unprimed system gives

$$k_{ij} = \sum_{n=1}^{3} K_n \cos(x_n', x_i) \cos(x_n', x_j) \tag{A11}$$

The excursions in equation (A10) are to be taken without alteration of the foregoing direction cosines. Hence, with the aid of equation (A11), we get

$$N\delta Q = -\iiint \sum_{n=1}^{3} \delta K_n \cos(x_n', x_i) \frac{\partial T}{\partial x_i} \times \cos(x_n', x_j) \frac{\partial T}{\partial x_j} dV \tag{A12}$$

but

$$\cos(x_n', x_i)\frac{\partial T}{\partial x_i} = \frac{\partial T}{\partial x_n'}, \text{ etc.}$$

$$\therefore \quad N\delta Q = -\iiint \sum_{n=1}^{3} \delta K_n \left(\frac{\partial T}{\partial x_n'}\right)^2 dV \tag{A13}$$

If, for each "n," $\delta K_n \geqq 0$; i.e., if the "thermal conductivity is increased," then it is seen that Q is made more negative. Hence Theorem I is proved.

APPENDIX B

Proof of Theorem II

To demonstrate the first part of Theorem II concerning isotherms, hypothesize that a single infinity of isothermal surfaces $\phi(\vec{r}) = \beta$ has been named within the body of Fig. 7 (see Fig. 8), and that the temperature solution, $T'(\beta)$ has been found by elementary heat balances. For example, let us perform such a heat balance on the elementary shaded volume element lying between "β" and "$\beta + d\beta$" in Fig. 8. Let S^I denote the internal surface reduces to of this element, and S^E denote the surface it shares externally with the entire body. A heat balance gives

$$\iint_S q_n' dS - \iint_{S^E} h(T_a - T') dS \tag{B1}$$

Now, extending the conductive flux integral to include the bounding surface, S^E, as well, and using the expression for an anisotropic medium, we get

$$\iint_{S^I} -k_{ij}\frac{\partial T'}{\partial x_j} dS_i + \iint_{S^E} -k_{ij}\frac{\partial T'}{\partial x_j} dS_i = \iint_{S^E} \left\{h(T_a - T') - k_{ij}\frac{\partial T'}{\partial x_j}\hat{n}_i\right\} dS \tag{B2}$$

Or:

$$\iiint \frac{\partial}{\partial x_i} k_{ij}\frac{\partial T'}{\partial x_j} dV = \iint_{S^E} \left\{h(T' - T_a) + k_{ij}\frac{\partial T'}{\partial x_j}\hat{n}_i\right\} dS \tag{B3}$$

We have here energy conservation for a nearly isothermal layer of prescribed shape. *If* the isotherms were not prescribed, the conservation principle would be applicable to volume elements two infinities smaller (i.e., of differential extent in all directions). Then, of course, the integrand on the left-hand side of equation (B3) would be zero, yielding the usual differential equation for heat conduction. And the right-hand side could also be proved zero at each local point on the surface, yielding the usual convective boundary condition. These reductions are not available for the fictitious temperature distribution, T'.

It is clear that equation (B3) can be reduced in the limit, as $d\beta \to 0$, to a surface integral on the left, and a line integral on the right. We shall not bother to do so, but observe, rather, that each side is presently of $0(\delta T')$. Hence if some function of T' is introduced inside the integrals of equation (B3), the variation of this function being of $(0\delta T')$, the error is only $0(\delta T')^2$, and the modified equation is equally valid, thus

$$\iiint T' \frac{\partial}{\partial x_i} k_{ij}\frac{\partial T'}{\partial x_j} dV = \iint_{S^E} T' \left\{h(T' - T_a) + k_{ij}\frac{\partial T'}{\partial x_j} n_i\right\} dS \tag{B4}$$

Since this equation applies to each isothermal layer of the solid, it also applies *globally*, based on the presumption that $\phi(\vec{r})$ is unique. Rearrangement of equation (B4), and the use of Gauss' theorem yields

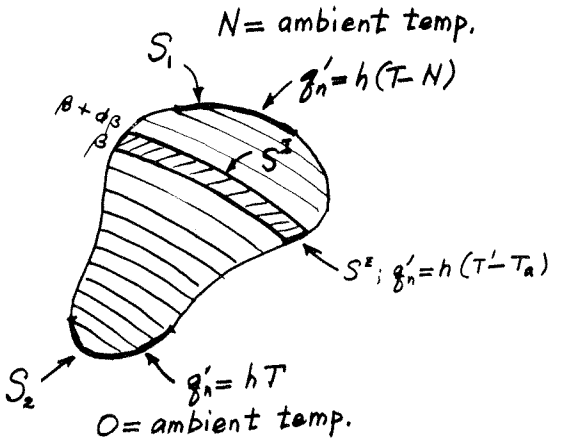

Fig. 8 Heat balance with arbitrary isotherms, $T'(\beta)$

[1] Numbers in brackets designate References at end of paper.

$$\iint T'h(T' - T_a)dS = \iint T'q_n'dS$$

$$= \iiint T' \frac{\partial}{\partial x_i} k_{ij} \frac{\partial T'}{\partial x_j} dV - \iint T'k_{ij} \frac{\partial T'}{\partial x_j} dS_i$$

$$= - \iiint k_{ij} \frac{\partial T'}{\partial x_i} \frac{\partial T'}{\partial x_j} dV \quad \text{(B5)}$$

To compare the heat flow with prescribed isotherms and distribution T' with the heat flow obtained with the exact distribution T, form the quantity (see Fig. 8)

$$J \equiv N \iint_{S_1} q_n'dS + \iint_{S_1+S_2} \frac{{q'_n}^2}{n} dS + N \iint_{S_1} q_n \, dS$$

$$+ \iint_{S_1+S_2} \frac{{q_n}^2}{h} dS - 2N \iint_{S_1} q_n dS - 2 \iint_{S_1+S_2} \frac{q_n q_n'}{h} dS \quad \text{(B6)}$$

With $q_n' = h(T' - T_a)$ and $q_n = h(T - T_a)$, and with $h = 0$ on all surfaces except S_1 and S_2, we obtain

$$J = \iint T'q_n'dS + \iint Tq_n dS - 2 \iint T'q_n dS \quad \text{(B7)}$$

Use Gauss' theorem, equation (B5), and the fact that $\text{div}(\vec{q}) = 0$ to reduce the above expression to

$$J = - \iiint k_{ij} \frac{\partial}{\partial x_i} (T' - T) \frac{\partial}{\partial x_j} (T' - T) dV \quad \text{(B8)}$$

"k_{ij}" is a positive symmetric matrix, so that the integrand in equation (B8) is everywhere greater than or equal to zero (see the argument for equations (A11–13)).

On the other hand, it is readily seen from equation (B6) that

$$J = N(Q' - Q) + \iint_{S_1+S_2} \frac{(q_n' - q_n)^2}{h} dS \quad \text{(B9)}$$

Equate the two equations for "J" to obtain finally

$$N(Q' - Q) = - \iiint k_{ij} \frac{\partial(T' - T)}{\partial x_i} \frac{\partial(T' - T)}{\partial x_j} dV$$

$$- \iint_{S_1+S_2} \frac{(q_n' - q_n)^2}{h} dS \quad \text{(B10)}$$

Now it was shown in Appendix A that Q is necessarily negative. According to equation (B10), then, "Q"' is even more negative. In other words, the heat flow has been increased by specification of the isotherms.

To prove the second part of Theorem II, namely, that the specification of adiabats can only tend to decrease total heat flow, consider the formulation when an interior surface, S^I, divides the solid of Fig. 7 into two parts, A and B. For the purposes of obtaining a good lower bound for heat transfer, this interior surface should stretch from S_1 to S_2. However, it need not. In fact, we do not even presume at the moment that S^I is adiabatic.

The expression for "I," as in equation (A1), reduces to

$$I = \iint_S Tq_n dS = \iint_S T^A q_n{}^A dS + \iint_{S^I} T^A q_n{}^A dS$$

$$- \iint_{S^I} T^A q_n{}^A dS + \iint_S T^B q_n{}^B dS + \iint_{S^I} T^B q_n{}^B dS$$

$$- \iint_{S^I} T^B q_n{}^B dS \quad \text{(B11)}$$

Here regions A and B have both been shown sharing the external surface, S, although such supposition plays no role in the proof. Gauss' theorem, and the fact that $q_n{}^B = -q_n{}^A$, immediately reduce equation (B11) to

$$I = \iiint_{A+B} \vec{q} \cdot \nabla T dV - \iint_{S^I} q_n{}^A (T^A - T^B) dS \quad \text{(B12)}$$

At this point, we specify which portions of S^I are to become adiabatic, and we do so by designating uniformly thereon a contact coefficient, "h^*." Then $q_n{}^A = h^*(T^A - T^B)$. Elsewhere on S^I, where temperature continuity is to be maintained, the surface integral can be ignored. Hereafter, S^I shall denote only the "active" parts of the original internal surface, thus

$$I = \iiint_{A+B} \vec{q} \cdot \nabla T dV - h^* \iint_{S^I} (T^A - T^B)^2 dS \quad \text{(B13)}$$

Or:

$$NQ = \iiint_{A+B} \vec{q} \cdot \nabla T dV - \iint_{S_1+S_2} \frac{{q_n}^2}{h} dS$$

$$- h^* \iint_{S^I} (T^A - T^B)^2 dS \quad \text{(B14)}$$

Variations in Q are now considered as they are produced solely by variations of h^*. The analysis here is so parallel to that in Appendix A that it will not be reproduced here. The result is

$$N \frac{dQ}{dh^*} = - \iint_{S^I} (T^A - T^B)^2 dS \quad \text{(B15)}$$

Now from equation (B14) it can be argued that Q is always negative, and from equation (B15) it is seen that a decrease in h^* tends to increase Q; i.e., reduce its absolute value. Moreover, if it be granted that $(T^A - T^B)^2 \leq N^2$, then the derivative dQ/dh^* exists for all values of h^*, ranging from 0 (adiabatic) to ∞ (zero interfacial resistance, and consequently zero temperature discontinuity). It is seen then that the introduction of an arbitrary adiabatic surface within the solid can only tend to reduce the absolute value of the total heat flow.

By induction we can infer the result for the introduction of further adiabatic surfaces, since, after the addition of each such surface, new problems in solid heat transfer are generated which belong to the original class; namely, consisting of solids exposed at one surface to ambient temperature, N, and at another surface to temperature, 0, with all other surfaces adiabatic. Hence each successive introduction of an adiabatic surface tends to diminish the magnitude of the total heat flow.

APPENDIX C

Temperature Specifications for Inhomogeneous Solid

With reference to Fig. 5, we suppose that the material has infinite extent in the x-direction, and that planes at $y = \pm L$ are specified as isotherms. In such circumstances, $\overline{AD}$ and $\overline{BC}$ lie on planes of symmetry. Furthermore, if "L" is much greater than either of the transverse edge dimensions of the imbedded bars (i.e., $L \gg a$ or b), then the temperature drop per layer of bars must become uniform within the interior. Thus if $T = T_D + f(x)$ along $\overline{DC}$, the temperature along $\overline{AB}$ must be $T = T_D + f(x) + \delta$. As noted, $\overline{AD}$ and $\overline{BC}$ are adiabats.

With the foregoing boundary conditions on temperature, the heat flow problem in ABCD can, by reason of linearity, be broken into three parts: (a) a problem for which $T = T_D$ uniformly on $\overline{AB}$ and $\overline{DC}$; (b) a problem for which $T = \delta$ uniformly on $\overline{AB}$ and zero uniformly on $\overline{CD}$; (c) a problem for which $T = f(x)$ on both $\overline{AB}$ and $\overline{DC}$.

By reasons of symmetry, the net heat flow in the y-direction for problems (a) and (c) in the foregoing is zero. Thus the calculation of the net heat flow in the y-direction from problem (b) alone is justified.

References

1 Payne, L. E., and Weinberger, H. F., "New Bounds in Harmonic and Biharmonic Problems," *Journal of Mathematics and Physics*, Vol. 33, 1954, pp. 291–307.

2 Carslaw, and Jaeger, *Conduction of Heat in Solids*, Oxford at the Clarendon Press, Second ed., 1959, p. 41.

3 Giedt, W. H., TRANS. ASME, Vol. 71, 1949, p. 375.

V. K. Dhir
Res. Assoc. Assoc. Mem. ASME

J. H. Lienhard
Professor. Mem. ASME

Boiling and Phase-Change Laboratory,
Mechanical Engineering Department,
University of Kentucky,
Lexington, Ky.

Peak Pool Boiling Heat Flux in Viscous Liquids[1]

The stability of a gas jet in a surrounding viscous liquid is studied. An expression is developed for the critical velocity at which the jet becomes unstable in a returning viscous liquid. The stability analysis is made to correspond with the geometrical configuration of gas jets and liquid columns similar to those observed near the peak pool boiling heat flux. The critical velocity of the gas jet is then used to obtain the functional form of the peak heat flux on flat plates and cylindrical heaters. The expressions are compared with original observations of the peak heat flux in very viscous liquids on flat plate, and cylindrical, heaters at both earth-normal, and elevated, gravities.

Introduction

Most prior studies of the peak pool boiling heat flux, $q_{\max}$, have ignored the liquid viscosity. Kutateladze's [1][2] and Zuber's [2] expressions for the peak flux on infinite heaters were for inviscid liquids. They predicted that the peak would occur when the jets in an escaping vapor configuration (as shown in Fig. 1) became Helmholtz unstable. Zuber's expression for the peak heat flux was substantially the same as Kutateladze's, namely

$$q_{\max_Z} = \frac{\pi}{24} \rho_g^{1/2} h_{fg} [\sigma g(\rho_f - \rho_g)]^{1/4} \tag{1}$$

Borishanski [3] subsequently suggested dimensionless groups to characterize the boiling problem. One of these was the Borishanski number, $(\rho_f \sigma/\mu_f^2)\sqrt{\sigma/g(\rho_f - \rho_g)}$. Including its contribution in equation (1), he was able to make a small correction for the influence of viscosity in existing data.

However, a difficulty arises in interpreting the influence of viscosity—it can affect $q_{\max}$ in two very different ways: 1 In 1970, Lienhard and Keeling [4] correlated $q_{\max}$ data for long ribbons which admitted a sidewise inflow of liquid. This inflow led (as Costello, et al. [5] noticed in 1965) to large variations of $q_{\max}$. In [4] these variations were correlated with the help of a modified Borishanski number. 2 The other viscosity influence is one which operates internally in the hydrodynamic process. When the liquid is very viscous the wave collapse mechanisms that cause transition, change and with them q_{max}, are affected. This even occurs on a flat plate with vertical side walls to prevent any induced convective flow, if the viscosity is large enough.

Our present interest is in the latter *internal* viscous influence. We shall consider two configurations: the flat plate and the horizontal cylinder, neither of which induces a side flow into the rising vapor jets. Cylinders were considered by Bobrovich, et al. [6] and by Lienhard, et al. [7,8] who showed that $q_{\max}$ in inviscid liquids could be correlated by expressions of the type:

$$q_{\max}/q_{\max_Z} = f(R') \quad \text{where} \quad R' \equiv R\sqrt{g(\rho_f - \rho_g)/\sigma} \tag{2}$$

Sun [9] subsequently formulated a hydrodynamic theory which showed what form equation (2) should take. He found that for cylinders, so small that the vapor jet diameter is less than half the Taylor unstable wavelength, λ_d, the vapor jets will be as shown in Fig. 1. He took the Helmholtz unstable disturbance in the jets to be the Rayleigh wavelength, $2\pi(R + \delta)$, regardless of λ_d, and the Helmholtz wavelength to equal λ_d. He obtained:

$$q_{\max}/q_{\max_Z} = 0.89 + 2.27 \exp(-3.44\sqrt{R'}) \tag{3}$$

Equation (3) was obtained by using an experimental expression for the thickness of the vapor blanket, δ, surrounding a cylindrical heater. We [10] subsequently showed how to get the following simplified expressions (which differ only slightly from equation (3)) for $q_{\max}$ on cylinders:

$$\frac{q_{\max}}{q_{\max_Z}} = \begin{cases} 0.94/\sqrt[4]{R'}, & R' \leq 1.17 \\ 0.904, & R' \geq 1.17 \end{cases} \tag{4}$$

In [10] we also showed that equation (1) is low since Zuber used the Rayleigh wavelength for the Helmholtz unstable wavelength, instead of λ_d. This change yielded a more accurate result for the peak heat flux on a flat plate, $q(\max_F)$, in an inviscid liquid:

$$q_{\max_{F_{\text{inviscid}}}} = 1.14\, q_{\max_Z} \tag{5}$$

The present work will obtain the functional form of an expres-

[1] This work was supported by NASA Grant NGR-18-001-035, under the cognizance of the Lewis Research Center.
[2] Numbers in brackets designate References at end of paper.
Contributed by the Heat Transfer Division for publication in the Journal of Heat Transfer. Manuscript received by the Heat Transfer Division, April 24, 1973. Paper No. 74-HT-J.

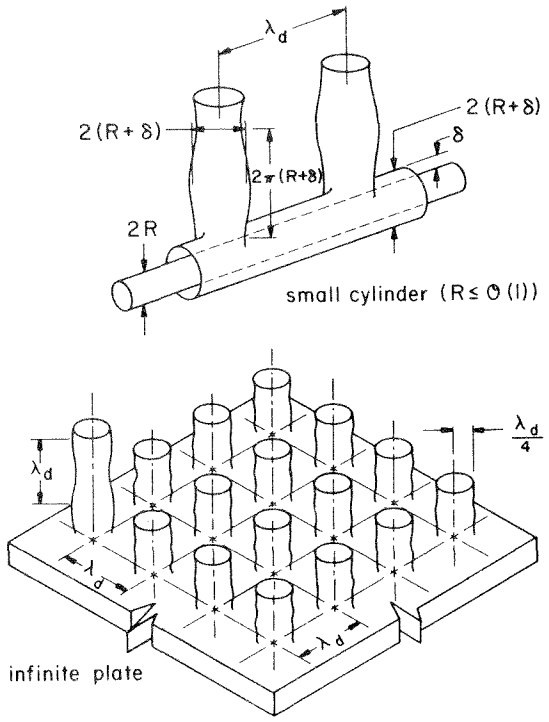

Fig. 1 Vapor removal configuration on an "infinite" flat plate and cylindrical heaters

sion for the peak heat flux in these geometries when the fluid viscosities are taken into account. This will be done by first determining what form the critical velocity of gas jets in viscous liquids takes, and then combining this function with the energy equation. Finally, we will compare these predictions with data for flat plates and cylindrical heaters operating under both earth-normal and elevated gravities.

Analysis

The peak heat flux on a heater can be written quite easily by making an energy balance at the surface of the heater:

$$q_{\max} = \rho_g h_{fg} U_H A_j / A_h \tag{6}$$

where A_j is the total area of the jets on an area A_h of the heater. U_H is the maximum, or critical, velocity at which the gas jets become unstable and obstruct the flow of liquid to the heater surface.

In the viscous analysis we assume that A_j/A_h is the same as in the inviscid case; hence it is the same as given in [10]. This involves the supposition that the same vapor-escape models hold good as far as jet size, location and orientation are concerned. Thus our aim will be to find the velocity at which the jets become unstable in a viscous liquid.

Infinite Horizontal Flat Plate. The vapor jets are assumed to be located at the points where a two-dimensional grid of Taylor-unstable waves collapses. It was recently shown by Sernas, et al. [11] that a three-dimensional wave analysis gives jets at the same locations on the grid as Zuber assumed in his two- dimensional analysis. The wavelength, λ_d, has been shown [12] to be influenced by liquid viscosity, and its dependence on liquid viscosity is known from that analysis.

The assumed configuration of the vapor jet, along with the liquid-vapor velocity profiles, is shown in Fig. 2. The figure contrasts the vapor removal idealization for the inviscid case with that which we assume for the viscous case. In the viscous case we cannot treat a circular jet in a square area if the analysis is to be at all tractable. Thus we inscribe a circular liquid return path inside the square area. We also assume:

1 The vapor and liquid velocities, U_g and U_f, = 0 on the interface. Actually the interface velocity might be positive or negative, but it will be small.

2 The Poiseuille velocity profile is valid in the vapor jet.

3 The analysis is two-dimensional. The pressure resulting from curvature of the jet will be added later and velocities will be adjusted such that:

4 The mass inflow of liquid in the circular annulus is matched by the gas outflow in the circular jet. U_f must be locally maximum or minimum at $y = 2R_j$ to satisfy the symmetry condition: $(dU/dy) = 0$ at $y = 2R_j$.

5 The shear stresses are matched at the interface.

The resulting velocity profiles are obtained by fitting even polynomial functions in y/R_j to these conditions. For the gas we obtain

Nomenclature

A_h = area of flat plate, or cylindrical, heater

A_j = combined cross-sectional area of vapor jets escaping from an area, A_h, of the heater

c = speed of a travelling disturbance in a liquid-vapor interface

F = perturbation amplitude function, see equation (A2)

g, g_e = actual gravity or body force acting on the heater, subscript, e, denotes earth-normal gravity

h_{fg} = latent heat of vaporization

k = wave number, 2π/wavelength

M = a dimensionless group characterizing the influence of liquid viscosity, $\rho_f \sigma^{3/4}/\mu_f g^{1/4}(\rho_f - \rho_g)^{3/4}$

P, $\bar{P}$ = dimensionless perturbation pressure as defined in equation (A14); overbar denotes the absolute pressure on the heater surface

p, p_f = dimensionless perturbation pressure, in the gas and liquid phase, respectively, (physical pressures divided by $\rho_g U(f_m)^2$)

$q_{\max}$, $q(\max_F)$ = peak flux for a particular heater geometry and for an "infinite" flat plate, respectively

$q(\max_Z)$ = Zuber's prediction of the peak heat flux on an infinite flat plate, defined in equation (1) (used as a dimensionless group in the present study)

R = radius of a cylindrical heater

R' = dimensionless radius of a cylindrical heater, $R\sqrt{g(\rho_f - \rho_g)/\sigma}$

Re = Reynold's number, $U(f_m)$-$R_j\rho_g/\mu_g$

R_j = radius of an escaping vapor jet

S = a dimensionless number (product of reciprocal Weber number and Reynolds number) as defined in equation (A14)

T = dimensionless perturbation tangential stress as defined in equation (A14)

t = dimensionless time (physical time divided by $R_j/U(f_m)$)

(Continued on next page)

$$U_g = U_{g_m}(1 - r^2/R_j^2) \tag{7}$$

where the subscript m denotes the maximum value; and for the liquid

$$U_f = U_{g_m}\left\{\left[\frac{107}{54}\frac{\mu_g}{\mu_f} - \frac{11}{81}\frac{\rho_g}{\rho_f}\right] - \left[\frac{168}{54}\frac{\mu_g}{\mu_f} - \frac{24}{81}\frac{\rho_g}{\rho_f}\right]\frac{r^2}{R_j^2} + \left[\frac{69}{54}\frac{\mu_g}{\mu_f} - \frac{15}{81}\frac{\rho_g}{\rho_f}\right]\frac{r^4}{R_j^4} - \left[\frac{8}{54}\frac{\mu_g}{\mu_f} - \frac{2}{81}\frac{\rho_g}{\rho_f}\right]\frac{r^6}{R_j^6}\right\} \tag{8}$$

These results incorporate considerable physical approximation and, indeed, when we complete the analysis we shall find it necessary to adjust one constant before the theory will fit the experimental results. However, the actual physical configuration is so complicated that we could hope for no more. What the present analysis will yield is the proper form of the dependence of the peak heat flux on the relevent dimensionless groups. In the light of this objective our failure to represent the configuration more precisely is of no great importance.

Equation (8) gives a maximum downward velocity of:

$$U_{f_m} = -U_{g_m}\left[0.3557\frac{\mu_g}{\mu_f} + 0.0388\frac{\rho_g}{\rho_f}\right] \tag{9}$$

which occurs at $r = 1.28\ R_j$. It is worth noting that this maximum occurs near the interface and that there is a slight upward recirculation of liquid at $r = 2R_j$. We should also be aware that the constants in equation (9) fully reflect any crudity in our assumptions as the liquid and vapor flow configurations.

Formulation of the Stability Problem. To study the stability of the interface we superpose perturbation components of velocity and pressure on the mean flow of gas.

We nondimensionalize velocity, distance, pressure, and time with $U(f_m)$, R_j, $\rho_g U(f_m)^2$, and $R_j/U(f_m)$, respectively. We then define, u, v, and p as the dimensionless perturbation components of axial velocity, radial velocity, and pressure. The subscripts t, x, and y designate differentiation with respect to the dimensionless independent variables.

The continuity and Navier-Stokes equations for the perturbed flow on the gas side are then:

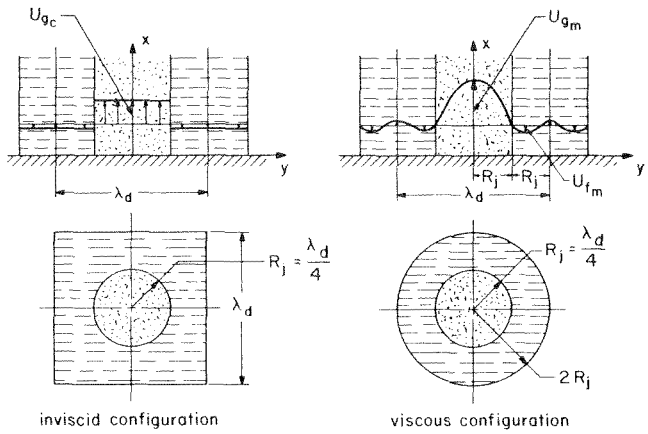

Fig. 2 Assumed theoretical models of boiling near the peak heat flux

$$u_x + v_y = 0 \tag{10}$$

$$u_t + Uu_x + U_y v = -p_x + \mathrm{Re}^{-1}(u_{xx} + u_{yy}) \tag{11}$$

$$v_t + Uv_x = -p_y + \mathrm{Re}^{-1}(v_{xx} + v_{yy}) \tag{12}$$

where $\mathrm{Re} \equiv U(f_m)R_j\rho_g/\mu_g$. The boundary conditions are:

$$v = 0 \qquad \text{at } y = 0 \tag{13}$$

$$u_y = 0 \qquad \text{at } y = 0 \tag{14}$$

$$p - 2\mathrm{Re}^{-1}v_y + \sigma\eta_{xx}/(\rho_g U_{f_m}{}^2 R_j) + \sigma\eta/(2\rho_g U_{f_m}{}^2 R_j) = p_{f_{\text{complex}}}, \text{ at } y = 1 \tag{15}$$

$$u_y + v_x = \mathrm{Re}\,\tau_{f_{\text{complex}}}, \text{ at } y = 1 \tag{16}$$

where η is the displacement of the interface between the gas jet and the liquid column from its mean position. $p(f_{complex})$ and

Nomenclature

U = unperturbed value of dimensionless velocity, used only in Appendix (cf., u)

$U_f, U(f_m)$ = velocity of liquid in the liquid column; subscript, m, denotes maximum downward liquid velocity

$U_g, U(g_m)$ = velocity of gas in the gas jet; subscript, m, denotes maximum upward gas velocity

U_H = gas velocity which causes a jet to become Helmholtz unstable

u = dimensionless perturbation gas velocity in the x direction (physical velocity divided by $U(f_m)$)

V = a dimensionless group characterizing the influence of gas viscosity, $\sqrt{\rho_g\rho_f}\ \sigma^{3/4}/\mu_g g^{1/4}(\rho_f - \rho_g)^{3/4}$

v = dimensionless perturbation gas velocity in the y direction (physical velocity divided by $U(f_m)$)

x, y = dimensionless position coordinates perpendicular to, and parallel with, the heater surface (physical coordinates divided by R_j)

α, β = dimensionless wave number, kR_j; $\beta \equiv kR_j - 1$, a perturbation quantity

δ = thickness of the vapor blanket on a cylindrical heater near q_{max}

η, η_0 = ordinate of interface in y direction from its mean position; subscript, o, denotes value of η at some reference t and x

Λ, Λ_d = dimensionless wavelength, $(\lambda/2\pi)\sqrt{g(\rho_f - \rho_g)/3\sigma}$; subscript denotes "most susceptible" Taylor wavelength on a flat plate

λ, λ_d = wavelength; subscript denotes "most susceptible" Taylor wavelength

μ_f, μ_g = viscosity of liquid and vapor, respectively

ρ_f, ρ_g = density of saturated liquid and vapor, respectively

σ = surface tension between a liquid and its vapor

τ_f = dimensionless perturbation shear stress in liquid, (physical shear stress divided by $\rho_g U(f_m)^2$)

ψ = perturbation stream function as defined in equation (A2)

Subscripts

f, g = denote saturated liquid and vapor properties

i = denotes imaginary component of a complex number

r = denotes real component of a complex number

$\tau(f_{complex})$ are the complex perturbation pressure and shear stress, respectively, from the liquid side.

Equations (10) through (12), with boundary conditions (13) through (16), have been solved for small Re and for dimensionless wave numbers of the disturbance near unity. Complete details of the analysis are given in the Appendix. For a neutral disturbance with a wavelength equal to the "most susceptible" Taylor wavelength in the interface of the gas jet and the liquid column,[3] it is shown in the Appendix that:

$$\frac{1.607\ \lambda_d}{2\pi R_j}\ \frac{\tau_f}{\eta} - \frac{p_f}{\eta} = \frac{\sigma}{2R_j\rho_g U_{f_m}^2} \tag{17}$$

where τ_f represents the magnitude of the imaginary component of the complex fluctuating shear stress and p_f represents the real components of the complex fluctuating normal stress that results from the downward flow of the liquid.

The evaluations of τ_f/η and p_f/η are extremely difficult. They involve solving the equations of motion with appropriate boundary conditions. Brooke Benjamin [13] has solved the comparable problem for a boundary layer type of exterior flow on a wavy wall, with no pressure gradient. For the shear stress and pressure perturbations, he obtained:

$$\frac{p_f}{\eta} = -\frac{2\pi}{\lambda_d} R_j \frac{\rho_f}{\rho_g} \tag{18}$$

$$\frac{\tau_f}{\eta} = -1.188\left(\frac{2\pi R_j}{\lambda_d}\right)^{5/3}\left(\frac{\rho_f}{\rho_g}\right)\left[\frac{\mu_f}{\rho_f (U_f)_y R_j^2}\right]^{1/3}_{y=R_j} \tag{19}$$

We shall use these expressions in equation (17) with the realization that they represent the incorrect configuration. The liquid velocity profile in our case is flatter and it has a negative pressure gradient in the direction of flow. However, if we did obtain equations equivalent to (18) and (19) for our situation, they would differ only in the lead constant on the right-hand side. Substituting equations (18) and (19) in equation (17) and rearranging the result, we obtain:

$$U_{f_m}^2\left\{1-1.63\left[\frac{\mu_f}{\rho_f (U_f)_y R_j^2}\right]^{1/3}_{y=R_j}\right\} = \frac{\sigma}{\pi R_j \rho_f} \tag{20}$$

To get the desired expression for the maximum stable vapor velocity in the jet we combine equations (20) and (9) and replace R_j with $\lambda_d/4$. The result is

$$U_{g_m}^2\left[0.3557\ \frac{\mu_g}{\mu_f} + 0.0389\ \frac{\rho_g}{\rho_f}\right]\left[1-2.05\left(\frac{\mu_f^2}{\rho_f \mu_g U_{g_m} \lambda_d}\right)^{1/3}\right] = \frac{4\sigma}{\pi\lambda_d\rho_f} \tag{21}$$

The form of equation (21) is correct within the limitations of the three constants 0.3557, 0.0388, and 2.05, which reflect the approximations that have been introduced in the various configurational assumptions.

Peak Heat Flux Prediction for Flat Plate Heaters. The average vapor velocity for Poiseuille flow in a cylindrical jet at the point of instability is $U(g_m)/2$. Using $U(g_m)/2$ for U_H in equation (5) and $A_J/A_h = \pi/16$ we obtain:

$$q_{\max_F} = \frac{\pi}{32}\rho_g h_{fg} U_{g_m} \tag{22}$$

Substituting equation (21) for $U(g_m)$ with $\rho_g/\rho_f \ll 1$, and dividing by $q(\max_F) \equiv 1.14\ q(\max_Z)$ we obtain the desired expression for the dimensionless viscous peak heat flux on a flat plate (this assumes that $0.0389\ \rho_g/\rho_f \ll 0.356\ \mu_g/\mu_f$ or that $\upsilon_g/\upsilon_f \gg 0.11$)

$$\frac{q_{\max_F}}{(q_{\max_F})_{inviscid}} = \frac{0.63\ V/M\Lambda_d^{1/2}}{\sqrt{1-0.81\left[\frac{V}{M^2\Lambda_d}\frac{(q_{\max_F})_{inviscid}}{q_{\max_F}}\right]^{1/3}}} \tag{23}$$

Our approximations as to the flow configuration are now reflected entirely in the two constants: 0.63 and 0.81.

In the expression (23) M and V are the liquid and gas viscosity parameters, respectively. Λ_d is the dimensionless "most dangerous" wavelength. The dependence of Λ_d for infinite plates ($R' \to \infty$) is known from the analysis given in reference [12]. The dimensionless groups are defined as

$$M \equiv \frac{\rho_f \sigma^{3/4}}{\mu_f g^{1/4}(\rho_f - \rho_g)^{3/4}} \tag{24}$$

$$V \equiv \frac{\sqrt{\rho_g \rho_f}\ \sigma^{3/4}}{\mu_g g^{1/4}(\rho_f - \rho_g)^{3/4}} \tag{25}$$

$$\Lambda_d \equiv \frac{\lambda_d}{2\pi\sqrt{3}}\left[\frac{g(\rho_f - \rho_g)}{\sigma}\right]^{1/2} \tag{26}$$

Peak Heat Flux on Small Horizontal Cylinders. In this case we assume the same model for the size of the gas jets, their location, and the dominant wavelength, at the gas-liquid interface as was assumed by Sun and Lienhard [9] for inviscid liquids. Thus, if R is the radius of the heater and δ is the thickness of the vapor blanket, the gas jet radius is taken to be $(R + \delta)$. The spacing of the jets is λ_d, the most rapidly growing Taylor unstable wavelength. The Helmholtz unstable disturbance in the gas jet is now the Rayleigh wavelength, $2\pi(R + \delta)$, instead of λ_d. Thus we replace R_j and λ_d, in equations (17), (18), and (19), with $(R + \delta)$ and $2\pi(R + \delta)$, respectively. Then, using equation (9), we obtain for the maximum stable gas velocity:

$$U_{g_m}^2\left[0.3557\ \frac{\mu_g}{\mu_f} + 0.0389\ \frac{\rho_g}{\rho_f}\right]\left[1-2.41\left(\frac{\mu_f^2}{\rho_f \mu_g U_{g_m}(R+\delta)}\right)^{1/3}\right] = \frac{\sigma}{\pi(R+\delta)\rho_f} \tag{27}$$

The energy balance at the surface of the heater, equation (6) gives

$$q_{\max} = \rho_g h_{fg}\ \frac{U_{g_m}}{2}\ \frac{\pi(R+\delta)^2}{2\pi R\lambda_d} \tag{28}$$

Substituting equation (27) for $U(g_m)$ in equation (28), and dividing by the form of equation (4) which applies to small R', we obtain

$$\frac{q_{\max}}{(q_{\max})_{inviscid}} = \frac{0.296 R'^{3/4}(1+\delta/R)^{3/2} V/M\Lambda_d}{\sqrt{1-0.869\left[\frac{V}{M^2\Lambda_d}\frac{q_{\max_Z}(1+\delta/R)}{q_{\max}}\right]^{1/3}}} \tag{29}$$

The vapor blanket thickness around a cylindrical heater near the peak heat flux has been correlated by Sun and Lienhard [9] from the experimental data for inviscid liquids. We do not anticipate any serious change in the vapor blanket thickness with viscosity and therefore use their results. Their correlation for the vapor blanket thickness for small cylinders is:

$$\frac{\delta}{R} = \sqrt{\frac{3.72}{R'}} - 1 \tag{30}$$

Making use of equation (30) in (29), we obtain for the dimensionless peak heat flux:

$$\frac{q_{\max}}{(q_{\max})_{inviscid}} = \frac{0.79\ V/M\Lambda_d}{\sqrt{1-1.08\left[\frac{V}{M^2\Lambda_d}\frac{(q_{\max})_{inviscid}}{q_{\max}(R')^{1/4}}\right]^{1/3}}} \tag{31}$$

It is interesting to note at this point that Borishanski [3] sug-

[3] The actual value of λ_d depends on viscosity as described in reference [12]. The values of λ_d used here were obtained from [12].

Table 1 Peak heat flux data for cyclohexanol on circular flat plate heaters

g/g_e	P (kPa)[a]	M	V	$q_{max_F} \times 10^{-5}$ (W/m^2)	$q_{max_F}/(q_{max_F})_{inviscid}$ Uncorrected observation	Correction factor [14]	Corrected
1	1.61	20	260	1.67	2.19	1.36	2.98
	3.62	35	337	1.99	1.75	1.43	2.51
	5.66	48	380	2.10	1.54	1.47	2.26
	11.73	100	490	2.55	1.34	1.0	1.36
	22.52	155	600	2.81	1.25	1.0	1.25
↓	99.50	250	920	5.65	1.02	1.0	1.02
4.97	11.86	70	437	3.75	1.48	1.0	1.48
8.95	7.31	38	350	3.53	1.48	1.0	1.48

[a] The S.I. unit of pressure, the kPa, is equal to 0.01 bar.

gested that a variety of up to eight dimensionless groups might be involved in the viscous peak heat flux problem. These included groups which could be combined to give both M and V. However, he suggested that a group equivalent to M, alone, would be sufficient to characterize the viscous effects.

Peak Heat Flux on Larger Horizontal Cylinders. Reference [9] shows clearly that the transition from small to large cylinder behavior is not a sharp one. While the break between our equations (4) occurs at $R' = 1.17$, Sun showed that the transition regime extended as far as $R' \simeq 3.5$. We therefore expect to be able to use equation (31) (which depends far more weakly on R' than equation (4) does) up to values of R' considerably beyond 1.17.

For large values of R', it is difficult to formulate models of viscous behavior because serious scaling problems are introduced. Turbulence can enter the problem and other kinds of transitions can occur. No model should be advanced unless it is supported by a great deal of good visual, as well as q_{max}, data for $R' > 4$ in very viscous fluids. Such observations are beyond our present capabilities.

Experiments

The peak heat flux was observed on a flat plate and on horizontal cylinders at both earth-normal gravity and at elevated gravities. The boiled liquid was cyclohexanol, $CH_2(CH_2)_4CHOH$, which is very viscous when it is boiled at low saturation pressures near room temperature. The relevant physical properties of cyclohexanol are listed in reference [14].

The Flat Plate Heater Experiments. A 6.35-cm-dia copper cylinder was used as a test heater. Complete details of the experiments are given in [14] and we only summarize a few essential features of the apparatus and procedure here.

The straight run of cylinder extends downward for about 4 cm and the heater flares to a diameter of 10 cm in the next 4 cm. Coils of nichrome resistance heating wire are mounted on the bottom of the flared copper block. The surface heat flux was obtained by measuring the temperature gradient with the help of thermocouples embedded in the straight-cylindrical section, immediately below the surface.

A pyrex jar of the same diameter as the heater surface, and allowing a liquid head of about 6 cm, sits on the heater surface. Other components of the heater assembly were a heater support, an automatic power shut-off mechanism to avoid runaway temperatures at the peak heat flux and a reflux condenser.

Before each test, the boiling surface was polished with 220 grit-size emery paper and then cleaned with soap and water and finally rinsed with the test liquid. The resistance heating wire was energized and the current was gradually increased in steps. The transition from nucleate to tranitional boiling was identified by noting a slowdown of the boiling process and a sudden continuous increase in the reading of a thermocouple mounted near the heating surface. The thermocouple reading continued to increase for a while, even after power was removed. The peak heat flux data from these tests are listed in Table 1.

Cylindrical Heaters. The peak heat flux on horizontal cylinders was observed in the same apparatus as used by Sun and Lienhard [9]. Nichrome wires approximately 10 cm long were cleaned with soap and hot water to remove any grease or oily matter and were then rinsed with the test liquid. The surface of the heaters were smooth and had a cold rolled finish (as supplied by the manufacturer). The wires were then mounted in a test capsule which was then filled with the test liquid to a level of about 2.5 cm above the wire.

A vacuum pump was used to maintain the desired pressure in the capsule. The current in the wire was steadily increased until q_{max} was reached and the transition from nucleate to film boiling was observed. Similar observations were made at higher gravities in the centrifuge facility of the Boiling and Phase Change Laboratory. Details of the centrifuge, capable of running at 100 times earth-normal gravity, are also given in reference [9]. The peak heat flux data for cylinders are tabulated in Table 2.

Discussion of Results. For a particular fluid at earth-normal gravity, there is a unique value of V for every value of M. Thus equation (23) takes the form $q(\max_F)/(q(\max_F))_{inviscid} = f(M)$ and equation (31) reduces to $q_{max}/(q_{max})_{inviscid} = f(M,R')$. In Fig. 3 we plot the data for flat plates and cylindrical heaters at earth-normal gravity. The flat plate data for M less than 100 have been corrected for the effect of finite flat plate size. Since fewer than three wavelengths are accommodated on the plate, after the wavelength is corrected for viscosity, there can be a slight variation of q_{max} with A_h as jets are added and subtracted from the surface. This effect of finite flat plate size has been discussed in detail in reference [14]. The present data have accordingly been nondimensionalized by dividing them by the corresponding inviscid values for finite plates.

Fig. 3 also includes equations (23) and (31) for comparison. However, as we noted in deriving these expressions, the two decimal fractions in them (one in the numerator and the other in the denominator) should be regarded as free constants which might have to be altered empirically. The constants in the denominator are relatively less influential; thus we shall not tamper with them. On the basis of the data in Fig. 3, however, we shall divide the values 0.63 and 0.79 in the numerator by 3 and obtain 0.21 and 0.26 in equations (23) and (31), respectively. In Fig. 3 we plot equation (31) for $R' = 0.15$ and $R' = 2.5$, in the range in which our small-cylinder hydrodynamic model is applicable. With the adjustment in the constant in the numerator, the comparison between theory and experiment is very good indeed.

When we go to variable gravity experiments in cyclohexanol, V and M are no longer constant, but vary with g. Accordingly $q_{max}/(q_{max})_{inviscid}$ becomes a function of two variables, M and V. Equation (31), with the lead constant equal to 0.27, has been plotted as a three-dimensional surface in Fig. 4. Fifteen high-gravity data for horizontal cylinders (Table 2) are included in the figure. The dependence on R' is not shown in Fig. 4 as $\sqrt[4]{R'}$, for the present data, is close enough to unity that it is uninfluential in equation (31).

We see that these data faithfully bear out the independent influence of the parameter, V, as it is predicted by equation (31).

It is important to note that as M increases or as V decreases, the prediction of $q_{max}/(q_{max})_{inviscid}$ eventually falls below unity.

Table 2 Peak heat flux data for cyclohexanol on horizontal cylindrical heaters

R (mm)	R'	g/g_e	$\bar{P}$ (kPa)	M	V	$q_{max} \times 10^{-5}$ $\left(\frac{W}{m^2}\right)$	$\frac{q_{max}}{(q_{max})_{inviscid}}$
0.4128	0.216	1	0.30	5.4	125	3.60	8.00
0.5144	0.268		0.30	5.4	125	2.72	6.43
0.6540	0.343		0.30	5.4	125	2.74	6.88
0.8001	0.419		0.30	5.4	125	3.31	8.60
0.5144	0.284		2.68	29	312	4.60	4.15
↓	0.289		5.00	44	366	4.89	3.43
↓	0.294		7.72	66	425	4.79	2.88
0.6540	0.354		1.06	16	233	3.18	4.50
↓	0.362		2.41	27	300	3.59	3.58
↓	0.368		5.47	47	375	4.00	2.90
↓	0.373		7.17	61	420	4.26	2.83
0.4128	0.222		0.94	14	215	3.25	4.34
↓	0.228		2.76	30	317	3.37	2.87
↓	0.233		7.86	67	429	3.69	2.01
↓	0.241	↓	13.31	104	500	4.29	1.92
↓	0.669	8.5	3.54	20	196	5.27	3.01
↓	0.997	18.3	5.34	23	181	6.24	2.66
↓	1.194	25.7	6.89	26	182	8.67	2.96
↓	0.680	8.3	8.00	37	247	5.48	2.23
↓	1.020	18.3	10.41	37	218	7.16	2.24
↓	1.220	25.7	11.99	36	209	8.10	2.29
↓	0.672	8.3	5.45	28	224	5.71	2.76
↓	0.998	17.8	8.00	30	205	7.00	2.50
↓	1.207	25.7	9.44	32	193	7.95	2.44
↓	0.687	8.3	10.40	44	262	5.80	2.13
↓	1.011	17.8	11.58	39	221	6.69	2.08
↓	1.220	25.7	12.82	39	209	8.10	2.19
↓	0.702	8.3	16.52	63	295	5.48	1.65
↓	1.032	17.8	17.99	55	251	7.44	1.90
↓	1.240	25.7	19.23	53	239	8.10	1.90

At this point we simply abandon the viscous prediction and embrace the inviscid prediction. This is reasonable since a basic limitation of a viscous theory is that it does not necessarily pass to the limit of inviscid behavior as μ is made very small.

Conclusions

1 We have shown that on flat plate heaters

$$\frac{q_{max_F}}{(q_{max_F})_{inviscid}} = \frac{\text{constant } V/M\Lambda_d^{1/2}}{\sqrt{1-0.81\left[\frac{V}{M^2\Lambda_d}\frac{(q_{max_F})_{inviscid}}{q_{max_F}}\right]^{1/3}}}$$

for viscous liquids. The constant has been evaluated experimentally. It is $\simeq 0.21$.

2 A similar expression has been developed for small cylinders, $R' < 3$ or 4,

$$\frac{q_{max}}{(q_{max})_{inviscid}} = \frac{0.26\ V/M\Lambda_d}{\sqrt{1-1.08\left[\frac{V}{M^2\Lambda_d}\frac{(q_{max})_{inviscid}}{q_{max}(R')^{1/4}}\right]^{1/3}}}$$

The constant in the numerator has again been fixed experimentally.

3 The viscous expressions are only valid when they predict higher peak heat fluxes than the equivalent inviscid theory.

4 The derivation of equation (24) required the solution of an original stability problem, namely the prediction of the maximum stable velocity of a gas jet in a viscous liquid. This velocity is given by equation (21). This problem might well find applications beyond the present one.

References

1 Kutateladze, S. S., "On the Transition to Film Boiling Under Natural Convection," *Kotloturbostroenie*, No. 3, 1948, p. 10.

2 Zuber, N., "Hydrodynamics Aspects of Boiling Heat Transfer," AEC Report No. AECU-4439, *Physics and Mathematics*, 1959.

3 Borishanski, V. M., "An Equation Generalizing Experimental Data

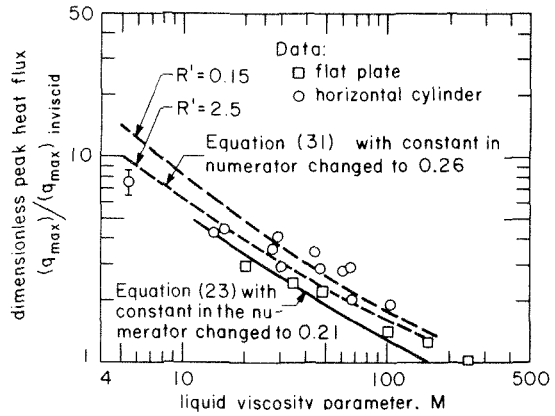

Fig. 3 Effect of liquid viscosity on the peak heat flux for both flat plates and cylinders in cyclohexanol at earth-normal gravity

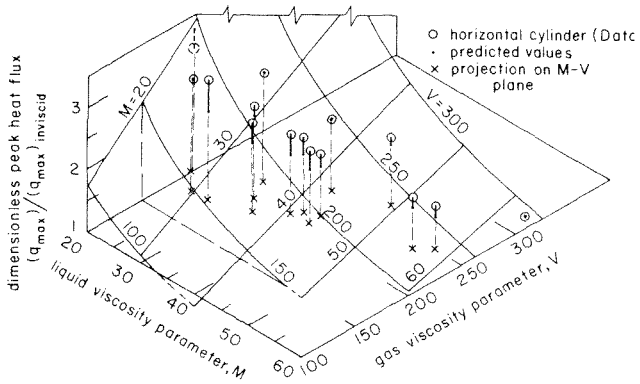

Fig. 4 Effect of liquid and gas viscosity on the peak heat flux at elevated gravities

on the Cessation of Bubble Boiling in a Large Volume of Liquid," *Zhurn. Tekh. Fiz.*, Vol. 26, 1956, p. 452; translated in *Soviet Physics-Technical Physics*, Vol. 1, p. 438.

4 Lienhard, J. H., and Keeling, K. B., Jr., "An Induced-Convection Effect Upon the Peak Boiling Heat Flux," JOURNAL OF HEAT TRANSFER, TRANS. ASME, Series C, Vol. 92, No. 1, Feb. 1970, pp. 1–5.

5 Costello, C. P., Bock, C. O., and Nichols, C. C., "A Study of Induced Convective Effects on Pool Boiling Burnout," *CEP Symposium Series*, Vol. 61, 1965, pp. 271–280.

6 Bobrovich, G. I., Gogonin, I. I., and Kutateladze, S. S., "Influence of Size of Heater Surface on the Peak Pool Boiling Heat Flux," *Jour. App. Mech. and Tech. Phys.*, (πMTΦ), No. 4, 1964, pp. 137–138.

7 Lienhard, J. H., and Watanabe, K., "On Correlating the Peak and Minimum Boiling Heat Fluxes With Pressure and Heater Configuration," JOURNAL OF HEAT TRANSFER, TRANS. ASME, Series C, Vol. 88, No. 1, Feb. 1966, pp. 94–100.

8 Lienhard, J. H., "Interacting Effects of Gravity and Size Upon the Peak and Minimum Pool Boiling Heat Fluxes," NASA CR-1551, May 1970.

9 Sun, K. H., and Lienhard, J. H., "The Peak Pool Boiling Heat Flux on Horizontal Cylinders," *International Journal of Heat and Mass Transfer*, Vol. 13, 1970, pp. 1425–1439.

10 Lienhard, J. H., and Dhir, V. K., "Hydrodynamic Prediction of Peak Pool-Boiling Heat Fluxes From Finite Bodies," JOURNAL OF HEAT TRANSFER, TRANS. ASME, Series C, Vol. 95, No. 2, May 1973, pp. 152–158.

11 Sernas, V., Lienhard, J. H., and Dhir, V. K., "The Taylor Wave Configuration During Boiling From a Flat Plate," *International Journal of Heat and Mass Transfer*, Vol. 16, 1973, pp. 1820–1821.

12 Dhir, V. K., and Lienhard, J. H., "Taylor Stability of Viscous Fluid With Application to Film Boiling," *International Journal of Heat and Mass Transfer*, Vol. 16, 1973, pp. 2097–2109.

13 Brooke Benjamin, T., "Shearing Flow Over a Wavy Boundary," *Journal of Fluid Mechanics*, TRANS. ASME, Vol. 6, 1959, pp. 161–205.

14 Dhir, V. K., "Viscous Hydrodynamic Instability Theory of the Peak and Minimum Pool Boiling Heat Fluxes," PhD dissertation, College of Engineering, Bulletin No. UKY BU-100, University of Kentucky, Nov. 1972.

APPENDIX

To get the relation between τ_f and p_f, equation (17), we assume that the gas-liquid interface has the following two-dimensional wave form:

$$\eta = \eta_0 \exp[i\alpha(x - ct)] \tag{A1}$$

where α is the dimensionless wave number, kR_j, and c is the dimensionless wave velocity whose imaginary part is the growth rate of the disturbance.

We next define a perturbation stream function

$$\Psi = \eta_0 F(y) \exp[i\alpha(x - ct)] \tag{A2}$$

such that

$$u = \Psi_y = F^I\eta \text{ and } v = -\Psi_x = -i\alpha F\eta \tag{A3}$$

Substituting these definitions of η, u and v in equations (11) and (12) we get:

$$-i\alpha cF^I\eta + i\alpha UF^I\eta - i\alpha U^I F\eta = -p_x + Re^{-1}(-F^I\eta\alpha^2 + F^{III}\eta) \tag{11a}$$

$$-\alpha cF\eta + \alpha F\eta = -p_y + Re^{-1}(i\alpha^2 F\eta - iF\eta) \tag{12a}$$

where Roman superscripts denote differentiations with respect to y.

Elimination of pressure from equation (11a) and (12a) gives

$$F^{IV} - 2\alpha^2 F^{II} + \alpha^4 F = i\alpha Re[(U - c)(F^{II} - \alpha^2 F) - U^{II}F] \tag{A4}$$

Equation (A4) is an Orr-Sommerfeld equation with boundary conditions:

$$F(0) = F^{II}(0) = 0 \tag{A5}$$

and at $y = 1$, the two conditions:

$$F^{III} - 3\alpha^2 F^I = i\alpha Re[p_f/\eta + \sigma(\alpha^2 - 1/2)/(\rho U_0{}^2 R_j)] - i\alpha Re[cF^I(1) - U^I F(1)] \tag{A6}$$

$$F^{II} + \alpha^2 F = \tau_f Re/\eta \tag{A7}$$

The kinematic condition at the interface can be written as

$$c = F(1) \tag{A8}$$

Solution of Orr-Sommerfeld Equation. We must now solve equation (A4) with boundary conditions (A5) through (A7) for values of α close to 1 and Re < 1. This choice for $\alpha \equiv 2\pi R_j/\lambda$ is made because λ is of the order of the circumference of the jet. Thus we write $\alpha = 1 + \beta$ where $\beta < 1$, and assume a series form for the perturbation function, F

$$F = F_0 + \beta F_1 + \beta^2 F_2 \ldots . \tag{A9}$$

Substituting these α and F in equations (A4) through (A7) we get for terms of the order of β^0:

$$F_0{}^{IV} - 2F_0{}^{II} + F_0 = 0 \tag{A10}$$

The boundary conditions for equation (A10) are:

$$F_0(0) = F_0{}^{II}(0) = 0, \quad F_0{}^{III}(1) - 3F_0{}^I(1) = i(P + S), \text{ and } F_0{}^{II}(1) - F_0(1) = iT \tag{A11}$$

For terms of the order of β^1 the equation and its boundary conditions are:

$$F_1{}^{IV} - 2F_1{}^{II} + F_1 = [(U - c)(F_0{}^{II} - F_0) - U^{II}F_0]\cdot i\mathrm{Re}/\beta \tag{A12}$$

$$F_1(0) = F_1{}^{II}(0) = 0, \quad F_1{}^{II}(1) + F_1(1) = 0, \text{ and } F_1{}^{III}(1) - 3F_1{}^I(1) = -i(P + S) - i[cF_0{}^I(1) + U^1(1)F_0(1)] \tag{A13}$$

In the foregoing equations

$$P \equiv \frac{p_f \mathrm{Re}}{\eta}; \quad S \equiv \frac{\sigma \mathrm{Re}}{2\rho_g U_{f_m}{}^2 R_j}; \quad T \equiv \frac{\tau_f \mathrm{Re}}{\eta} \tag{A14}$$

The solutions for F_0 and F_1 can be written as follows:

$$F_0 = [0.0434T - 0.2008i(P + S)](e^y - e^{-y}) + [0.0732T + 0.0868i(P + S)]y(e^y + e^{-y}) \tag{A15}$$

$$F_1 = \{-(P + S) + c[0.5319T - 0.1478i(P + S)] + U^1(1)[0.3279T - 0.2041i(P + S)]\}\{0.2008i(e^y - e^{-y}) - 0.0868iy(e^y + e^{-y})\} + \{2(U - c)[0.0732T + 0.0868i(P + S)] - U^{II}[0.0434T - 0.2008i(P + S)]\}\{\frac{y^2}{8}(e^y - e^{-y})\}i\frac{\mathrm{Re}}{\beta} - \{U^{II}[0.0434T - 0.2008i(P + S)]\}\{e^y(y^3/24 - y^2/8) + e^{-y}(y^3/24 + y^2/8)\}i\mathrm{Re}/\beta \tag{A16}$$

Kinematic Condition at the Interface. The functions F_0 and F_1, evaluated at the interface $y = 1 + \eta \simeq 1$, are:

$$F_0(1) = 0.3279T - 0.2041i(P + S) \tag{A17}$$

$$F_1(1) = -0.2041i\{-(P + S) + c[0.5319T - 0.1478i(P + S)] + U^1(1)[0.3279T - 0.2041i(P + S)]\} - c\{0.0431T + 0.0511i(P + S)\}i\mathrm{Re}/\beta - U^{II}(1)\{0.0056T - 0.0258i(P + S)\}i\mathrm{Re}/\beta \tag{A18}$$

The quantities c, P, and T are complex. Writing them as the sum of real and imaginary parts, we have:

$$c = c_r + ic_i;\ P = P_r + iP_i;\ T = T_r + iT_i: \quad \text{(A19)}$$

The kinematic condition (A8) at the interface can be written as:

$$c = F_0(1) + \beta F_1(1) \quad \text{(A8}a\text{)}$$

Substituting equations (A17) through (A19) in (A8a) and collecting real and imaginary parts we obtain

$$c_r = 0.3279T_r + 0.2041(1 + \beta)P_i - \beta[0.1085(T_i c_r + T_r c_i) + 0.0302c_i P_i - 0.0302c_r(P_r + S) + 0.0669U^{\mathrm{I}}(1)T_i - 0.0416U^{\mathrm{I}}(1)(P_r + S)] + Re[0.0056U^{\mathrm{II}}(1)T_i - 0.0258U^{\mathrm{II}}(1)(P + S)] + Re[0.0431(T_i c_r + T_r c_i) - 0.0511c_i P_i + 0.0511c_r(P_r + S)] \quad \text{(A20)}$$

$$c_i = 0.3279T_i - 0.2041(1 + \beta)(P_r + S) + \beta[0.0652(T_r c_r - T_i c_i) + 0.0813(c_r P_i + c_i P_r) + 0.0669U^{\mathrm{I}}(1)T_r + 0.0416U^{\mathrm{I}}P_i] - Re[0.0056U^{\mathrm{II}}(1)T_r + 0.0258U^{\mathrm{II}}(1)P_i] - Re[0.0431(T_r c_r - T_i c_i) - 0.0511(c_r P_i + c_i P_r)] \quad \text{(A21)}$$

We are interested in the imaginary part of the wave velocity, as it represents the rate of growth of the disturbance. For a neutral disturbance ($c_i = 0$), to the first order approximation, equation (A21) reduces to

$$\frac{1.6068}{\alpha}\frac{\tau_f}{\eta} - \frac{p_f}{\eta} = \frac{\sigma}{2\rho_g U_{f_m}{}^2 R_j}, \quad \text{(A22)}$$

after the substitution of equation (A14); where τ_f now represents only the imaginary part, and p_f the real part, of tangential and normal stresses.

E. J. Thorgerson[2]
D. H. Knoebel
Savannah River Laboratory,
E. I. du Pont de Nemours and Co.,
Aiken, S. C.

J. H. Gibbons
College of Engineering,
University of South Carolina,
Columbia, S. C.

A Model to Predict Convective Subcooled Critical Heat Flux[1]

A friction factor correlation based on pressure drop measurements at burnout in an annular channel is presented. From Reynolds analogy and this correlation, critical heat fluxes were predicted within ±10 percent of the values measured with ideal geometry (no ribs), stainless steel heaters, and H_2O coolant flowing vertically downward at a velocity of 15 to 45 ft/sec and subcoolings greater than 25 deg C. Tubular critical heat fluxes are predicted within ±20 percent using the friction factor correlation and Reynolds analogy. A short theoretical discussion is presented.

Introduction

The prediction of burnout or critical heat flux in forced convection boiling continues to be a challenge to those interested in heat transfer mechanisms. Many correlations have been developed for specific systems, which are adequate for practical usage. However, the basic mechanisms for burnout are not reliably known, and critical heat fluxes for novel heat transfer systems cannot presently be predicted with confidence. This paper presents a simple method using a friction factor correlation with Reynolds analogy to predict critical heat fluxes.

Theoretical Discussion

Before postulating a physical model of burnout, it is necessary to qualitatively examine the phenomena of burnout and nucleate boiling at burnout.

Evidence indicates that heat transfer from a wall in boiling is primarily a change of phase phenomenon with vaporization occurring at the bubble base and condensation at the top of the bubble [1, 2, 3].[3] Near the critical heat flux with bubble activity at the maximum, it is assumed that essentially all the heat is transferred from the wall by vaporization. Bankoff noted that near burnout, the temperatures at the top of the bubbles are at saturation [4]. Thus, at the burnout condition, the vapor no longer condenses but expands the bubble at the velocity of the vapor leaving the wall. Sabersky and Mulligan [5], and later Jordan and Leppert [6] have shown that Reynolds analogy between heat and momentum transport applies in convection nucleate boiling. This implies that the heat transfer mechanism from the top of the bubbles to the bulk fluid is entirely turbulent convection. Hence, burnout would be expected to occur when either vaporization at the wall or turbulent transport from the bubbles limits the heat transfer rate. In the former case liquid cannot reach the wall at the critical condition, and in the latter the vapor cannot get away from the wall at the critical condition. Vaporization is controlling in the low subcooling and saturated boiling region, and turbulent transport is controlling in the higher subcooled region.

Kutateladze and Leont'ev suggested that the critical heat flux is related to the general problem of flow stagnation with injection from the wall [7, 8]. They postulated that an injection stream normal to the main stream arises from vapor generation at the wall in the nucleate boiling channel. At the critical conditions, the injection stream causes a local stagnation of the boiling, two-phase boundary layer resulting in film boiling at the stagnation point. The criterion for flow stagnation with wall injection of a fluid into a stream of the source fluid is given as [9]

$$G_{inj} = 2f_{nb}G_{stream} \tag{1}$$

where f_{nb} is the friction factor with no injection or boiling. Assuming that α is the fraction of fluid leaving the wall, Kutateladze and Leont'ev derived the following expression for critical heat flux at saturation conditions:

$$\phi_{sat} = 2f_{nb}\alpha(1-\alpha)\lambda(\rho_v\rho_l)^{1/2}U \tag{2}$$

For the subcooled region, using superposition, the following expression was postulated

$$\phi = 2f_{nb}\alpha(1-\alpha)\lambda(\rho_v\rho_l)^{1/2}U + h\Delta T \tag{3}$$

where ΔT is the temperature difference of the wall and bulk fluid, and the heat transfer coefficient was estimated using the Colburn analogy:

---

[1] This paper was prepared in connection with work under Contract No. AT(07-2)-1 with the U. S. Atomic Energy Commission.

[2] Present Address: Polaroid Corp., Waltham, Mass.

[3] Numbers in brackets designate References at end of paper.

Contributed by the Heat Transfer Division for publication in the Journal of Heat Transfer. Manuscript received by the Heat Transfer Division, March 13, 1973. Paper No. 74-HT-L.

$$h = \frac{f_{nb}}{2}\left(\frac{\rho C_P U}{N_{\mathrm{Pr}}^{0.6}}\right)_l \tag{4}$$

Considering the forces on a bubble, Chang [10] derived an expression for the critical heat flux that is very similar to equation (3). For subcooled boiling, Chang arrived at the following equation with two constants, C_1 and C_2, adjusted to fit the data:

$$\phi = [C_1(\rho_v\rho_l)^{1/2}\lambda + C_2\rho_l C_{P_l}\Delta T_{\mathrm{sub}}]U \tag{5}$$

where ΔT_{sub} is equal to the difference between saturation and bulk coolant temperature.

Tong attempted to link the separation criterion to the entire range of quality, i.e., subcooled and quality regions [11]. Tong suggested the following expression for the critical heat flux:

$$\phi = 2f_{BO}\lambda\rho_l U \tag{6}$$

The friction factor, f_{BO}, estimated from boiling experiments is

$$f_{BO} = C\ N_{\mathrm{Re}}^{-0.6} \tag{7}$$

where the constant C was empirically evaluated by relating it to both negative (subcooled) and positive qualities, so that equation (6) correlated burnout data. The expression for C is

$$C = 0.88 - 3.716\chi + 6.111\chi^2 \tag{8}$$

The friction factor calculated from equation (7) was obtained to give the best fit of equation (6) to burnout data and was not based on independent measurements of the axial pressure drop in the boiling channel.

The similarity between equation (6) and Reynolds analogy is apparent; although the liquid momentum is used, the heat capacity of the vapor (in terms of latent heat of vaporization) is used rather than that for the liquid. Equation (6) attempts to include both vaporization and turbulent heat transfer effects as do equations (3) and (5) via superposition.

Tong's relative success at fitting both subcooled and quality burnout data with equation (6), the reduction of equations (3) and (5) at high subcoolings (>25 deg C) to the following equation,

$$\phi = h\Delta T \tag{9}$$

and the fact that subcooled nucleate boiling data have been correlated by Reynolds analogy [5, 6] suggest that the critical heat flux at high subcooling could be correlated by Reynolds analogy [12]. For Reynolds analogy to predict the burnout heat flux, the limiting heat transport must occur between the bubbles and the bulk stream, and a critical or burnout friction factor must exist which is a function of Reynolds number only. The latter would require that at a given velocity the amount of vapor present at burnout must be constant over the range of subcoolings considered. Fig. 1 shows measured pressure drop data at burnout in an annular channel which for higher subcooling (>25 deg C) indicate that the void fraction at burnout is not a function of subcooling. The small decrease in pressure drop with decreasing subcooling is related to viscosity changes.

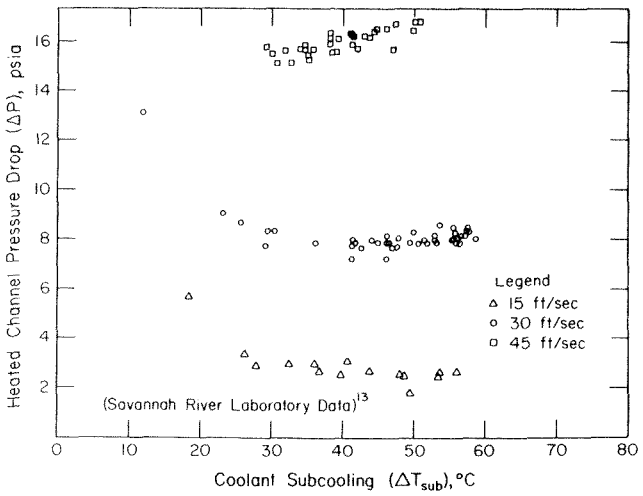

Fig. 1 Pressure drop versus subcooling at burnout

Using Reynolds analogy to calculate the heat transfer coefficient at the critical condition, the critical heat flux in the subcooled region ($T_{\mathrm{sub}} > 25$ deg C) is given by

$$\phi = \frac{f_{BO}}{2}(\rho_l C_{P_l} U\Delta T) \tag{10}$$

where ΔT is the difference between the surface and bulk coolant temperatures. The friction factor at burnout is related to the boiling pressure drop at burnout by the following equation:

$$f_{BO} = g_c\Delta P_{BO} D_e/2L\rho_l U^2 \tag{11}$$

Results discussed in the next section show the adequacy of using Reynolds analogy and a burnout friction factor to predict the critical heat flux in highly subcooled, forced convection boiling.

Results

Pressure drop data at burnout were measured in Savannah River Laboratory tests [13]. The data used in this study[4] were obtained on ½-in-dia stainless steel heaters 24 in. long with water flowing vertically downward past the heater in an annulus. The outer surface of the annulus was formed by a 0.875-in-inner-dia precision bore glass tube. System pressure was nominally 40 psig, and inlet velocities varied from 15 to 45 ft/sec. The water used in these tests was deionized, deaerated, and filtered. The heater surfaces were drawn stainless steel; heaters with circumferential marks were not used. Inlet and exit temperatures were measured via thermocouples, the latter located sufficiently downstream to assure good mixing. The bulk temperature at the burnout point was calculated by linear extrapolation between the inlet and outlet temperatures. Because the heaters were uniformly heated, burnout always occurred near or at the exit. The heat balances (electric power input versus thermal balance on coolant) for these tests had an absolute average deviation of 1.9 percent.

The pressure drop data are shown in Fig. 1 and indicate that the pressure drop and hence, friction factor is at most a weak function of subcooling. On this basis, the friction factor is assumed nonvarying in the following discussion. The friction factors were evaluated from these pressure drop data at burnout and are plotted versus Reynolds number in Fig. 2. The velocity based on inlet conditions is used to calculate the friction factors from equation (11) and the Reynolds number. The bulk coolant properties at the burnout site were used to calculate the Reynolds number. The use of inlet velocity is adequate where the void fraction is low (<5 percent) and constant as in the high subcooled data under study herein [14].

The system friction factor at burnout for the annular channel data is predicted by

$$f_{BO} = 0.694\ N_{\mathrm{Re}}^{-0.386} \tag{12}$$

The change in effective e/D_e in Fig. 2 with velocity corresponds to the effect of velocity on bubble size. Chang [10] derived an expression for the detaching bubble radius as:

$$r = k\sigma_l/\rho_l U^2 \tag{13}$$

With constant physical properties, the bubble radius is inversely proportional to the square of the velocity. The data in Fig. 2 (temperature range of ~40 deg C) have e/D_e of approximately 0.004, 0.0012, and 0.0006 for velocities of 15, 30, and 45 ft/sec, respectively. The functionality of equation (13) would indicate e/D_e values of 0.004, 0.001, and 0.00045, respectively. The larger scatter

[4] Runs 619-835 in reference [13].

of the friction factor data at 15 ft/sec is due to the scatter in the pressure drop measurement.

The critical heat fluxes calculated from equations (10) and (12) are shown in Fig. 3 plotted versus the experimental values. The wall temperature was calculated using the Weatherhead correlation [15].

$$T_w - T_{sat} = (47.7 - 0.127\ T_{sat})\left(\frac{\phi}{10^6}\right)^{1/4} \qquad (14)$$

where temperatures are in deg C, and ϕ is the burnout heat flux in Btu/hr ft^2. The agreement between calculated and measured values in Fig. 3 is generally within ±10 percent, which is within the accuracy of the heat transfer data. The data and correlation not applicable to subcoolings less than 25 deg C where acceleration effects due to significant void formation become more important. The correlation should not be extended to higher pressures without experimental data.

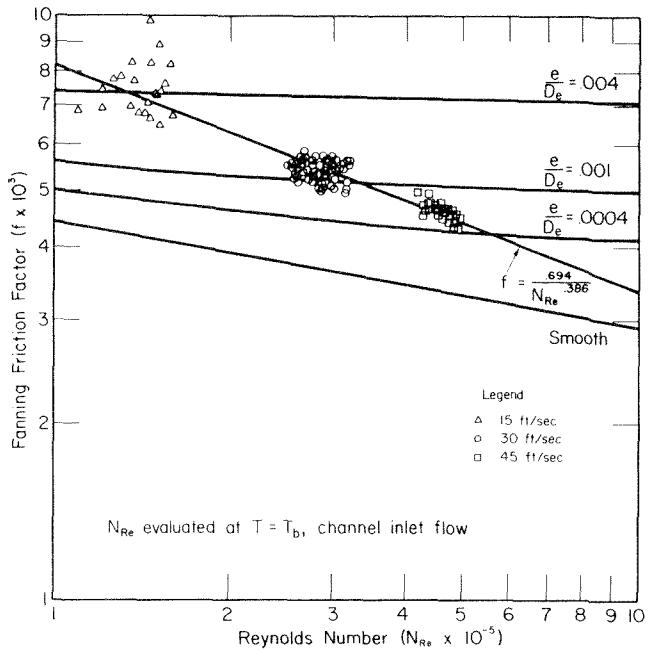

Fig. 2 System friction factor as a function of Reynolds number in boiling

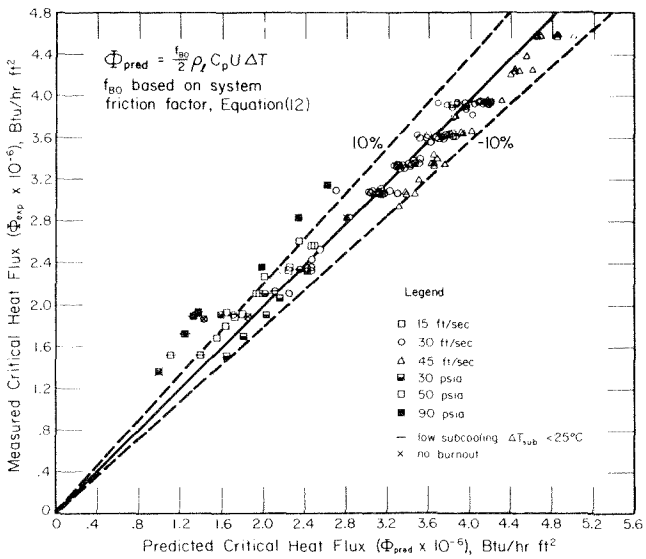

Fig. 3 Comparison of annular experimental and predicted critical heat flux results

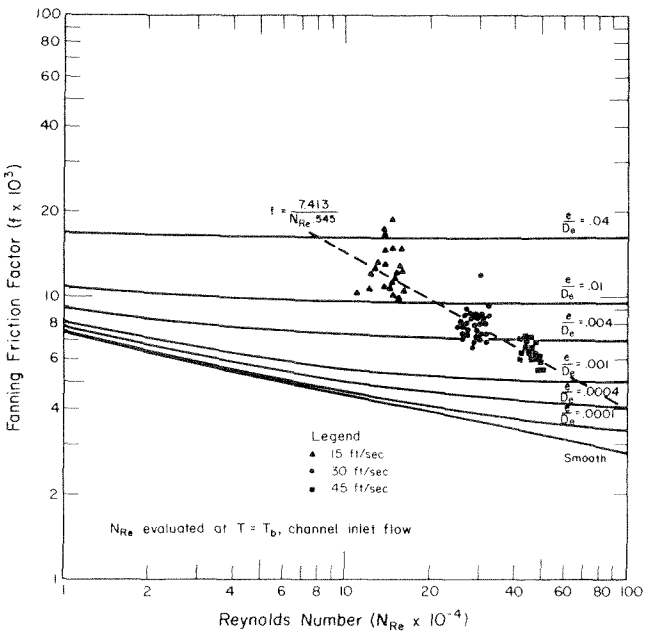

Fig. 4 Friction factor as a function of Reynolds number in boiling; hot wall friction factor from annular flow

The preceding approach can be extended to burnout in tubular geometries. Unlike the annulus that is heated from one side, the fluid in the tube is entirely exposed to boiling surfaces. Therefore, the friction drag should be all boiling friction drag. The system friction factor for the tube may be found by estimating the boiling wall friction factor in the annulus. An estimate of the contribution to drag of each wall can be found by taking a force balance on the annulus and relating the shear stress to the friction factor yielding

$$f_{BO} = \left(\frac{D_i}{D_o + D_i}\right) f_{bw_{BO}} + \left(\frac{D_o}{D_o + D_i}\right) f_{nb} \qquad (15)$$

where $f(bw_{BO})$ is the boiling wall friction factor at burnout, and f_{BO} is given by equation (12) for the annulus. The nonboiling wall friction factor f_{nb} may be taken from a Moody chart.

The friction factor results calculated for the boiling wall at burnout (Fig. 4) can be represented by

$$f_{bw_{BO}} = 7.413\ N_{Re}^{-0.545} \qquad (16)$$

Two points of interest are noted from Fig. 4: *(a)* the velocity effect on e/D_e is present in the same way as discussed for the annular system, Fig. 2, and *(b)* for the boiling wall, the power is −0.545, which compares to Tong's value of −0.6 given in equation (7).

This friction factor correlation represents boiling effects empirically. The success of this correlation indicates that the boiling contribution and the rate of vaporization are important only in influencing turbulence at the wall.

Critical heat flux results calculated using a friction factor given by equation (13) are compared with some Savannah River Laboratory subcooled, convection burnout data for tubes (Fig. 5).[5] These data were obtained on stainless steel tubes cooled by forced downward flow of water. The pressure range of these data was 25 to 193 psi, and the velocities ranged from 10 to 60 ft/sec. No pressure drop data were available for tubes to assess the accuracy of the friction factor prediction by equation (13). The experimental critical heat flux data for tubes exhibited a much larger scatter than the annular data. The agreement shown in Fig. 5 is generally within ±20 percent, the accuracy of the data. Initial attempts

[5] A complete tabulation of these data is available from the authors on request.

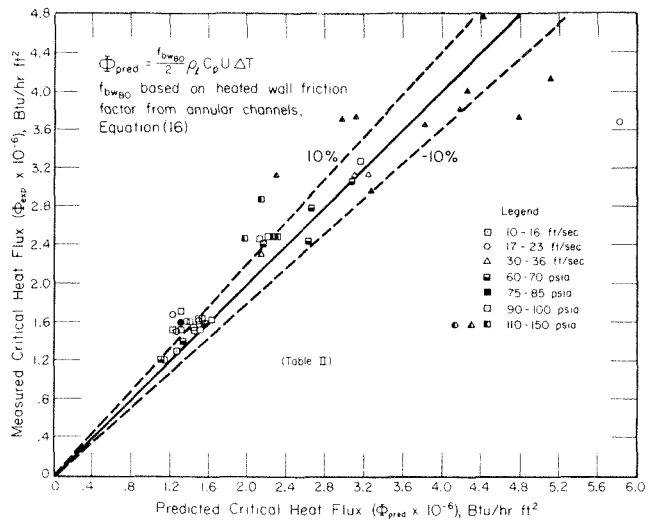

Fig. 5 Comparison of tubular experimental and predicted critical heat flux results

to extend the correlation to other data from the literature have not been successful. However, most available data from the literature are for higher pressures. Both the prediction for surface temperature and the frictional pressure drop are affected by the pressure. Therefore, more critical heat flux data are required with pressure drop data to extend the proposed correlation.

Conclusions

The use of Reynolds analogy between heat and mass transport and measured pressure drop data provides a simple means of correlating critical heat flux data with velocities in excess of 10 ft/sec and subcoolings greater than 25 deg C. A generalized correlation based on a friction factor chart will require more critical heat flux data on different coolants and coolant conditions (different velocity, pressure, and temperature ranges). The correlation also substantiates that the void fraction at burnout is constant at subcooling greater than 25 deg C and the pressure drop can be represented as a frictional loss, i.e., the acceleration caused by phase change is constant for conditions considered. The friction factor does not appear to be a function of the subcooling.

Acknowledgments

This paper is based on the PhD thesis of E. J. Thorgerson who carried out the work at the Savannah River Laboratory under Contract AT(07-2)-1 with sponsorship by the Oak Ridge Associated Universities. The thesis was in partial fulfillment of the requirements for a PhD degree at the University of South Carolina.

References

1 Snyder, N. W., and Robin, T. T., "Mass Transfer Model in Subcooled Nucleate Boiling," ASME Paper No. 68-HT-51, 1968.

2 Moore, F. D., and Mesler, R. B., "The Measurement of Rapid Surface Temperature Fluctuations During Nucleate Boiling of Water," *AIChEJ*, Vol. 7, No. 4, 1961, p. 620.

3 Graham, R. W., and Hendricks, R. C., "Assessment of Convection, Conduction and Evaporation in Nucleate Boiling," NASA-TN-D-3943, 1967.

4 Bankoff, S. G., "On the Mechanism of Subcooled Nucleate Boiling," Parts I and II, *Chem. Eng. Prog. Symp. Ser.*, Vol. 57, No. 32, 1961, p. 156.

5 Sabersky, R. H., and Mulligan, H. E., "On the Relationship Between Fluid Friction and Heat Transfer in Nucleate Boiling," *Jet Propulsion*, Vol. 25, No. 1, 1955, p. 9.

6 Jordan, D. P., and Leppert, G., "Pressure Drop and Vapor Volume With Subcooled Nucleate Boiling," *International Journal of Heat and Mass Transfer*, Vol. 5, 1962, p. 751.

7 Kutateladze, S. S., "The Concept of a Fluid With Disappearing Viscosity and Some Problems of the Phenomenological Theory of Turbulence Near the Wall," Invited Lecture, Third International Heat Transfer Conference, Chicago, 1966.

8 Kutateladze, S. S., and Leont'ev, A. I., "Some Applications of the Asymptotic Theory of the Turbulent Boundary Layer," *Proc. Third International Heat Transfer Conference, AIChE*, Vol. III, New York 1966, p. 1.

9 Fiori, M. P., and Bergles, A. E., "Model of Critical Heat Flux in Subcooled Flow Boiling," MIT Report DSR 70821-56, Sept. 1968.

10 Chang, Y. P., "An Analysis of the Critical Conditions and Burnout in Boiling Heat Transfer," USAEC Report TID-14004, 1961.

11 Tong, L. S., "Boundary Layer Analysis of the Flow Boiling Crisis," *International Journal of Heat and Mass Transfer*, Vol. 11, 1968, p. 1208.

12 Thorgerson, E. J., "Hydrodynamic Aspects of the Critical Heat Flux in Subcooled Convection Boiling," PhD thesis, University of South Carolina, 1969.

13 Knoebel, D. H., Harris, S. D., Crain, B., and Biderman, R. M., "Forced Convection Subcooled Critical Heat Flux: D_2O and H_2O Coolant; Aluminum and Stainless Steel Heaters," USAEC Report DP-1306, Savannah River Laboratory, 1972.

14 Rouhani, S. Z., "Calculation of Steam Volume Fraction in Subcooled Boiling," ASME Paper No. 67-HT-31, 1967.

15 Weatherhead, R. J., "Nucleate Boiling Characteristics and the Critical Heat Flux Occurrence in Subcooled Axial-Flow Water System," USAEC Report ANL-6675, 1962.

J. W. RAUSCHER
Postgraduate Research Engineer,
Pratt and Whitney Aircraft,
E. Hartford, Conn.
Assoc. Mem. ASME

A. F. MILLS
Associate Professor. Mem. ASME

V. E. DENNY
Associate Professor.

University of California,
Los Angeles, Calif.

Experimental Study of Film Condensation From Steam-Air Mixtures Flowing Downward Over a Horizontal Tube[1]

Experiments have been performed to study the effects of air on filmwise condensation from steam-air mixtures undergoing forced flow over a 3/4 in. OD horizontal tube. Local condensation rates at the stagnation point are reported for saturation temperatures of 100–150 deg F, bulk to wall temperature differences of 3–30 deg F, bulk air mass fraction 0–7 percent and oncoming vapor velocity 1–6 ft/sec. For pure steam the average value of q/q_{Nu}, where q_{Nu} is the Nusselt result, was 0.98 ± 0.10, which compares favorably with the value of 1.04 predicted by a theory which accounts for vapor drag. For steam-air mixtures the reduction in heat transfer was found to be in excellent agreement with the theoretical analysis of Denny and South; the average discrepancy in q/q_{Nu} was −2.7 percent, while the maximum was 7.1 percent.

Introduction

Small concentrations of noncondensable gas in a vapor can lead to significant reductions in condensation rates. Since the usual industrial situation involves condensation under partial vacuum, in-leakage of air diminishes condenser effectiveness in, for example, power generating stations and sea water distillation plants. It is well known that forced vapor flow markedly alleviates the deleterious effects of the noncondensable, and current design practice is to employ tube and baffle configurations which optimize the vapor flow pattern. Analysis of the forced vapor flow noncondensable gas problem has been made for the vertical wall [1][2] and the single horizontal tube [2, 3]; in the latter work it was shown that the condensation rate from steam-air mixtures, with air mass fractions in the range 0.01 to 0.15, approximately doubled as the oncoming vapor velocity increased from 1 to 10 ft/sec.

The present study was initiated in order to obtain precise experimental validification of the assumptions and techniques of the aforementioned analyses. The horizontal tube geometry was chosen over the vertical wall as it was easier to model in a small scale laboratory experiment. In [2] self-similar solutions to the coupled two-phase flow problem were obtained which are valid at and near the forward stagnation point. In [3] a forward marching solution procedure based on finite difference analogs to the governing conservation equations was used to obtain solutions for an isothermal tube up to the vapor boundary layer separation point (~110 deg). Exact solutions for the remainder of the bottom half of the tube are not available. In the experimental study we have emphasized the measurement of local condensation rates at the forward stagnation point in order to effect direct comparisons between analysis and experiment.

Previously, experimental studies of the effects of noncondensables on filmwise condensation of steam on a horizontal tube have been made by Othmer [4] and Henderson and Marchello [5]; however, in both cases the vapor flow pattern was uncertain and relatively quiescent. The data obtained were correlated by empirical curve-fitting owing to the unavailability of a theoretical analysis.

Apparatus and Procedure

Test Loop. The major components of the experimental system are shown schematically in Fig. 1. The system operates essentially closed loop, steam being generated in a 12 liter RB flask fitted with a 3.5 kw immersion heater and condensate being returned to the boiler from the heat transfer tube and auxiliary condenser. After testing several designs for the heater, it was found that an 0.5 in. dia coil of 18-gauge nichrome wire wrapped with fiberglass tape produced rather smooth boiling down to the lowest pressures considered. Air entered the system via a sparge located beneath the heating coil, the resulting flow of air

[1] This work was sponsored by the Office of Saline Water on Grant No. 14-30-2678, and by the University of California Water Resources Center on Project No. S142. Computer time was supplied by the Campus Computing Network of the University of California, Los Angeles, Calif.

[2] Numbers in brackets designate References at end of paper.

Contributed by the Heat Transfer Division for publication (without presentation) in The Journal of Heat Transfer. Manuscript received by the Heat Transfer Division April 12, 1973. Paper No. 74-HT-D.

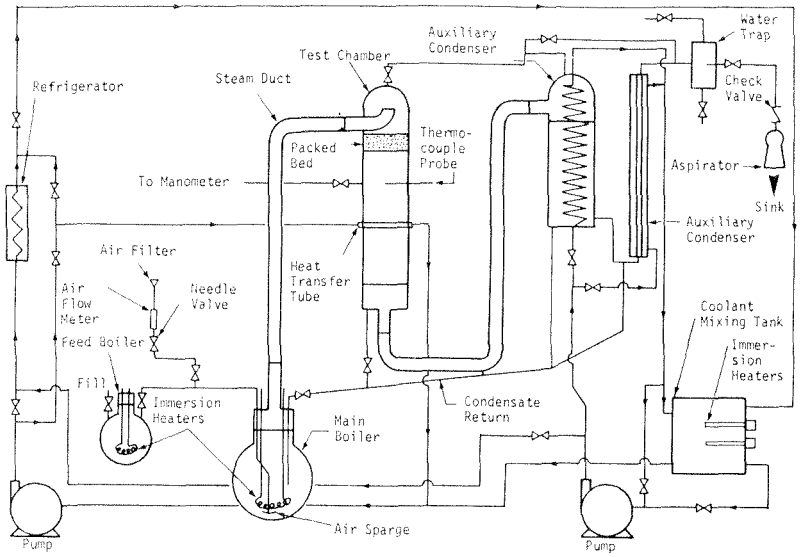

Fig. 1 Major components of the system

bubbles serving to further enhance smooth boiling. The air flow rate was measured with a Fischer-Porter all glass rotameter of accuracy 2 percent. Power input to the heater was calculated from voltage and current measurements using G.E. type AP-9 volt and ammeters having an accuracy of 0.5 percent at full scale.

The 3 ft long test chamber was fabricated in three sections from 5 in. ID, 0.25 in. thick glass pipe, the section joints being sealed with Viton O-rings. To promote mixing, the entering steam-air mixture was directed upwards toward the hemispherical chamber top and then down through a packed bed of 8 mm glass raschig rings. A copper-constantan thermocouple probe for checking superheat of the oncoming vapor (negligible at <1 deg F) and a manometer tap for measuring pressure were positioned midway between the packed bed and the heat transfer tube. The mercury manometer was mounted in a plexiglass case through which hot air was blown to prevent vapor condensation. A cathetometer of least count 0.05 mm was used to measure column heights, the reference pressure in the open leg being measured with a certified absolute barometer. Temperature corrections for steam saturation temperatures based on mercury at 32 deg F [6] were effected by means of a set of 10 thermocouples cemented to the manometer legs.

By-pass steam from the test chamber was condensed on a copper coolant coil, the auxiliary condenser being exhausted through an 0.75 in. aspirator preceded by a check valve and water trap. Coolant flow, consisting of two parts water and one part ethylene glycol, was supplied to the heat transfer tube and auxiliary condenser from a 3-ton Freon-12 refrigeration plant. The necessary differences in coolant temperature within the tube and auxiliary condenser were effected by splits between the refrigerant efflux and that from an electrically heated intermediate mixing tank. In this way, the coolant temperature to the tube could be varied from 20 to 100 deg F while maintaining a constant load on the refrigerator.

The test loop was insulated with polyurethane foam and cotton batting; the resulting low heat losses (<2 percent) enabled both the test chamber vapor velocity and air mass fraction to be determined from a system energy and mass balance [7]. Care was taken to minimize the possibility of contaminating the steam and to ensure a vacuum tight system. Glass was used wherever possible and the only organic materials in contact with the steam were the Viton O-rings at the joints, and lead-ins (Cajon ultra-torr and Swagelok).

Heat Transfer Tube. The heat transfer tube was fitted with five pairs of thermocouples which were calibrated to act as local heat flux meters. Various details of the tube are shown in Fig. 2. Stainless steel was chosen because its low thermal conductivity ensures a large temperature drop across the thermocouple pairs. The thermocouples were fabricated from Omegaclad 38-gauge iron-constantan wire with MgO insulation encased in a 0.020 in. stainless steel sheath. Installation of the inner thermocouples was relatively straightforward [7]. The outer thermocouples were prepared by spot welding (in an argon atmosphere) a junc-

Nomenclature

$\mathcal{B}$ = mass transfer driving force, $(m_{1,\infty} - m_{1,s})/(m_{1,s} - 1)$
C_p = heat capacity (Btu/lb deg R)
D = tube diameter (ft)
$\mathcal{D}_{12}$ = binary diffusion coefficient (ft^2/sec)
g = normal gravity (ft/sec^2), also mass transfer conductance (lb/ft^2 sec)
h_{fg} = latent heat of vaporization (Btu/lb)
k = thermal conductivity (Btu/sec ft deg R)
m = mass fraction
$\dot{m}''$ = condensation rate (lb/ft^2 sec)
p = pressure (atm)
Pr = Prandtl number, $C_p\mu/k$
q = wall heat flux (Btu/ft^2 sec)
Re = Reynolds number, $\rho U_\infty D/\mu_\infty$
Sc = Schmidt number, $\mu/\rho\mathcal{D}_{12}$
T = temperature (deg F)
u, v = velocity components (ft/sec)
U_∞ = oncoming velocity (ft/sec)
x, y = boundary layer coordinates (ft)
δ = condensate film thickness (ft)
θ = angle measured from forward stagnation point
μ = absolute viscosity (lb/ft sec)
ρ = density (lb/ft^3)
τ = shear stress (lb/ft sec^2)

Subscripts

i = at the liquid-vapor interface, also inner thermocouple
l = liquid
Nu = Nusselt theory result
o = outer thermocouple
s = in the vapor phase, just adjacent to the interface
u = in the liquid phase, just adjacent to the interface
v = vapor
w = tube surface
∞ = bulk vapor
1, 2 = vapor and noncondensable, respectively

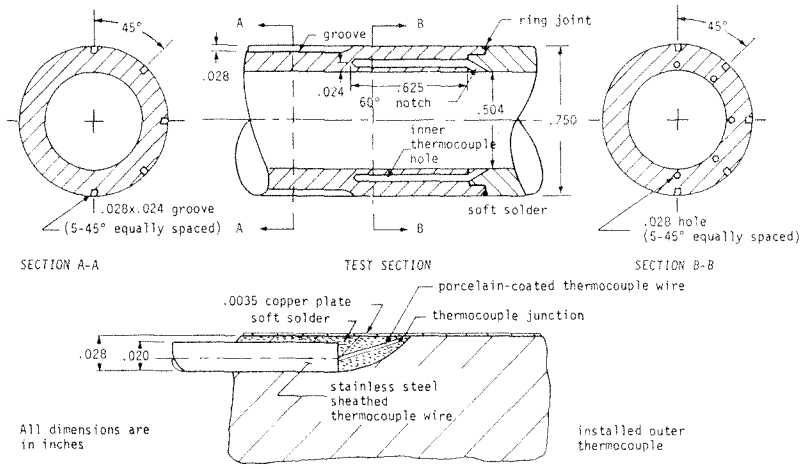

Fig. 2 Details of the heat transfer tube

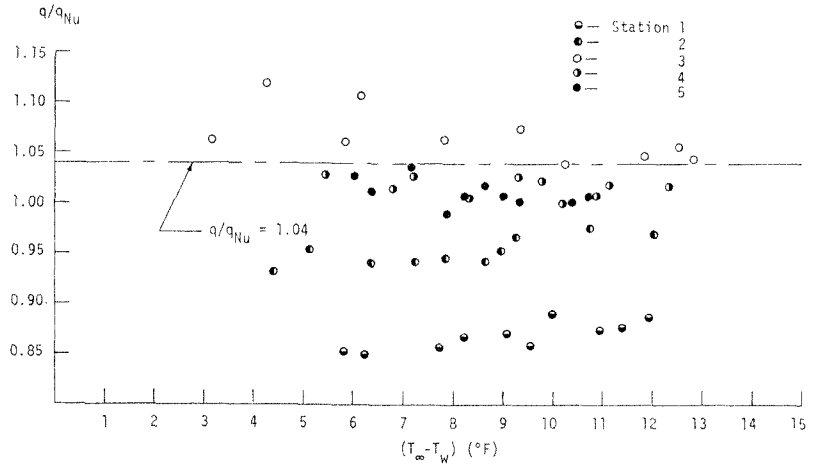

Fig. 3 Normalized heat flux at the stagnation point—all stations

tion about 0.25 in. from the sheath. The bare wires leading to the junction were coated with a thin layer of Saureisen No. 1 porcelain cement and were then vapor coated with about 5000 Å of copper to promote wetting by solder. The thermocouples were then soft-soldered within longitudinal grooves with the junctions being positioned just below the surface (~0.004 in.). Finally, the tube was carefully polished and about 0.0035 in. of copper plating was deposited, giving a final OD of 0.7505 in.

The thermocouple pairs and associated selector switch and lead wires were calibrated in situ at the Leeds and Northrup Standards Laboratory, North Wales, Pa. Calibration equations for each thermocouple were then developed, following Benedict and Ashby [8], and included in the data reduction code. Opposed pairs of thermocouples were calibrated as heat-flux-meters in a rig consisting of a metered electrical heater uniformly wound on the outside of the tube together with a coolant flow loop. Spurious heat losses and end effects were minimized through careful insulation and use of guard heaters. The calibration constant $K_{cal} = q/(T_o - T_i)$ took on the values 1044, 719, 767, 932, and 997 Btu/hr ft² deg F for meters 1–5, respectively. The variation in K_{cal} is due mainly to variations in location of the inner thermocouples. The thermocouple emf outputs were measured with a Leeds and Northrup K-2 potentiometer having a least count of 0.0005 mV. Further details of fabrication, calibration, and instrumentation of the heat transfer tube may be found in [7].

Test Procedures. Prior to performing a series of runs, the system was leak tested; usually, this was done by evacuating the system, letting it fill with water and then searching for air bubbles. In addition, periodic checks for leaks were made by measuring the air concentration during pure steam runs using a Claassen-type gauge; in no instance did the latter tests yield a bulk mass fraction of air in excess of 5×10^{-5} which, according to the analysis in [2], has no measurable effect on condensation rates. Filmwise condensation was easily established on a day-to-day basis by means of the freezing technique first described by Mills and Seban [9]. After a film had been established, the detrainment pattern of drops was observed and tube releveled if necessary by adjusting the rig support screws. After running for a few hours, the rig was presumed to be at steady state for given operating conditions and test data were then recorded at approximately 30 min intervals. Steady state was assumed to exist when the steam saturation temperature varied by less than 0.1 deg F between successive intervals. When operating conditions were changed, a new steady state usually was reached in about one hour.

Results and Discussion

Pure Steam. Local values of the flux q, as measured by the heat flux meters, were normalized by values of q calculated from Nusselt theory

$$q_{Nu}(\theta) = \left[\frac{2k^3(T_\infty - T_w)^3 h_{fg} g \rho_l(\rho_l - \rho_v)\sin^{1/3}\theta}{3D\mu_l\left(\frac{4}{3}\right)\int_0^\theta \sin^{1/3}\theta d\theta}\right]^{1/4}$$

with liquid properties, taken from sources listed in [10], being evaluated at $T_r = T_w + 0.33(T_\infty - T_w)$. The local surface temperature T_w was obtained by linearly extrapolating the outermost thermocouple reading T_o

$$T_w = T_o + q(\delta_1/k_1 + \delta_2/k_2)$$

with 1 and 2 denoting soft-solder and copper, respectively. The conductivities k_1 and k_2 were taken as 25.8 and 220 Btu/hr ft deg F while δ_1 and δ_2 were estimated to be 0.004 and 0.0035 in. For the pure steam runs, T_∞ and $\Delta T \equiv T_\infty - T_w$ varied from 108 to 152 and 3 to 21 deg F, respectively. Stable operation of the system required oncoming velocities which were not inappreciable, the range being 1.25 to 3.16 ft/sec. An analytical study by South [3] indicates an increase in q/q_{Nu}, due to vapor drag, of 2 to 8 percent in this range of U_∞. However, a careful examination of the experimental results revealed no discernible systematic effect of this parameter owing to the background level of random error (see Fig. 3). Thus the data for pure steam in this velocity range has been lumped together and compared with an average value of q/q_{Nu} predicted by the South analysis.

Typical data for q/q_{Nu} versus ΔT at the forward stagnation point ($\theta = 0$ deg) are shown in Fig. 3 for each of the five heat-flux-meter stations. Complete tabulations are given in [7]; the averaged values of q/q_{Nu} together with standard deviations σ are reproduced in Table 1 for each of the five stations. The average for q/q_{Nu} for all stations is 0.98 ± 0.10, which compares favorably with the average predicted value, 1.04 (obtained by running the computer code developed in [3] for a range of parameter values corresponding to the experimental conditions).

Typical data for local values of q/q_{Nu}, using station 4, are displayed in Fig. 4 for θ in the range -45 deg $\leq \theta \leq 135$ deg. Local data as measured by each station at locations $\theta = 0$, 45, 90, 135 deg are summarized in Table 2. The increased values of σ are attributed to temperature fluctuations at $\theta = 135$ deg F ($\sim \pm 2$ deg F) associated with the detachment of liquid droplets from the bottom of the tube. For quiescent steam, Chung [11] has shown by means of numerical solutions to the two-dimensional heat conduction problem in the wall, coupled with nonisothermal Nusselt theory, that the assumption of purely radial heat flow is excellent up to $\theta = 135$ deg. His results indicate that the heat-flux-meter calibration constants should be in error by no more than 1 percent at 90 deg and by only $1^1/_2$ percent at 135 deg.

Table 1 Summary of stagnation point pure steam results

Station	q/q_{Nu}	σ
1	0.87	0.01
2	0.95	0.01
3	1.07	0.03
4	1.01	0.01
5	1.00	0.01
Average	0.98	0.01

Table 2 Summary of pure steam data for the upper three quarters of the tube

Station	q/q_{Nu}	σ
1	0.88	0.01
2	0.95	0.01
3	1.05	0.03
4	1.01	0.02
5	1.03	0.02
Average	0.99	0.02

A complete error analysis was performed [7] to ascertain probable causes for the station-to-station variations of q/q_{Nu}. It was concluded that the probable cause was inaccurate extrapolation of T_o to obtain T_w, as augmented by inaccuracies in the heat-flux-meter calibrations. Similar difficulties have plagued other researchers attempting precise measurement of condensation heat transfer (see, for example, [12]), and we view our results to be satisfactory. Indeed, it now will be argued that the Nusselt theory affords a more precise method for calibrating the heat transfer tube. Such a calibration was carried out for each station using $\theta = 0$ deg data, and the new calibrations were used to reduce the steam-air mixture data.

Steam-Air Mixtures. Heat transfer data for condensation from steam-air mixtures were obtained at $\theta = 0$, 45, and 90 deg. Due to increased effects of the nonisothermal wall for $\theta > 0$ deg with gas present and the lack of a suitable theory for comparison, attention will be primarily focused on the stagnation point data. Using station 3, data were obtained at $\theta = 0$ deg with saturation temperatures, bulk air mass fractions, oncoming vapor velocities, and bulk-to-wall temperature drops in the ranges 98–142 deg F, 0.0006–0.07, 0.95–5.80 ft/sec, and 5.3–31 deg F, respectively. Due to the complexity of both system operation and data reduction, the problem parameters were not varied systematically; it would, for example, have been impractical to vary ΔT while holding T_∞, $m_{1,\infty}$, and U_∞ fixed. Instead, the parameters for a given experimental run were introduced into a computer code developed by South [3] to obtain numerical solutions of the forced flow noncondensable gas problem; these results were then compared with experiment. The Appendix of this paper presents the analytical formulation of the theory.

Typical results for comparison between theory and experiment at $\theta = 0$ are given in Fig. 5, where q/q_{Nu} is seen to range from 0.27 to 1.06 for the parameter ranges studied. Again, complete tabulations are given in [7]. The average percent discrepancy

$$\epsilon = 100 \frac{(q/q_{Nu})_{exp} - (q/q_{Nu})_{Num}}{(q/q_{Nu})_{Num}}$$

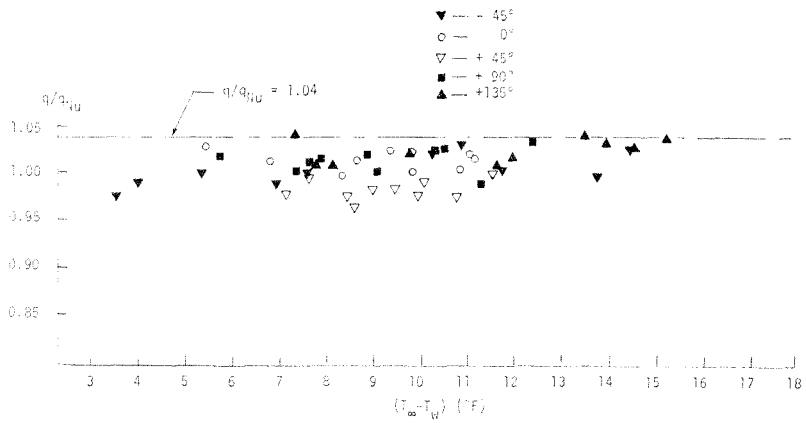

Fig. 4 Normalized local heat flux as measured by station 4

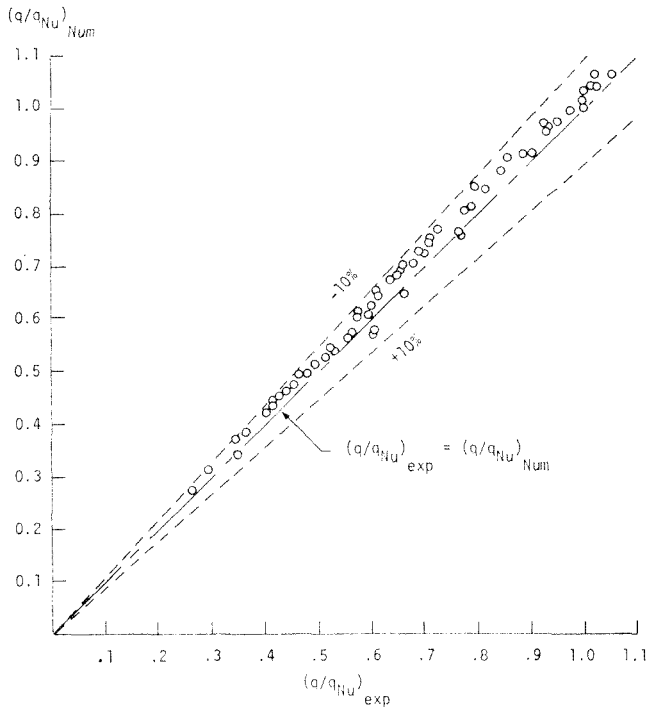

Fig. 5 Comparison of steam-air experimental stagnation point results with numerical solutions

between theory and experiment is −2.7 percent, the maximum deviation being 7.1 percent. The validity of the physical model and analysis of [2] has been therefore established in the range of parameters tested. The upper limit of 6 ft/sec on U_∞ was set by the maximum power input to the boiler (3.5 kw). At 6 ft/sec the effect of vapor drag on the liquid film is relatively small so that we cannot claim that this feature of the theory has been adequately tested. However, it is important to note that the dominant effect on condensation rate of vapor velocity is through the mass transfer conductance and not through vapor drag. The reader is referred to [2] for a detailed presentation of the theory and interpretation of the effects of the problem parameters on q/q_{Nu}. Of interest in the present context, however, is the apparent success of the theory at the low Reynolds numbers

$$16 \leq \mathrm{Re} = \rho D U_\infty/\mu_\infty \leq 75$$

which obtained in the current study: Further, it is found that a simpler semi-empirical theory reported in [2, 3], in which the mass transfer conductance g was taken as

$$g = [g_0^{3/2} + (-\mathcal{B}g_{-1})^{3/2}]^{2/3}$$

and the interfacial shear τ as

$$\tau = (\tau_0^{11/8} + \tau_{-1}^{11/8})^{8/11}$$

where 0 and −1 denote expressions [3] for $\dot{m}'' \to 0$ and $\dot{m}'' \to \infty$, respectively, also is in excellent agreement with experiment. For the data reported here, the average discrepancy between the simplified theory and experiment is about the same as that cited in the foregoing for the exact theory, and the simplified theory is recommended for engineering calculations.

For completeness, typical results for the local heat transfer coefficient over the upper half of the tube are displayed in Fig. 6. Apart from the expected effects of noncondensable gas on the level of heat transfer, the experimental results indicate a nearly uniform heat flux on the upper half of the tube, rather than the monotone decreasing distribution predicted by isothermal wall theory; this is due to the relatively large resistance of the wall and inside film. Due, however, to increased uncertainty in the accuracy of the heat flux meters as caused by nonradial flux lines

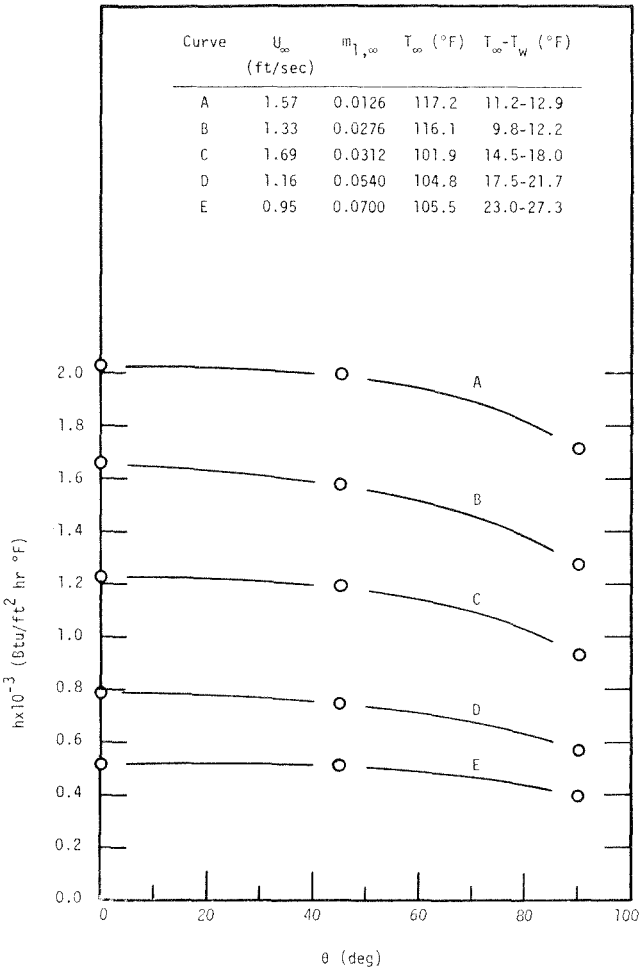

Fig. 6 Local values of heat transfer coefficient $h = q/[T_\infty - T_w]$ for steam-air

away from the stagnation point, further conclusions are not warranted.

Conclusions

1 For pure saturated steam q/q_{Nu} at the forward stagnation point was found to be 0.98 ± 0.10. For the range of parameters tested, a theoretical analysis, accounting for the effects of vapor drag, gives $q/q_{Nu} = 1.04$. The discrepancy is attributed to inaccurate tube surface temperature measurements.

2 For steam-air mixtures q/q_{Nu} at the forward stagnation point was found to be in excellent agreement with predictions of a laminar boundary layer analysis by Denny and South [2]. The average discrepancy between experiment and theory was −2.7 percent, while the maximum discrepancy was 7.1 percent.

References

1 Denny, V. E., Mills, A. F., and Jusionis, V. J., "Laminar Film Condensation From a Steam-Air Mixture Undergoing Forced Flow Down a Vertical Surface," JOURNAL OF HEAT TRANSFER, TRANS. ASME, Series C, Vol. 93, 1971, pp. 297–304.

2 Denny, V. E., and South, V., III, "Effects of Forced Flow, Noncondensables, and Variable Properties on Film Condensation of Pure and Binary Vapors at the Forward Stagnation Point of a Horizontal Cylinder," *International Journal of Heat and Mass Transfer*, Vol. 15, 1972, pp. 2133–2142.

3 South, V., III, "Laminar Film Condensation From Binary Vapor Mixtures on the Outside of a Horizontal Cylinder and the Inside of a Vertical Tube," PhD dissertation, University of California, Los Angeles, 1972.

4 Othmer, D. F., "The Condensation of Steam," *Industrial and Engineering Chemistry*, Vo. 21, 1929, pp. 576–583.
5 Henderson, C. L., and Marchello, J. M., "Film Condensation in the Presence of a Noncondensable Gas," JOURNAL OF HEAT TRANSFER, TRANS. ASME, Series C, Vol. 91, 1969, pp. 447–450.
6 Keenan, J. H., and Keyes, F. G., "Thermodynamic Properties of Steam," First ed., Wiley, New York, 1936.
7 Rauscher, J. W., "An Experimental Investigation of Laminar Film Condensation From Steam-Air Mixtures Flowing Downward Over a Horizontal Tube," PhD dissertation, University of California, Los Angeles, 1973.
8 Benedict, R. P., and Ashby, H. F., "Empirical Determination of Thermocouple Characteristics," *Journal of Power Engineering*, TRANS. ASME, Series A, Vol. 85, 1963, pp. 9–26.
9 Mills, A. F., and Seban, R. A., "The Condensation Coefficient of Water," *International Journal of Heat and Mass Transfer*, Vol. 10, 1967, pp. 1815–1827.
10 Denny, V. E., and Mills, A. F., "Nonsimilar Solutions for Laminar Film Condensation on a Vertical Surface," *International Journal of Heat and Mass Transfer*, Vol. 12, 1969, pp. 965–979.
11 Chung, D. K., "Verification of Nusselt Theory of Condensation on a Horizontal Tube," MS thesis, University of California, Los Angeles, 1972.
12 Wilcox, S. J., and Rohsenow, W. M., "Film Condensation of Potassium Using a Copper Condensing Block for Precise Wall-Temperature Measurement," JOURNAL OF HEAT TRANSFER, TRANS. ASME, Series C, Vol. 92, 1970, pp. 359–371.

APPENDIX

Analytical Formulation

Coordinates x and y are taken along and normal to the tube wall with x measured from the forward stagnation point, $\theta = 0$ deg; the corresponding velocity components are u and v. The oncoming vapor-gas mixture has velocity U_∞, vapor mass fraction $m_{1,\infty}$ and saturation temperature T_∞. The tube has radius R and the surface is at T_w. The governing equations are taken as

$$\frac{\partial}{\partial x}(\rho_v u) + \frac{\partial}{\partial y}(\rho_v v) = 0 \tag{A1}$$

$$\rho_v u \frac{\partial u}{\partial x} + \rho_v v \frac{\partial u}{\partial y} = \frac{\partial}{\partial y}\left(\mu_v \frac{\partial u}{\partial y}\right) + \rho_v g \sin\frac{x}{R} - \frac{dP}{dx} \tag{A2}$$

$$\rho_v u \frac{\partial m_1}{\partial x} + \rho_v v \frac{\partial m_1}{\partial y} = \frac{\partial}{\partial y}\left(\frac{\mu_v}{\mathrm{Sc}} \frac{\partial m_1}{\partial y}\right) \tag{A3}$$

$$\rho_v u \frac{\partial T}{\partial x} + \rho_v v \frac{\partial T}{\partial y} = \frac{\partial}{\partial y}\left(\frac{\mu_v}{\mathrm{Pr}} \frac{\partial T}{\partial y}\right) + \frac{\mu_v}{\mathrm{Pr}} \frac{\partial T}{\partial y}\left[\frac{\partial \ln C_{pv}}{\partial y} + \frac{\mathrm{Pr}}{\mathrm{Sc}} \frac{C_{p1} - C_{p2}}{C_{pv}} \frac{\partial m_1}{\partial y}\right] \tag{A4}$$

for the vapor boundary layer, and

$$\mu_l \frac{d^2u}{dy^2} = -\left[\rho_l g \sin(x/R) - \frac{dP}{dx}\right] \tag{A5}$$

$$\frac{d^2T}{dy^2} = 0 \tag{A6}$$

for the liquid film. Neglecting second order effects of nonuniform suction, the static pressure gradient is

$$-\frac{dP}{dx} = [(4\rho_\infty U_\infty^2/R)\cos(x/R) - \rho_\infty g]\sin(x/R) \tag{A7}$$

Equations (A1) through (A6) are subject to the boundary conditions

$$u \to u_e = 2U_\infty \sin(x/R), \qquad m_1 \to m_{1,\infty}, \quad \text{and} \quad T \to T_\infty \tag{A8}$$

at the edge of the vapor boundary layer;

$$u = 0, \quad \text{and} \quad T = T_w \tag{A9}$$

at the tube surface; and

$$u|_u = u|_s = u_i \tag{A10}$$

$$\mu_l \frac{\partial u}{\partial y}\bigg|_u = \mu_v \frac{\partial u}{\partial y}\bigg|_s = \tau_i \tag{A11}$$

$$\dot{m}'' = \dot{m}'' m_{1,s} - \rho_v \mathfrak{D}_{12} \frac{\partial m_1}{\partial y}\bigg|_s \tag{A12}$$

$$T_u = T_s = T_i(m_{1,s}, P) \tag{A13}$$

$$k_l \frac{\partial T}{\partial y}\bigg|_u = -\dot{m}'' h_{fg} + k_v \frac{\partial T}{\partial y}\bigg|_s \tag{A14}$$

at the vapor-liquid interface. In equation (A13) thermodynamic equilibrium is assumed to hold. The condensation rate is given by

$$\rho_v v|_s \equiv \dot{m}'' = -\frac{d}{dx}\int_0^\delta \rho u dy|_l \tag{A15}$$

where δ is the condensate film thickness. Thermophysical properties for steam-air mixtures were evaluated following [1].

R. H. Pletcher

Assoc. Professor,
Department of Mechanical Engineering
and Engineering Research Institute,
Iowa State University,
Ames, Iowa. Mem. ASME

Prediction of Transpired Turbulent Boundary Layers

A model for the mixing length distribution near the wall in turbulent boundary layer flow with transpiration is presented. The model is based on a new formulation of the exponential damping function originally suggested by Van Driest. The analysis used to evaluate the damping function employs the same set of assumptions successfully used by several investigators in the past to develop the law of the wall with blowing. This mixing length model is then used with the calculation method previously developed by the author to solve the governing conservation equations of mass, momentum, and energy in partial differential form. Predicted velocity profiles, skin friction coefficients, and Stanton numbers are compared with experimental results taken over a wide range of transpiration for both incompressible and compressible flows.

Introduction

In recent years, considerable research activity on the transpired turbulent boundary layer (both with blowing and suction) has been observed. Flows with transpiration have continued to be important in applications as a means of providing cooling for surfaces and for boundary layer control. Several recent experimental programs [1, 2, 3][1] have contributed to our understanding of the manner in which wall blowing or suction influences skin-friction and heat transfer.

Considerable progress has also been made in recent years in calculation methods for turbulent flows. Differential methods, which employ a finite-difference technique to solve the governing conservation equations in partial differential form, have been shown to be an effective way of predicting turbulent flows under a wide range of conditions, including heat transfer and pressure gradients [4, 5, 6]. These methods employ a mixing length or eddy viscosity model for the turbulent transport mechanism. Models of this type for wall boundary layers have been found to be remarkably general, being largely independent of Mach number, heat transfer, and to a large degree, pressure gradient. Some workers have been exploring more complex models for turbulent flows which require the simultaneous solution of one or more additional differential equations. These models, discussed by Launder and Spalding [7], offer great promise for turbulent flows in general but usually result in predictions which are in agreement with simple mixing length theory for flows which are nearly in equilibrium.

Several workers have employed differential methods to predict flows with transpiration [1, 5, 6, 8–11]. At this point the generality of the simple mixing models which work well for flows over impermeable walls breaks down and some modification is required near the wall to accurately predict flows with anything but very small blowing rates. Since several investigators, especially Stevenson [12], Squire [13], and Simpson [14], have observed that the experimental data for transpired boundary layers still indicate the existence of a fully turbulent region for which the mixing length l is proportional to κy, where κ is the von Karman constant, just as for flows with no transpiration, the modification typically has been to the Van Driest [15] damping function which has been a part of the model employed by most investigators to date. All of these analyses except that of Cebeci [6] have utilized additional empirical input based on recent experiments in order to achieve this modification. A detailed description of the status of analytical and experimental research on turbulent boundary layers with transpiration can be found in the recent reviews by Jeromin [16] and Coles [17].

The purpose of the present paper is to propose a generalization of the Van Driest damping function to handle flows in which the shear stress near the wall varies significantly. This interpretation of the damping function together with the analysis sometimes known as "the law of the wall with blowing" [12, 13] leads with no additional empirical input to a mixing length model which predicts well most details of the transpired turbulent boundary layer. This model, like all others suggested to date, is based on "empiricism" but it differs from most others introduced recently in that it suggests a generalization of the damping function suitable for flows with transpiration and then predicts the influences of the transpiration on the mixing length by solving an approximate form of the momentum equation near the wall. This is in contrast with the most common procedure suggested by others which essentially maintains the original form of the damping function proposed by Van Driest but modifies the magnitude to account for blowing according to a curve fit to the available experimental data.

This mixing length model is then used with an explicit finite-

[1] Numbers in brackets designate References at end of paper.

Contributed by the Heat Transfer Division for publication in the JOURNAL OF HEAT TRANSFER. Manuscript received by the Heat Transfer Division, November 6, 1972. Paper No. 74-HT-M.

difference method [4, 5, 18] to solve the governing conservation equations for several incompressible and compressible transpired turbulent boundary layer flows with and without heat transfer. Predicted velocity profiles, skin-friction coefficients, and Stanton numbers are compared with experimental results.

Analysis

The Conservation Equations. Neglecting normal stress terms, the equations governing the two-dimensional compressible turbulent boundary layer can be written as

Momentum:

$$\rho u \frac{\partial u}{\partial x} + (\rho v + \overline{\rho' v'}) \frac{\partial u}{\partial y} = \rho_e u_e \frac{du_e}{dx} + \frac{\partial}{\partial y} \left(\mu \frac{\partial u}{\partial y} - \rho \overline{u' v'}\right) \tag{1}$$

Energy:

$$\rho u \frac{\partial H}{\partial x} + (\rho v + \overline{\rho' v'}) \frac{\partial H}{\partial y} = \frac{\partial}{\partial y} \left[\frac{k}{c_p} \frac{\partial h}{\partial y} - \rho \overline{v' h'} + u\left(\mu \frac{\partial u}{\partial y} - \rho \overline{u' v'}\right) \right] \tag{2}$$

Continuity:

$$\frac{\partial}{\partial x} (\rho u) + \frac{\partial}{\partial y} (\rho v + \overline{\rho' v'}) = 0 \tag{3}$$

State:

$$p/\rho = RT \tag{4}$$

Appropriate boundary conditions are

$$u(x, 0) = 0, \quad v(x, 0) = v_w, \quad H(x, 0) = H_w \text{ or}$$

$$\frac{\partial H}{\partial y}(x, 0) = \left(\frac{\partial h}{\partial y}\right)_w, \quad \lim_{y \to \infty} u(x, y) = u_e(x), \quad \lim_{y \to \infty} H(x, y) = H_e(x). \tag{5}$$

In addition, initial values must be provided for the axial component of velocity and the enthalpy:

$$u(x_0, y) = F_1(y), \quad h(x_0, y) = F_2(y), \tag{6}$$

and $u_e(x)$ must be specified for pressure gradient flows.

Model for the Turbulent Transport. Using Prandtl's mixing length concept, it is assumed that

$$-\rho \overline{u' v'} = \rho l^2 \left|\frac{\partial u}{\partial y}\right| \frac{\partial u}{\partial y} \tag{7}$$

where $\rho l^2 |\partial u/\partial y|$ will be identified as μ_T, a turbulent or "eddy" viscosity. Thus the total or effective shearing stress can be described by

$$\tau = (\mu + \mu_T) \frac{\partial u}{\partial y}. \tag{8}$$

It is assumed that the turbulent diffusivities for heat and momentum are related in a manner analogous to laminar flows resulting in

$$k_T = c_p \mu_T / \mathrm{Pr}_T \tag{9}$$

where k_T is the turbulent or eddy conductivity and Pr_T is the turbulent Prandtl number which was set equal to a constant value of 0.9 for all predictions of this paper. The turbulent conductivity concept allows

$$-\rho \overline{v' h'} = (\mu_T/\mathrm{Pr}_T) \frac{\partial h}{\partial y} = (\mu_T/\mathrm{Pr}_T) \frac{\partial H}{\partial y} - (\mu_T/\mathrm{Pr}_T) u \frac{\partial u}{\partial y}. \tag{10}$$

It is assumed that the mixing length is given by

$$l/\delta = 0.41\, Dy/\delta, y/\delta \leq \frac{0.089}{0.41\, D} \tag{11}$$

$$l/\delta = 0.089, \quad y/\delta > \frac{0.089}{0.41\, D} \tag{12}$$

where D is a damping function which accounts for the effects of the kinematic viscosity on the turbulence near the wall and δ is the boundary layer thickness. For flows without transpiration, the form suggested by Van Driest [15] works well:

$$D = 1 - e^{-y^+/26}. \tag{13}$$

The Mixing-Length Distribution for Transpired Flows. To generalize the damping function to flows with transpiration let

$$D = 1 - e^{-z} \tag{14}$$

where z must specialize to $y^+/26$ for flows without transpiration. The term e^{-z} must be a function which equals one at the wall and becomes negligibly small in the fully turbulent region where experimental evidence indicates that $l = \mathfrak{K} y$ requiring that $D = 1$. Since the function z in effect bridges the gap between the wall where the kinematic viscosity plays the dominant role in the momentum transport mechanism and the fully turbulent region where turbulent transport is dominant, it seems plausible that z should contain parameters reflecting the state of fluid stress at the wall and near the beginning of the fully turbulent region or at some reference point within the fully turbulent region. Flows for which $z = y^+/26$ works well are those for which the shear stress is nearly constant throughout the wall layer. It is proposed that when the shear stress does vary significantly near the wall, a generalized form for the damping function, which to date appears to lead to good agreement with a wide range of experiments, can be based upon

$$z = (\rho_w y/26\mu_w)(\tau/\rho_w)^{1/2}(\tau_{FT}/\tau_w)^{1/2} \tag{15}$$

where τ is the local shear stress and τ_{FT} is the characteristic shear stress near the beginning of the fully turbulent region. Equation (15) is perhaps the simplest functional form which contains the stress quantities which are believed to be significant and yet reduces to the well-established Van Driest form when the shear stress is constant near the wall. For unblown flows the fully turbulent region begins for y^+ somewhere between 26 and 60. Curiously enough, the analysis of considerable experimental data [2,

Nomenclature

B = blowing parameter, $\rho_w v_w/\rho_e u_e$
c_f = local skin-friction coefficient
c_p = specific heat at constant pressure
h = specific enthalpy
H = total enthalpy, $h + \frac{u^2}{2}$
k = thermal conductivity
l = mixing length
M = Mach number
Pr = Prandtl number
R = gas constant in ideal gas equation of state
Re_x = Reynolds number, $\rho_e u_e x/\mu_e$
Re_θ = Reynolds number, $\rho_e u_e \theta/\mu_e$
St = Stanton number, $k(\partial T/\partial y)_w/\rho_e u_e (H_{aw} - H_w)$
T = absolute temperature
u = x component of time mean velocity
u^* = $(\tau_w/\rho_w)^{1/2}$
u^+ = u/u^*
v = y component of time mean velocity
v_w^+ = v_w/u^*
x = distance along surface
y = distance normal to wall
y^+ = dimensionless distance, $\rho_w y u^*/\mu_w$
δ = boundary layer thickness
θ = momentum thickness
μ = dynamic viscosity
ρ = time mean density
τ = total shear stress

Subscripts

e = evaluated at outer edge of boundary layer
w = evaluated at wall
T = turbulent flow

Superscripts

$( )'$ = primes denote fluctuating quantities
$(\bar{\ })$ = bars denote time mean quantity

14, 16] suggests that the beginning of the fully turbulent region (region of straight line velocity profile in law of the wall with blowing coordinates) is largely independent of transpiration. In the present work we will assume that the shear stress characteristic of the beginning of the fully turbulent region for damping purposes, τ_{FT}, occurs at $y^+ = 26$. It should be pointed out that the basic form of the damping function is independent of the extent of transpiration, i.e., does not contain v_w^+ as a parameter.

Using this model, τ_{FT} can be evaluated by using the well-known [13] approximate solution to the momentum and continuity equation which results when streamwise derivatives are neglected near the wall:

$$\frac{\tau}{\tau_w} = 1 + v_w^+ u^+ \tag{16}$$

Finite difference methods which predict velocities at the $i + 1$ level based on stress gradients approximated at the i level could then use equation (16) to evaluate both the local τ and τ_{FT} in equation (15) to evaluate the damping function, the latter simply by evaluating u^+ at $y^+ = 26.0$. Here i is the finite difference index corresponding to the x direction. Alternatively, τ_{FT} can be evaluated by utilizing the "law of the wall with blowing" which can be developed from equation (16) with the additional "fully turbulent" assumptions that $\tau = \rho l^2 |\partial u/\partial y| \partial u/\partial y$ and $l = \mathcal{K} y$. This results in

$$\phi = \frac{2}{v_w^+}\left[(1 + v_w^+ u^+)^{1/2} - (1 + v_w^+ u_a^+)^{1/2} \right] = \frac{1}{\mathcal{K}} \ln \left| \frac{y^+}{y_a^+} \right| \tag{17}$$

The term u_a^+ and y_a^+ are constants of integration which can be evaluated as $u_a^+ = 11.0$ at $y_a^+ = 11.0$ as suggested by Simpson [14] who found that these constants appeared to be nearly independent of the transpiration rate. Making this evaluation of the constants u_a^+ and y_a^+ and letting the von Karman constant equal 0.41 gives

$$\phi = \frac{2}{v_w^+}\left[(1 + v_w^+ u^+)^{1/2} + (1 + 11 v_w^+)^{1/2} \right] = \frac{1}{0.41} \ln \left| \frac{y^+}{11} \right| \tag{18}$$

For flows without transpiration, equation (17) reduces to the law of the wall for impermeable surfaces in the form

$$u^+ = \frac{1}{0.41} \ln y^+ + 5.15 \tag{19}$$

Letting $\phi = 2.09$ for the beginning of the fully turbulent region, corresponding to $y^+ = 26$, τ_{FT} can be computed in terms of v_w^+ and τ_w by combining equations (16) and (18):

$$\frac{\tau_{FT}}{\tau_w} = 1.0 + 1.092 v_w^{+2} + 2.09 v_w^+ (1 + 11 v_w^+)^{1/2} + 11 v_w^+ \tag{20}$$

The damping function then becomes

$$D = 1 - \exp\left\{ - (\rho_w y/26\mu_w)(\tau/\rho_w)^{1/2} \left[1 + 1.092 v_w^{+2} + 2.09(1 + 11 v_w^+)^{1/2} + 11 v_w^+ \right]^{1/2} \right\} \tag{21}$$

In equation (21) the local shear stress τ can be evaluated in the manner most compatible with the calculation method or analysis scheme being utilized. In all results presented in this paper, τ was evaluated as indicated in equation (16) and τ_{FT} according to equation (20) except as noted below for flows with pressure gradients.

For transpired flows without pressure gradient, predicted skin friction coefficients made by evaluating τ_{FT} according to equation (20) and by using τ for $y^+ = 26.0$ from the solution at the i level, agreed to within 1 percent, which tends to substantiate that streamwise derivatives are indeed small very near the wall. Since good results have been obtained in previous work [4] by evaluating all properties in the damping function at wall conditions, equation (17), which assumes constant density, has also been used in developing the damping function for compressible flows.

Comments on Flows With Pressure Gradients. For flows with transpiration the damping factor clearly needs modification in order for a mixing length model to provide good agreement with experimental results. The matter is not so clear cut for flows with pressure gradients, and reasonably good agreement with experimental data is often observed for flows with no transpiration when the damping factor in the form originally suggested by Van Driest, equation (13), is used. It is doubtful that sufficient experimental data exist for both favorable and adverse pressure gradients with and without transpiration to allow a conclusive study of transport processes very near the wall. Based on comparisons with the favorable pressure gradient data of Julien [19], the following modification to the damping factor resulted in small changes in the predicted skin friction coefficient in the right direction as to give better agreement with the experimental results.

If streamwise derivatives continue to be negligible near the wall (this assumption certainly becomes more questionable for flows with pressure gradients), the momentum equation can be integrated near the wall to give, in dimensionless form,

$$\tau/\tau_w = 1 + v_w^+ u^+ + p^+ y^+ \tag{22}$$

where

$$p^+ = (\mu_w/\rho_w^2 u^{*3}) \frac{dp}{dx}$$

Evaluating τ in equation (22) according to mixing-length assumptions ($\tau = \mathcal{K}^2 y^2 |\partial u/\partial y| \partial u/\partial y$) leads to an expression which cannot be integrated analytically for flows with both transpiration and pressure gradients. Thus it does not appear possible to develop an expression from equation (22) analogous to equation (18) which would be "the law of the wall with blowing and pressure gradient." This integration was circumvented in the present calculations by evaluating τ in the damping function according to equation (22), using values for v_w^+, u^+, p^+ obtained at station i to compute the new velocities from the governing equations in finite difference form at station $i + 1$, where again i is the index associated with the x direction. This procedure is completely consistent with the finite difference procedure [4] in that the finite difference molecules used for the x momentum equation were centered about the point (i, j). τ_{FT} was evaluated from equation (22) for $y^+ = 26.0$.

Comparison of Calculated and Experimental Results

In order to assess the effect of transpiration on the damping function, a damping parameter A^+ is commonly defined according to

$$D = 1 - \exp\left[- (y \rho_w/\mu_w A^+)(\tau/\rho_w)^{1/2} \right] \tag{23}$$

Comparing equations (21) and (23) it is clear that, in the absence of pressure gradients,

$$A^+ = 26/\left[1 + 1.092 v_w^{+2} + 2.09(1 + 11 v_w^+)^{1/2} + 11 v_w^+ \right]^{1/2} \tag{24}$$

and that $A^+ = 26$ for flows without transpiration. It should be pointed out that, according to the present definition, the value of A^+ does not reflect the entire influence of transpiration on the damping function because in this work the local τ also appears in the expression for D and, according to equation (16), $\tau = \tau_w + v_w^+ u^+ \tau_w$. Thus for flows with blowing, the viscous sublayer thickness is always less than indicated by equation (24) alone. Other workers such as Cebeci [6], who do not include the local τ in their damping functions, consequently employ different definitions of A^+. This should be kept in mind as comparisons are made. Fig. 1 shows a comparison between A^+ computed according to equation (24), the correlation equation of Kays [1], and the data of Simpson [14]. The general agreement between the present analysis and the correlation equation of Kays [1], which is reported to be based on an extensive series of experiments, is quite encouraging.

Fig. 2 shows some comparisons of predicted skin friction coefficients with the experimental data of Simpson [14] for four different blowing ratios, $B = \rho_w v_w/\rho_e u_e$. The predictions of Cebeci [9] are also plotted for three of these cases. Cebeci's predictions are

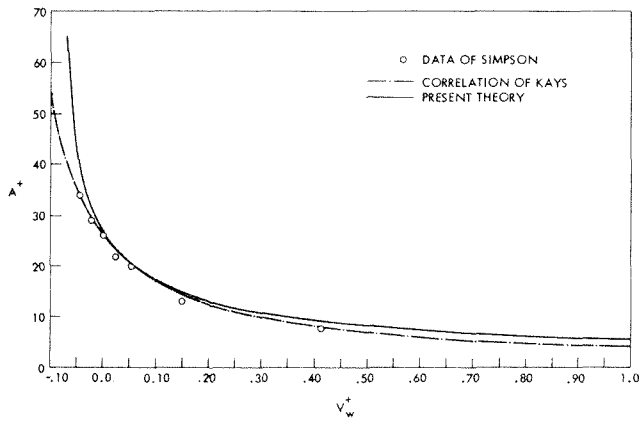

Fig. 1 Comparison of A^+ calculated according to present theory, the correlation equation of Kays [1],and the data of Simpson (1968)

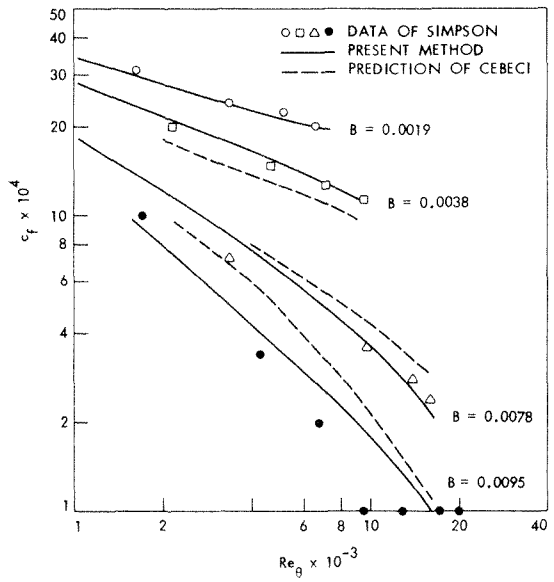

Fig. 2 Comparison of calculated and experimental results for the wall blowing data of Simpson [14]

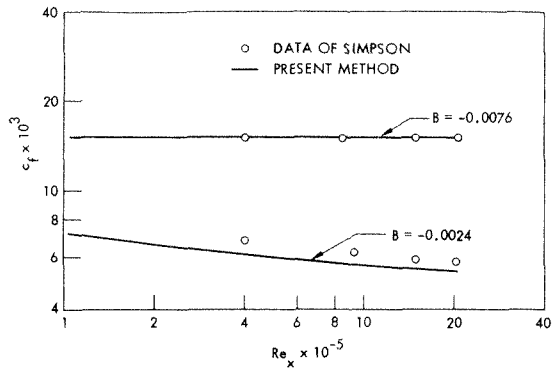

Fig. 3 Comparison of calculated and experimental results for the wall suction data of Simpson [14]

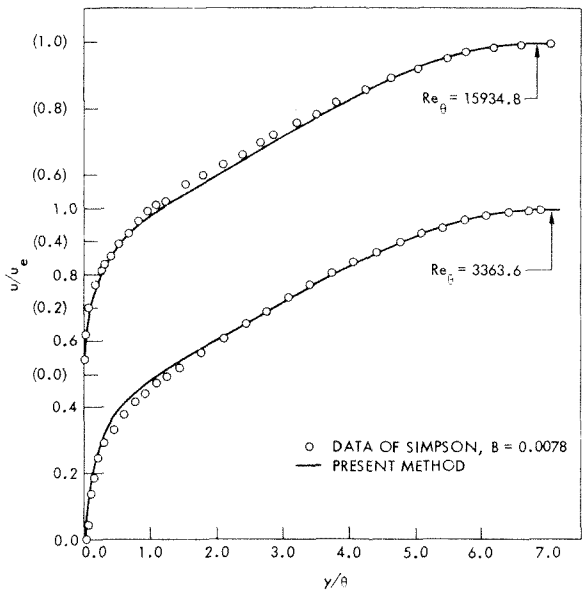

Fig. 4 Comparison of calculated and experimental velocity profiles for the boundary layer with blowing measured by Simpson [14], B = 0.0078

also based on an analytical extension of the Van Driest damping function, but the present method seems to give slightly better agreement with the experimental data. Fig. 3 shows similar comparisons with Simpson's data [14] for two different suction rates, $B = -0.0076$ and -0.0024. Predicted velocity profiles have been compared with Simpson's measurements [14] for all the blowing rates indicated in Figs. 2 and 3, and the agreement has been found to be reasonably good. A representative velocity profile comparison is shown in Fig. 4 for $B = 0.0078$.

Several comparisons were made with the compressible adiabatic turbulent boundary layer data reported by Squire [3] at Mach numbers 1.8, 2.5, and 3.6 and for blowing ratios ranging up to $B = 0.0025$. Comparisons of skin friction coefficients are given in Table 1. The agreement appears satisfactory considering the estimated uncertainty in c_f reported by the author ranging from ± 0.0001 at $B = 0$ to ± 0.0025 for $B = 0.0036$. This agreement tends to substantiate that the model for incompressible flow readily extends to compressible flow, at least up to Mach numbers covered by the Squire [3] report, when the local density is used in the mixing length formulation, equation (7), and the damping function is evaluated using wall values for properties. Fig. 6 shows some representative velocity profile comparisons with the measurements of Squire [3]. The agreement is not quite as good as is usually observed for incompressible flows with comparable blowing ratios.

Comparisons were also made with the experimental data of McQuaid [2]. Agreement between most predicted boundary layer parameters, such as the momentum thickness and velocity profiles, was quite good. Several investigators have remarked about the uncertainty in the skin friction coefficients obtained by McQuaid [9, 11, 14]. Fig. 6 shows a comparison of the predictions of the present method and the method of Brundrett, et al., with the skin friction coefficient determined by McQuaid from the momentum integral equation for $B = 0.008$. Although the predictions of the present method appear to agree a little better with the experimental data than the Brundrett, et al., predictions, both are within the error estimate of about 100 percent which is usually associated with this particular set of data. Simpson [14] discusses the probable reasons why McQuaid's skin friction results should

Table 1 Comparison of calculated and experimental skin friction coefficients for the data of Squire [3]

M_e	$B \times 10^3$	$c_f \times 10^3$(exp)	$c_f \times 10^3$(calc)
1.8	0	2.03	2.02
1.8	1.3	1.40	1.26
1.8	2.5	0.5	0.629
2.5	0	1.67	1.65
2.5	0.6	1.15	1.15
2.5	1.3	1.0	0.92
2.5	2.4	0.48	0.476
3.6	1.2	0,56	0.559

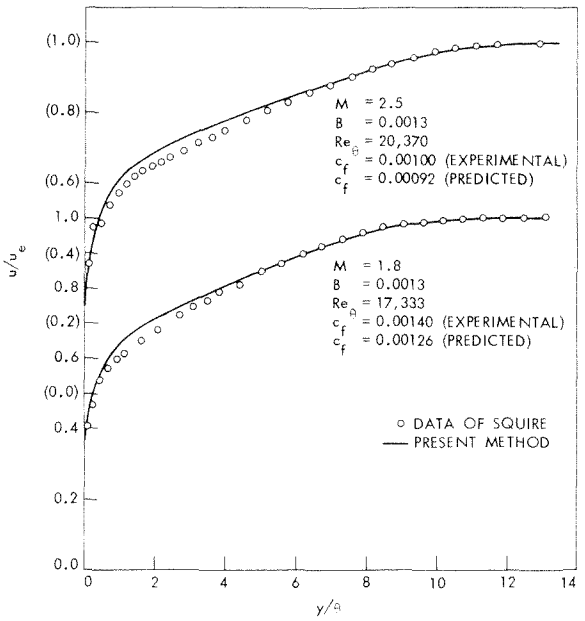

Fig. 5 Comparison of calculated and experimental results for the compressible boundary layer with blowing measured by Squire [3], B = 0.0013

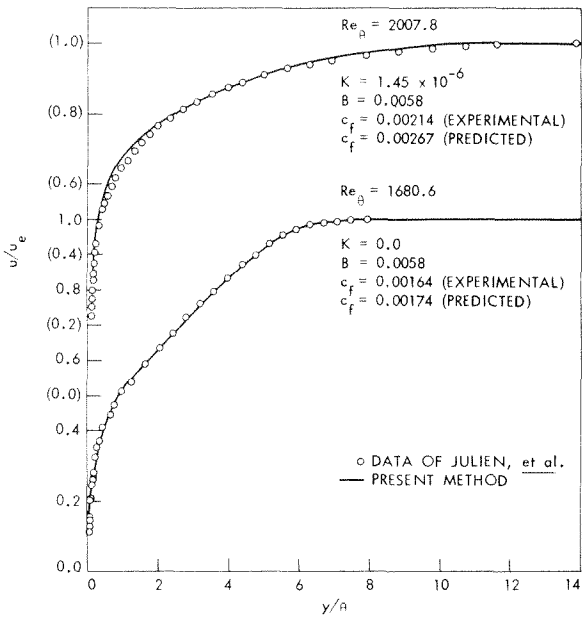

Fig. 7 Comparison of calculated and experimental results for the accelerating boundary layer with blowing measured by Julien [19], B = 0.0058

be considered unreliable. Other skin friction comparisons with McQuaid's experiments are being omitted because of this experimental uncertainty. A comparison between predicted and measured values of momentum thickness is also shown in Fig. 6 and the agreement is seen to be quite good.

Fig. 7 presents comparisons with the data of Julien [19] for the turbulent boundary layer with blowing, B = 0.0058, in a favorable pressure gradient. Velocity profile agreement can be observed to be quite good.

One of the most extensive series of experiments involving the transpired turbulent boundary layers with heat transfer was reported on by Moffat and Kays [20]. Fig. 8 shows comparisons of predicted Stanton numbers with their measurements for several flows with both blowing and suction. The general level of agreement between predictions and the experimental results is good

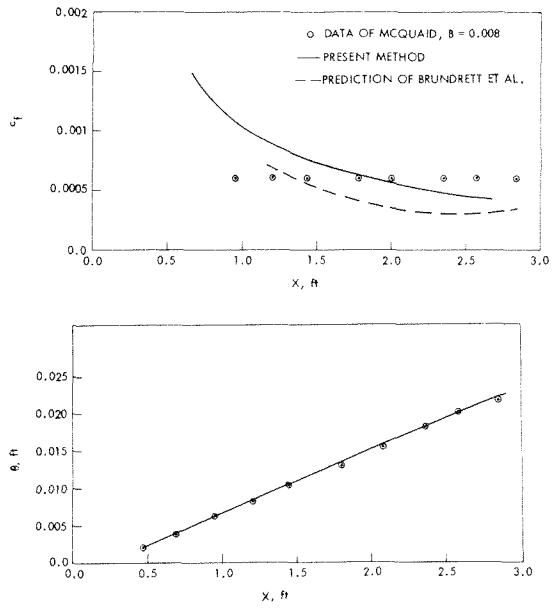

Fig. 6 Comparison of calculated and experimental momentum thickness and skin friction values for the boundary layer with blowing measured by McQuaid [2], U_e = 50.0, B = 0.008

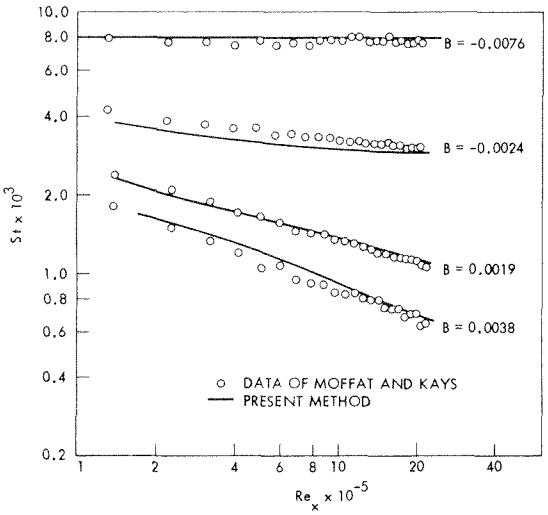

Fig. 8 Comparison of calculated and experimental Stanton numbers for the transpired boundary layer with heat transfer measured by Moffat and Kays [20]

considering the estimated uncertainty interval of ±0.0001 in St units for the measurements as reported by Moffat and Kays [20]. This tends to substantiate that the range of applicability of the present analysis includes flows with heat transfer and leads to useful predictions for the Stanton number in flows with transpiration.

Summary and Conclusions

In the present analysis, we have attempted to reexamine existing concepts which have been substantiated within limits by experiments, such as the law of the wall with blowing and the Van Driest damping function, to see if a transport model consistent with these existing concepts could be developed for predicting the development of the transpired turbulent boundary layer under a wide range of conditions. To this end, the damping function for the inner wall region, originally proposed by Van Driest, has been generalized to a form which is believed to be logically more suitable to flows for which the local shearing stress varies significantly very near the wall, as is observed particularly for transpired turbulent boundary layers.

This model, when used with the explicit calculation procedure previously developed by the author, has been shown to provide generally good agreement with the measured velocity profiles, skin friction coefficients, and Stanton numbers from several investigators over a wide range of blowing and suction ratios for both incompressible and compressible turbulent flow.

Acknowledgments

This work was supported by the Engineering Research Institute, Iowa State University, through funds provided by the National Science Foundation under Grant No. GK18810.

References

1 Kays, W. M., "Heat Transfer to the Transpired Turbulent Boundary Layer," *International Journal of Heat and Mass Transfer,* Vol. 15, 1972, pp. 1023–1045.

2 McQuaid, J., "Experiments on Incompressible Turbulent Boundary Layers With Distributed Injection," ARC R and M No. 3549, 1967.

3 Squire, L. C., "Further Experimental Investigations of Compressible Turbulent Boundary Layers With Air Injection," ARC R and M No. 3627, 1970.

4 Pletcher, R. H., "Calculation Method for Compressible Turbulent Boundary Flows With Heat Transfer," *AIAA Journal,* Vol. 10, 1972, pp. 245–246.

5 Pletcher, R. H., "On a Solution for Turbulent Boundary Layer Flows With Heat Transfer, Pressure Gradients, and Wall Blowing or Suction," *Heat Transfer 1970,* Vol. 2, Elsevier Publishing, Amsterdam, 1970.

6 Cebeci, T., "Calculation of Compressible Turbulent Boundary Layers With Heat and Mass Transfer," *AIAA Journal,* Vol. 9, 1971, pp. 1091–1097.

7 Launder, B. E., and Spalding, D. B., *Mathematical Models of Turbulence,* Academic Press, 1972.

8 Cebeci, T., "Behavior of Turbulent Flow Near a Porous Wall With Pressure Gradient," *AIAA Journal,* Vol. 8, 1970, pp. 2152–2156.

9 Cebeci, T., "Calculation of Incompressible Turbulent Boundary Layers With Mass Transfer Including Highly Accelerated Flows," JOURNAL OF HEAT TRANSFER, TRANS. ASME, Series C, Vol. 93, 1971, pp. 271–280.

10 Bushnell, D. M., Beckwith, I. E., "Calculations of Non-Equilibrium mental Data," *AIAA Journal* Vol. 8, 1970, pp. 1462–1469.

11 Brundrett, E., Nicoll, W. B., Strong, A. B., "Heat and Mass Transfer in an Incompressible Turbulent Boundary Layer," JOURNAL OF HEAT TRANSFER, TRANS. ASME, Series C, Vol. 94, 1972, pp. 23–28.

12 Stevenson, T. N., "A Law of the Wall for Turbulent Boundary Layers With Suction or Injection," College of Aeronautics (Cranfield) Rep. Aero 166, 1963.

13 Squire, L. C., "A Law of the Wall for Compressible Turbulent Boundary Layers With Air Injection," *Journal of Fluid Mechanics,* Vol. 37, 1969, pp. 449–456.

14 Simpson, R. L., "The Turbulent Boundary Layer on a Porous Plate: An Experimental Study of the Fluid Dynamics With Injection and Suction," PhD thesis, Stanford University, 1968.

15 Van Driest, E. R., "On Turbulent Flow Near a Wall," *J. Aero. Sci.,* Vol. 23, 1956, pp. 1007–1011.

16 Jeromin, L. O. F., "The Status of Research in Turbulent Boundary Layers With Fluid Injection," *Progress in Aeronautical Sciences,* Vol. 10, Pergamon Press, 1970, pp. 55–189.

17 Coles, D., "A Survey of Data for Turbulent Boundary Layers With Mass Transfer," AGARD-CP-93, Turbulent Shear Flows, 1972.

18 Pletcher, R. H., "On a Finite Difference Solution for the Constant-Property Turbulent Boundary Layer," *AIAA Journal,* Vol. 7, 1969, pp. 305–311.

19 Julien, H. L., "The Turbulent Boundary Layer on a Porous Plate: Experimental Study of the Effects of a Favorable Pressure Gradient," PhD thesis, Stanford University, 1969.

20 Moffat, R. J., Kays, W. N., "The Turbulent Boundary Layer on a Porous Plate: Experimental Heat Transfer With Uniform Blowing and Suction," *International Journal of Heat and Mass Transfer,* Vol. 11, 1968, pp. 1547–1566.

G. E. Geiger
Professor. Mem. ASME

S. J. Collucio[1]
N. S. F. Trainee.

Department of Mechanical Engineering,
University of Pittsburgh,
Pittsburgh, Pa.

The Heat Transfer and Drag Behavior of a Heated Circular Cylinder With Integral Heat-Conducting Downstream Splitter Plate in Crossflow

The heat transfer and drag behavior of a heated circular cylinder with integral heat conducting downstream splitter plate in transverse airflow has been experimentally investigated. The wind tunnel model was a thick-walled aluminum cylinder internally heated with electric resistance heaters and having a splitter plate whose length was varied for each test. Test results indicate the addition of the plate improved heat transfer characteristics with increased plate length, the most dramatic increase in Nusselt number being at the transition from a plate length of ⅓ the cylinder diameter to ⅔ the diameter at the higher speeds. Drag reduction was, in general, also evident with increased plate length.

Introduction

An understanding of the heat transfer and drag behavior of a circular cylinder in transverse airflow is necessary for the design of tube-type heat exchangers. Primarily, an increase in the heat transfer coefficient without a proportional unfavorable increase in drag is desirable.

Fluid dynamic and heat transfer theory have been adequately established for the frontal region of the cylinder before separation where the boundary layer is predominantly laminar; but in the rear separated region of flow, solutions to the momentum and energy equations become complex. For this reason much emphasis is placed on empirical observations in lieu of analytical solutions.

The most commonly used correlation of data expressing the overall heat transfer coefficient from a single cylinder in crossflow in the range of Re = 40,000 to Re = 400,000 is (from reference [1][2]):

$$\mathrm{Nu} = 0.0239(\mathrm{Re})^{0.805} \tag{1}$$

References [2-5], have shown that at lower Reynolds numbers a minimum point in the heat transfer coefficient occurs at approximately the point of separation with an increase in the heat transfer coefficient on the rear side, due to turbulent eddy motion. At higher Reynolds numbers, a minimum occurs at the transition from laminar to turbulent flow and again where the turbulent boundary layer separates. In each case, the minimum is followed by a rapid increase in heat transfer.

With an interest in the wake of blunt bodies, Roshko [6] studied the turbulent structure and velocity distribution in this region and showed that changes in the wake flow field dramatically changed the total drag coefficient. These changes included the placement of a splitter plate in the wake which affected the ability of the forming eddies to "see" each other, thereby preventing regular oscillations in the wake. The most effective plate length was five cylinder diameters, while a shorter length altered the magnitude of drag reduction, as well as the amplitude and frequency of wake oscillations. Also, at the point where the splitter plate touched the cylinder, a large increase in pressure coefficient was noted.

Seban and Levy [7] studied the effect of a very long splitter plate on the heat transfer from a cylinder in crossflow. This investigation was also conducted with the plate separated from the cylinder by a small gap. It was found that the heat transfer was reduced significantly on the rear portion of the cylinder with the forward portion relatively unaffected. This was attributed to the fact that the splitter plate altered the downstream flow to a sepa-

[1] Presently, General Electric Company, Schenectady, N.Y.

Contributed by the Heat Transfer Division for publication in the JOURNAL OF HEAT TRANSFER. Manuscript received by the Heat Transfer Division, November 10, 1972. Paper No. 74-HT-H.

[2] Numbers in brackets designate References at end of paper.

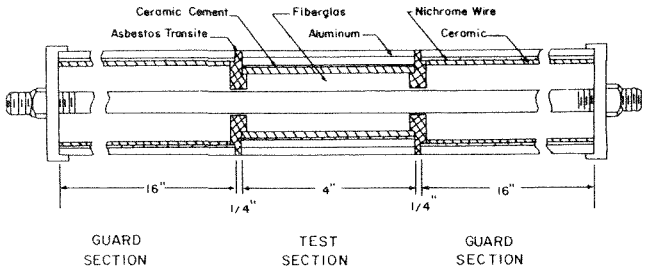

Fig. 1

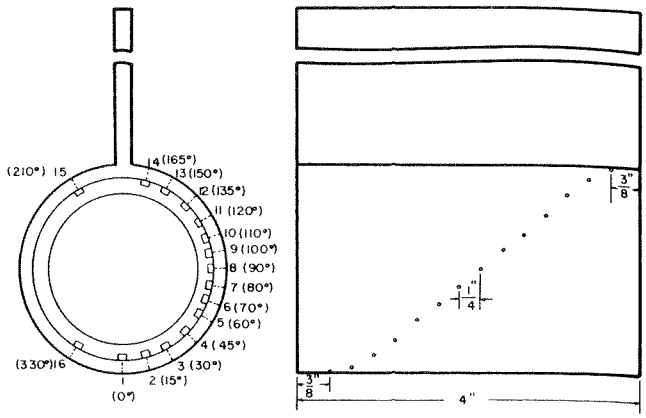

Fig. 2

rated and reattached boundary layer enclosing a region of reverse flow between it and the surfaces of the plate and the cylinder.

The object of the present work is to use the splitter plate as a heat transfer surface or fin by integrally attaching the splitter plate to the cylinder. In this way there will be a reduction in drag, and the heat transfer will increase due to the fin effect. The length of the splitter plate is varied to determine whether an optimal condition exists.

Experimental Apparatus

This investigation was conducted in the University of Pittsburgh open circuit subsonic wind tunnel and utilized the associated pyramidal strain gauge balance for drag measurement. The model spanned the 28 in. × 20 in. working section of the tunnel and was rigidly attached to the balance. Cloth seals prevented air leakage into the tunnel and insured unrestricted movement of the model at the tunnel wall-model interfaces.

A cross section of the model is shown in Fig. 1. The model was machined from aluminum and assembled in three sections, the test section and two guard sections, each with a $\frac{3}{16}$-in-thick splitter plate welded to its rear center-line position. The test section consisted of an outer cylinder and inner grooved cylinder. The outer cylinder, $2\frac{3}{8}$ in. OD, was drilled at 16 different angular locations for the thermocouple junctions and the inner cylinder was correspondingly grooved to accommodate thermocouple leads. Thick-walled aluminum was used for the test section in order that large circumferential temperature gradients were minimized. As a precaution, a greater population of thermocouples was located in the 60-deg to 120-deg region where the greatest likelihood of gradients would occur, Fig. 2.

A thermocouple was installed in each guard section at a position corresponding to one test section thermocouple for the purpose of matching guard section temperature with test section temperature to minimize the axial conduction losses from the test section.

Each section was individually fitted with a hand-made electric resistance heater constructed from ceramic cores coiled with AWG 26 Nichrome wire and covered with electric resistor cement.

The guard sections were insulated from the test section with asbestos transite spacers while balsa wood fixed with aluminum epoxy provided the insulation for the guard section-test section splitter plate interfaces. All thermocouple and heater leads were led through the heater cores to the outside of the tunnel. In the final assembly the centers of the heaters were filled with fiberglass as further protection against radial heat leakage.

All three heaters were individually powered by a variable voltage supply connected to a-c line voltage. The test heater circuit included an a-c voltmeter and ammeter for the determination of the total power input to the test section.

All thermocouples were taken from the same spool of AWG 30 iron constantan glass on glass insulated wire and calibrated against an NBS standard thermometer. The thermocouple millivolt output was measured by two precision potentiometers, one for free steam stagnation temperature readings and the other for the surface temperature-free stream stagnation temperature difference.

Total drag readings were determined directly from the digital readout of the pyramidal strain gauge balance. Free stream airspeed was measured by a Pitotstatic tube connected to a micromanometer.

Experimental Results

The air property values used in the determination of the Reynolds numbers, Nusselt numbers, and drag coefficients were evaluated at the film temperature, which is the arithmetic average of the wall and free stream stagnation temperatures. The average Nusselt numbers were based on the cylinder area alone except where indicated.

For this investigation, two basic parameters were studied for their influence on the heat transfer from the cylinder-splitter plate geometry in crossflow. These were the splitter plate length, and the Reynolds number based on cylinder diameter. The experiment was conducted such that at each plate length, local surface temperature data was acquired at several specified speeds and three particular power inputs. Fig. 3 is typical of the local temperature differences obtained at a given Reynolds number. It is seen that the thick-walled aluminum model successfully smoothed the circumferential gradients usually encountered with insulating or thin-walled models. The decrease in the temperature difference for the longer plate lengths is clearly the result of the heat transfer through the splitter plate. In addition to reducing rear temperature readings, the heat transfer through the plate reduced the forward temperatures as indicated by a shift in the

Nomenclature

C_D = drag coefficient, dimensionless
d = cylinder diameter, in.
F = total drag force, lb_f
g_c = gravitational constant, 32.2 lb_m-ft/lb_f-sec^2
L = plate length, in.
Nu = Nusselt number based on cylinder diameter, dimensionless
Q'' = heat rate per unit area (based on cylinder surface area), Btu/hr-ft^2
Re = Reynolds number based on cylinder diameter, dimensionless
S = frontal area exposed to flow, ft^2
V = velocity, ft/sec
X = plate length, L/d, dimensionless
ν = kinematic viscosity, ft^2/hr
ρ = density, lb_m/ft^3
ΔT = temperature difference between cylinder surface and free stream stagnation temperature, deg F

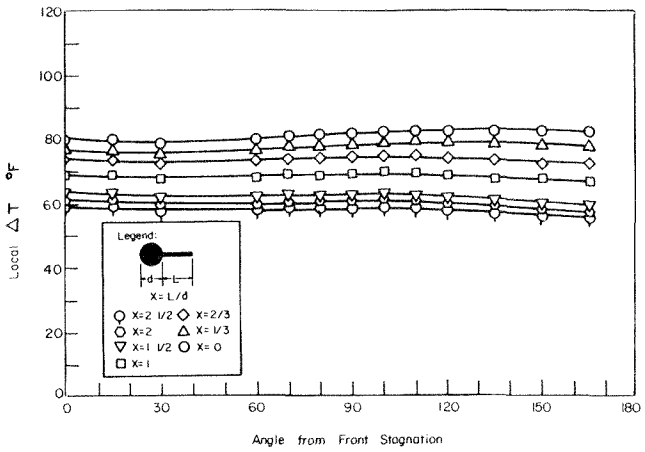

Fig. 3

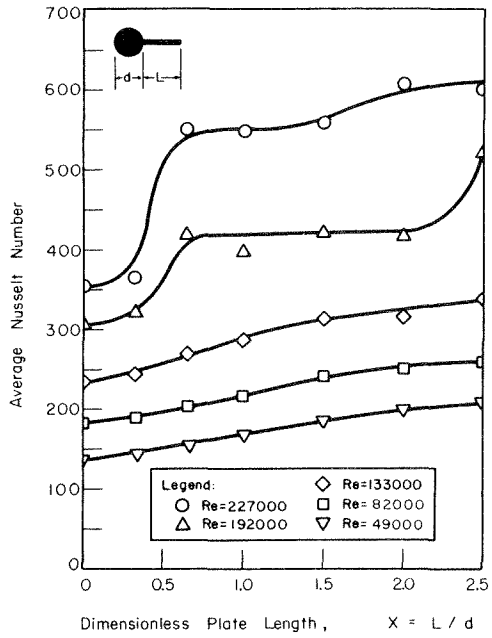

Fig. 4

magnitude of the curves for different plate lengths.

Fig. 4 shows that the average Nusselt number, based on the cylinder surface area only, rises moderately with increased plate length at the lower Reynolds numbers; at the two highest Reynolds numbers, there is a "critical" plate length as indicated by a large increase in heat transfer coefficients. The critical plate length appears to be ⅔ cylinder diameters. It is apparent from these data that the increased heat transfer coefficient due to an increased surface area surpassed the influence of reduced rear turbulence or other resultant flow alterations, as indicated by the generally positive slope. In Fig. 5 the "average Nusselt number based on the cylinder and plate surface area" is defined as the Nusselt number multiplied by the ratio of the surface area of the cylinder to the total surface area of the cylinder and plate. The negative slopes indicate that the total surface area increase is greater than the increase in the heat transfer rate due to the increased area.

Fig. 6 has the average Nusselt number, based on the cylinder surface area only, as a function of the Reynolds number of various splitter plate lengths to the diameter ratios, L/d. For L/d of zero and ⅓, the plots are essentially straight lines on the log-log plot, with the L/d of ⅓ indicating a slightly better heat transfer capability, due to the increased area. The other L/d ratios starting with L/d of ⅔ show the same trend up to a Reynolds number of approximately 130,000, after which the heat transfer increases quite rapidly, possibly due to a change in the flow pattern behind the cylinder.

The total heat transferred will be affected by the material used for the splitter plate, since the fin efficiency is a function of the thermal conductivity of the material. An estimate of the average heat transfer coefficient is also needed to compute the fin efficiency. Unfortunately, nothing has been published on heat transfer coefficients on plates behind cylinders. An approximation can be made from Seban's [8] work on heat transfer coefficients on surfaces downstream of a step. His work shows that a value of 20 Btu hr ft² deg F would be a reasonable estimation for the average heat transfer coefficient. It will also be assumed that for each different material, the root temperature would be approximately the same as shown in Fig. 3. The following calculations are for a splitter plate where $x = L/d = ⅔$ and for Re = 82,000.

Material	Fin. eff.	Percent of total heat
aluminum	0.58	11.8
copper	0.71	14.3
steel (1.5 C)	0.32	6.4
stainless steel (18 Cr, 8 Ni)	0.18	3.7

It is obvious that a splitter plate made of a material of high thermal conductivity will improve the heat transfer.

Drag results are indicated in Fig. 7. The results indicate that the addition of a splitter plate reduces total drag and, as plate length is increased, the total drag is decreased. The clean cylinder results were found to compare very well with published work.

It was expected that the addition of a splitter plate would alter the amplitude and frequency of vibration of the cylinder by affecting the shedding of vortexes in the wake region. Although not directly measured in this investigation, the amplitude of vibration was observed to increase with decreasing plate length, as observed by the digital drag readout. In addition to affecting the vortex shedding, the splitter plate invariably stiffens the tube structurally thereby minimizing the problem of flow induced vibration.

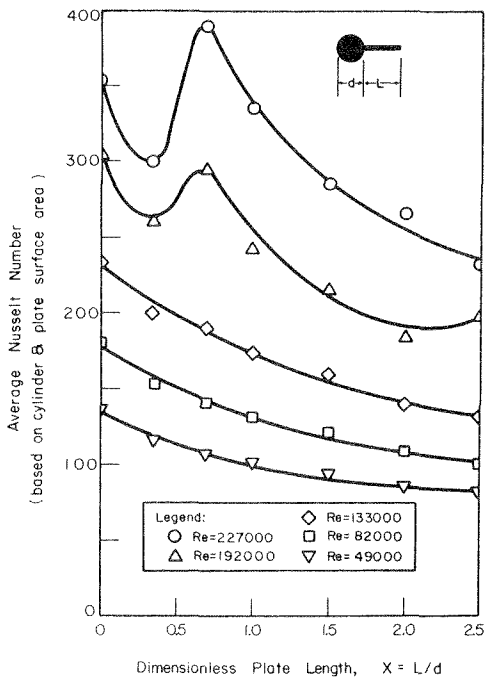

Fig. 5

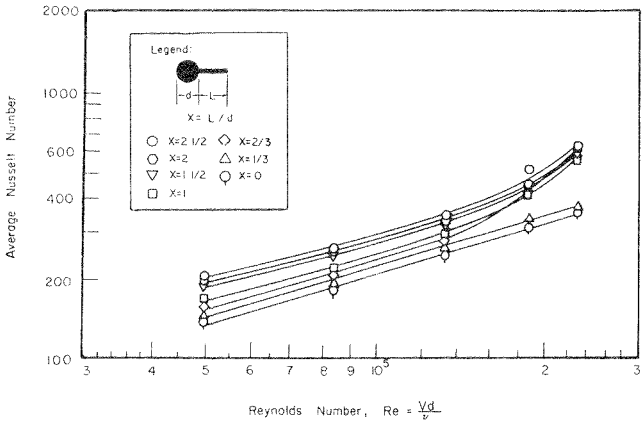

Fig. 6

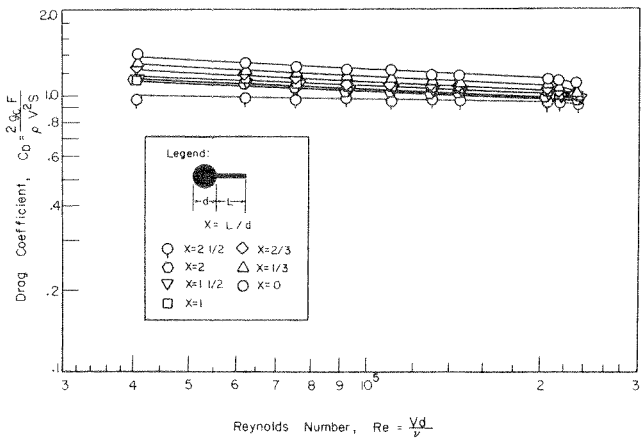

Fig. 7

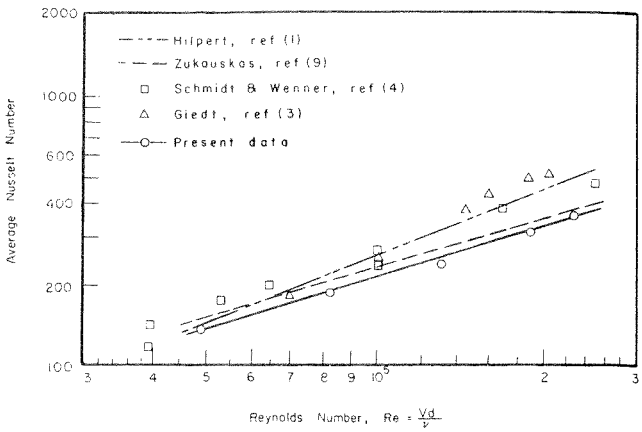

Fig. 8

In Fig. 8 the heat transfer data from a cylinder without splitter plate are compared to published data. For the corresponding Reynolds number range of 49,000 to 227,000, Hilpert's [1] data were taken from test cylinders of 44, 90, and 150 mm dia, and 500, 500, and 142 mm length, respectively. His cylinders were placed lengthwise horizontally in the free jet. The flow pattern is quite different than our case, which had the 2⅞-in-dia cylinder horizontally wall to wall in the 28 in. wide by 20 in. high working section of the wind tunnel. The turbulence level of the tunnel was well below 1 percent, and our data have been corrected for blockage effects.

Schmidt and Wenner's [4] data were taken using a flow nozzle which issued a narrow jet of air, similar to Hilpert's setup. Analysis of their data indicates that a cylinder diameter effect might be present in their data.

Giedt's [3] data were taken from a test section consisting of a nichrome ribbon wound around a lucite cylinder. Although the ribbon was only 0.002 in. in thickness, it is possible that the ribbon was not completely in contact with the lucite cylinder and this produced an irregular surface causing higher heat transfer. Also the fact that the heated surface was not isothermal, and the fact that an average Nusselt number was taken from the locally measured Nusselt numbers could cause quite a deviation from average Nusselt numbers taken from essentially isothermal cylinders.

The correlation of A. Zukauskas [9] shows that our data are only about 6 percent lower. It is also seen that the date of Stasiulevicius and Samoska (which is shown in Zukauskas' correlation) lies at least 10 percent lower than this correlation, and would thus tend to verify our experimental data.

It appears that the available data for circular cylinders normal to an airstream for Reynolds numbers greater than 49,000 are questionable, and that an effort should be made to resolve the problem.

Summary

The investigation was performed under the following conditions:

Plate length	0–2½ d
Free stream stagnation temperature, deg F	78–87
Barometeric pressure, in. of Hg	28.6–29.9
Free stream velocity, ft/sec	46–194
Reynolds number	49,000-227,000
Temperature difference, deg F (wall temp-free stream stagnation temp.)	11–160
Average Nusselt number	135–610

Conclusions

In general, these conclusions may be made:

1 The addition of a downstream integral heat-conducting splitter plate to a heated cylinder in transverse airflow will, in general, improve the overall heat transfer coefficient, based on the area of the cylindrical surface.

2 The most dramatic increase in Nusselt number occurs with a splitter plate length ⅔ the cylinder diameter.

3 The addition of a downstream integral splitter plate to a cylinder, in general, decreases total drag.

4 Even the shortest plate length (⅓ d) reduces drag appreciably with improved effects with increased length.

5 The increase of heat transferred due to increased surface area for flow past the cylinder-splitter plate geometry surpasses the decrease in heat transferred due to reduced rear turbulence or other resultant flow alterations.

6 A thick-walled cylinder of high thermal conductivity will effectively eliminate large circumferential temperature gradients on the outer surface of the cylinder for the transverse flow of air across the cylinder.

References

1 Hilpert, R., "Warmeabgabe von geheizten Drahten und Rohren im Luftstrom," *Forschung*, Vol. 4, Bd/Heft, 5 Sept./Oct. 1933.

2 Kroujilin, G., "The Heat Transfer of a Circular Cylinder in a Transverse Airflow in the Range of Re = 6000–425000," *Technical Physics USSR*, Vol. 5, 1938, pp. 289–297.

3 Giedt, W. H., "Investigation of Variation of Point Unit-Heat Transfer Coefficient Around a Cylinder Normal to an Airstream," TRANS. ASME, Vol. 71, 1949, pp. 275–381.

4 Schmidt, E., and Wenner, K., "Heat Transfer Over the Circumfer-

ence of a Heated Cylinder in Transverse Flow" NACA Tech. Memo. No. 1050, Washington: U. S. Government Printing Office, 1943.

5 Johnson, T. R., and Joubert, P. N., "The Influence of Vortex Generators on the Drag and Heat Transfer From a Circular Cylinder Normal to an Airstream," JOURNAL OF HEAT TRANSFER, TRANS. ASME, Series C, Vol. 91, 1969, pp. 91–99.

6 Roshko, A., "On the Drag and Shedding Frequency of Bluff Bodies," NACA Technical Note No. 3169, Washington: U. S. Government Printing Office, 1954.

7 Seban, R. A., and Levy, A. M., "The Effect of a Downstream Splitter Plate on the Heat Transfer From a Circular Cylinder Normal to an Airstream" WADC Technical Report No. 57-479, Washington: U. S. Government Printing Office, 1957.

8 Seban, R. A., "Heat Transfer to the Turbulent Separated Flow of Air Downstream of a Step in the Surface of a Plate," JOURNAL OF HEAT TRANSFER, TRANS. ASME, Series C, Vol. 84, pp. 259–264.

9 Zukauskas, A., *Advances in Heat Transfer,* J. P. Harnett, and T. F. Irvine, Jr., eds., Academic Press, New York, 1972, pp. 93–160.

R. I. Pedroso

Professional Staff Member,
Philips Laboratories,
Briarcliff Manor, N. Y.
Assoc. Mem. ASME

Thermal Analysis of Laminar Fluid Film Under Side Cyclic Motion

An analytical study is presented for a constant-thickness incompressible laminar one-dimensional fluid film undergoing cyclic side motion. The fluid film is bounded by a stationary and a cyclically-moving wall. The heat flux is calculated at both the stationary and moving boundaries. Formulas are presented for the frictional resistance and power dissipation at the moving wall. Application is made to the varying-thickness fluid film between an eccentric round shaft with reciprocating axial motion and its stationary cylindrical housing. In the analysis, quantities assumed constant are the pressure along the edges of the fluid film, its properties, and the temperature along each of the two walls bounding the fluid. The lateral dimensions of the fluid film are assumed large compared to its thickness such that end effects can be neglected.

Introduction

The basic problem considered is that of one-dimensional constant-property laminar flow of an incompressible fluid between two parallel walls. As shown in Fig. 1*(a)*, the constant-thickness fluid film is bounded by a stationary and a cyclically-moving wall. The width and length are assumed large compared to the fluid film thickness, Y^*, such that end effects can be neglected. The ratio of length to film thickness for negligible end effects would be dependent on the fluid temperature entering the gap and on the wall temperatures bounding the fluid film. The pressure is assumed given as constant and equal along all edges of the fluid film. The stationary wall is assumed constant at temperature T_s, and the moving wall constant at temperature T_m.

Application is made of the basic solution described in the foregoing to the varying-thickness fluid film between an eccentrically-positioned round shaft with axial reciprocating motion and its parallel stationary cylindrical housing. The diametral clearance between shaft and cylinder is limited to be small compared to the shaft diameter such that a negligible film curvature results. Fig. 1*(b)* shows an end view of the stationary cylinder enclosing the cyclically-moving shaft. Calculations are presented for the heat transfer at both the stationary and moving boundaries, and for the frictional force and power dissipation at the moving boundary.

With the assumptions made, the problem described in the foregoing finds application in a variety of heat exchangers. For example, cooling of the piston in the drive of a gas compressor can be achieved through a cylindrical annulus of oil situated close to the compression seal. A flowing coolant could surround the oil annulus which can simply be splattered in place such that it fills at all times the cylindrical gap. Another application is found in heat transfer through the air film between moving and stationary parts of a linear reciprocating electric motor. In the latter case the fluid is compressible. However, if the gap is properly designed, a low temperature drop occurs across the fluid film which renders the compressibility of the fluid film unimportant. Other applications are encountered in friction and thermal analysis of fluid film bearings undergoing reciprocating linear motion.

The solution sought is a regular-parameter series expansion. The perturbation parameter being a form of Reynolds number, represents qualitatively the ratio of fluid inertia to viscous forces. The zeroth-order terms in the solution neglect completely motion and thermal inertia. Four subsequent correction terms are presented for the time-average heat transfer at the walls and for the friction power dissipation at the moving wall. Three correction terms are presented for the instantaneous temperature distribution and heat transfer at the walls.

Analysis

Parallel Surfaces. Geometrically the basic problem under consideration has been shown in Fig. 1*(a)*. The wall temperatures are given to be uniform, the pressure is equal at all edges of the constant-thickness fluid film, and end effects are neglected. Hence, the velocity, U, and the temperature distribution, T, are only functions of the time, t, and of the normal distance, Y, from the stationary wall. The velocity of the reciprocating plate will be assumed sinusoidal in time with amplitude, U^*. With the assumptions discussed in the foregoing, the governing equations of motion and energy balance for incompressible fluids are satisfied by a constant pressure and require

Contributed by the Heat Transfer Division for publication in the JOURNAL OF HEAT TRANSFER. Manuscript received by the Heat Transfer Division, May 29, 1973. Paper No. 74-HT-G.

$$\rho \frac{\partial U}{\partial t} = \mu \frac{\partial^2 U}{\partial Y^2}, \quad U(Y=0,t)=0, \quad U(Y=Y^*,t)=U^* \sin \omega t \tag{1}$$

$$\rho C \frac{\partial T}{\partial t} = k \frac{\partial^2 T}{\partial Y^2} + \mu \left(\frac{\partial U}{\partial Y}\right)^2, \quad T(Y=0,t)=T_s, \quad T(Y=Y^*,t)=T_m$$

In the foregoing equations, the fluid properties introduced are: density, ρ, viscosity, μ, specific heat, C, and thermal conductivity, k. The frequency of motion of the moving wall has been denoted as ω. The exact solution to the velocity distribution in equation (1) and the frictional force at the walls is presented in Landau and Lifshitz [1].[1] An alternative solution will be derived here applicable only for small values of Reynolds number. Emphasis will be placed on the solution to the energy equation for small Reynolds number. In the Appendix, the time-average energy equation is considered and its approximate solution is directly derived. For the reader interested in thermal solutions for large Reynolds number in laminar flows it is recommended that the exact velocity distribution from [1] be substituted in equation (A1) in order to calculate the exact time-average temperature distribution.

Introduce the following dimensionless quantities: position, y, time, τ, velocity, u, temperature, θ, characteristic Reynolds number, δ, Prandtl number, λ_1, and Brinkman number, λ_2. The boundary-value problem in dimensionless form is then obtained from equations (1) as

$$\frac{\partial^2 u}{\partial y^2} = \delta \frac{\partial u}{\partial \tau}, \quad u(y=0,\tau)=0, \quad u(y=1,\tau)=\sin\tau$$

$$\frac{\partial^2 \theta}{\partial y^2} = \lambda_1 \delta \frac{\partial \theta}{\partial \tau} - \lambda_2 \left(\frac{\partial u}{\partial y}\right)^2, \quad \theta(y=0,\tau)=0, \quad \theta(y=1,\tau)=1 \tag{2}$$

[1] Numbers in brackets designated References at end of paper.

Assume perturbation series solutions in powers of δ:

$$u(y,\tau;\delta) = \sum_{i=0} \delta^i u_i(y,\tau)$$

$$\theta(y,\tau;\lambda_1,\lambda_2,\delta) = \sum_{i=0} \delta^i \theta_i(y,\tau;\lambda_1,\lambda_2) \tag{3}$$

Substitution of equations (3) into (2) yields, after coefficients of equal powers of δ are equated:

$$\frac{\partial^2 u_i}{\partial y^2} = \begin{cases} 0 \text{ for } i=0 \\ \dfrac{\partial u_{i-1}}{\partial \tau} \text{ for } i \geq 1 \end{cases}$$

$$u_i(y=0,\tau)=0, \quad u_i(y=1,\tau) = \begin{cases} \sin\tau \text{ for } i=0 \\ 0 \text{ for } i \geq 1 \end{cases} \tag{4}$$

$$\frac{\partial^2 \theta_i}{\partial y^2} = \begin{cases} -\lambda_2 \left(\dfrac{\partial u_0}{\partial y}\right)^2 \text{ for } i=0 \\ \lambda_1 \dfrac{\partial \theta_{i-1}}{\partial \tau} - 2\lambda_2 \sum\limits_{j=1}^{\frac{i+[1-(-1)^i]/2}{2}} \dfrac{\partial u_{j-1}}{\partial y} \dfrac{\partial u_{i-j+1}}{\partial y} \\ -\lambda_2 \dfrac{1+(-1)^i}{2} \left(\dfrac{\partial u_{i/2}}{\partial y}\right)^2 \text{ for } i \geq 1 \end{cases}$$

$$\theta_i(y=0,\tau)=0, \quad \theta_i(y=1,\tau) = \begin{cases} 1 \text{ for } i=0 \\ 0 \text{ for } i \geq 1 \end{cases}$$

The first five terms of the velocity distribution satisfying equations (4) are

$$u_0 = y \sin\tau$$

$$u_1 = -\frac{y-y^3}{6} \cos\tau$$

$$u_2 = -\frac{1}{36}\left(\frac{7}{10}y - y^3 + \frac{3}{10}y^5\right) \sin\tau$$

$$u_3 = \frac{1}{720}\left(\frac{31}{21}y - \frac{7}{3}y^3 + y^5 - \frac{y^7}{7}\right) \cos\tau$$

Nomenclature

μ = fluid viscosity
ρ = fluid density
ω = frequency of motion
C = fluid specific heat
E = power dissipation per unit length for eccentric fluid annulus between shaft and cylindrical housing
F = friction force per unit length at moving wall for eccentric fluid annulus between shaft and cylindrical housing
H_m, H_s = respective radial heat transfer per unit length through moving shaft and stationary cylindrical housing
k = fluid thermal conductivity
P = power dissipation per unit area
Q_m, Q_s = respective heat fluxes in $-Y$ direction through moving and stationary walls
R = shaft radius
R_c = radial clearance between shaft and cylindrical housing
S = friction stress at moving wall
t = time
T = fluid temperature
T_m, T_s = respective temperatures of moving and stationary walls
U = fluid velocity
U^* = velocity amplitude of moving wall
Y = normal distance from stationary wall
Y^* = normal distance between stationary and moving walls
$Y_{\min}{}^*$ = minimum film thickness between eccentric shaft and cylindrical housing

Dimensionless quantities

$\delta = \rho\omega Y^{*2}/\mu$, $\delta_c = \rho\omega R_c{}^2/\mu$, characteristic Reynolds numbers
$\epsilon = 1 - Y^*_{\min}/R_c$
$\theta = (T - T_s)/(T_m - T_s)$
θ_i = coefficient of δ^i in series solution for θ
$\lambda_1 = \mu C/k$, Prandtl number
$\lambda_2 = \mu U^{*2}/(k(T_m - T_s))$, Brinkman number
$\sigma = Y^*S/(\mu U^*)$, $\sigma_c = R_cS/(\mu U^*)$
$\tau = \omega t$
ϕ = angle measured from position of minimum film thickness for eccentric fluid annulus between shaft and cylindrical housing
$e = R_cE/(2\mu RU^{*2})$
$f = R_cF/(2\mu RU^*)$
$h_m = R_cH_m/(2Rk(T_m - T_s))$
$h_s = R_cH_s/(2Rk(T_m - T_s))$
$p = Y^*P/(\mu U^{*2})$
$q_m = Y^*Q_m/(k(T_m - T_s))$, $q_{mc} = R_cQ_m/(k(T_m - T_s))$
$q_s = Y^*Q_s/(k(T_m - T_s))$, $q_{sc} = R_cQ_s/(k(T_m - T_s))$
$u = U/U^*$
u_i = coefficient of δ^i in series solution for u
$y = Y/Y^*$, $y_c = Y/R_c$

Time-average quantities

$$\underline{\theta} = \frac{1}{2\pi}\int_0^{2\pi} \theta d\tau, \quad \underline{e} = \frac{1}{2\pi}\int_0^{2\pi} e d\tau, \quad \underline{h}_m = \frac{1}{2\pi}\int_0^{2\pi} h_m d\tau, \quad \underline{h}_s = \frac{1}{2\pi}\int_0^{2\pi} h_s d\tau$$

$$\underline{p} = \frac{1}{2\pi}\int_0^{2\pi} p d\tau, \quad \underline{q}_m = \frac{1}{2\pi}\int_0^{2\pi} q_m d\tau, \quad \underline{q}_s = \frac{1}{2\pi}\int_0^{2\pi} q_s d\tau$$

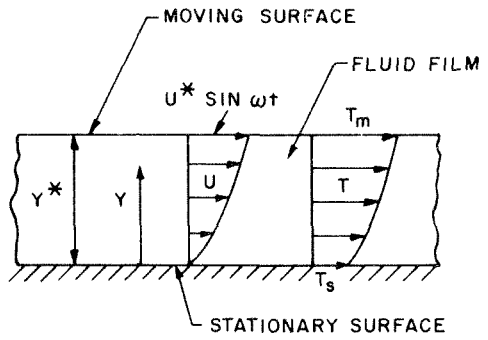

1a

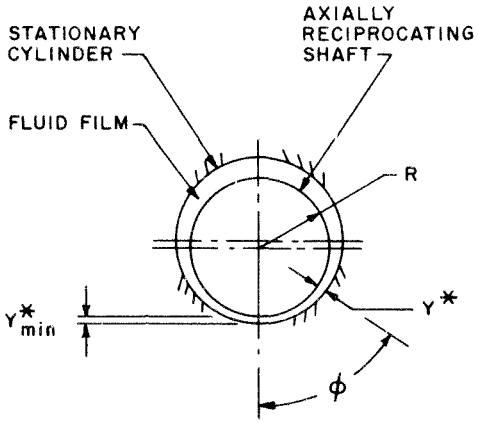

1b

Fig. 1(a) Constant-thickness fluid film bounded by stationary and cyclically moving walls; (b) varying-thickness fluid film bounded by stationary cylindrical housing and axially reciprocating shaft

$$u_4 = \frac{1}{4320}\left(\frac{127}{140}y - \frac{31}{21}y^3 + \frac{7}{10}y^5 - \frac{1}{7}y^7 + \frac{1}{84}y^9\right)\sin\tau \quad (5)$$

From equations (4) and (5), the first four terms of the temperature distribution are given by

$$\theta_0 = y\left[1 + \frac{\lambda_2}{2}(1-y)\sin^2\tau\right]$$

$$\theta_1 = -\frac{\lambda_2 \sin\tau\cos\tau}{6}\, y\left(\frac{1+2\lambda_1}{4} - \frac{y}{2} - \lambda_1 y^2 + \frac{1+2\lambda_1}{4}y^3\right)$$

$$\theta_2 = \frac{\lambda_2}{24}\, y\Big\{\cos^2\tau\Big[\frac{1}{5}\Big(1 + \frac{\lambda_1}{6} + \lambda_1^2\Big) - \frac{y}{3} - \lambda_1\frac{1+2\lambda_1}{6}y^2 + \frac{1}{3}\Big(1 + \frac{\lambda_1}{2}\Big)y^3 + \frac{\lambda_1^2}{5}y^4 - \Big(1 + \frac{\lambda_1}{6} + \frac{\lambda_1^2}{3}\Big)\frac{y^5}{5}\Big]$$

$$- \sin^2\tau\Big[\frac{1}{5}\Big(1 + \frac{\lambda_1}{6} + \lambda_1^2\Big) - \frac{7}{15}y - \lambda_1\frac{1+2\lambda_1}{6}y^2 + \frac{1}{3}\Big(1 + \frac{\lambda_1}{2}\Big)y^3 + \frac{\lambda_1^2}{5}y^4 - \Big(1 + \frac{\lambda_1}{2} + \lambda_1^2\Big)\frac{y^5}{15}\Big]\Big\} \quad (6)$$

$$\theta_3 = \frac{\lambda_2}{180}\, y\sin\tau\cos\tau\Big[\Big(\frac{10}{21} + \frac{11}{42}\lambda_1 + \frac{11}{168}\lambda_1^2 + \frac{17}{28}\lambda_1^3\Big) - \frac{20}{21}y - \lambda_1\Big(1 + \frac{\lambda_1}{6} + \lambda_1^2\Big)y^2 + (1+\lambda_1)y^3 + \frac{\lambda_1^2}{4}(1+2\lambda_1)y^4 - \frac{1}{3}\Big[2 + \lambda_1\Big(1 + \frac{\lambda_1}{2}\Big)\Big]y^5 - \frac{\lambda_1^3}{7}y^6 + \frac{1}{56}(8 + 4\lambda_1 + \lambda_1^2 + 2\lambda_1^3)y^7\Big]$$

To obtain more terms in the solution to the temperature distribution involves a considerable amount of algebraic work.

The frictional stress and power dissipation per unit area at the moving wall are, respectively, given by $S = \mu\,(\partial U/\partial Y)_{Y=Y^*}$ and $P = SU^* \sin\omega t$. After introducing dimensionless quantities, these become $\sigma = (\partial u/\partial y)_{y=1}$ and $p = \sigma\sin\tau$, respectively. In view of equations (3) and (5), one obtains

$$\sigma = \left(1 + \frac{\delta^2}{45} - \frac{\delta^4}{4725} + \ldots\right)\sin\tau + \frac{\delta}{3}\left(1 - \frac{2}{315}\delta^2 + \ldots\right)\cos\tau \quad (7)$$

At the stationary and moving walls, the heat fluxes (in the $-Y$ direction) are, respectively, given by $Q_s = k(\partial T/\partial Y)_{Y=0}$ and $Q_m = k(\partial T/\partial Y)_{Y=Y^*}$. After introducing dimensionless quantities, these become $q_s = (\partial\theta/\partial y)_{y=0}$ and $q_m = (\partial\theta/\partial y)_{y=1}$, respectively. In view of equations (3) and (6), one obtains

$$q_s = 1 + \frac{\lambda_2}{2}\sin^2\tau - \delta\lambda_2\frac{1+2\lambda_1}{24}\sin\tau\cos\tau + \delta^2\frac{\lambda_2}{120}\Big(1 + \frac{\lambda_1^2}{6}\Big)(\cos^2\tau - \sin^2\tau) + \delta^3\frac{\lambda_2}{180}\Big(\frac{10}{21} + \frac{11}{42}\lambda_1 + \frac{11}{168}\lambda_1^2 + \frac{17}{28}\lambda_1^3\Big)\sin\tau\cos\tau + \ldots$$

$$q_m = 1 - \frac{\lambda_2}{2}\sin^2\tau - \delta\lambda_2\frac{1-2\lambda_1}{24}\sin\tau\cos\tau - \delta^2\frac{\lambda_2}{120}\Big[\frac{5+3\lambda_1^2}{3}\cos^2\tau + (1-\lambda_1^2)\sin^2\tau\Big] - \delta^3\frac{\lambda_2}{630}\Big(1 + \frac{7}{12}\lambda_1 + \frac{7}{48}\lambda_1^2 + \frac{17}{8}\lambda_1^3\Big)\sin\tau\cos\tau + \ldots \quad (8)$$

The time-average of p, q_s, and q_m are given, respectively, by

$$\underline{p} = \frac{1}{2}\left(1 + \frac{\delta^2}{45} - \frac{\delta^4}{4725}\right) + 0(\delta^6)$$

$$\underline{q}_s = 1 + \frac{\lambda_2}{4} + 0(\delta^6) \quad (9)$$

$$\underline{q}_m = 1 - \frac{\lambda_2}{4} - \delta^2\frac{\lambda_2}{90} + \delta^4\frac{\lambda_2}{9450} + 0(\delta^6)$$

where the terms of $0(\delta^4)$ in q_s and q_m were obtained from the Appendix. Note that equations (9) satisfy the relation $\lambda_2 p = q_s - q_m$, which can be shown to be the overall energy balance.

Eccentric Annulus. The solution presented in the foregoing for constant-thickness fluid film can be applied with modification to problems with varying film thickness in the direction normal to fluid flow. Consider the case of an eccentric but parallel round shaft in its cylindrical housing. The shaft moves axially with reciprocating motion. In order to neglect the fluid film curvature, the radial clearance, R_c, between shaft and cylinder bore will be assumed small compared to the shaft radius R (i.e., $R_c/R \ll 1$). Let the minimum fluid film thickness be denoted by $Y^*_{\min}$, then one obtains [2] for $R_c/R \ll 1$:

$$Y^* = R_c(1 - \epsilon\cos\phi), \quad \epsilon = 1 - \frac{Y^*_{\min}}{R_c} \quad (10)$$

where, as shown in Fig. 1(*b*), the angle ϕ is measured from the position of minimum film thickness. The eccentric annulus results will be obtained from the parallel wall equations through substitution of equations (10).

Using R_c as the characteristic length, introduce the following dimensionless quantities: position, y_c, characteristic Reynolds number, δ_c, frictional stress at the moving wall, σ_c, heat fluxes at the stationary wall, q_{sc}, and at the moving wall, q_{mc}.

Calculated on a unit length basis, the frictional force at the moving wall, F, the corresponding power dissipation, E, the radial heat transfer through the stationary wall, H_s, and through the

moving wall, H_m are all given by

$$F = 2R\int_0^{\pi} S\, d\phi\,, \quad E = FU^* \sin \omega t \tag{11}$$

$$H_s = 2R\int_0^{\pi} Q_s\, d\phi\,, \quad H_m = 2R\int_0^{\pi} Q_m\, d\phi$$

After dimensionless quantities are introduced, these quantities become, respectively

$$f = \int_0^{\pi} \sigma_c\, d\phi\,, \quad e = f \sin \tau \tag{12}$$

$$h_s = \int_0^{\pi} q_{sc}\, d\phi\,, \quad h_m = \int_0^{\pi} q_{mc}\, d\phi$$

Combine equations (7), (10), and (12) to obtain for the dimensionless frictional force:

$$f = \pi \sin\tau \left[\frac{1}{\sqrt{1-\epsilon^2}} + \frac{1}{45}\left(1 + \frac{3}{2}\epsilon^2\right)\delta_c^{\,2} - \frac{1}{4725}\left(1 + \frac{21}{2}\epsilon^2 + \frac{105}{8}\epsilon^4 + \frac{35}{16}\epsilon^6\right)\delta_c^{\,4} + \ldots\right] + \frac{\pi}{3}\cos\tau\left[\delta_c - \frac{2}{315}\left(1 + 5\epsilon^2 + \frac{15}{8}\epsilon^4\right)\delta_c^{\,3} + \ldots\right] \tag{13}$$

Combine equations (8), (10), and (12) to obtain for the dimensionless heat transfer through the stationary and moving walls:

$$h_s = \frac{\pi}{\sqrt{1-\epsilon^2}}\left(1 + \frac{\lambda_2}{2}\sin^2\tau\right) - \delta_c \pi\lambda_2 \frac{1 + 2\lambda_1}{24}\sin\tau\cos\tau + \delta_c^{\,2}\pi\,\frac{\lambda_2}{120}\left(1 + \frac{\lambda_1}{6} + \lambda_1^{\,2}\right)\left(1 + \frac{3}{2}\epsilon^2\right)(\cos^2\tau - \sin^2\tau) + \delta_c^{\,3}\pi\,\frac{\lambda_2}{360}\left(\frac{20}{21} + \frac{11}{21}\lambda_1 + \frac{11}{84}\lambda_1^{\,2} + \frac{17}{14}\lambda_1^{\,3}\right)\left(1 + 5\epsilon^2 + \frac{15}{8}\epsilon^4\right) \times \sin\tau\cos\tau + \ldots \tag{14}$$

$$h_m = \frac{\pi}{\sqrt{1-\epsilon^2}}\left(1 - \frac{\lambda_2}{2}\sin^2\tau\right) - \delta_c\pi\lambda_2\frac{1 - 2\lambda_1}{24}\sin\tau\cos\tau - \delta_c^{\,2}\pi\,\frac{\lambda_2}{120}\left(1 + \frac{3}{2}\epsilon^2\right)\left[\frac{5 + 3\lambda_1^{\,2}}{3}\cos^2\tau + (1 - \lambda_1^{\,2})\sin^2\tau\right] - \delta_c^{\,3}\pi\,\frac{\lambda_2}{630}\left(1 + \frac{7}{12}\lambda_1 + \frac{7}{48}\lambda_1^{\,2} + \frac{17}{8}\lambda_1^{\,3}\right)\left(1 + 5\epsilon^2 + \frac{15}{8}\epsilon^4\right) \times \sin\tau\cos\tau + \ldots$$

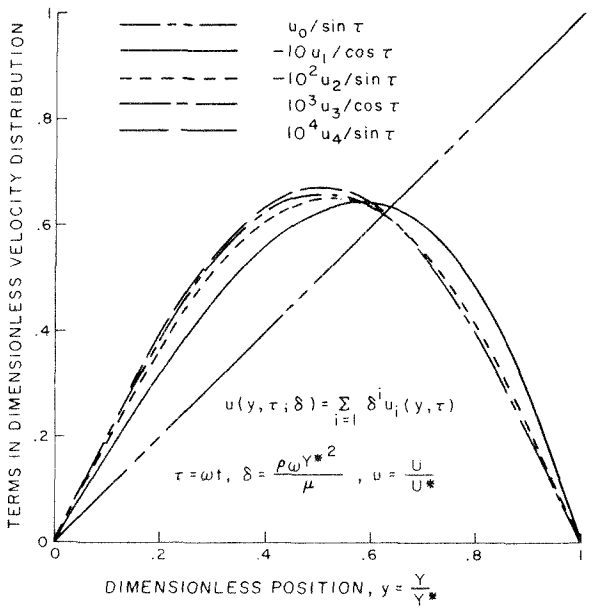

Fig. 2 Terms in series solution for dimensionless velocity distribution for constant thickness fluid film bounded by stationary and cyclically moving walls

The time-average of e, h_s, and h_m are given, respectively, by

$$\underline{e} = \frac{\pi}{2}\left[\frac{1}{\sqrt{1-\epsilon^2}} + \frac{1}{45}\left(1 + \frac{3}{2}\epsilon^2\right)\delta_c^{\,2} - \frac{1}{4725}\left(1 + \frac{21}{2}\epsilon^2 + \frac{105}{8}\epsilon^4 + \frac{35}{16}\epsilon^6\right)\delta_c^{\,4}\right] + 0(\delta_c^{\,6})$$

$$\underline{h}_s = \pi\,\frac{1 + \lambda_2/4}{\sqrt{1-\epsilon^2}} + 0(\delta_c^{\,6})$$

$$\underline{h}_m = \pi\left[\frac{1 - \lambda_2/4}{\sqrt{1-\epsilon^2}} - \frac{\lambda_2}{90}\left(1 + \frac{3}{2}\epsilon^2\right)\delta_c^{\,2} + \frac{\lambda_2}{9450}\left(1 + \frac{21}{2}\epsilon^2 + \frac{105}{8}\epsilon^4 + \frac{35}{16}\epsilon^6\right)\delta_c^{\,4}\right] + 0(\delta_c^{\,6}) \tag{15}$$

where the terms of $0(\delta^4)$ in h_s and h_m were obtained from equations (9). The value of the parameter λ_2 resulting in no net heat transfer from the moving surface can be obtained from the last of equations (15) as

$$\lambda_2 = 4/\left\{1 + \frac{2}{45}\sqrt{1-\epsilon^2}\,\delta_c^{\,2}\left[1 + \frac{3}{2}\epsilon^2 - \frac{\delta_c^{\,2}}{105}\left(1 + \frac{21}{2}\epsilon^2 + \frac{105}{8}\epsilon^4 + \frac{35}{16}\epsilon^6\right)\right]\right\} + 0(\delta_c^{\,6}) \tag{16}$$

If λ_2 exceeds this value, then net heat is transferred from the fluid film into the moving wall, although its temperature exceeds that of the stationary surface. Note that equations (15) satisfy the relation $\lambda_2 \underline{e} = \underline{h}_s - \underline{h}_m$, which can be shown to be the overall energy balance.

Discussion of Solution

Parallel Surfaces. Fig. 2 shows the terms, u_i in the dimensionless velocity distribution, equations (5). The first term, u_0, neglects completely fluid motion inertia and is of order one. Each successive term decreases in order of magnitude by a factor of ten. Rapid convergence will occur for moderate values of the characteristic Reynolds number, δ. For $y > 0.7$ the values of $10^3 u_3/\cos\tau$ and $10^4/\sin\tau$ agree sufficiently close to warrant no graphical distinction.

From equations (6), the coefficients θ_i of powers of the characteristic Reynolds number, δ^i, are found to depend on the Prandtl number, λ_1, and on the Brinkman number, λ_2. Values of λ_2 much less than one result in negligible heat dissipation with almost pure thermal conduction throughout the fluid film thickness. Hence, θ_0 becomes very accurate for $\lambda_2 \ll 1$. For moderate values of λ_1 and δ, the series solution for θ seems rapidly convergent; however, it becomes divergent for $\lambda_1 \gg 1$ and $\delta \gg 1$. It should be noted that gases have Prandtl numbers generally of order one while liquids can have much larger values. For example, water at 27 deg C has $\lambda_1 \cong 5.9$ while a light oil would have $\lambda_1 \cong 570$. Application of the series solution for large Prandtl number is possible only at a reduced value of Reynolds number.

Equations (9) are the time average-solutions for the dimensionless frictional power dissipation, $\underline{p}$, the dimensionless heat flux at the stationary surface, $\underline{q}_s$, and at the moving surface, $\underline{q}_m$. These equations are the most important results of the analysis on parallel surfaces. Note that the Prandtl number does not enter into the time-average thermal solutions. The value of $\underline{q}_s$ is found to be independent of the Reynolds number at least up to and including $0(\delta^4)$, and the solution for $\underline{q}_m$ is only a function of even powers of δ. It should be emphasized that if only time-average thermal results are desired, the method described in the Appendix using the averaged energy equation should be used for simplicity.

Eccentric Annulus. Equations (13) through (15) were obtained through application of the basic solution for constant-thickness fluid film to the circumferential fluid annulus between an axially

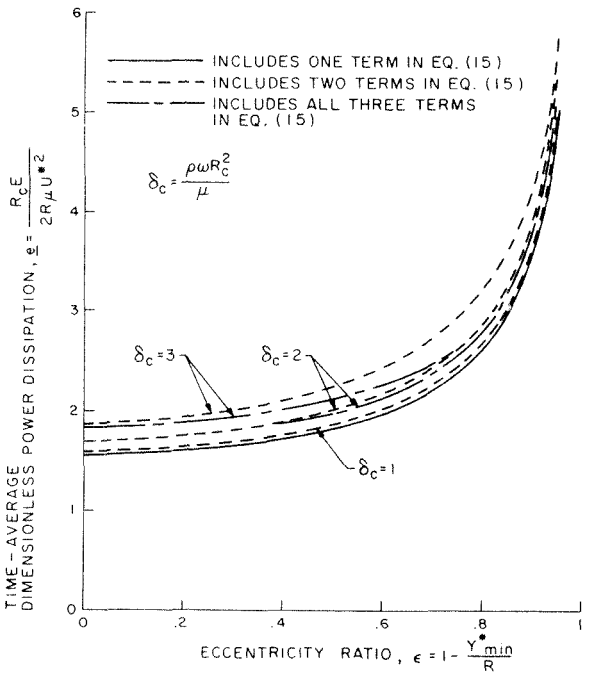

Fig. 3 Dimensionless power dissipation for eccentric film annulus bounded by stationary cylindrical housing and axially reciprocating shaft

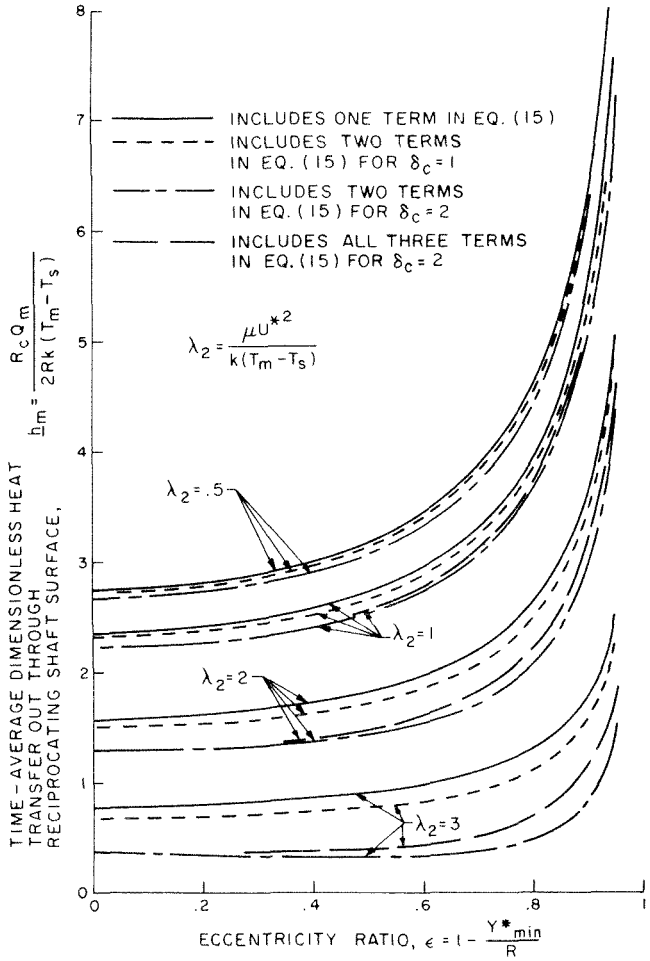

Fig. 4 Dimensionless radial heat transfer through axially reciprocating shaft surface enclosed by eccentric fluid annulus and stationary cylindrical housing

reciprocating cylindrical shaft and its stationary cylindrical housing. Rapidly convergent series solutions are found for nearly concentric annuli (i.e., $\epsilon \ll 1$). A slower rate of convergence is associated with intermediate values of eccentricity ratio. As ϵ approaches unity, the zeroth-order solutions for f, h_s, and h_m become infinite while the higher-order terms remain finite and convergent. Hence, the relative effect of fluid inertia becomes negligible for a nearly perfectly eccentric annulus.

Equations (15) represent the time averages of dimensionless shaft frictional power, $\underline{e}$, and dimensionless heat transfer at the stationary cylindrical housing, $\underline{h}_s$, and at the axially reciprocating shaft surface, $\underline{h}_m$. These equations are simple in form and dependent only on the Brinkman number, λ_2, on the Reynolds number, δ_c, and on the shaft eccentricity ratio, ϵ. Fig. 3 shows curves of $\underline{e}$ versus ϵ for $\delta_c = 1$, 2, and 3. The solutions for $\delta_c = 1$ including two and three terms in the first of equations (15) were so close in value to warrant no graphical distinction. For $\delta_c = 2$ the series solution for $\underline{e}$ is still rapidly convergent with the second-order solution showing only a slight deviation from the first-order solution. However, note that the first correction on the zeroth-order term has significant effect for $\delta_c = 2$. For $\delta_c = 3$, the series solution for $\underline{e}$ seems still rapidly convergent as long as small values of ϵ are considered (i.e., $\epsilon < 0.4$). A slowly convergent trend is visible for larger values of ϵ (i.e., $\epsilon = \approx 0.8$). As ϵ approaches one, the zeroth-order term in the series for e becomes infinite and the series corrections assume relatively negligible values.

Fig. 4 shows values of $\underline{h}_m$ plotted versus eccentricity ratio, ϵ, for $\lambda_2 = 0.5$, 1, 2, and 3 with values of 1 and 2 assigned to the Reynolds number, δ_c. As expected the zeroth-order solution for $\underline{h}_m$ is quite accurate for the lower values of λ_2. The perturbation corrections in the series solution for $\underline{h}_m$ become important as λ_2 and/or δ_c increase in value. For $\lambda_2 = 0.5$ and/or $\delta_c = 1$, the solutions shown for $\underline{h}_m$ including two and three terms agree closely and warrant no graphical distinction.

Application of Solution

Parallel Surfaces. In heat exchangers where heat must pass through a reciprocating fluid film with parallel surfaces of the type considered here, the important thermal quantities are the heat flux extracted from the reciprocating surface, Q_m, and the heat flux transmitted to the stationary surface, Q_s. It is usually the time average of these heat fluxes which are of practical interest. Denote these average values, respectively, as $\underline{Q}_m$ and $\underline{Q}_s$. The quantity $\underline{Q}_m$ is the effective heat removal from the system in unit area of the fluid film. The quantity $\underline{Q}_s$ is the heat removal in unit area the cooler must absorb. Only if the energy dissipation within the fluid film becomes negligible (e.g., if the Brinkman number, λ_2, approaches zero), will Q_m and Q_s approach each other in value. The solutions presented in the foregoing apply only in the small and moderate Reynolds number, δ, range. Hence, from equations (9), one concludes that fluid motion inertia reduces the system heat removal, $\underline{Q}_m$, and leaves unaffected (at least up to and including $0(\delta^4)$) the heat flux transmitted to the cooler, $\underline{Q}_s$. The value of Brinkman number resulting in no heat removal can be obtained by setting equal to zero the last of equations (9). For $\underline{Q}_m = 0$, the value of λ_2 reaches its maximum value of 4 when $\delta = 0$.

Consider the effect of the fluid film thickness on the system heat removal per unit area, Q_m, by writing the last of equations (9) in dimensional form as

$$\frac{Q_m}{k(T_m - T_s)} = \left(1 - \frac{\lambda_2}{4}\right)\frac{1}{Y^*} - \frac{\lambda_2}{90}\left(\frac{\rho\omega}{\mu}\right)^2 Y^{*3} + \frac{\lambda_2}{9450}\left(\frac{\rho\omega}{\mu}\right)^4 Y^{*7} + 0(\delta^6) \qquad (17)$$

Consider a fluid film of water at 27 deg C, yielding the following property values [3]: $k = 0.611\ (10)^5$ dyne/(sec deg C), $\rho = 0.996$ gm/cm^3 and $\mu = 0.860\ (10)^{-2}$ dyne sec/cm^2. Let the maximum

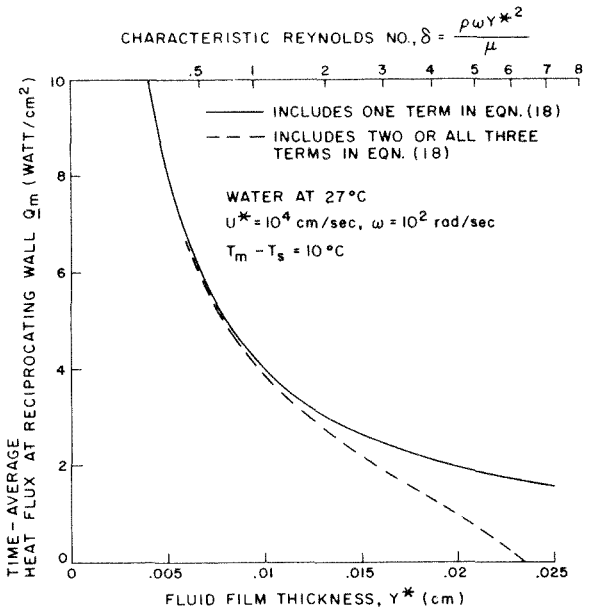

Fig. 5 Time-average heat flux at moving wall as function of the fluid film thickness for film bounded by parallel walls

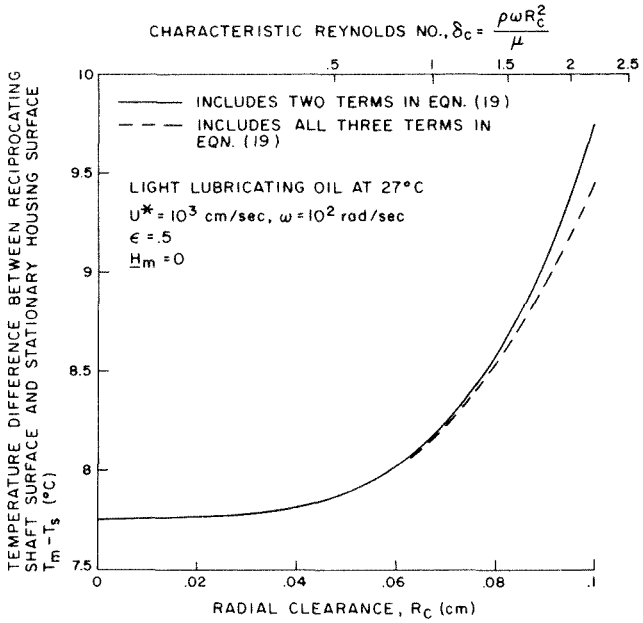

Fig. 6 Difference between shaft surface and cylindrical housing surface temperature as function of the radial clearance for an insulated shaft

value of the reciprocating wall velocity be $U = 10^4$ cm/sec at a frequency $\omega = 10^2$ rad/sec. Assign a value to the difference in wall temperatures $T_m - T_s = 10$ deg C. The resulting Brinkman number is $\lambda_2 = 1.41$, and the value of the parameter $\rho\omega/\mu = 1.16\ (10)^4$ cm^{-2}. Substitute these values into equation (17) and convert the units of Q_m to watt/cm^2, yielding

$$Q_m = \frac{0.0396}{Y^*} - 0.129(100Y^*)^3 + 0.165(10)^{-4}\,(100Y^*)^7 + \ldots \tag{18}$$

where the unit of cm must be used for Y^*. Fig. 5 shows equation (18) plotted with the fluid film thickness, Y^*, or the Reynolds number as the independent variable. The solid line in the figure neglects completely fluid motion inertia and represents the first term in the foregoing equation. The dashed line in the figure includes the first two terms in the R.H.S. of equation (18); fluid inertia is included with a single correction term. The curve obtained if the third term in the R.H.S. of equation (18) is also included agrees closely and cannot be distinguished graphically from the results including the first two terms in the equation. Fig. 5 shows the great significance of fluid inertia under certain conditions. Note that fluid inertia has caused Q_m to vanish at a rather low value of Reynolds number (i.e., $\delta \cong 6.4$). For larger Reynolds number, Q_m assumes negative values. Equation (18) and Fig. 5 show the importance of the first correction term including fluid flow inertia and the rapid convergence of higher-order terms, which property is typical of the perturbation expansions presented in the manuscript.

Eccentric Annulus. Consider an eccentric shaft with axial reciprocating motion inside its parallel cylindrical stationary housing. Assume the shaft surface to be insulated, $H_m = 0$ (where H_m denotes the time average of H_m), and at a uniform temperature, T_m. The cylindrical housing surface transmits a time-average heat per unit length, H_m, and is maintained at a uniform temperature, T_s. Under these conditions there will occur the maximum temperature difference possible between shaft surface and cylindrical housing surface. It is of practical importance, because in many applications the bearing housing can be cooled much more effectively than the reciprocating shaft. In any case, the solution to be obtained yields the worst case for thermal expansions which reduce the radial thickness of the fluid annulus. In order for the solution presented here to be of practical significance, the length of the bearing or bushing must be considerably larger than the stroking motion; otherwise, end effects can become important. Let the velocity amplitude $U^* = 10^3$ cm/sec at a frequency $\omega = 10^2$ rad/sec. Consider a light lubricating oil at 27 deg C yielding [3]: $\mu = 0.413$ dyne sec/cm^2, $\rho = 0.910$ gm/cm^3 and $k = 1.33\ (10)^4$ dyne/(sec deg C). Assume a value of eccentricity ratio $\epsilon = 0.5$ and substitute into equation (16) to obtain

$$T_m - T_s = 7.76 + 1.99(10R_c)^4 - 0.299(10R_c)^8 + \ldots \tag{19}$$

where T_m and T_s are in deg C, and the radial clearance, R_c, is in cm. Fig. 6 shows the effect of the radial clearance on $T_m - T_s$. The value of this temperature difference would be 7.76 if fluid motion inertia were neglected. Hence, the first correction term including inertia in the solution is important while the second correction term, for the conditions given, has a much smaller contribution. Note from equation (19) that the two correction terms presented are of opposite sign, which is typical of the perturbation series presented in the manuscript. This change in sign of successive correction terms should exist as well for higher-order terms. Hence, the exact solution in Fig. 6 should lie somewhere between the solid and dashed lines shown, since the series seems convergent for the range of R_c considered.

References

1 Landau, L. D., and Lifshitz, E. M., *Fluid Mechanics*, Addison-Wesley, Reading, Mass., 1959.

2 Cameron, A., *The Principles of Lubrication*, Wiley, New York, 1966.

3 Kreith, F., *Principles of Heat Transfer*, International Textbook Co., Scranton, Pa., 1965.

APPENDIX

If only the time average quanties are desired, as presented in equations (16) and (24), it is simpler to start with the averaged form of the energy equation:

$$\frac{\partial^2\bar{\theta}}{\partial y^2} = -\frac{\lambda_2}{2\pi}\int_0^{2\pi}\left(\frac{\partial\mu}{\partial y}\right)^2 d\tau \tag{A1}$$

where the time-average temperature distribution, $\bar{\theta}$, has been introduced. The solution for u in equations (5) is

$$u(y, \tau; \delta) = f(y; \delta)\ \sin\tau + g(y; \delta)\ \cos\tau \tag{A2}$$

where the first few terms to the series solutions for f and g can be obtained from equations (6). Combine equations (A1) and (A2) to obtain

$$\frac{\partial^2 \theta}{\partial y^2} = -\frac{\lambda_2}{2}\left[\left(\frac{df}{dy}\right)^2 + \left(\frac{dg}{dy}\right)^2\right] \tag{A3}$$

Integrating and satisfying the temperature boundary conditions in equations (3), one obtains

$$\theta = y + \frac{\lambda_2}{4}(y - y^2) + \frac{\lambda_2}{360}\delta^2(y^2 - y^6) - \frac{\lambda_2}{8640}\delta^4\left(\frac{26}{105}y^2 - \frac{4}{15}y^6 + \frac{2}{105}y^{10}\right) + 0(\delta^6) \tag{A4}$$

Differentiation of equation (A4) yields the time-average heat flux which can be evaluated at $y = 0$ and 1 to obtain the last two equations in (16).

L. C. Thomas

R. Rajagopal

B. T. F. Chung

Mechanical Engineering Department,
The University of Akron, Akron, Ohio

An Analysis of Heat Transfer in Turbulent Pipe Flow With Variable Properties

A new approach to the analysis of variable property heat transfer for turbulent flow is presented. The mathematical model developed herein is based on the principle of surface renewal and involves the use of an integral technique. The proposed expressions for heat transfer account for both variable conductivity and variable viscosity and are applicable to heating and cooling. The theoretical predictions are in good agreement with available experimental heat transfer data for moderate Prandtl number fluids.

Introduction

Various theoretical analyses have been proposed for variable property heat transfer to fluids associated with laminar flow in the boundary layer and thermal entrance region [1, 2, 3].[1] These analyses have proven to be adequately representative of available experimental data. However, less success has been realized in the modeling of turbulent heat transfer for variable property flow. Aside from semiempirical analyses [4, 5] which are based on the eddy diffusivity concept, studies of this complex problem have been limited to empirical correlations coupled with dimensional analysis. Although Deissler's [4] analysis yields predictions for the mean Nusselt number which qualitatively describe the variable property effect on heat transfer, these results tend to overpredict the available experimental data [6].

A different approach to the analysis of variable property heat transfer for turbulent flow of liquids is now proposed which is based on the surface renewal principle. This concept is in basic accord with recent experimental studies which utilize: *(a)* flow visualization techniques [7], and *(b)* flush mounted hot film probes [8, 9]. These studies demonstrate the active nature of the wall region. The proposed model stipulates that eddies intermittently move from the turbulent core to the wall region. In addition, one-dimensional molecular transfer is assumed to govern during the residency of eddies within the vicinity of the wall. This type of model, known as the surface renewal and penetration model, was first proposed by Danckwerts [10] in connection with turbulent mass transfer for a fluid-fluid interface. The model has been subsequently adapted to a broad range of turbulent transport processes for solid-fluid interfaces [11–15].

[1] Numbers in brackets designate References at end of paper.

Contributed by the Heat Transfer Division of THE AMERICAN SOCIETY OF MECHANICAL ENGINEERS and presented at the AIChE-ASME Heat Transfer Conference, Denver, Colo., August 6–9, 1972. Manuscript received by the Heat Transfer Division, April 10, 1972; revised manuscript received November 29, 1972. Paper No. 72-HT-59.

Formulation

Thermal Analysis. Based on the surface renewal and penetration model, the energy equation can be written for individual elements of fluid at the wall as

$$\frac{\partial t}{\partial \theta} = \frac{1}{\rho c} \frac{\partial}{\partial y} \left(K \frac{\partial t}{\partial y} \right) \tag{1}$$

The pertinent boundary-initial conditions can be written as

$$t = T_o \qquad \text{at } y = 0 \tag{2}$$

$$t = T_i \qquad \text{at } y = \infty \tag{3}$$

$$t = T_i \qquad \text{at } \theta = 0 \tag{4}$$

where θ represents the instantaneous contact time and T_i represents the temperature of eddies at the first instant of renewal; T_i may be set equal to the bulk stream temperature, T_b, for moderate to high Prandtl number fluids [13]. Letting $\psi = (t - T_b)/(T_0 - T_b)$, $\eta_t = y/\delta_t$, and assuming $K/K_b = 1 + \beta\psi$, with constant density, ρ, and constant specific heat, c, the integral form of equation (1) may be written as

$$\frac{d}{d\theta} \delta_t \int_0^1 \psi \, d\eta_t = \frac{-1}{\rho c \delta_t} \left(K \frac{\delta \psi}{\partial \eta_t} \right)_0 \tag{5}$$

δ_t is the thermal penetration depth, β is a constant, and K_b is the thermal conductivity evaluated at the bulk stream temperature, T_b.

It is assumed that the temperature profile can be approximated by a fourth-degree polynomial of the form

$$\psi = c_1 + c_2\eta_t + c_3\eta_t^2 + c_4\eta_t^3 + c_5\eta_t^4 \tag{6}$$

This profile must satisfy the conditions

$$\psi = 1 \qquad \text{at} \qquad \eta_t = 0 \tag{7}$$

$$\psi = 0 \qquad \text{at} \qquad \eta_t = 1 \tag{8}$$

$$\frac{\partial \psi}{\partial \eta_t} = 0 \qquad \text{at} \qquad \eta_t = 1 \tag{9}$$

$$\frac{\partial^2 \psi}{\partial \eta_t^2} = 0 \qquad \text{at } \eta_t = 1 \tag{10}$$

and

$$(1 + \beta)\frac{\partial^2 \psi}{\partial \eta_t^2} + \beta\left(\frac{\partial \psi}{\partial \eta_t}\right)^2 = 0 \qquad \text{at } \eta_t = 0 \tag{11}$$

Equation (11) is obtained on the basis of an assumed constant wall temperature. Based on these conditions, equation (6) becomes

$$\psi = (1 - 6\eta_t^2 + 8\eta_t^3 - 3\eta_t^4) + D(\eta_t - 3\eta_t^2 + 3\eta_t^3 - \eta_t^4) \tag{12}$$

where

$$D = \frac{1}{\beta}\left[3(1 + \beta) \mp \left[(1 + \beta)(9 + 21\beta)\right]^{1/2}\right] \tag{13}$$

Only the negative root is taken since it yields similar profiles for velocity and temperature in the case of constant properties. Note that equation (12) contains the time variation implicitly in the variable δ_t. The substitution of equation (12) into equation (5) gives

$$\frac{d}{d\theta}\left[\delta_t(2/5 + \frac{D}{20})\right] = \frac{-K_b(1 + \beta)D}{\rho c \delta_t} \tag{14}$$

Hydrodynamic Analysis. Similarly, the axial momentum equation for individual elements of fluid at the wall can be written as

$$\frac{\partial u}{\partial \theta} = \frac{1}{\rho}\frac{\partial}{\partial y}\left(\frac{\mu \partial u}{\partial y}\right) \tag{15}$$

with boundary conditions

$$u = 0 \qquad \text{at} \qquad y = 0 \tag{16}$$

$$u = u_i \qquad \text{at} \qquad y = \infty \tag{17}$$

$$u = u_i \qquad \text{at} \qquad \theta = 0 \tag{18}$$

The eddy velocity at the first instant of renewal, u_i, can be approximated by the bulk stream velocity, u_b [12]. Assuming $\mu/\mu_b = 1/(1 + \gamma\psi)$ with $\eta = y/\delta$ and constant density, the integral momentum equation can be written as

$$\frac{d}{d\theta}\left[\delta\left[\int_0^1 \frac{u}{u_b}\, d\eta - 1\right]\right] = \frac{-1}{\rho\delta}\left(\frac{\mu \frac{\partial(\frac{u}{u_b})}{\partial \eta}}{}\right)_0 \tag{19}$$

where δ is the momentum penetration depth, γ is a constant (with $\gamma > 0$ representing heating and $\gamma < 0$ denoting cooling for liquids), and μ_b represents the viscosity evaluated at T_b.

A velocity profile of the form

$$\frac{u}{u_b} = (3\eta - 3\eta^2 + \eta^3) - A(\eta - 3\eta^2 + 3\eta^3 - \eta^4) \tag{20}$$

satisfies the boundary conditions

$$\frac{u}{u_b} = 0 \qquad \text{at} \qquad \eta = 0 \tag{21}$$

$$\frac{u}{u_b} = 1 \qquad \text{at} \qquad \eta = 1 \tag{22}$$

$$\frac{\partial(\frac{u}{u_b})}{\partial \eta} = 0 \qquad \text{at} \qquad \eta = 1 \tag{23}$$

$$\frac{\partial^2(\frac{u}{u_b})}{\partial \eta^2} = 0 \qquad \text{at } \eta = 1 \tag{24}$$

and

$$\frac{(1 + \gamma)}{\delta}\frac{\partial^2(\frac{u}{u_b})}{\partial \eta^2} - \frac{\gamma}{\delta_t}\frac{\partial(\frac{u}{u_b})}{\partial \eta}\frac{\partial \psi}{\partial \eta_t} = 0 \quad \text{at} \quad \eta = 0 \tag{25}$$

where

$$A = \frac{6\Delta(1 + \gamma) + 3\gamma D}{6\Delta(1 + \gamma) + \gamma D} \qquad \text{and} \qquad \Delta = \delta_t/\delta$$

Equations (19) and (20) lead to an expression for δ of the form

$$\frac{d}{d\theta}\left[\delta(1/4 + \frac{A}{20})\right] = \frac{\mu_b}{\delta\rho}\frac{(3 - A)}{(1 + \gamma)} \tag{26}$$

Consideration of the Parameter A. The parameter A now is shown to be independent of time, θ, by an analysis which is analogous to a presentation by Hanna and Myers [1] for the variable property laminar boundary layer problem. With equation (14) rewritten as

$$\frac{d}{d\theta}\left[\Delta\delta\right] = \frac{-K_b(1 + \beta)D}{\rho c(2/5 + \frac{D}{20})\Delta\delta} \tag{27}$$

equations (26) and (27) lead to

Nomenclature

A = dimensionless parameter in velocity profile
c = specific heat at constant pressure
D = dimensionless parameter in temperature profile
E = dimensionless parameter, $1/4 + A/20$
F = dimensionless parameter
f = friction factor; dimensionless
h = coefficient of heat transfer
K = thermal conductivity
K_b = thermal conducitivity evaluated at bulk stream temperature
K_w = thermal conductivity evaluated at wall temperature
Nu = Nusselt number, $\frac{hD}{K}$
Pr = Prandtl number, $\frac{\nu}{\alpha}$
q_i = instantaneous heat flux at the wall
Re = Reynolds number, $\frac{u_b D}{\nu}$
t = temperature
T_0 = wall temperature
T_b = bulk stream temperature
T_i = temperature of eddies at first instant of renewal
u = instantaneous velocity
u_b = bulk stream velocity
u_i = velocity of eddies at first instant of renewal
y = transverse coordinate direction
α = thermal diffusivity, $\frac{K}{\rho c_p}$
θ = instantaneous contact time
μ = dynamic viscosity
ν = kinematic viscosity
σ_0 = mean wall shear stress
ρ = density
τ = mean residence time
ψ = dimensionless temperature, $(t - T_b)/(T_0 - T_b)$
δ = hydrodynamic penetration depth
δ_t = thermal penetration depth
β = dimensionless parameter for variable conductivity
γ = dimensionless parameter for variable viscosity
η = dimensionless hydrodynamic parameter, y/δ
η_t = dimensionless thermal parameter, y/δ_t
Δ = ratio of thermal to hydrodynamic penetration depth, δ_t/δ

$$\frac{d(\Delta\delta)}{d(\delta E)} = F \tag{28}$$

where

$$E = 1/4 + \frac{A}{20} \tag{29}$$

and

$$F = \frac{-K_b(1+\beta)D(1+\gamma)}{c(2/5 + \frac{D}{20})\,\Delta\mu_b(3-A)} \tag{30}$$

With $\Delta = 0$ at $\delta = \delta_0$, separation of variables and integration gives

$$\delta = \delta_0 \exp\left\{\int_0^{\Delta} \frac{FdE - d\Delta}{\Delta - FE}\right\} \tag{31}$$

Equation (31) should yield nonzero values of δ for any initial condition δ_0. Hence as $\delta_0 \to 0$ equation (31) indicates that $(\Delta - FE) \to 0$. Thus for the case of $\delta_0 = 0$

$$\Delta = FE \tag{32}$$

The substitution for F and E in equation (32) yields

$$\Delta = (1/4 + \frac{A}{20})\left(\frac{-D}{2/5 + \frac{D}{20}}\right)\left(\frac{K_b(1+\beta)}{\rho c}\right)\left(\frac{\rho(1+\gamma)}{\mu_b}\right)\frac{1}{\Delta\,(3-A)} \tag{33}$$

From equation (33) an expression can be written as

$$\mathrm{Pr}_w = \left(\frac{-D}{8+D}\right)\left(\frac{1}{\Delta^2}\right)\left(\frac{5+A}{3-A}\right) \tag{34}$$

where $\mathrm{Pr}_w = \mu_w c/K_w$. Substituting the expression for the parameter A into equation (34) gives

$$\mathrm{Pr}_w = \left(\frac{-D}{8+D}\right)\left(\frac{3}{\Delta^2} + \frac{2\,\gamma D}{3\Delta^3(1+\gamma)}\right) \tag{35}$$

For a constant wall temperature, Pr_w is a constant. Hence Δ is independent of θ and it is concluded that the parameter A is independent of θ.

Formulation for Local Mean Nusselt Number. Equations (14) and (26) give rise to expressions for the penetration thicknesses δ_t and δ of the form

$$\delta_t^2 = \frac{40\,K_b(1+\beta)(-D)\theta}{(8+D)\,\rho c} \tag{36}$$

and

$$\delta^2 = \frac{40\,\mu_b(3-A)\theta}{\rho(1+\gamma)\,(5+A)} \tag{37}$$

Hence Δ can be expressed as

$$\Delta^2 = \frac{(-D)\,(5+A)}{(8+D)\,(3-A)\,\mathrm{Pr}_w} \tag{38}$$

(Equation (38) and the expression for the parameter A are solved simultaneously to determine A and Δ.) Based on equations (12) and (36), an expression can be written for the local instantaneous heat flux, q_i, of the form

$$q_i = -\left(\frac{K\partial t}{\partial y}\right)_0 = \frac{-K_w(T_o - T_b)D}{\left[\frac{40(-D)\,K_w}{(8+D)\,\rho c}\theta\right]^{1/2}} \tag{39}$$

A consideration of the effect on the mean heat transfer of the numerous eddies in contact with the surface leads to the relationship for the local mean heat flux in terms of the contact time distribution function, $\phi(\theta)$, of the form [11, 14]

$$q = \int_0^{\infty} q_i\,\phi(\theta)d\theta \tag{40}$$

The contact time distribution is defined such that $\phi(\theta)d\theta$ represents the fraction of fluid elements in contact with the surface with contact time between θ and $\theta + d\theta$. The form of the contact time distribution function has been shown to have very little influence on the resulting expression for the temperature (concentration) profile [12]. Hence, the use of the simple uniform distribution proposed by Higbie [16] will be employed; this distribution takes the form

$$\phi(\theta) = \frac{1}{\tau} \qquad 0 < \theta < \tau$$
$$= 0 \qquad \theta > \tau \tag{41}$$

where τ is the mean residence time of fluid elements at the surface. The coupling of equations (39), (40), and (41) leads to an expression for the local mean coefficient of heat transfer of the form

$$h = \frac{2\,K_b\,(1+\beta)\,(-D)}{\left[40\left(\frac{-D}{8+D}\right)\frac{K_b(1+\beta)}{\rho c}\tau\right]^{1/2}} \tag{42}$$

For constant properties, $D = -2$ such that equation (42) reduces to

$$h = 1.097\sqrt{\frac{K\rho c}{\tau}} \tag{43}$$

This compares very well (within −3 percent) with the exact solution (derived for mass transfer [10])

$$h = \frac{2}{\sqrt{\pi}}\sqrt{\frac{K\rho c}{\tau}} \tag{44}$$

From equations (20) and (37) an expression can be written for the local instantaneous wall shear stress as

$$\sigma_{0i} = \left(\frac{\mu\partial u}{\partial y}\right)_0 = u_b\left[\frac{\mu_b\rho}{40\,(1+\gamma)\theta}\,(3-A)\,(5+A)\right]^{1/2} \tag{45}$$

The use of Higbie's uniform contact time distribution then gives

$$\frac{\sigma_0}{\rho} = u_b\left[\frac{\mu_b}{\rho(1+\gamma)\tau}\,\frac{(3-A)\,(5+A)}{10}\right]^{1/2} \tag{46}$$

Hence, the mean residence time can be expressed in terms of the Fanning friction factor, f, as [14]

$$\sqrt{\frac{1}{\tau}} = u_b\frac{f}{2}\left[\frac{\rho}{\mu_b}\,\frac{(1+\gamma)\,10}{(3-A)(5+A)}\right]^{1/2} \tag{47}$$

The substitution of equation (47) into equation (42) yields an expression for the local mean Nusselt number of the form

$$\mathrm{Nu} = \frac{f}{2}\,\mathrm{Re}\,\sqrt{\mathrm{Pr}}\left[\frac{(-D)(8+D)\,(1+\beta)\,(1+\gamma)}{(3-A)\,(5+A)}\right]^{1/2} \tag{48}$$

where the Reynolds number, Re, and Prandtl number are evaluated at the bulk stream temperature.

Discussion

For constant properties ($A = 1$, $D = -2$) equation (48) reduces to an expression of the form

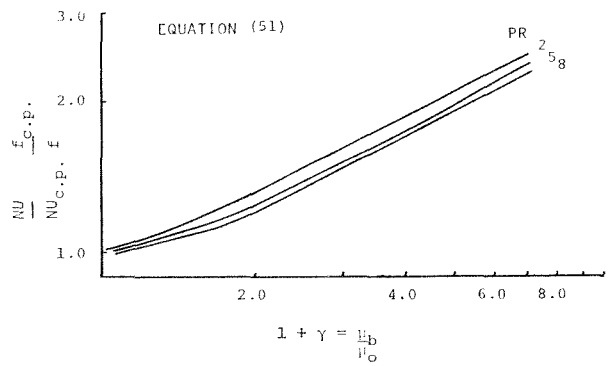

Fig. 1 *Influence of viscosity ratio on heat transfer for the heating of liquids*

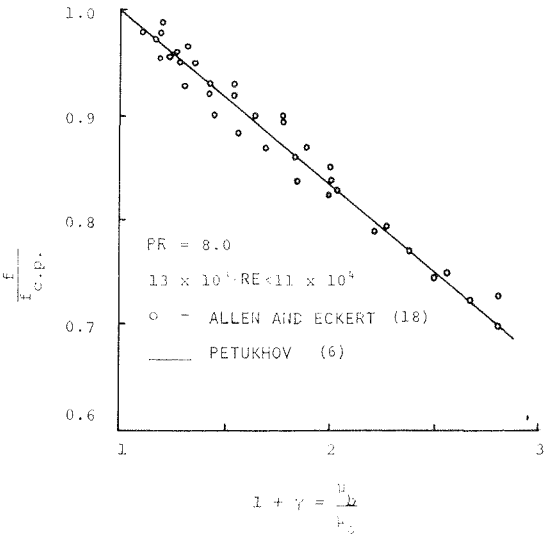

Fig. 2 Friction factor data for the heating of water

$$\mathrm{Nu}_{c.p.} = \frac{f_{c.p.}}{2} \mathrm{Re} \sqrt{\mathrm{Pr}} \tag{49}$$

which is identical to the exact solution for uniform properties obtained on the basis of the elementary surface renewal and penetration model and which correlates experimental data for turbulent pipe flow with moderate Prandtl numbers [13]. Accordingly, equation (48) can be written more conveniently as

$$\frac{\mathrm{Nu}}{\mathrm{Nu}_{c.p.}} = \frac{f}{f_{c.p.}} \left[\frac{(-D)\ (8+D)\ (1+\beta)\ (1+\gamma)}{(3-A)\ (f+A)} \right]^{1/2} \tag{50}$$

This expression reduces further for constant conductivity (i.e., $\beta = 0$) to

$$\frac{\mathrm{Nu}}{\mathrm{Nu}_{c.p.}} = 3.46 \frac{f}{f_{c.p.}} \left[\frac{(1+\gamma)}{(3-A)\ (5+A)} \right]^{1/2} \tag{51}$$

The influence of the viscosity ratio, bulk to wall, on the product $\mathrm{Nu}/\mathrm{Nu}_{c.p.}$ predicted by equation (51) for heating is shown in Fig. 1 for values of the Prandtl number ranging from 2 to 8. It must be mentioned that when $\gamma \geq 0.648$ and Pr = 8 the present computations yield negative values of Δ. This obviously has no physical meaning. To overcome this mathematical breakdown, the smoothing condition (after Goodman [17])

$$\frac{\partial^3 u}{\partial y^3} = 0 \qquad \text{at } y = \delta \tag{52}$$

is employed in place of equation (25). The use of equation (52) yields the value -1 for the parameter A and this value is used in equation (51) only when $\gamma \geq 0.648$ for Pr = 8.0. This figure suggests that the effect of variable viscosity on the heat transfer is somewhat dependent upon the Prandtl number.

Although friction factor data for turbulent variable viscosity flow are somewhat scarce for moderate values of the Prandtl number, some experimental friction factor data for water at a Prandtl number equal to 8 have been published by Allen and Eckert [18]. These data for heating are shown in Fig. 2. An equation of the form

$$\frac{f}{f_{c.p.}} = 1/6 \left[7 - (1+\gamma) \right] \tag{53}$$

suggested by Petukhov [6] fits the data well. Based on these data for friction factor, equation (51) is compared in Fig. 3 with experimental heat transfer data for heating of water (thermally developed, constant wall heat flux) by Allen and Eckert [18]. The proposed model correlates these data reasonably well. Although this analysis assumes a constant wall temperature condition, equation (51) can be expected to apply for the uniform wall flux condition for moderate Prandtl number fluids. For comparison purposes, the semitheoretical prediction for $\mathrm{Nu}/\mathrm{Nu}_{c.p.}$ by Deissler [4] and

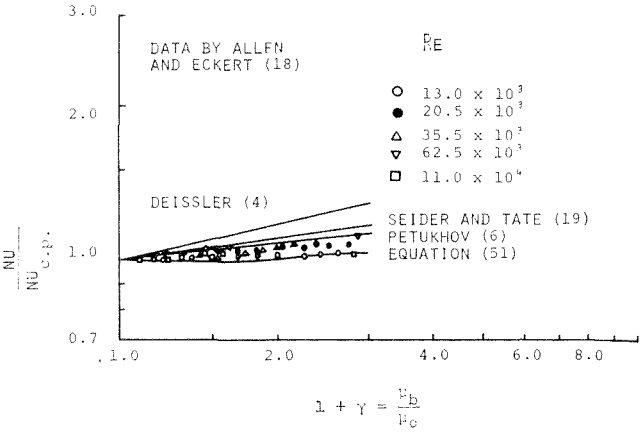

Fig. 3 Variable viscosity influence on heat transfer for water

the empirical correlation proposed by Petukhov [6] and Seider and Tate [19] are also included in Fig. 3.

Fig. 4 shows the influence of variable conductivity on heat transfer as predicted by equation (50) for heating and cooling. It is observed that the influence of variable conductivity is more pronounced for the case of heating than for cooling.

Conclusion

The elementary surface renewal and penetration model together with an approximate integral formulation has been shown to correlate available experimental heat transfer data for variable viscosity moderate Prandtl number fluids. Based on this formulation, the effect of both viscosity and conductivity variation on the turbulent heat transfer appears to be mildly dependent upon the Prandtl number. Accordingly, the familiar empirical relationship given by

$$\frac{\mathrm{Nu}}{\mathrm{Nu}_{c.p.}} = \left(\frac{\mu_b}{\mu_0} \right)^n$$

where n has been said to be constant [20], may be somewhat in error. However, additional experimental evidence is needed to form a firm conclusion.

Although the method presented herein can be extended to incompressible gas flow, this analysis must be restricted to fluids of moderate Prandtl number ($0.5 \lesssim \mathrm{Pr} \lesssim 10$). For low values of the Prandtl number, molecular conduction becomes significant during the flight of eddies such that T_l in equations (3) and (4) can not be set equal to T_b. For large values of the Prandtl number, the thermal resistance of unreplenished fluid which remains adja-

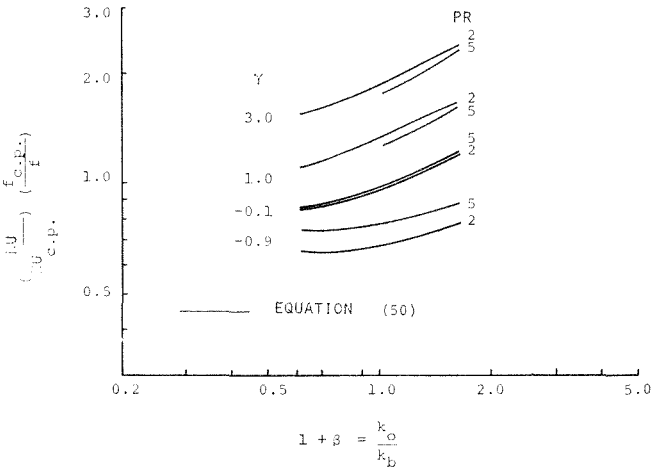

Fig. 4 Variable conductivity influence on heat transfer for the heating ($\gamma > 0$) and cooling ($\gamma < 0$) of liquids

cent to the wall becomes important. Due to recent success in the modeling of both low and high Prandtl number fluids by use of the principle of surface renewal [14, 15], the present analysis would appear to provide direction in the analysis of variable property heat transfer for these fluids.

References

1 Hanna, O. T., and Myers, J. E., "Laminar Boundary Layer Flow and Heat Transfer Past a Flat Plate for a Liquid of Variable Viscosity," *AIChE Journal*, Vol. 7, 1961, p. 437.

2 Sinha, P. C., "Forced Convection Flow Past a Flat Plate With Variable Viscosity and Thermal Conductivity," *Journal of the Physical Society of Japan*, Vol. 27, 1969, p. 478.

3 Yang, K. T., "Laminar Forced Convection of Liquids in Tubes With Variable Viscosity," JOURNAL OF HEAT TRANSFER, TRANS. ASME, Series C, Vol. 84, 1962, p. 353.

4 Deissler, R. G., "Analysis of Turbulent Heat Transfer, Mass Transfer, and Friction in Smooth Tubes at High Prandtl and Schmidt Numbers," NACA Tech. Report 1210, 1955.

5 Viskanta, R., and Touloukian, Y. S., "Heat Transfer to Liquid Metals With Variable Properties," JOURNAL OF HEAT TRANSFER, TRANS. ASME, Series C, Vol. 82, 1960, p. 333.

6 Petukhov. B. S., "Heat Transfer and Friction in Turbulent Pipe Flow," *Advances in Heat Transfer*, Academic Press, Vol. 6, 1970, p. 503.

7 Popovich, A. T., and Hummel, R. L., "Experimental Study of the Viscous Sublayer in Turbulent Pipe Flow," *AIChE Journal*, Vol. 13, 1967, p. 854.

8 Meek, R. L., and Baer, A. D., "The Periodic Viscous Sublayer in Turbulent Flow," *AIChE Journal*, Vol. 16, 1970, p. 841.

9 Thomas, L. C., Greene, H. L., Nokes, R. F., and Chu, M., "Turbulence Studies for Steady and Pulsed Flow of Drag Reducing Solutions," 72nd National AIChE Meeting, St. Louis, Mo., 1972; *AIChE Symposium Series*, 130, Vol. 69, 1973, p. 14.

10 Danckwerts, P. V., "Significance of Liquid-Film Coefficients in Gas Absorption," *I&EC*, Vol. 43, 1951, p. 1460.

11 Chung, B. T. F., Fan, L. T., and Hwang, C. L., "A Model of Heat Transfer in Fluidized Beds," JOURNAL OF HEAT TRANSFER, TRANS. ASME, Series C, Vol. 94, 1972, p. 104.

12 Hanratty, T. J., "Turbulent Exchange of Mass and Momentum With a Boundary," *AIChE Journal*, Vol. 2, 1956, p. 359.

13 Thomas, L. C., and Fan, L. T., "Adaptation of the Surface Rejuvenation Model to Turbulent Heat and Mass Transfer at a Solid-Fluid Interface," *I&EC Fundamentals*, Vol. 10, 1971, p. 135.

14 Thomas, L. C., "Temperature Profiles for Liquid Metals and Moderate Prandtl Number Fluids," JOURNAL OF HEAT TRANSFER, TRANS. ASME, Series C, Vol. 92, 1970, p. 565.

15 Thomas, L. C., Chung, B. T. F., and Mahaldar, S. K., "Temperatures Profiles for Turbulent Flow of High Prandtl Number Fluids," *International Journal of Heat and Mass Transfer*, Vol. 14, 1971, p. 1465.

16 Higbie, R., "Rate of Absorption of a Gas Into a Still Liquid," *AIChE Trans.*, Vol. 31, 1935, p. 365.

17 Goodman, T. R., "The Heat Balance Integral—Further Considerations and Refinements," JOURNAL OF HEAT TRANSFER, TRANS. ASME, Series C, Vol. 83, 1961, p. 83.

18 Allen, R. W., and Eckert, E. R. G., "Friction and Heat Transfer Measurements to Turbulent Pipe Flow of Water (Pr = 7 and 8) at Uniform Wall Heat Flux," JOURNAL OF HEAT TRANSFER, TRANS. ASME, Series C, Vol. 86, 1964, p. 301.

19 Sieder, E. N., and Tate, G. N., "Heat Transfer and Pressure Drop of Liquids in Tubes," *I&EC*, Vol. 28, 1936, p. 1429.

20 Kays, W. M., *Convective Heat and Mass Transfer*, McGraw-Hill, New York, 1966.

journal of heat transfer

technical briefs

This section consists of contributions of 1500 words or less (about 5 double-spaced typewritten pages, including figures). Technical briefs will be reviewed and approved by the specific division's reviewing committee prior to publication. After approval such contributions will be published as soon as possible, normally in the next issue of the journal.

Apparent Hemispherical Emittance of Baffled Cylindrical Cavities

E. M. SPARROW,[1] R. P. HEINISCH,[2] and N. SHAMSUNDAR[3]

Introduction

In this paper, an efficient Monte Carlo method is employed to determine how the radiant energy streaming from an isothermal cylindrical cavity is affected by a baffle partially obstructing the opening. Consideration is given both to baffles that are at the same temperature as the cavity wall (emitting baffles) and to baffles that are at temperatures well below the wall temperature (nonemitting baffles). The other parameters that were varied included the emittance of the wall, the depth-to-radius ratio of the cavity, and the baffle size. The calculations were performed for gray, diffusely emitting and reflecting surfaces. The results are presented in terms of the apparent hemispherical emittance of the cavity.

The Monte Carlo method used here is an adaptation of that described in detail in connection with an investigation of baffled conical cavities [1].[4] Although a number of modifications were made to accommodate the cylindrical geometry, the essential features of the method remain intact. Consequently, only a qualitative outline of the method will be presented here. The basis of the method is the realization that the radiant energy streaming out of the aperture consists of two components. One component is the emitted radiant energy that reaches the aperture directly, without internal reflections. The second component includes the radiant energy that reaches the aperture after one or more internal reflections within the cavity. Consistent with the foregoing, the energy content of each photon bundle is partitioned into two portions. One portion leaves the cavity without undergoing internal reflections, whereas the second portion remains in the cavity where it may either experience reflections and ultimately emerge from the aperture or be absorbed. Since such photon bundles generally make at least one contribution to the outstreaming radiation, the results are obtained with substantially fewer photon bundles than would be required by conventional Monte Carlo methods.

A schematic diagram of a baffled cylindrical cavity is shown in Fig. 1. The cavity has depth L and radius R_0, and the radius of the aperture in the baffle is R_a. The axial and radial coordinates are r and z, respectively. Also pictured in the figure are the angles θ and ϕ of a spherical coordinate system locally implanted at a typical point P on the cylindrical wall of the cavity.

Previous investigations of baffled cylindrical cavities have been

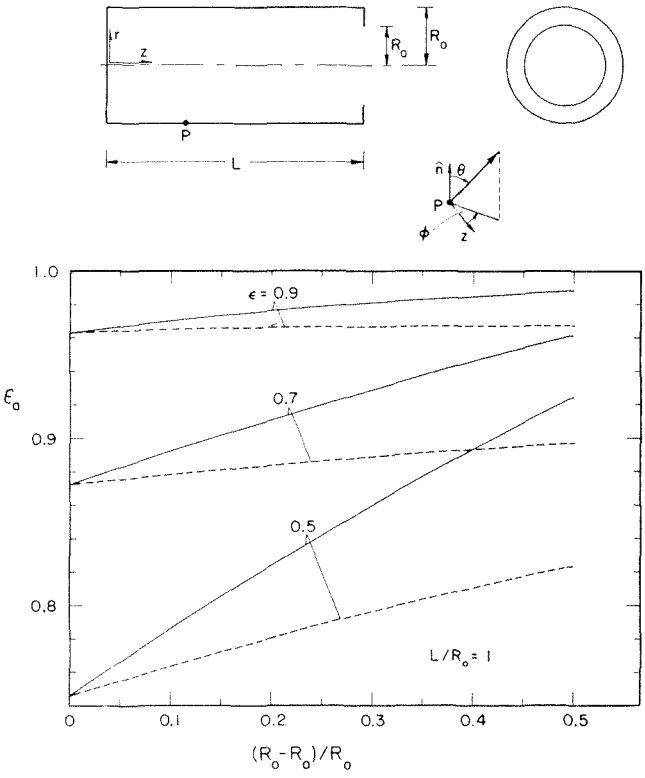

Fig. 1 Upper portion: schematic diagram of a baffled cylindrical cavity; lower portion: apparent emittance results for a cylindrical cavity with depth-radius ratio $L/R_0 = 1$

[1] Department of Mechanical Engineering, University of Minnesota, Minneapolis, Minn. Mem. ASME.

[2] Honeywell, Inc., St. Paul, Minn.

[3] Department of Mechanical Engineering, University of Minnesota, Minneapolis, Minn.

[4] Numbers in brackets designate References at end of technical brief.

Contributed by the Heat Transfer Division of THE AMERICAN SOCIETY OF MECHANICAL ENGINEERS. Manuscript received by the Heat Transfer Division December 6, 1972.

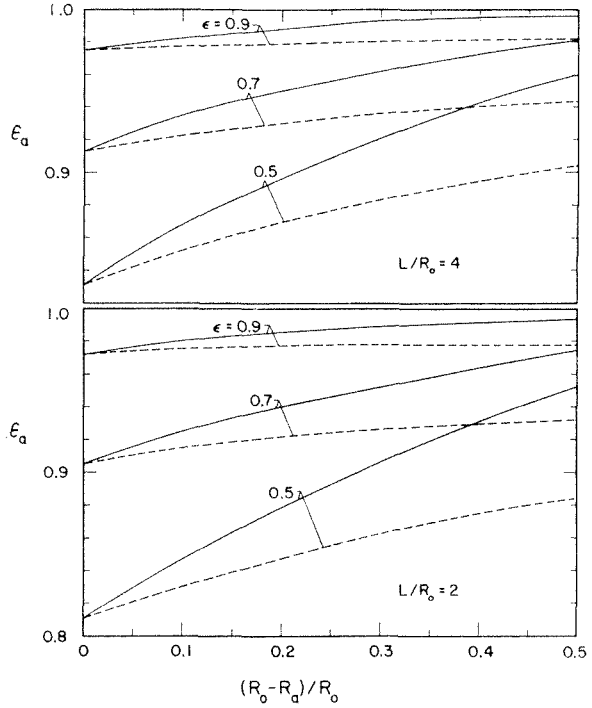

Fig. 2 Apparent emittance results for cylindrical cavities with depth-radius ratios $L/R_0 = 2$ and 4

concerned with the apparent normal emittance of an element at the center of the cavity base [2, 3], the series method of DeVos [4] having been employed by both investigators.

Outline of the Analysis

In a Monte Carlo model of the radiant interchange process, photon bundles are released at random locations on the cavity wall and (if emitting) on the baffle. If there are N photon (or ray) bundles, then each bundle is assigned an energy content E^* given by

$$E^* = \epsilon\sigma T^4 A_w/N \tag{1}$$

where T is the wall temperature and A_w is the surface area that is actually emitting.

The Monte Carlo calculation is begun by selecting a surface location from which the ray bundle is released, for which purpose a random number between zero and one is drawn. The coordinate of the point of release is related to the random number by an algebraic equation that expresses the fact that emission is equally probable from all area elements on an isothermal wall. If the baffle is nonemitting, then the point of release is constrained to lie on the cavity wall, whereas if the baffle is emitting, the ray bundle may depart from either the cavity wall or the baffle.

Once the point of release of the ith bundle has been determined, its energy content E^* is partitioned into two portions F_iE^* and $(1 - F_i)E^*$. The portion F_iE^* passes directly out of the aperture and is immediately tallied, whereas the portion $(1 - F_i)E^*$ remains within the cavity. The quantity F is an angle factor. For points of departure on the cylindrical wall or on the base surface, algebraic formulas for F are given in configurations 16 and 15 in Appendix C of [5]. On the other hand, $F = 0$ if the point of departure is on the baffle.

Before tracing the trajectory of the portion $(1 - F_i)E^*$ that remains within the cavity, a random number R_α is drawn to test whether the ray bundle will be absorbed at its point of impingement. If absorption occurs, then a new ray bundle is considered. On the other hand, if absorption does not occur, then the trajectory is traced using the departure angles θ and ϕ of a locally implanted spherical coordinate system (for example, Fig. 1). The departure angles are related to random numbers R_θ and R_ϕ by equations of the form

$$R_\theta = a \sin^2 \theta + b \qquad R_\phi = c\phi + d \tag{2}$$

where a, b, c, and d are functions of position. Equations (2) are so constituted that for all random numbers between zero and one the departing ray bundle remains within the cavity. The functions a, b, c, and d are derived in a manner similar to that described in detail in [1].

At the point of impingement, a second partitioning takes place. If F_{i1} denotes the angle factor of the aperture as seen from the point of impingement, then the two partitioned portions are $F_{i1}(1 - F_i)E^*$ and $(1 - F_{i1})(1 - F_i)E^*$. The angle factor F_{i1} is computed from the same expressions that are used to compute the F_i at the point of emission. The portion $F_{i1}(1 - F_i)E^*$ exits through the aperture and is tallied, whereas the portion $(1 - F_{i1})(1 - F_i)E^*$ remains in the cavity and continues its life cycle until it is ultimately absorbed.

The contribution of each photon bundle to the out-streaming radiation may be expressed as

$$(E_{\text{out}})_i = (F_i + G_i)E^* \tag{3}$$

where $G_i = 0$ if there are no reflections, $G_i = (1 - F_i)F_{i1}$ if there is one reflection, $G_i = (1 - F_i)F_{i1} + (1 - F_i)(1 - F_{i1})F_{i2}$ if there are two reflections, and so forth.

The apparent hemispherical emittance of the cavity is defined as $\epsilon_a = E_{\text{out}}/\sigma T^4 A_a$, where A_a is the area of the aperture. Since E_{out} is the sum of the contributions from each photon bundle and E^* is given by equation (1), ϵ_a may be expressed as

$$\epsilon_a = \frac{\epsilon(A_w/A_a)}{N}\left[\sum_{i=1}^{N}(F_i + G_i)\right] \tag{4}$$

Results and Discussion

The apparent emittance results are presented in Figs. 1 and 2. In each graph, ϵ_a is plotted against the baffle size parameter $(R_0 - R_a)/R_0$, which gives the fraction of the cylinder radius that is blocked by the baffle. The three graphs presented in the aforementioned figures correspond, respectively, to cavity depth-to-radius ratios L/R_0 of 1, 2, and 4. The curves appearing in each graph are parameterized by values of the wall emittance ϵ of 0.5, 0.7, and 0.9. The solid lines correspond to the case in which the baffle is emitting, and the dashed lines are for the case of the nonemitting baffle.

An examination of the figures reveals several interesting trends. The apparent emittance is seen to increase as more and more of the cavity opening is blocked by the baffle. The effect of the baffle is more marked when the cavity is relatively shallow (i.e., smaller L/R_0) and also at lower values of the wall emittance ϵ. From a comparison of the solid and dashed lines, it may be concluded that an emitting baffle brings about greater increases in the apparent emittance than does a nonemitting baffle.

The differences between the apparent emittance results for cavities with $L/R_0 = 2$ and $L/R_0 = 4$ were found to be rather small, especially for the larger values of ϵ. For $\epsilon = 0.5$, the differences were of the order of one or two in the second significant figure.

An assessment of the accuracy of the present results may be made by comparing the ϵ_a values for the unbaffled cavity with those of Lin [6] obtained from numerical solutions of integral equations. Typically, the two sets of results agreed to within two in the third significant figure.

References

1 Heinisch, R. P., Sparrow, E. M., and Shamsundar, N., "Radiant Emission from Baffled Conical Cavities," *Journal of the Optical Society of America*, Vol. 63, 1973, pp. 152–158.

2 Quinn, T. J., "The Calculation of the Emissivity of Cylindrical Cavities Giving Near Black-Body Radiation," *British Journal of Applied Physics*, Vol. 18, 1967, pp. 1105–1109.

3 Fussell, W. B., "Normal Emissivity of an Isothermal, Diffusely Reflecting Cavity (With Top) as a Function of Inside Radius," *National Bureau of Standards Journal of Research*, Vol. A76, 1972, pp. 347–349.
4 DeVos, J. C., "Evaluation of the Quality of a Blackbody," *Physica*, Vol. 20, 1954, pp. 669–689.
5 Siegel, R., and Howell, J. R., *Thermal Radiation Heat Transfer*, McGraw-Hill, New York, N. Y., 1972.
6 Lin, S. H., "Radiant Interchange in Cavities and Passages with Specularly and Diffusely Reflecting Surfaces," PhD thesis, Department of Mechanical Engineering, University of Minnesota, Minneapolis, Minn., 1964.

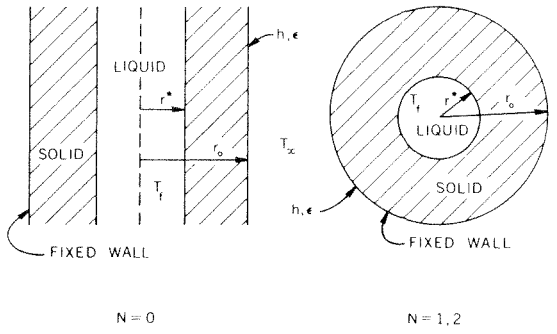

Fig. 1

Inward Solidification With Radiation–Convection Boundary Condition

J. S. GOODLING[1] and M. S. KHADER[2]

Nomenclature

Bi = Biot number, $\frac{hr_0}{k}$

C_1 = radiation parameter, $\frac{\sigma \epsilon T_f^3 r_0}{k}$

C_2 = environmental temperature parameter, $\frac{T_\infty}{T_f}$

N = coordinate system designator

S* = Stefan number, $\frac{C_p T_f}{L}$

y = spatial coordinate, $\frac{r}{r_0}$

$\bar{r}$ = interface position, $\frac{r^*}{r_0}$

τ = time, $\frac{kT_f t}{r_0^2 \rho L}$

τ^* = total time to solidify

τ_0^* = total time to solidify with no radiation present

θ = temperature distribution, $\frac{T}{T_f}$

Introduction

The problem of predicting solidification rates has application in many fields ranging from freeze-drying to metals casting. When the solidification takes place at high temperatures, as in the case of metals castings, radiation and convective heat transfer are both significant mechanisms of cooling at the fixed outer surface. Several investigators [1–4][3] have solved the inward or outward solidification problems with constant temperature, constant heat flux, or convective boundary conditions using a variety of techniques. These types of boundary conditions allow for a simplified closed-form solution by the method of London and Seban [1], where the quasi-steady assumption is used to neglect the heat capacity of the solidifying material. For the radiative problem, solutions based on the quasi-steady temperature distribution are not possible due to the nonlinearity of the boundary condition.

By writing the governing equations in dimensionless form, the problem is stated in generalized form in terms of three controlling parameters; a modified Stefan number, the Biot number, and a radiation parameter. An implicit numerical scheme is used to solve the complete inward solidification problem for slabs, cylinders, and spheres with a mixed radiative and convective boundary condition at the outer surface.

Analysis

Fig. 1 shows schematically the configuration of the problem to be solved. Initially, the entire region is liquid at the fusion temperature, T_f. Cooling of the outer surface by radiation and convection leads to removal of energy from the liquid region sufficient to cause a phase change. The governing equation in nondimensional form for heat transfer in the newly formed solid region for the three coordinate systems is

$$\frac{\partial^2 \theta}{\partial y^2} + \frac{N}{y}\frac{\partial \theta}{\partial y} = S^* \frac{\partial \theta}{\partial \tau} \qquad \begin{matrix} N = 0 \text{ Cartesian system} \\ N = 1 \text{ cylindrical system} \\ N = 2 \text{ spherical system} \end{matrix} \quad (1)$$

Assuming that the outer surface is approximately gray, the associated boundary conditions are

$$-\frac{\partial \theta}{\partial y}(1, \tau) = C_1[\theta^4(1, \tau) - C_2^4] + \text{Bi}[\theta(1, \tau) - C_2] \quad (2)$$

$$\theta(\bar{r}, \tau) = 1 \; ; \quad \frac{d\bar{r}}{d\tau} = \frac{\partial \theta}{\partial y}(\bar{r}, \tau) \; , \quad \bar{r}(0) = 1 \quad (3)$$

The three significant dimensionless parameters are the modified Stefan number, S*, the Biot number, Bi, and a radiation parameter, C_1. The Stefan number is usually specified as to include a characteristic temperature difference ($C_p \Delta T/L$), but when radiation is an important heat transfer mechanism, an absolute value is used as the characteristic temperature. In the solidification process of metals, the fusion temperature, T_f, can be high ($\simeq$ 2000R) and the latent heat of fusion low, yielding typically high values of $C_p T_f/L$.

Solution

Because of the nonlinearity of the previously stated problem, methods of determining analytical solutions are not known, even for the simplified case of S* $\rightarrow$ 0. However, by replacing the spatial differentials in equations (1), (2), and (3) with central difference quotients and the time differential with backward implicit quotients, a set of nonlinear algebraic equations is generated which can be solved.

The method of solution for the algebraic equations consists of fixing the point of interface advancement for a finite number of regular intervals of Δy starting at $y = 1$ and determining the time required for this movement to occur by satisfying all applicable difference equations. Because of the nonlinearity of the problem, a predictor corrector technique is used. This is done by estimating the temperature of the space grid point immediately next to the solidification grid point and working backwards through the equations to find the temperature at the fixed wall grid point. If the boundary condition is not satisfied, the procedure is repeated with a new estimated temperature near the solidification front.

[1] Associate Professor, Department of Mechanical Engineering, Auburn University, Auburn, Ala.
[2] Instructor, Department of Mechanical Engineering, Auburn University, Auburn, Ala.
[3] Numbers in brackets designate References at end of technical brief.
Contributed by the Heat Transfer Division of THE AMERICAN SOCIETY OF MECHANICAL ENGINEERS, Manuscript received by the Heat Transfer Division June 22, 1973.

3 Fussell, W. B., "Normal Emissivity of an Isothermal, Diffusely Reflecting Cavity (With Top) as a Function of Inside Radius," *National Bureau of Standards Journal of Research*, Vol. A76, 1972, pp. 347–349.
4 DeVos, J. C., "Evaluation of the Quality of a Blackbody," *Physica*, Vol. 20, 1954, pp. 669–689.
5 Siegel, R., and Howell, J. R., *Thermal Radiation Heat Transfer*, McGraw-Hill, New York, N. Y., 1972.
6 Lin, S. H., "Radiant Interchange in Cavities and Passages with Specularly and Diffusely Reflecting Surfaces," PhD thesis, Department of Mechanical Engineering, University of Minnesota, Minneapolis, Minn., 1964.

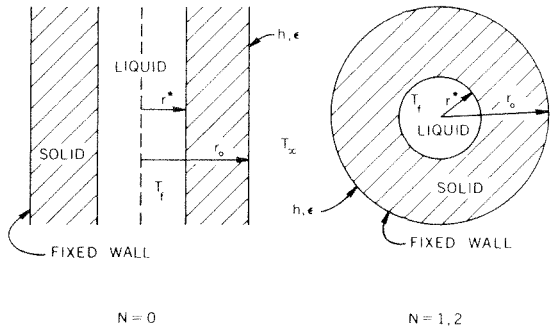

Fig. 1

Inward Solidification With Radiation–Convection Boundary Condition

J. S. GOODLING[1] and M. S. KHADER[2]

Nomenclature

Bi = Biot number, $\frac{hr_0}{k}$

C_1 = radiation parameter, $\frac{\sigma \epsilon T_f^3 r_0}{k}$

C_2 = environmental temperature parameter, $\frac{T_\infty}{T_f}$

N = coordinate system designator

S* = Stefan number, $\frac{C_p T_f}{L}$

y = spatial coordinate, $\frac{r}{r_0}$

$\bar{r}$ = interface position, $\frac{r^*}{r_0}$

τ = time, $\frac{kT_f t}{r_0^2 \rho L}$

τ^* = total time to solidify

τ_0^* = total time to solidify with no radiation present

θ = temperature distribution, $\frac{T}{T_f}$

Introduction

The problem of predicting solidification rates has application in many fields ranging from freeze-drying to metals casting. When the solidification takes place at high temperatures, as in the case of metals castings, radiation and convective heat transfer are both significant mechanisms of cooling at the fixed outer surface. Several investigators [1-4][3] have solved the inward or outward solidification problems with constant temperature, constant heat flux, or convective boundary conditions using a variety of techniques. These types of boundary conditions allow for a simplified closed-form solution by the method of London and Seban [1], where the quasi-steady assumption is used to neglect the heat capacity of the solidifying material. For the radiative problem, solutions based on the quasi-steady temperature distribution are not possible due to the nonlinearity of the boundary condition.

By writing the governing equations in dimensionless form, the problem is stated in generalized form in terms of three controlling parameters; a modified Stefan number, the Biot number, and a radiation parameter. An implicit numerical scheme is used to solve the complete inward solidification problem for slabs, cylinders, and spheres with a mixed radiative and convective boundary condition at the outer surface.

Analysis

Fig. 1 shows schematically the configuration of the problem to be solved. Initially, the entire region is liquid at the fusion temperature, T_f. Cooling of the outer surface by radiation and convection leads to removal of energy from the liquid region sufficient to cause a phase change. The governing equation in nondimensional form for heat transfer in the newly formed solid region for the three coordinate systems is

$$\frac{\partial^2 \theta}{\partial y^2} + \frac{N}{y}\frac{\partial \theta}{\partial y} = S^* \frac{\partial \theta}{\partial \tau} \qquad \begin{matrix} N = 0 \text{ Cartesian system} \\ N = 1 \text{ cylindrical system} \\ N = 2 \text{ spherical system} \end{matrix} \quad (1)$$

Assuming that the outer surface is approximately gray, the associated boundary conditions are

$$-\frac{\partial \theta}{\partial y}(1, \tau) = C_1[\theta^4(1, \tau) - C_2^4] + \text{Bi}[\theta(1, \tau) - C_2] \quad (2)$$

$$\theta(\bar{r}, \tau) = 1 \; ; \quad \frac{d\bar{r}}{d\tau} = \frac{\partial \theta}{\partial y}(\bar{r}, \tau) \; , \quad \bar{r}(0) = 1 \quad (3)$$

The three significant dimensionless parameters are the modified Stefan number, S*, the Biot number, Bi, and a radiation parameter, C_1. The Stefan number is usually specified as to include a characteristic temperature difference ($C_p \Delta T/L$), but when radiation is an important heat transfer mechanism, an absolute value is used as the characteristic temperature. In the solidification process of metals, the fusion temperature, T_f, can be high ($\simeq$ 2000R) and the latent heat of fusion low, yielding typically high values of $C_p T_f/L$.

Solution

Because of the nonlinearity of the previously stated problem, methods of determining analytical solutions are not known, even for the simplified case of S* $\rightarrow$ 0. However, by replacing the spatial differentials in equations (1), (2), and (3) with central difference quotients and the time differential with backward implicit quotients, a set of nonlinear algebraic equations is generated which can be solved.

The method of solution for the algebraic equations consists of fixing the point of interface advancement for a finite number of regular intervals of Δy starting at $y = 1$ and determining the time required for this movement to occur by satisfying all applicable difference equations. Because of the nonlinearity of the problem, a predictor corrector technique is used. This is done by estimating the temperature of the space grid point immediately next to the solidification grid point and working backwards through the equations to find the temperature at the fixed wall grid point. If the boundary condition is not satisfied, the procedure is repeated with a new estimated temperature near the solidification front.

[1] Associate Professor, Department of Mechanical Engineering, Auburn University, Auburn, Ala.
[2] Instructor, Department of Mechanical Engineering, Auburn University, Auburn, Ala.
[3] Numbers in brackets designate References at end of technical brief.
Contributed by the Heat Transfer Division of THE AMERICAN SOCIETY OF MECHANICAL ENGINEERS, Manuscript received by the Heat Transfer Division June 22, 1973.

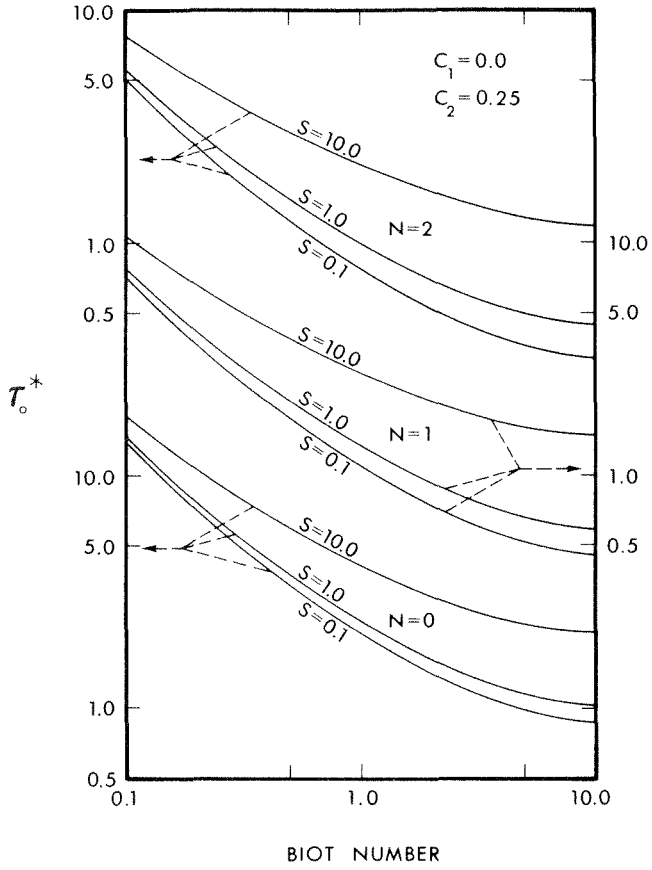

Fig. 2

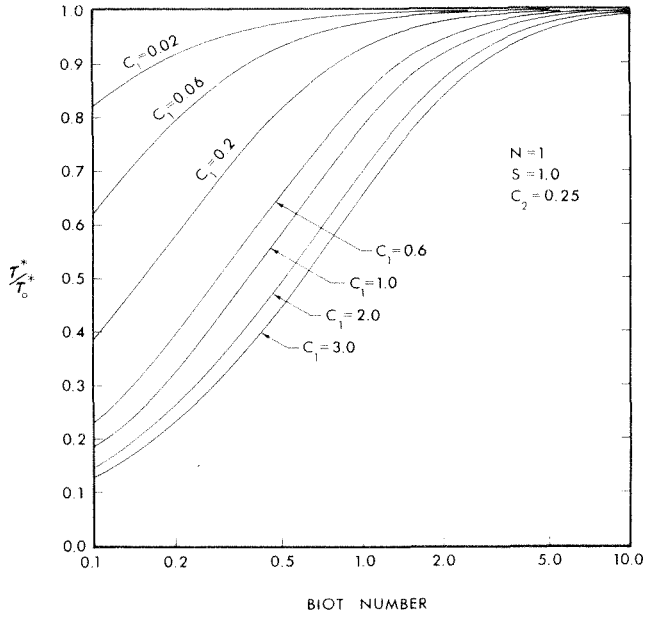

Fig. 3

This procedure is iterated until the boundary condition becomes an equality to within a small error.

In the limiting case of $S^* \to 0$ and $C_1 \to 0$, analytical solutions can be obtained by the method of [1]. This yields both the temperature distribution and the movement of the solidification front with time.

Results and Discussion

Numerical calculations were performed as mentioned in the foregoing with space steps $\Delta y = 0.05$. Iterations of the algebraic equations were performed to determine the temperature near the interface to within $\pm 10^{-7}$. The equality of the boundary condition at the outer surface was satisfied within an average value of 10^{-4} over all ranges of the parameters considered in the present analysis.

Authentication of the computational scheme was made by comparison with exact analytical solutions by the method of [1] for $S^* = 0$. The numerical results for $S^* = 0$ and $C_1 = 0$ yielded results for $\bar{r} = f(\tau)$ that were within 3.8 percent of the analytical results.

Fig. 2 shows the effect of S^* and Biot number upon the total time to solidify, τ_o^*, for the three coordinate systems when radiation is absent.

It is of interest to determine under what conditions radiation can be neglected for inward solidification calculations. This can be found by comparing the total time to solidify for the case of radiation and convection, τ^*, to that for pure convection, τ_o^*. The ratio τ^*/τ_o^* was formed for all reasonable ranges of the parameters. It was found that the ratio showed very little dependence upon all parameters except C_1 and Bi. Fig. 3 is a plot of τ^*/τ_o^* for the range of Biot number and radiation parameter, C_1 (with $S^* = 1.0$ and $C_2 = \frac{1}{4}$ for the cylindrical system). As expected for large Bi, radiation contributes only a small amount to changing the total time to solidify. For $Bi < 1$, the presence of a radiative mechanism of heat transfer can reduce τ^* by a factor of two or more. Similar curves were obtained for the three coordinate systems over the range of Stefan number and C_2, but the ratio varied only a few percent from the case shown in Fig. 3.

It was found from these computations that if $C_1 < \frac{1}{3}\,Bi^2$ the total solidification time with radiation was within 10 percent of the values obtained by neglecting radiation. Several other conclusions were reached upon examination of the results:

1 Since S^* is typically much greater than zero in the solidification of metals, the assumption $S^* \simeq 0$ and resulting analytical solution by the method of [1] can lead to large errors in the determination of total solidification time.

2 The temperature distribution inside the solid region is not uniform even when the Biot number is small. The temperature at the outer surface was typically 0.7 near the end of the solidification process.

References

1 London, A. L., and Seban, R. A., "Rate of Ice Formation," TRANS. ASME, Vol. 65, 1943, p. 771.

2 Murray, W. D., and Landis, F., "Numerical and Machine Solutions of Transient Heat—Conduction Problems Involving Melting or Freezing," JOURNAL OF HEAT TRANSFER, TRANS ASME, Vol. 81, 1959, pp. 106–112.

3 Tao, L. C., "Generalized Numerical Solution of Freezing a Saturated Liquid in Cylinders and Spheres," *AIChE Journal*, Vol. 13, No. 1, 1967, p. 165.

4 Pedroso, R. I., and Domoto, G. A., "Perturbation Solutions for Spherical Solidification of Saturated Liquids," ASME Paper No. 72-HT-Q, 1972.

Free Convection From a Vertical Cone at High Prandtl Numbers

S. ROY[1]

Introduction

Heat transfer by laminar free convection from a solid, slender

[1] Research Fellow, Department of Chemical Engineering, University of Aston, Birmingham, U. K. (Present address: Pool Officer, Department of Mathematics, University of Delhi, Delhi, India.)

Contributed by the Heat Transfer Division of THE AMERICAN SOCIETY OF MECHANICAL ENGINEERS. Manuscript received by the Heat Transfer Division, September 22, 1972.

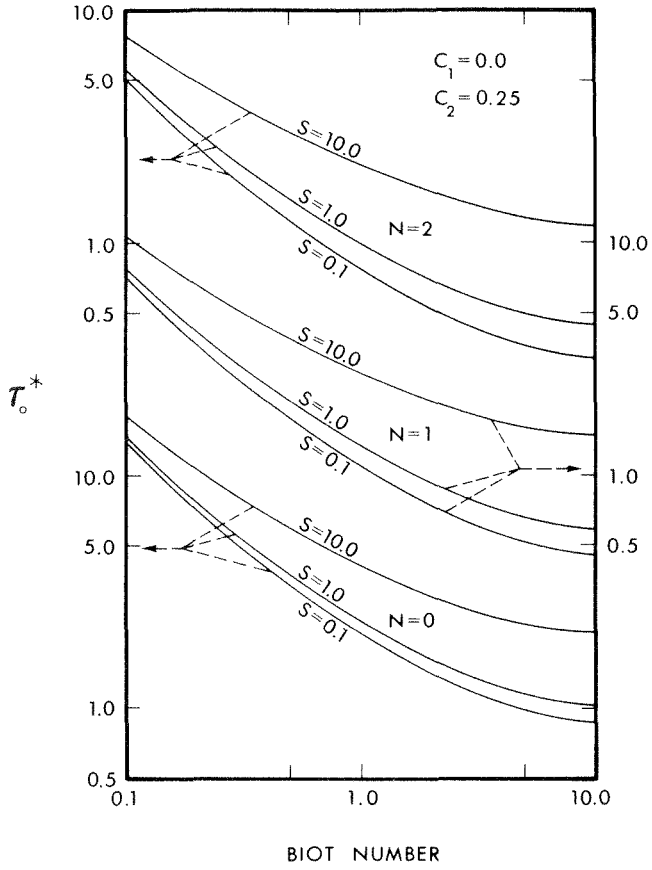

Fig. 2

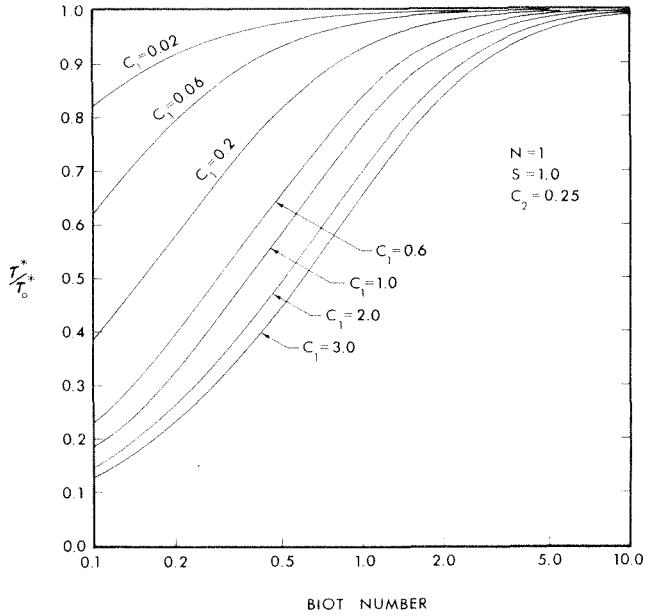

Fig. 3

This procedure is iterated until the boundary condition becomes an equality to within a small error.

In the limiting case of $S^* \to 0$ and $C_1 \to 0$, analytical solutions can be obtained by the method of [1]. This yields both the temperature distribution and the movement of the solidification front with time.

Results and Discussion

Numerical calculations were performed as mentioned in the foregoing with space steps $\Delta y = 0.05$. Iterations of the algebraic equations were performed to determine the temperature near the interface to within $\pm 10^{-7}$. The equality of the boundary condition at the outer surface was satisfied within an average value of 10^{-4} over all ranges of the parameters considered in the present analysis.

Authentication of the computational scheme was made by comparison with exact analytical solutions by the method of [1] for $S^* = 0$. The numerical results for $S^* = 0$ and $C_1 = 0$ yielded results for $\bar{r} = f(\tau)$ that were within 3.8 percent of the analytical results.

Fig. 2 shows the effect of S^* and Biot number upon the total time to solidify, τ_o^*, for the three coordinate systems when radiation is absent.

It is of interest to determine under what conditions radiation can be neglected for inward solidification calculations. This can be found by comparing the total time to solidify for the case of radiation and convection, τ^*, to that for pure convection, τ_o^*. The ratio τ^*/τ_o^* was formed for all reasonable ranges of the parameters. It was found that the ratio showed very little dependence upon all parameters except C_1 and Bi. Fig. 3 is a plot of τ^*/τ_o^* for the range of Biot number and radiation parameter, C_1 (with $S^* = 1.0$ and $C_2 = \frac{1}{4}$ for the cylindrical system). As expected for large Bi, radiation contributes only a small amount to changing the total time to solidify. For $Bi < 1$, the presence of a radiative mechanism of heat transfer can reduce τ^* by a factor of two or more. Similar curves were obtained for the three coordinate systems over the range of Stefan number and C_2, but the ratio varied only a few percent from the case shown in Fig. 3.

It was found from these computations that if $C_1 < \frac{1}{3}\,Bi^2$ the total solidification time with radiation was within 10 percent of the values obtained by neglecting radiation. Several other conclusions were reached upon examination of the results:

1 Since S^* is typically much greater than zero in the solidification of metals, the assumption $S^* \simeq 0$ and resulting analytical solution by the method of [1] can lead to large errors in the determination of total solidification time.

2 The temperature distribution inside the solid region is not uniform even when the Biot number is small. The temperature at the outer surface was typically 0.7 near the end of the solidification process.

References

1 London, A. L., and Seban, R. A., "Rate of Ice Formation," TRANS. ASME, Vol. 65, 1943, p. 771.

2 Murray, W. D., and Landis, F., "Numerical and Machine Solutions of Transient Heat—Conduction Problems Involving Melting or Freezing," JOURNAL OF HEAT TRANSFER, TRANS ASME, Vol. 81, 1959, pp. 106–112.

3 Tao, L. C., "Generalized Numerical Solution of Freezing a Saturated Liquid in Cylinders and Spheres," *AIChE Journal*, Vol. 13, No. 1, 1967, p. 165.

4 Pedroso, R. I., and Domoto, G. A., "Perturbation Solutions for Spherical Solidification of Saturated Liquids," ASME Paper No. 72-HT-Q, 1972.

Free Convection From a Vertical Cone at High Prandtl Numbers

S. ROY[1]

Introduction

Heat transfer by laminar free convection from a solid, slender

[1] Research Fellow, Department of Chemical Engineering, University of Aston, Birmingham, U. K. (Present address: Pool Officer, Department of Mathematics, University of Delhi, Delhi, India.)

Contributed by the Heat Transfer Division of THE AMERICAN SOCIETY OF MECHANICAL ENGINEERS. Manuscript received by the Heat Transfer Division, September 22, 1972.

Table 1 The Solutions

n	ϕ	1/5	1
$F_{10}''(0)$	0.943396	0.916645	0.836937
$-F_{11}''(0)$	0.295433	0.284891	0.254478
$F_{12}''(0)$	0.212035	0.199521	0.168483
$-\Phi_{10}'(0)$	0.621352	0.655796	0.762440
$\Phi_{11}'(0)$	0.137078	0.142109	0.156909
$-\Phi_{12}'(0)$	0.042224	0.044783	0.052248
$F_{20}(0)$	0.0	0.0	0.0
$F_{20}'(0)$	0.668432	0.638329	0.548648
$-F_{20}''(0)$	0.541055	0.525712	0.477784
$-F_{21}(0)$	0.397944	0.369109	0.304122
$F_{21}'(0)$	0.371846	0.360626	0.319559
$-F_{21}''(0)$	0.193896	0.211722	0.238619
$-F_{22}(0)$	0.345433	0.333139	0.285344
$F_{22}'(0)$	0.447106	0.443524	0.399938
$-F_{22}''(0)$	0.280934	0.309436	0.337941

right circular cone, with its apex downwards and axis vertical, has been studied by Merk and Prins [1],[2] Hering and Grosh [2], and Hering [3]. In [2 and 3] one finds extensive studies of the case when the surface temperature is given by

$$T_w - T_\infty = x^n(T_0 - T_\infty), \tag{1}$$

where T is the temperature, the suffixes w, ∞, and 0 stand for the values on the surface, at a large distance from the surface and at $x = 1$, x being the nondimensional coordinate along a generator, defined by $x = (X/L)$, L being the slant height. The corresponding similarity solutions are given by the equations

$$F''' + (\frac{7+n}{4})FF'' - (\frac{1+n}{2})(F')^2 + \theta = 0, \tag{2}$$

$$\theta'' + \Pr\{(\frac{7+n}{4})F\theta' - nF'\theta\} = 0, \tag{3}$$

subject to the boundary conditions

$$F(0) = F'(0) = F'(\infty) = 0,$$
$$\theta(0) = 1, \theta(\infty) = 0 \tag{4}$$

In the foregoing, F, θ, and Pr are, respectively, the nondimensional stream function, nondimensional temperature, and Prandtl number of the fluid. A prime denotes differentiation with respect to the similarity variable η.

The purpose of this note is to extend the works of Hering and Grosh [2, 3] to include fluids with Prandtl numbers greater than unity—a case that has not been considered so far.

High Prandtl Number Analysis

For large values of Pr, one can divide the whole boundary layer into two regions—one in which the inertial forces are negligible compared with the viscous forces and in which the temperature difference is brought to zero, and another which is an isothermal shear layer and in which the velocity parallel to the surface is brought to zero again. These regions, of thicknesses 0 ($\Pr^{-1/4}$) and 0 ($\Pr^{1/4}$), may be called the inner and outer layers, respectively. We shall use this so-called double-boundary-layer concept. This concept was developed by Le Fevre [4], Morgan and Warner [5b], Stewartson and Jones [6], and Kuiken [7], and described in detail by Roy [8]. The different variables suitable for these layers are defined as follows:

Inner layer

$$\left.\begin{aligned} \zeta_1 &= \Pr^{1/4}\eta, \\ F(\eta) &= \Pr^{-3/4}F_1(\zeta_1), \\ \theta(\eta) &= \Phi_1(\zeta_1); \end{aligned}\right\} \tag{5}$$

Outer layer

$$\left.\begin{aligned} \zeta_2 &= \Pr^{-1/4}\eta, \\ F(\eta) &= \Pr^{-1/4}F_2(\zeta_2), \\ \theta(\eta) &= 0 \end{aligned}\right\} \tag{6}$$

Substituting from (5) and (6) in (2) and (3) we see that the three equations for F_1, Φ_1, and F_2 suggest series solutions in some negative powers of Pr. By matching the inner solutions for large ζ_1, with the outer solutions for small ζ_2 we determine these series together with the missing boundary conditions at $\zeta_1 = \infty$ and $\zeta_2 = 0$. Thus the solutions may be written as

$$\left.\begin{aligned} F_1 &= F_{10} + \Pr^{-1/2}F_{11} + \Pr^{-1}F_{12} + \ldots. \\ \Phi_1 &= \Phi_{10} + \Pr^{-1/2}\Phi_{11} + \Pr^{-1}\Phi_{12} + \ldots. \\ F_2 &= F_{20} + \Pr^{-1/2}F_{21} + \Pr^{-1}F_{22} + \ldots. \end{aligned}\right\} \tag{7}$$

The equations for different F_1's, Φ_1's, and F_2's and the boundary condition are not given here as they can be very easily obtained exactly in the same way as shown by Roy [8].

These equations have been solved numerically on an electronic computer for $n = 0$, 1/5, and 1. The first two values of n correspond to the isothermal and uniform heat flux surface conditions, while $n = 1$ is the case when the similarity variable is independent of X. The results are presented in Table 1.

Skin Friction and Heat Transfer

Skin friction is proportional to $(\frac{d^2F}{d\eta^2})_{\eta=0}$

which is given by

$$(\frac{d^2F}{d\eta^2})_{\eta=0} = \Pr^{-1/4}[F_{10}''(0) + \Pr^{-1/2}F_{11}''(0) + \Pr^{-1}F_{12}''(0)] \tag{8}$$

However, the most important result of practical interest is the heat transfer. A local Nusselt number has been defined by Hering and Grosh [2] as

$$Nu_x = \frac{qX}{k(T_w - T_\infty)}, \quad q = -k\frac{\partial T}{\partial Y}\Big|_{Y=0} \tag{9}$$

which reduces to

$$Nu_x = -(Gr_x\Pr)^{1/4}[\Phi_{10}'(0) + \Pr^{-1/2}\Phi_{11}'(0) + \Pr^{-1}\Phi_{12}'(0)] \tag{10}$$

It is obvious that the greater the Prandtl number, the better are the formulas (8) and (10). The highest value of Pr for which results are available in the literature is 1. In Table 2 we compare the values of $F''(0)$ and Nu_x for Pr = 1 obtained from (8) and (10) with these given by Hering [3], who based his calculations on a small Prandtl number theory.

Table 2 Values of $F''(0)$ and $Nu_X\,Gr_X^{-1/4}$ for Pr = 1

	Present work		Hering [3]	
n	$F''(0)$	$Nu_X\,Gr_X^{-1/4}$	$F''(0)$	$Nu_X Gr_X^{-1/4}$
0	0.859998	0.527518	0.7694	0.5105
1/5	0.831275	0.558471	0.7475	0.5148
1	0.750942	0.657779	0.6815	0.6389

[2] Numbers in brackets designate References at end of technical brief.

References

1 Merk, H. J., and Prins, J. A., "Thermal Convection in Laminar Boundary Layers," *Applied Scientific Research*, Series A, Vol. 4, 1953-1954, pp. 11-24, 195-206.

2 Hering, R. G., and Grosh, R. J., "Laminar Free Convection From a Nonisothermal Cone," *International Journal of Heat and Mass Transfer*, Vol. 5, 1962, pp. 1059-1067.

3 Hering, R. G., "Laminar Free Convection From a Nonisothermal Cone at Low Prandtl Numbers," *International Journal of Heat and Mass*

Transfer, Vol. 8, 1965, pp. 1333–1337.
4 Le Fevre, E. J., "Laminar Free Convection From a Vertical Plane Surface," *Actes*, IX Congres International de Mecanique Appliquee, Brussels, Vol. 4, 1957, pp. 168–174.
5 Morgan, G. W., and Warner, W. H., "On Heat Transfer in Laminar Boundary Layers at High Prandtl Number," *Journal of Aeronautical Sciences*, Vol. 23, 1956, pp. 937–948.
6 Stewartson, K., and Jones, L. T., "The Heated Vertical Plate at High Prandtl Number," *Journal of the Aeronautical Sciences*, Vol. 24, 1957, pp. 379–380.
7 Kuiken, H. K., "An Asymptotic Solution for Large Prandtl Number Free Convection," *Journal of Engineering Mathematics*, Vol. 2, 1968, pp. 355–371.
8 Roy, S., "Double-Boundary-Layer Concept in Free Convection at High Prandtl Numbers," *Indian Journal of Physics*, Vol. 44, 1970, pp. 488–494.

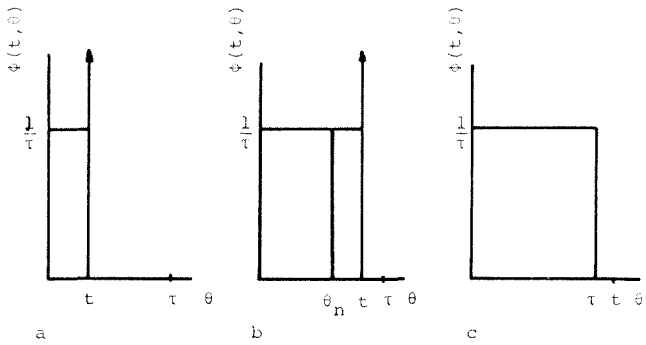

Fig. 1 Transient contact time distribution for various values of *t*

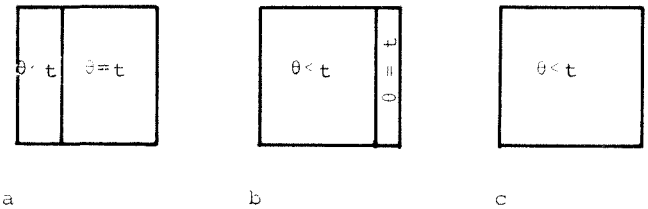

Fig. 2 Illustration of fraction of surface with old and new fluid

Unsteady Heat Transfer for Turbulent Boundary Layer Flow With Time Dependent Wall Temperature

L. C. THOMAS[1] **and B. T. F. CHUNG**[1]

Introduction

The surface renewal and penetration model has recently been adapted to the simplified problem of heat transfer for a turbulent boundary layer flow with a step change in wall temperature at process time, t, equal to zero [1].[2] The main modification of the steady state form of the surface renewal and penetration model was the development and utilization of the transient age distribution $\phi(t,\theta)$; this transient contact time distribution takes the form [1, 2]

$$\phi(t,\theta) = \frac{1}{\tau} + \left(1 - \frac{t}{\tau}\right)\bar{\delta}(\theta - t) \qquad \text{for } 0 \le \theta \le t \le \tau \quad (1)$$

and

$$\phi(t,\theta) = 0 \qquad \text{for } t < \theta \le \tau, \text{ or } \tau < \theta$$

$\bar{\delta}$ is the unit impulse function and τ is the mean residence time. This distribution accounts for the fact that the contact time, θ, can not be greater than the process time, t. The coupling of the basic surface renewal and penetration model and the transient contact time distribution function leads to an expression for the unsteady mean temperature profile, $T(t,y)$, of the form

$$T(t,y) = \int_0^\infty T(\theta,y)\phi(t,\theta)d\theta \quad (2)$$

The previous formulations of the unsteady surface renewal and penetration model have been restricted to the case for which the surface experiences a step change in potential. That is, the solution for $T(\theta,y)$ has been obtained on the basis of an expression of the form

$$\frac{\partial T}{\partial \theta} = \frac{\alpha \partial^2 T}{\partial y^2} \quad (3)$$

with $T(o,y) = T_i$, $T(\theta,o) = T_0$ and $T(\theta,\infty) = T_i$. The primary objective of the present paper is to develop the transient surface renewal and penetration model for the case in which the wall boundary condition is a function of time, such that a solution for the instantaneous profile $T(t,\theta,y)$ becomes available. An expression then can be written for $T(t,y)$ as

$$T(t,y) = \int_0^\infty T(t,\theta,y)\phi(t,\theta)d\theta \quad (4)$$

Formulation

Consider a turbulent flow process for which the fluid temperature and wall temperature are initially equal to T_i, with the wall temperature given as a function of time, t; i.e., $T(t,o) = F(t)$. Based on the surface renewal and penetration model, the energy equation for individual elements of fluid during their residency at the surface [away from the leading thermal edge] can be written in the form of equation (3). The initial condition and the boundary condition away from the wall given in the foregoing are used, along with a wall boundary condition of the form

$$T = \psi(\theta) \quad \text{at } y = 0 \quad (5)$$

where $\psi(\theta)$ remains to be determined.

In order to specify $\psi(\theta)$, attention is turned to the contact time distribution. The uniform transient contact time distribution given by equation (2) is shown in Fig. 1 for several values of t/τ. Each of these representative distribution conditions will now be considered in terms of a finite region of the surface. For t much less than τ (Fig. 1*(a)*), a small fraction of the fluid (equal to t/τ) has been removed from the surface and has been replaced as represented by Fig. 2*(a)*. This fresh fluid has been in contact with the surface for values of τ ranging from 0 to t. The remaining fraction of the surface is in contact with "old" fluid having been in thermal contact for $\theta - t$. For the case in which t is somewhat less than τ (Fig. 1*(b)*), only the small fraction of the surface $(1 - t/\tau)$ shown in Fig. 2*(b)* remains in contact with old fluid, for which $\theta = t$. The large fraction of the surface $[t/\tau]$ has been refreshed by the renewal process such that $\theta < t$. Finally, for the third representative condition with t greater than τ (Fig. 1*(c)*), all fluid which was in contact with the heating surface at $t = 0$ has been replaced by fresh fluid as shown by Fig. 2*(c)*.

Returning to Fig. 1*(b)*, the small fraction of fluid at the surface at the instant t with contact time θ_n arrived at the heating surface at process time $t - \theta_n$. This fraction of the fluid was exposed to a wall temperature which varied according to $F(t)$ from $F(t - \theta_n)$ to $F(t)$. This picture can be generalized for any process time, and for that matter, contact time distribution. That is, at any given process time t, the fraction of fluid which has been in contact with the heating surface for time θ_n can be considered to have been exposed to a wall condition prescribed by $T = F(t - \theta_n + \theta)$. Hence, the appropriate wall boundary condition becomes

[1] Department of Mechanical Engineering, The University of Akron, Akron, Ohio.
[2] Number in brackets designate References at end of technical brief.
Contributed by the Heat Transfer Division of THE AMERICAN SOCIETY OF MECHANICAL ENGINEERS. Manuscript received by the Heat Transfer Division, July 11, 1973.

Transfer, Vol. 8, 1965, pp. 1333–1337.
4 Le Fevre, E. J., "Laminar Free Convection From a Vertical Plane Surface," *Actes*, IX Congres International de Mecanique Appliquee, Brussels, Vol. 4, 1957, pp. 168–174.
5 Morgan, G. W., and Warner, W. H., "On Heat Transfer in Laminar Boundary Layers at High Prandtl Number," *Journal of Aeronautical Sciences*, Vol. 23, 1956, pp. 937–948.
6 Stewartson, K., and Jones, L. T., "The Heated Vertical Plate at High Prandtl Number," *Journal of the Aeronautical Sciences*, Vol. 24, 1957, pp. 379–380.
7 Kuiken, H. K., "An Asymptotic Solution for Large Prandtl Number Free Convection," *Journal of Engineering Mathematics*, Vol. 2, 1968, pp. 355–371.
8 Roy, S., "Double-Boundary-Layer Concept in Free Convection at High Prandtl Numbers," *Indian Journal of Physics*, Vol. 44, 1970, pp. 488–494.

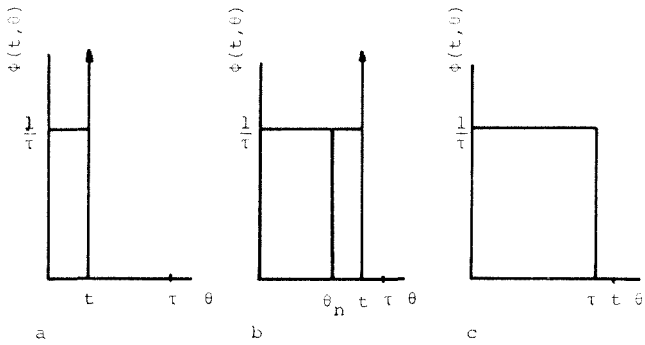

Fig. 1 Transient contact time distribution for various values of *t*

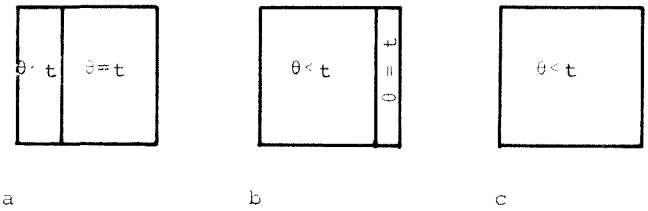

Fig. 2 Illustration of fraction of surface with old and new fluid

Unsteady Heat Transfer for Turbulent Boundary Layer Flow With Time Dependent Wall Temperature

L. C. THOMAS[1] **and B. T. F. CHUNG**[1]

Introduction

The surface renewal and penetration model has recently been adapted to the simplified problem of heat transfer for a turbulent boundary layer flow with a step change in wall temperature at process time, t, equal to zero [1].[2] The main modification of the steady state form of the surface renewal and penetration model was the development and utilization of the transient age distribution $\phi(t,\theta)$; this transient contact time distribution takes the form [1, 2]

$$\phi(t,\theta) = \frac{1}{\tau} + \left(1 - \frac{t}{\tau}\right)\bar{\delta}(\theta - t) \qquad \text{for } 0 \le \theta \le t \le \tau \quad (1)$$

and

$$\phi(t,\theta) = 0 \qquad \text{for } t < \theta \le \tau, \text{ or } \tau < \theta$$

$\bar{\delta}$ is the unit impulse function and τ is the mean residence time. This distribution accounts for the fact that the contact time, θ, can not be greater than the process time, t. The coupling of the basic surface renewal and penetration model and the transient contact time distribution function leads to an expression for the unsteady mean temperature profile, $T(t,y)$, of the form

$$T(t,y) = \int_0^\infty T(\theta,y)\phi(t,\theta)d\theta \quad (2)$$

The previous formulations of the unsteady surface renewal and penetration model have been restricted to the case for which the surface experiences a step change in potential. That is, the solution for $T(\theta,y)$ has been obtained on the basis of an expression of the form

$$\frac{\partial T}{\partial \theta} = \frac{\alpha \partial^2 T}{\partial y^2} \quad (3)$$

with $T(o,y) = T_i$, $T(\theta,o) = T_0$ and $T(\theta,\infty) = T_i$. The primary objective of the present paper is to develop the transient surface renewal and penetration model for the case in which the wall boundary condition is a function of time, such that a solution for the instantaneous profile $T(t,\theta,y)$ becomes available. An expression then can be written for $T(t,y)$ as

$$T(t,y) = \int_0^\infty T(t,\theta,y)\phi(t,\theta)d\theta \quad (4)$$

Formulation

Consider a turbulent flow process for which the fluid temperature and wall temperature are initially equal to T_i, with the wall temperature given as a function of time, t; i.e., $T(t,o) = F(t)$. Based on the surface renewal and penetration model, the energy equation for individual elements of fluid during their residency at the surface [away from the leading thermal edge] can be written in the form of equation (3). The initial condition and the boundary condition away from the wall given in the foregoing are used, along with a wall boundary condition of the form

$$T = \psi(\theta) \quad \text{at } y = 0 \quad (5)$$

where $\psi(\theta)$ remains to be determined.

In order to specify $\psi(\theta)$, attention is turned to the contact time distribution. The uniform transient contact time distribution given by equation (2) is shown in Fig. 1 for several values of t/τ. Each of these representative distribution conditions will now be considered in terms of a finite region of the surface. For t much less than τ (Fig. 1*(a)*), a small fraction of the fluid (equal to t/τ) has been removed from the surface and has been replaced as represented by Fig. 2*(a)*. This fresh fluid has been in contact with the surface for values of τ ranging from 0 to t. The remaining fraction of the surface is in contact with "old" fluid having been in thermal contact for $\theta - t$. For the case in which t is somewhat less than τ (Fig. 1*(b)*), only the small fraction of the surface $(1 - t/\tau)$ shown in Fig. 2*(b)* remains in contact with old fluid, for which $\theta = t$. The large fraction of the surface $[t/\tau]$ has been refreshed by the renewal process such that $\theta < t$. Finally, for the third representative condition with t greater than τ (Fig. 1*(c)*), all fluid which was in contact with the heating surface at $t = 0$ has been replaced by fresh fluid as shown by Fig. 2*(c)*.

Returning to Fig. 1*(b)*, the small fraction of fluid at the surface at the instant t with contact time θ_n arrived at the heating surface at process time $t - \theta_n$. This fraction of the fluid was exposed to a wall temperature which varied according to $F(t)$ from $F(t - \theta_n)$ to $F(t)$. This picture can be generalized for any process time, and for that matter, contact time distribution. That is, at any given process time t, the fraction of fluid which has been in contact with the heating surface for time θ_n can be considered to have been exposed to a wall condition prescribed by $T = F(t - \theta_n + \theta)$. Hence, the appropriate wall boundary condition becomes

[1] Department of Mechanical Engineering, The University of Akron, Akron, Ohio.
[2] Number in brackets designate References at end of technical brief.
Contributed by the Heat Transfer Division of THE AMERICAN SOCIETY OF MECHANICAL ENGINEERS. Manuscript received by the Heat Transfer Division, July 11, 1973.

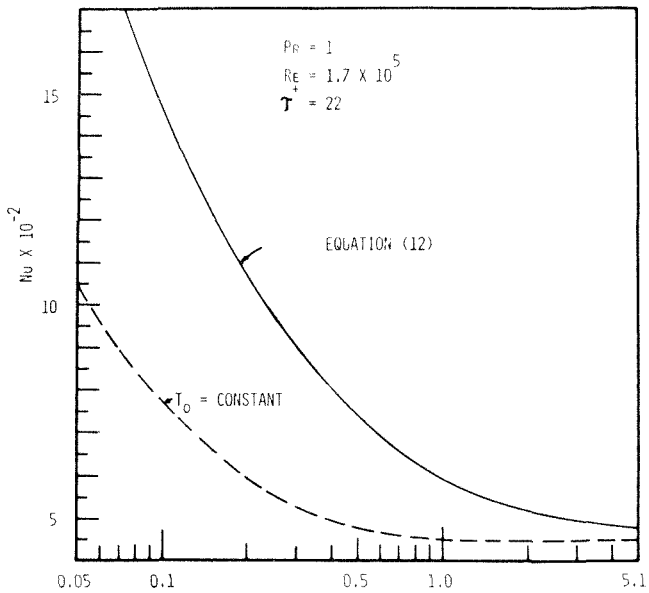

Fig. 3 Prediction for Nusselt number for linear increase in wall temperature

$$\psi(\theta) = F(t - \theta_n + \theta) \tag{6}$$

with $t - \theta_n$ held constant.

The solution of equation (3) with the prescribed conditions and with $\psi(\theta)$ given by equation (6) leads to a relationship for the instantaneous temperature profile within the wall region, $T(t, \theta_n, \theta, y)$. This expression actually represents the temperature history for process time ranging from $t - \theta_n$ to t of the fraction of the surface with contact time θ_n. Because the solution for the mean temperature profile at the process time t is desired, this instantaneous profile must be evaluated at $\theta = \theta_n$. The resulting instantaneous temperature profile $T(t, \theta_n, \theta, y)|_{\theta=\theta_n}$ represents the contribution to the overall mean profile at any given value of t of each θ_n-segment of the surface. Therefore, the mean temperature profile can be written as

$$T(t, y) = \int_0^\infty T(t, \theta_n, \theta, y)\big|_{\theta=\theta_n} \Phi(t, \theta_n) d\theta_n \tag{7}$$

Application

As illustrations of the use of the proposed formulation concept, turbulent boundary layer flow past a flat plate has been considered for several wall temperature conditions [3]. For a linear time-variation in wall temperature, $\psi(\theta)$ becomes $\psi(\theta) = t - \theta_n + \theta$. With this expression for ψ, the proposed analysis gives rise to an expression for $T(t, \theta_n, \theta, y)$ of the form

$$T(t, \theta_n, \theta, y) = T_i \operatorname{erf} X + (t - \theta_n) \operatorname{erfc} X + \theta\left[(1 + 2X^2) \operatorname{erfc} X - \frac{2}{\sqrt{\pi}} X \exp(-X^2)\right] \tag{8}$$

where $X = y/(2\sqrt{\alpha\theta})$. Equations (1), (3), and (8) [with $\theta = \theta_n$] give expressions for $T(t,y)$ of the forms

$$\frac{T(t, y)}{T_0} = \frac{T_i}{T_0}\left[\int_0^{t/\tau} \operatorname{erf}\left(Y\sqrt{\frac{\tau}{\theta_n}}\right) d\left(\frac{\theta_n}{\tau}\right) + \left(1 - \left(\frac{l^+}{\tau^+}\right)^2\right) \operatorname{erf}\left(Y\frac{\tau^+}{l^+}\right) + \left[\frac{4}{3} Y^4 \frac{\tau^+}{l^+} + 2Y^2\left(1 + \left(\frac{\tau^+}{l^+}\right)^2\right) + 1\right] \operatorname{erfc}\left(Y\frac{\tau^+}{l^+}\right) + \right. \left. - \frac{2Y}{\sqrt{\pi}} \frac{l^+}{\tau^+}\left[\frac{2}{3} Y^2 + \frac{2}{3}\left(\frac{l^+}{\tau^+}\right)^2 + 1\right] \exp\left(-Y^2\left(\frac{\tau^+}{l^+}\right)^2\right)\right) \quad \text{for } t \le \tau \tag{9a}$$

and

$$\frac{T(t, y)}{T_0} = \frac{T_i}{T_0} \int_0^1 \operatorname{erf}\left(Y\sqrt{\frac{\tau}{\theta_n}}\right) d\left(\frac{\theta_n}{\tau}\right) + \left[\frac{4}{3} Y^4 \frac{\tau^+}{l^+} + 2Y^2\left(1 + \left(\frac{\tau^+}{l^+}\right)^2\right) + 1\right] \operatorname{erfc} Y - \frac{2Y}{\sqrt{\pi}}\left(\frac{\tau^+}{l^+}\right)^2 \left[\frac{2}{3} Y^2 + \frac{2}{3} + \left(\frac{l^+}{\tau^+}\right)^2\right] \exp(-Y^2) \quad \text{for } t \ge \tau \tag{9b}$$

$$Y = y/(2\sqrt{\alpha\tau}), \quad l^+ = U^*\sqrt{l/\nu} \quad \text{and} \quad \tau^+ = U^*\sqrt{\tau/\nu}.$$

Expressions can also be written for the mean (spatially averaged) unsteady Nusselt number as (for T_i equal to 0)

$$Nu = \sqrt{\frac{f}{2}} \operatorname{Re}_L \sqrt{\operatorname{Pr}} \frac{1}{\sqrt{\pi} l^+}\left[2 + \frac{2}{3}\left(\frac{l^+}{\tau^+}\right)^2\right] \quad \text{for } t \le \tau \tag{10a}$$

and

$$Nu = \sqrt{\frac{f}{2}} \operatorname{Re}_L \sqrt{\operatorname{Pr}} \frac{1}{\sqrt{\pi}\tau^+}\left[2 + \frac{2}{3}\left(\frac{\tau^+}{l^+}\right)^2\right] \text{ for } t \le \tau \tag{10b}$$

Formulation for τ. Because a hydrodynamically steady turbulent flow condition is considered in this study, previous formulations for τ [4] can be adapted. Briefly, these formulations for τ are based on the adaptation of the surface renewal and penetration model to momentum transfer and lead to a relationship for boundary layer flow with $dP/dx = 0$ of the form

$$U^* \sqrt{\frac{\tau}{\nu}} = \frac{U_i}{U^*} \frac{2}{\sqrt{\pi}} \tag{11}$$

where U^* [$\equiv U_\infty \sqrt{f_x/2}$] is the friction velocity, f_x is the local Fanning friction factor, and U_i represents the velocity at the first instant of renewal. With U_i set equal to U_∞, U_i/U^* is simple equal to $\sqrt{2/f_x}$.

Results. Fig. 3 represents the unsteady mean Nusselt number results from equations (10*a*) and (10*b*) as well as Nusselt number results for a step change in wall temperature to T_0 at $t = 0$. Interestingly, the solutions for these two conditions come together for large t/τ.

Concluding Remarks

With the basic concept now in hand, the proposed model can be applied to more realistic situations for which experimental data are available. In this connection, the use of this principle in the analysis of transient heat transfer for turbulent flow over a flat plate with appreciable thermal capacity and a step jump in heat flux is now underway.

Acknowledgment

This investigation was partially supported by the National Science Foundation under grant GK-35883.

References

1 Chung, B. T. F., and Thomas, L. C., "Unsteady Heat Transfer for Turbulent Flow," *Can. J. Chem. Eng.*, Vol. 49, 1971, p. 877.

2 Chung, B. T. F., Fan, L. T., and Hwang, C. L., "The Surface Renewal and Penetration Models in Transient State," *AIChE Journal*, Vol. 17, 1971, p. 154.

3 Thomas, L. C., and Chung, B. T. F., "Unsteady Heat Transfer for Turbulent Flow With Time Dependent Wall Temperature," The University of Akron, Tech. Rept. 73-2, 1973.

4 Thomas, L. C., "Temperature Profiles for Liquid Metals and Moderate-Prandtl Number Fluids," JOURNAL OF HEAT TRANSFER, TRANS. ASME, Series C, Vol. 92, 1970, p. 565.

journal of heat transfer

discussion

Heat, Mass, and Momentum Transfer During the Melting of Glacial Ice in Seawater[1]

R. G. Watts.[2] This is a very interesting and timely paper in that it treats a problem that will surely become increasingly important to those arid regions of the world that are close enough to Antarctica to use fresh water derived from melting icebergs. The solution presented here has merits independent of the particular application to the melting of icebergs, of course. In regard to this particular application, however, I would like to raise the question of whether free convection might be a very important factor. I might add that it enters the problem in a very complex and interesting way. It happens that the density temperature curve for water has a maximum near 4 deg C. Hence, if an infinite flat plate of ice melts in water at, say, 4 deg C the water near the ice is relatively buoyant, and a fairly typical free convection problem results with the cooler liquid near the ice floating upwards. If the water is at 10 deg C the problem becomes more complicated. In the inner part of the thermal boundary layer $d\rho/dy$ is positive, but after the temperature reaches about 4 deg C $d\rho/dy$ becomes negative. What is the flow pattern? When I dunked a colored ice cube in cold water (about 10 deg C) the flow of colored melt was vigorously downward.

When you do this same experiment in salt water things are even more complicated. The fresh water that melts from an ice cube (or an iceberg) is a good deal lighter than the surrounding salt water. The density of the fresh water is about 1 g/cm^3, while that of salt water with a salt content or 35 ppt is about 1.03 g/cm^3. When I repeated the colored ice cube experiment in salt water and injected a little food coloring near the ice for good measure, I found the flow to be strongly *upwards*, except possibly very near the ice where there might have been a slight downward motion.

The buoyancy caused by the concentration gradient is stronger than that caused by the temperature gradient, especially if the water is fairly cold. The density difference between fresh water at 4 deg C and fresh water at 15 deg C is about 0.874×10^{-3} g/cc, compared to $\Delta\rho = 3 \times 10^{-2}$ g/cc for 35 ppt salt water and fresh water.

Finally, note that the ratio Gr/Re^2 using a conservative length scale of 300 m for an Antarctic iceberg and a velocity of 7 m/sec (corresponding to a Gulf Stream) is 2.3. This is computed on the basis of $\Delta\rho = 3 \times 10^{-2}$ g/cc.

[1] By O. M. Griffin, published in the Aug. 1973 issue of the JOURNAL OF HEAT TRANSFER, TRANS. ASME, Series C, Vol. 95, No. 3, pp. 317–323.

[2] Department of Mechanical Engineering, Tulane University, New Orleans, La.

Authors' Closure

The author wishes to thank Professor Watts for his interesting discussion of this paper. The use of Antarctic icebergs as a source of fresh water has recently become a topic of increased interest. A feasibility study has been made of one proposed concept for iceberg towing and harvesting [11],[3] and a detailed appraisal of icebergs as potential fresh water sources has been published this year [12]. These studies have aroused considerable interest in the media [13, 14], perhaps because there are $1.2(10^{12})$m^3 of glacial, or pure, icebergs formed each year in Antarctica.

Free convection heat transfer is often an important factor during the melting of ice, and the complexity of the system is increased because of the density maximum that is found in pure water at 4 deg C. Free convection with melting and freezing in a pure water-ice system has been studied by Boger and Westwater [15] and Yen and colleagues [16, 17, 18], among others. The interesting ice cube experiments described in Professor Watts' discussion seem to take place in a totally free convection environment, and his conclusions are correct from that standpoint.

The melting of glacial ice in seawater is further complicated by the dependence of the density maximum and the freezing temperature on the salinity or the concentration of dissolved species [19], as plotted in Fig. 6. For salinities greater than $\bar{C} = 24.7$ g/Kg there is no density maximum. Using the methods developed in the subject paper, when glacial ice at 0 deg C melts in seawater of 15 deg C and 35 g/Kg salinity, the thickness of the salinity boundary layer $\bar{\delta}_c$ extends over only 35 percent of the thermal boundary layer $\bar{\delta}_t$ and over only 17 percent of the momentum boundary layer $\bar{\delta}_m$. The water temperature at the edge of the salinity boundary layer under these conditions is 9 deg C, and the local water temperature is greater than the local inversion temperature (temperature of maximum density) for $\bar{y} > 0.07\,\bar{\delta}_t$.

If one assumes that a reasonable assessment of the free convection can be obtained from the temperature dependence alone, comparison with Professor Watts' estimates is possible. Buoyancy effects due to both temperature and salinity changes are confined to a thin stable layer near the horizontal undersurface of a large iceberg past which the seawater is in relative motion. If an iceberg 300 m in length is towed at a speed of 6 knots (3.1 m/sec) in water at 15 deg C, then the parameter Gr/Re^2 is equal to 0.12 when based on the density difference $\Delta\bar{\rho}$ in the re-

[3] Numbers in brackets designate Additional References at end of discussion.

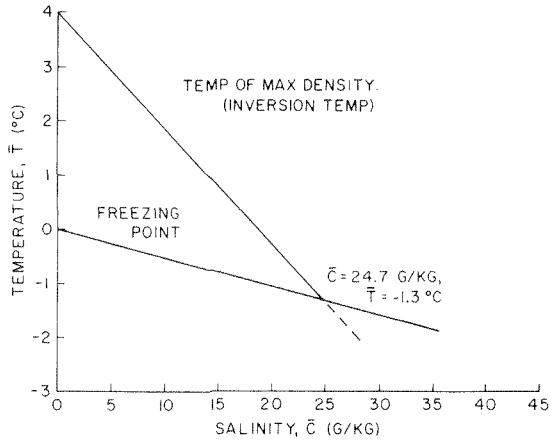

Fig. 6 The variation of freezing point temperature and inversion temperature (temperature of maximum density) with the salinity of seawater. The two temperatures become equal at $\bar{T} = -1.3$ deg C, $\bar{C} = 24.7$ g/Kg.

gion of uniform salinity and variable temperature. When a limiting value of $Gr/Re^2 = 1$ is employed for the same temperature conditions, the corresponding relative speed is 1.1m/sec (2.3 knots). For towing speeds or currents less than this value, the parameter $Gr/Re^2 > 1$ and free convection is likely to become an important factor in the heat transfer process. In his discussion Professor Watts has suggested a current of 7 m/sec as being representative of the Gulf Stream. This is equal to 13.6 knots, and one would not expect to find a current greater than 4–6 knots (2–3 m/sec) in the Gulf Stream.

As Weeks and Campbell [12] point out, there are many important engineering problems to be solved if a feasible and economical system is to be developed to transport and process part of the vast store of Antarctic glacial ice for fresh water supplies. Among the problems that await solution are several that involve both free and forced convection with phase transformation.

The correct form of equation (14) of the subject paper is written as follows:

$$\Delta_2^2 = \left(\frac{\delta_m^{**}}{\delta_c^{**}}\right) \frac{\mathrm{Le}\,\Delta_1 c_1 + a_1 D\,\Delta_2}{\mathrm{Pr}\,\Delta_1 b_1 + a_1 D}.$$

Additional References

11 Cooper, L., "Iceberg Farming: A New Supply of Fresh Water," *Ocean Industry*, Mar. 1973, pp. 28–31.

12 Weeks, W. F., and Campbell, W. J., "Icebergs As A Fresh Water Source: An Appraisal," Corps of Engineers, U. S. Army, Cold Regions Research and Engineering Laboratory (CRREL), Research Report 200, 1973; also published in *Journal of Glaciology*, Vol. 12, No. 65, 1973, pp. 207–233.

13 "Icebergs for the Desert," *Time*, Aug. 20, 1973, p. 57.

14 "Ice Cube for Paul Bunyan Cocktail," *Mechanical Engineering*, Sept. 1973, p. 41.

15 Boger, D. V., and Westwater, J. W., "The Effect of Buoyancy on the Melting and Freezing Process," JOURNAL OF HEAT TRANSFER, TRANS. ASME, Vol. 89, 1967, pp. 81–89.

16 Yen, Y. C., "Onset of Convection in a Layer of Water Formed by Melting Ice From Below," *Phys. Fluids*, Vol. 11, 1968, pp. 1263–1270.

17 Yen, Y. C., "On the Effect of Density Inversion on Natural Convection in a Melted Water Layer," *Chem. Eng. Symp. Series*, Vol. 65, No. 92, 1969, pp. 245–253.

18 Yen, Y. C., and Galea, F., "Onset of Convection in a Water Layer Formed Continuously by Melting Ice," *Phys. Fluids*, Vol. 12, 1969, pp. 509–516.

19 Pounder, E. R., *Physics of Ice*, Chapters 1 and 2, Pergamon, Oxford, 1965.